ERDA

UC62

Proceedings of the ERDA Solar Workshop on Methods for Optical Analysis of Central Receiver Systems

Organized by the
University of Houston Solar Energy Laboratory
for Sandia Laboratories, Livermore
Under ERDA Contract AT (29-1)—789

August 10-11, 1977
Houston, Texas

Sandia Laboratories

University of Houston

DISCLAIMER

NOTICE

Printed in the United States of America
Available from
National Technical Information Service
U.S. Department of Commerce
5285 Port Royal Road
Springfield, VA 22161
Price: Printed Copy ~~$9.25~~ 11.75; Microfiche $3.00

UC 62

ERDA

SOLAR WORKSHOP ON METHODS FOR OPTICAL ANALYSIS OF CENTRAL RECEIVER SYSTEMS

Organized by the
University of Houston Solar Energy Laboratory
for
Sandia Laboratories, Livermore

August 10-11, 1977
In Houston, Texas

ERDA Contract AT (29-1)-789

October 1977

TABLE OF CONTENTS

THIS PAGE

WAS INTENTIONALLY

LEFT BLANK

THIS PAGE

WAS INTENTIONALLY

LEFT BLANK

LIST OF TABLES

THIS PAGE

WAS INTENTIONALLY

LEFT BLANK

TABLE OF FIGURES

TABLE OF FIGURES

THIS PAGE

WAS INTENTIONALLY

LEFT BLANK

INTRODUCTORY COMMENTS

Roy Lee
Sandia Laboratories
Livermore, California

Good morning.

George Kaplan who is the Branch Chief of the Central Receiver Solar System at ERDA headquarters is unable to come because of his involvement with the selection process for the design of the 10MWe pilot plant. He has asked me to say a few words in his behalf. Consequently, this morning I am representing ERDA and Sandia at the same time. First of all, on behalf of ERDA and of Sandia Laboratories, I would like to extend a warm welcome to those attending this solar workshop and hope this workshop will be beneficial to all people here. In the last few years, during the conceptual development of the central receiver solar system, considerable effort has been expended to develop techniques, methodology, and computer codes to study the optical performance of the central receiver system. It is the intention of ERDA to disseminate these techniques and also this collection of computer codes to as wide an audience as possible so that this effort can be put to good use. It is also especially important that prospective contractors and commercial companies, be they small or large, be made aware of these computer codes and techniques so they can make the best use of these efforts for their response to ERDA's request for proposals for future central receiver projects. Therefore, the main purpose of this get together is to disseminate information about the existing state of the art, techniques and computer codes, and also to encourage exchange of information amongst specialists and potential users. Let us hope this workshop fulfills its purpose and will be beneficial for everyone concerned here.

This is the first workshop on the central receiver system, and we would certainly like to have your opinion and feedback on the usefulness of this workshop at tomorrow's session or by phone or in writing.

I would like to take this opportunity to thank the University of Houston for providing facilities and also to thank the Solar Energy Laboratory, especially the people who are involved in the workshop and have expended effort to make the workshop a possibility.

THIS PAGE

WAS INTENTIONALLY

LEFT BLANK

INTRODUCTORY COMMENTS

Lorin Vant-Hull
Solar Energy Laboratory
University of Houston

In his informal greetings to participants of the Workshop, University of Houston Vice-President Barry Munitz mentioned the Solar Energy Laboratory and the Energy Foundation of Texas. I wonder if you would say a few words about those organizations to clarify terms for the group.

Alvin F. Hildebrandt
Solar Energy Laboratory
University of Houston

The Solar Energy Lab was started at the University of Houston three years ago. Professor Vant-Hull and I were the key people from the Physics Department to start the Lab. Since that time, we have been joined by a number of others from the academic disciplines, including Ray Wentworth (Chemistry), William Prengle (Chemical Engineering), and Dr. Waldron who is in the audience today. We have twenty-five faculty and twenty graduate students involved in a summer program to develop proposals and concepts and to submit proposals. Through the years we have submitted programs to ERDA and four proposals on storage. To fund those on a continuing basis, we have formed a consortia between Texas Tech and the University of Houston called the Energy Foundation of Texas. It is essentially a research foundation between the two universities. The main reason for the Foundation is to be responsive to ERDA on proposals. Universities are known for having overhead and financial problems with the state legislatures and, to a certain extent, being somewhat unresponsive to large proposals and large operations. For that reason, the Energy Foundation of Texas was formed to have a rather short response time and to operate more directly responsive to ERDA.

Lorin Vant-Hull

Let me say a few words about our ERDA grant. We have support in that grant for computer code development and also support to develop the code center. This task is two-fold. First, we will document a reasonable set

of our own codes, preparing a users' guide for them, and submitting this set to our own code center. These will be made available for qualified distribution. Second, we will receive codes from those of you who are in a position to submit a reasonably documented code. Surely, HELIOS and MIRVAL will be among the first codes available from the library, and other government funded codes will be following shortly thereafter, I am sure. If anyone has a privately developed code that he wishes to contribute to the library, we would be willing to accept it also.

Later in this session, Dr. Lipps will distribute a preliminary document during one of his talks which will be a preliminary effort to organize the information that will be maintained in the code center.

Mike Walzel is currently designated as the coordinator of the code center, although he has not as yet had an opportunity to respond to the code center requirements. Our funding became effective only a month or so ago. He, Fred Lipps, and I will attempt to ensure that our inventory of documented codes is kept reasonably up to date and available. We will not be operational, in any sense, for several months, for our University computer is currently being converted from Univac to Honeywell, and we must become familiar with Honeywell operations before we undertake any operations with contributed codes--reading them, translating them into a form compatible with ours or any other computer, etc. I think there are substantive problems involved in translating or transferring codes from one computer to another, and I am not yet sure how these problems will be resolved.

I would now like to turn the floor over to Roy Lee who will chair the first technical session.

FUNDAMENTAL PHYSICS OF CONE OPTICS AND THE SIMULATION OF SOLAR-THERMAL SYSTEMS

George L. Schrenk
Department of Mechanical Engineering
University of Pennsylvania
Philadelphia, PA 19171

ABSTRACT

New and powerful analytical techniques were developed in the early 1960's for the design and analysis of solar-thermal energy conversion systems for space power applications; these techniques are also most useful in the design and analysis of terrestrial solar-thermal systems. The primary uniqueness of these techniques is that they are based on the fundamental physical realizations that we have an extended finite-sized source and that the resultant radiation transfer must therefore be analyzed using cones, either infinitesimal or finite, rather than optical rays as the basic vehicle for energy transport. Classical analytical optical procedures do not deal with the energy flux distribution in the image of an extended source. Accordingly, direct analytical methods and their accompaning computer codes have been developed for using finite-sized cones to treat the finite size flux distribution on any arbitrarily shaped absorber surface. These analytical methods include provisions for evaluating the effects of both concentrator surface errors and orientation errors. Moreover, a unique distinction is made between the prediction of the performance of a solar concentrator before it is actually built and calculation of the performance on a solar concentrator after construction. Utilizing the physical insights gained from these direct analytical methods, a comprehensive approach to the design, analysis, testing, and operational use of solar-thermal systems has been developed and will be presented. The accompanying computer codes, originally written as large FORTRAN IV programs, have recently been rewritten in APL on the APL-PLUS Scientific Time Sharing Corporation System. As a result, an extremely powerful and versatile interactive mathematical solar simulator has been created. APL-PLUS service is readily available on a nationwide basis; thus, it is quite easy for anyone, even with only limited programming experience, to utilize these existing APL routines.

INTRODUCTION

A central problem with solar-thermal energy conversion systems utilizing focusing solar concentrators is the efficient concentration of an adequate quantity of diffuse solar energy into a sufficiently confined space and the subsequent absorption thereof at the desired, often rather high, operating temperatures. Furthermore, these desired temperatures must be appropriately distributed and maintained over a range of power demands and environmental operating conditions without exceeding local material design limitations. The problems are similar in nature both for distributed systems (wherein each concentrator has its own absorber) and for central tower systems (wherein a large field of concentrators utilize a single absorber). In addition thermal energy storage may also be used to stabilize system operation in the presence of wide variations in input flux and output load.

Extensive work was carried out by this author and coworkers in the 1960's (Ref. 1-9) to develop general mathematical simulation procedures to analyze various solar-thermal energy conversion systems proposed for space-power systems. Almost all of this work is directly applicable to the systems under consideration today. The primary uniqueness of this work is in the realizations that we have an extended finite-sized source and that the resultant radiation transfer must be analyzed using cones, either infinitesimal or finite, rather than optical rays as the basic vehicle for energy transport. Classical analytical optical procedures primarily deal with information transfer and resolution, not with the energy flux distribution in the image of an extended source. Accordingly, procedures were developed for using finite-sized cones to treat the finite size of the solar source and therefore to calculate the energy flux distribution on any arbitrarily shaped absorber surface. Direct analytical methods and their accompanying computer codes were developed--methods that not only can be faster in computer time than alternative Monte-Carlo ray trace codes but also can offer additional valuable physical insights.

These analytical methods include provisions for evaluating the effects of both concentrator surface errors and orientation errors. Moreover, a distinction is made between the prediction of the performance of a solar concentrator before it is actually built and the calculation of the performance of a solar concentrator after construction. In the first case, before a solar concentrator is constructed, only the most probable

solar flux distribution can be predicted at any one point in time. To do this, a statistical description of the reflector surface contour (accuracy) must be used. This requires a priori knowledge about the surface and must therefore be based on engineering judgment.

After construction of a solar concentrator, the basis of the calculation of the solar flux distribution on the absorber surface is deterministic rather than probabilistic. The concentrator is now a unique, existing entity from which the actual surface contour can be measured. Only through a detailed measurement of the surface contour and its optical characteristics can sufficient information be specified about the solar concentrator to allow a unique simulation of its performance at any given point in time. This is most readily accomplished through the use of various types of experimental ray trace procedures (Ref. 4). Thereafter, the calculation proceeds via the actual reflector contour rather than the hypothetical route.

MATHEMATICAL SOLAR SIMULATOR

The broad scope and generality of this mathematical solar simulator can readily be seen from the following outline of the available input parameters:

Mathematical Solar Simulator Input Specifications

I. Source Parameters
   A. Solar half angle
   B. Source type
      1. Uniform
      2. Limb darkening

II. Reflector and Surface Parameters (including blockage effects)
   A. Arbitrarily shaped hypothetical reflector surface
      1. Perfect surface
      2. Imperfect surface (statistical errors of all sizes)
         a. One-dimensional normal distribution applied to surface normals
         b. Two-dimensional normal distribution applied to surface normals
   B. Actual reflector surfaces (as determined by experimental ray trace procedures)

III. Orientation Parameters
   Orientation errors of all sizes

IV. Vignetting Parameters*
   Arbitrary shape, position, size, and orientation of opening

V. Focal Surface Parameters
   Arbitrarily shaped focal surface

* The term vignetting refers specifically to blockage of reflected light by a cavity opening. This is in contrast to the term blockage, which is used to refer specifically to blockage (shadowing) of incident light on the reflector.

The fundamental equation that must be evaluated for a given point (infinitesimal area) on a receiver surface is

$$I/I_o = \iint_{\text{concentrator surface}} \frac{T P \cos\gamma'}{\pi \ell^2 \tan^2\alpha' \cos^3\zeta} \times \frac{\cos\gamma''}{C'} dA$$

where

I/I_o = concentration ratio for the specified point (x', y', z') on the receiver surface

T = coefficient of reflectivity of the surface of the concentrator

dA = infinitesimal area of the concentrator perpendicular to the principal axis of the concentrator (i.e. the projected area) located around the point (x_o, y_o, z_o)

P = the probability that the area at the point (x_o, y_o, z_o) of the concentrator contributes to the energy flux at (x', y', z'). $(0 \leq P \leq 1)$ *

α' = solar half angle

γ' = angle between surface normal of receiving surface (A_f, B_f, C_f) and line from (x_o, y_o, z_o) to receiving surface point (x', y', z')

ℓ = distance from (x_o, y_o, z_o) to receiving surface point (x', y', z')

ζ = angle between line from (x_o, y_o, z_o) to receiving surface point (x', y', z') and center line (central ray) of reflected cone

(A', B', C') = direction cosines of concentrator surface at (x_o, y_o, z_o)

γ'' = angle between center line(central ray) of incident cone and the concentrator surface normal at (x_o, y_o, z_o)

This equation is exact for a uniform solar disk. An energy flux distribution is obtained by evaluating this double integral over the concentrator surface for various values of (x', y', z') and (A_f, B_f, C_f). Furthermore, it is not necessary to restrict ourselves to uniform solar disks; this equation can easily be expanded to include Limb Darkening effects.

* For a perfect concentrator, P takes on only two values-1 or 0-depending on whether $\zeta \leq \alpha'$ or $\zeta > \alpha'$, respectively. For an imperfect concentrator, P can take any value between 0 and 1.

A detailed description of this mathematical solar simulator is beyond the scope of this paper; a more complete description is given in Ref. 2-4. As can readily be seen, the output of this simulation is the energy flux distribution on a specified absorber surface--assuming a specific definite orientation error; such results must then be integrated over "typical" operating days with an appropriate statistical distribution of orientation errors being folded into the result.

The power of this mathematical solar simulator can best be seen by examination of some typical results.

The importance of surface contour and orientation accuracy can be easily understood by examination of the incident flux distribution on a plane focal surface perpendicular to the optical axis and intersecting the optical axis at the point source focus. Let the source be a uniform disk subtending a half angle of .00465 radians (approximately 16 min. of arc). Let

σ_x = circumferential standard deviation of the surface normal;

σ_y = radial standard deviation of the surface normal

I = local concentration ratio of reflected light. Multiplication of I by the solar constant and the coefficient of reflection results in the actual energy flux per unit area incident on a given focal surface point;

β = polar orientation angle between the central ray from the sun and the optical axis of the reflector;

$\eta_{collection}$ = power concentrated in area πr^2 as a fraction of the total power reflected from the reflector**

** Total power reflected from the reflector = (coefficient of reflection) x (total power incident on the reflector); r denotes the focal plane radius.

Figure 1 shows the effect of surface contour errors on the performance of a perfectly aligned parabolic concentrator. Figure 2 shows the effects of solar misorientation on the performance of a parabolic solar concentrator with a perfect surface. However, since no energy transformation occurs at this point in an actual system, these results, though valid for the determination of $\eta_{\text{collection}}$ can be taken only in a qualitative sense for design purposes. These results show, for example, the extreme sensitivity of collection efficiency to both surface and orientation errors. The random errors of the surface normals which are related to concentrator fabricational techniques are most instrumental in spreading the reflected flux beyond a fixed aperture in the focal plane. The flux spreading due to misorientation is largely directional and can be compensated somewhat by automatic control of the concentrator and cavity locations.

Either a one or two dimensional normal distribution of surface normals is employed in this simulation to predict the most probable performance of a solar concentrator before it is built. Other choices of error distribution functions and frames of reference are possible and have been employed. For example, a normal distribution function can be applied to a scattering of points in a focal plane (Ref. 4). Such a choice, however, is a superficial approximation bearing no relation to the fabricated structure. For a distribution function to have any relevance to manufacturing procedures, it must be applied directly to the surface normals; only the choice of distribution function remains unanswered.

Considerable research has been devoted to establishing the validity of the normal distribution as applied to surface normals. While the question has not been answered for all conceivable types of solar collectors, those studied to date have been found to possess surface error characteristics that are reasonably well represented by a normal distribution applied to surface normals. For example, experimental ray trace data (Ref. 5) taken on the TAPCO S/N 4 reflector and reduced to σ_x's and σ_y's in the mathematical solar simulator is shown in Figure 3. This figure represents the actual cumulative probability distribution plots referred to a normal distribution taken about the mean errors. The data consisted of 5771 individual ray intercept points measured by TAPCO's grid inspection technique (Ref. 5). As would be expected from detailed investigation over the reflector surface, the local values of σ_x and σ_y can vary considerably from hub to rim

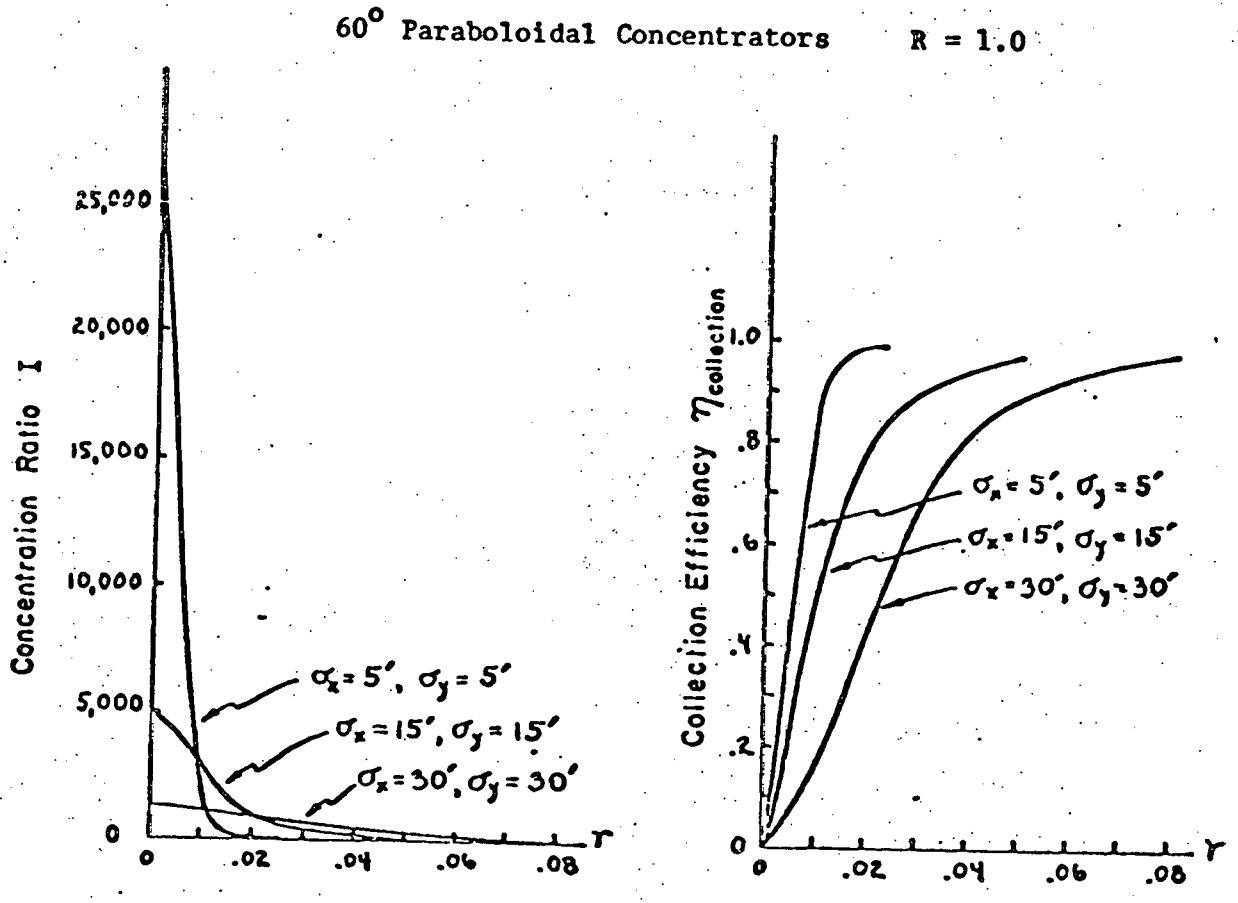

Figure 1. Surface error effects for a 60° paraboloidal solar concentrator with perfect solar orientation; r= focal zone radius, R= concentrator radius

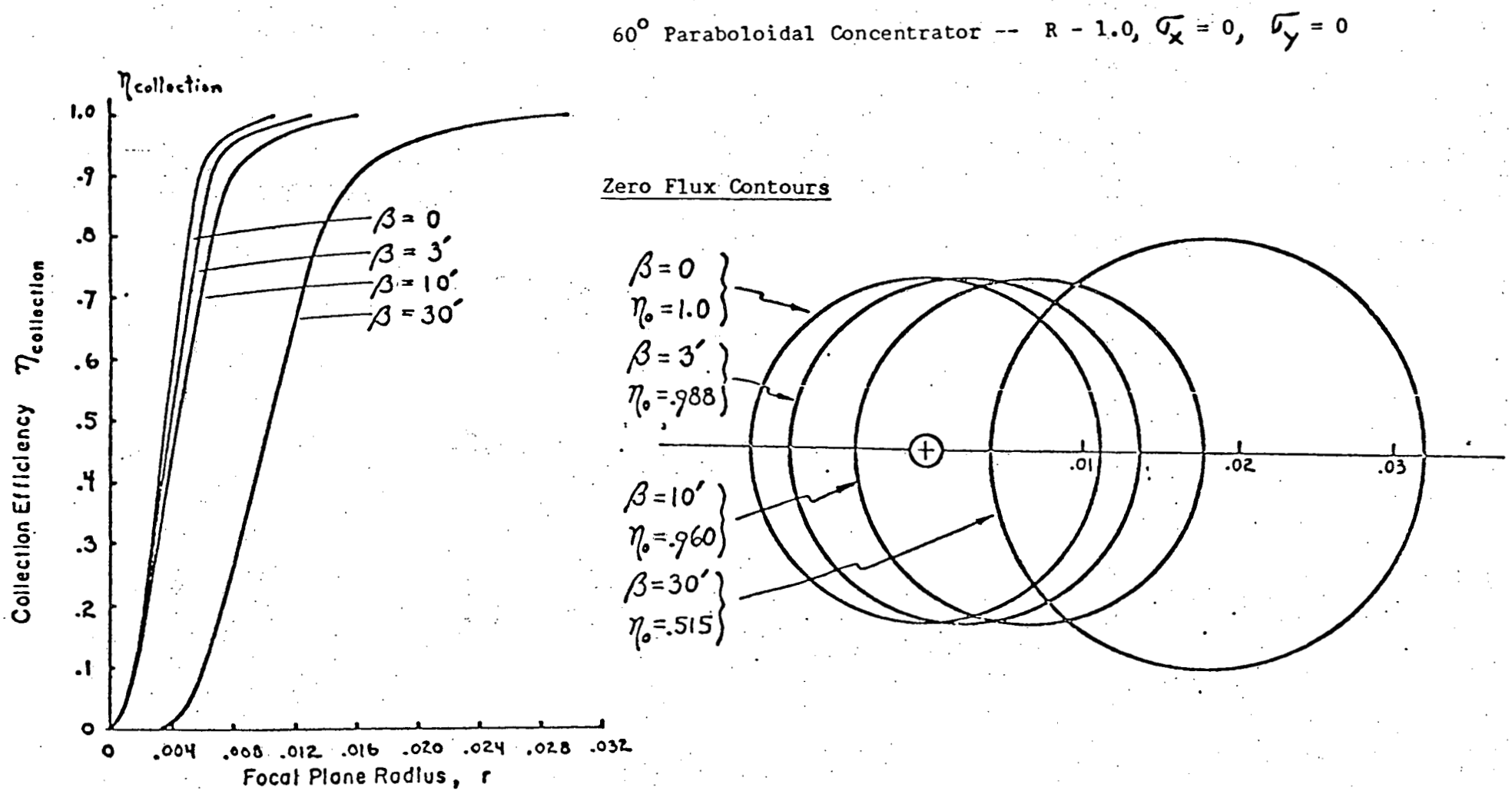

Figure 2. Orientation effects for a 60° paraboloidal concentrator with a perfect surface contour. η_0 =% of energy collected within a circle of radius .011 centered about the principal axis.

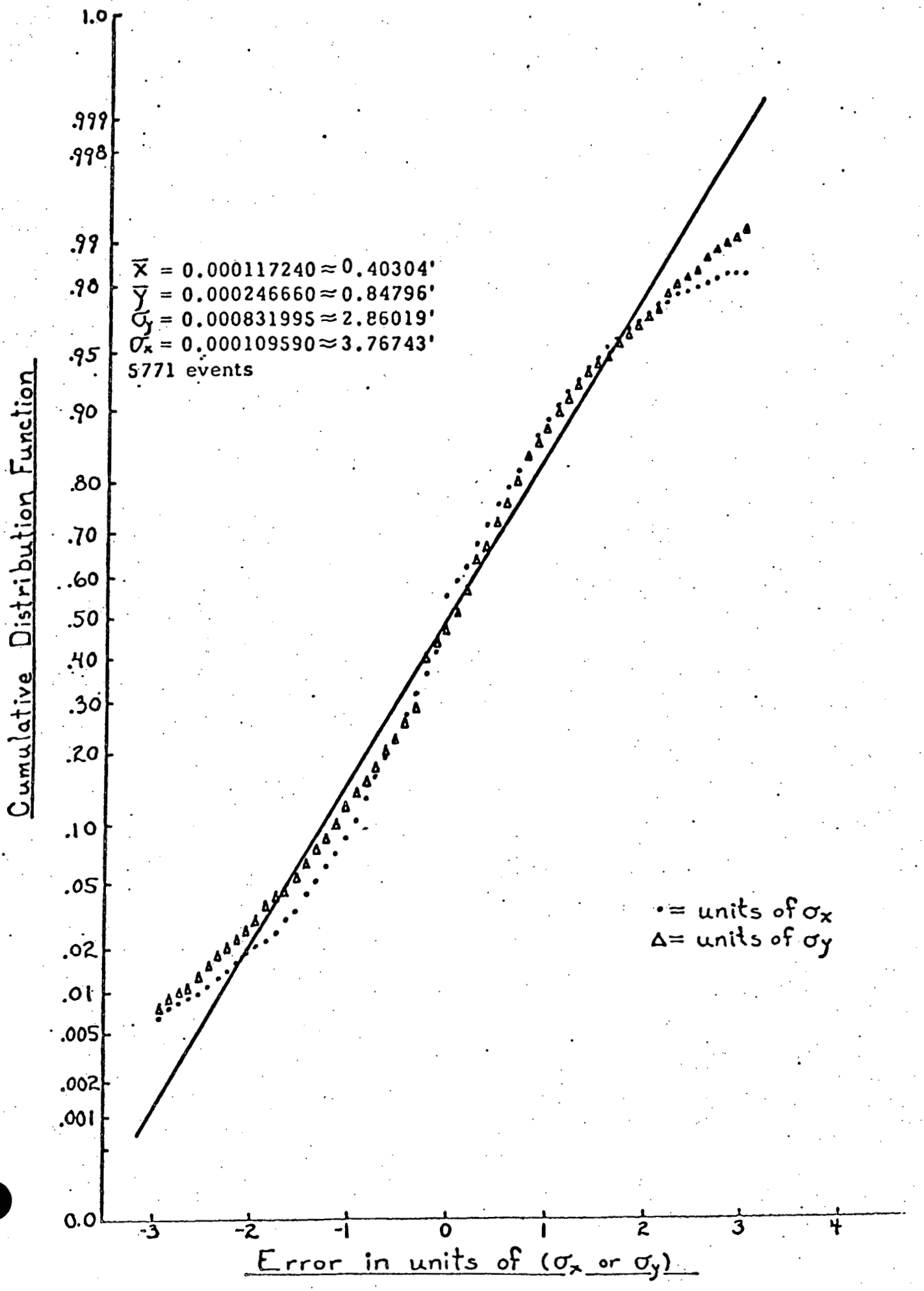

Figure 3. Surface error distribution for the TAPCO S/N 4 solar concentrator.

and from azimuthal zone to another. For this TAPCO reflector by sorting the data into a number of small azimuthal and radial zones, it was found that σ_x ranged from 1.3' to 9.8' and σ_y varied from 1.0' to 4.8'.

As pointed out previously, useful quantitative results from a solar concentrator simulation require a determination of the actual flux distribution on the absorber surface itself (as opposed to a plane focal surface). This requires, in turn, that a particular focal zone surface be specified prior to use of the mathematical solar simulator. Figure 4 shows the distribution of incident solar flux on the walls of a typical cylindrical cavity absorber with surface errors as specified thereon. The sharp variation of flux distribution on the cylinder is readily apparent and suggests that radical means would be necessary in cavity design to equalize the resultant temperature and net heat transfer distributions if this configuration is to be employed with a heat exchanger expecting a reasonably uniform flux distribution. The spherical cavity configuration shown in Figure 5 obtains a considerably more uniform flux distribution. The large difference in flux level between Figures 4 and 5 is due to the relative sizes chosen for these cavities in obtaining these sample results and is not inherently related to the cavity configurations.

SOLAR-THERMAL INTERFACES

Fundamental to solar-thermal energy conversion systems is a thorough understanding of the solar-thermal interface.

This mathematical solar simulator has allowed us to explore in detail the appropriate interfaces between various system components. For example, the concentrator/cavity-absorber interface has been explored in detail. Plane focal surface results have been used in the past both as a means of comparing various concentrators and for optimizing concentrator designs. The validity of this approach, however, is rather dubious. This approach was based on the premise that the prediction of the performance of the heat receiver could effectively be isolated from the reflector. More specifically, it was usually assumed that reradiation losses from the heat receiver could be calculated as if the cavity opening were a simple gray body. The reflector design was then optimized on the basis of this simple prediction of reradiation losses.

TAPCO S/N 4 is a 5.0 ft. diameter 60° rim angle paraboloidal reflector fabricated from eight rigid aluminum honeycomb-sandwich segments.

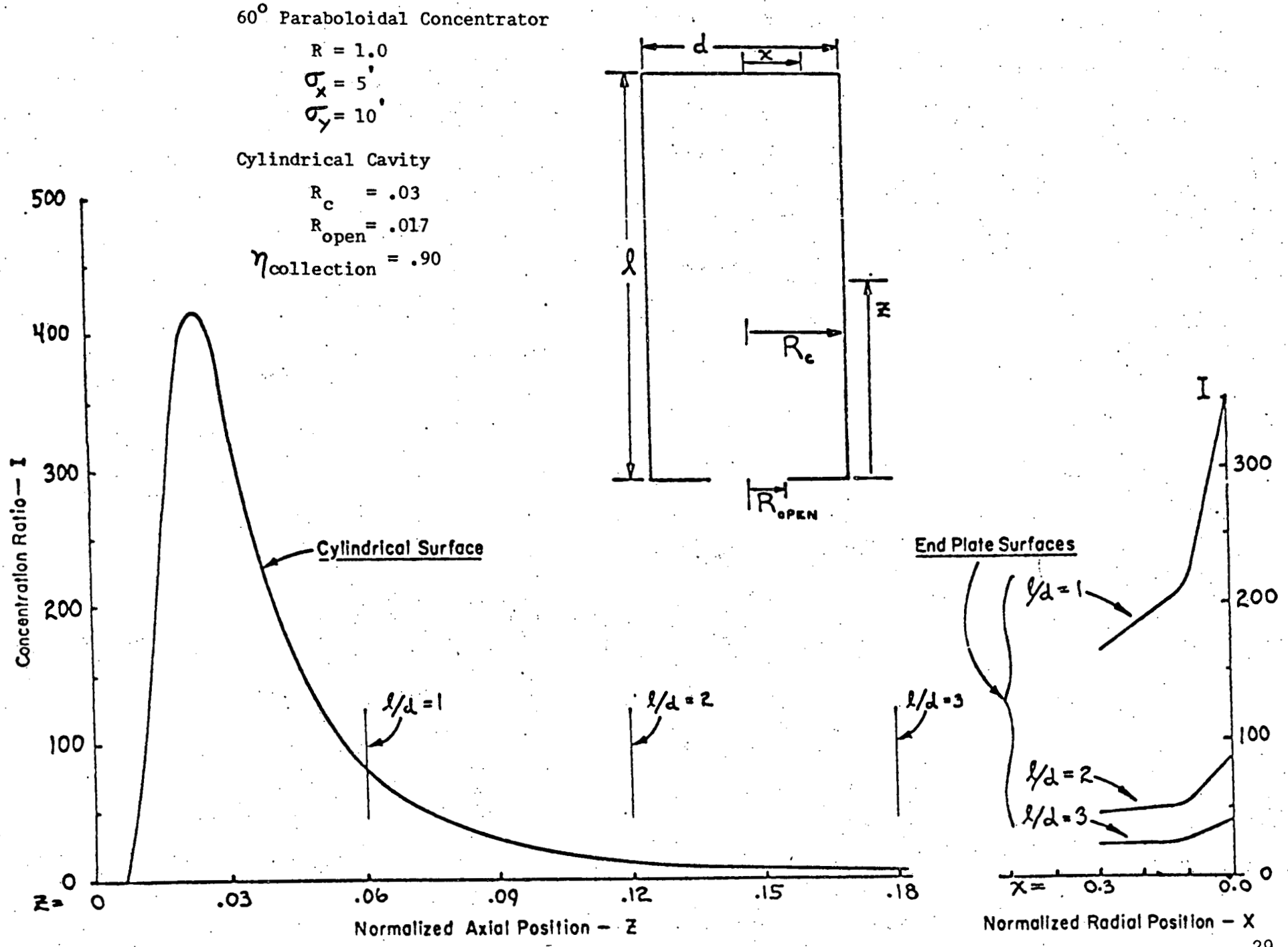

Figure 4. Incident solar flux distribution on the walls of a typical cylindrical cavity.

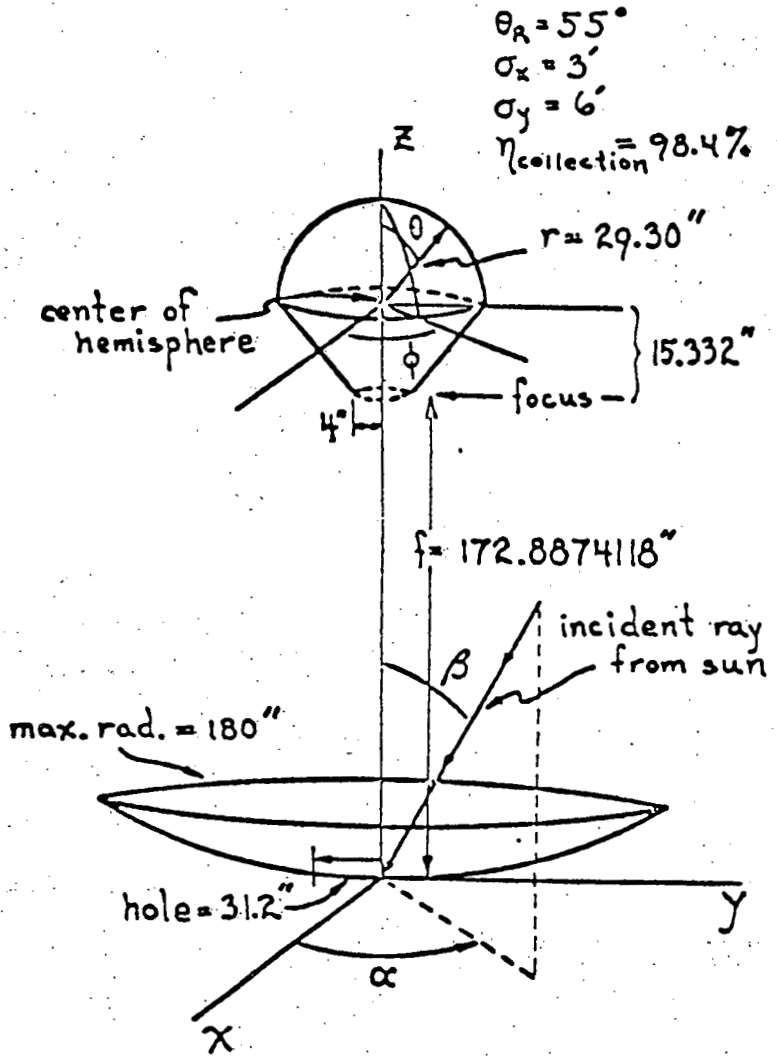

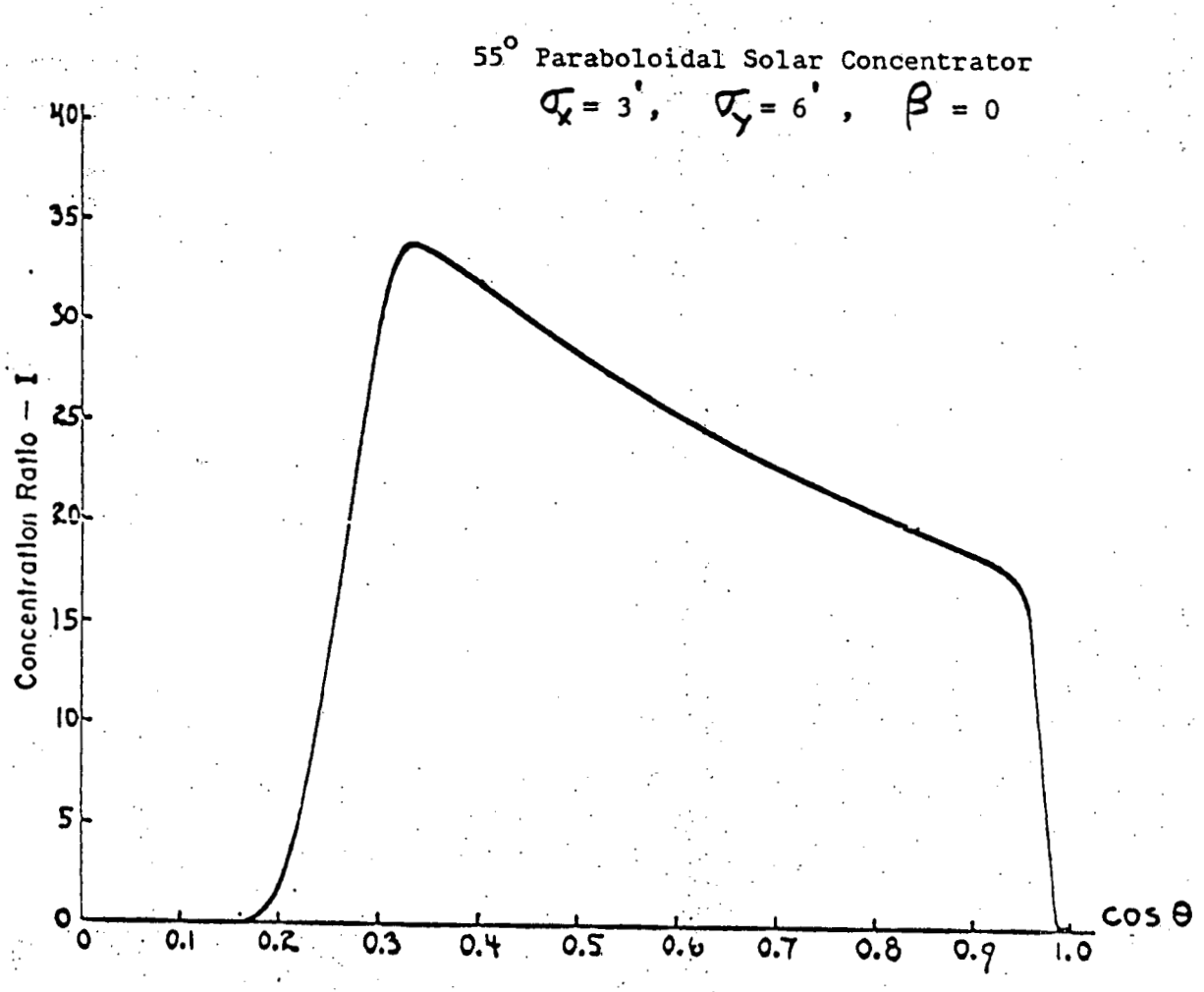

Figure 5. Incident solar flux distribution on the walls of a typical hemispherical cavity.

Detailed calculations of heat receiver performance have shown that the assumption that the cavity opening can be considered as if it were a simple gray body is incorrect; in fact, the reradiation losses for high temperature cavities are usually much greater than would be expected from simple gray and/or black body cavity concepts (Ref. 1,2,10). Thus, the optimization of the concentrator design can no longer be considered independent of the cavity; instead, they must be optimized as a system. Detailed calculations of the heat receiver performance are essential.

Now, in the detailed prediction of cavity performance another question arises that makes the usefulness of plane focal surface results even more dubious. In order to calculate the performance of the cavity, it is necessary to know the energy flux distribution on the walls of the cavity. Before the development of this extended mathematical model (Ref. 3), it was not possible to calculate this energy flux distribution directly. Instead, it was necessary to take plane focal surface results and make a crucial assumption about the directional distribution of the radiation entering the cavity. The directional assumption ordinarily made (Ref. 7,8) is that the cavity opening can be treated as if it were a plane surface that emitted radiation according to Lambert's Law (i.e., the cosine law). Thus, the predicted energy flux on plane focal surfaces was used--via Lambert's law--to calculate the solar energy flux incident on the walls of the cavity. Clearly, this type of approach tends to isolate the study and design of the cavity from that of the reflector, although to a lesser degree than the simple gray cavity approach. (An alternative assumption occasionally made is that the energy flux distribution on a spherical surface is uniform (Ref. 9). This can also be shown to be in substantial error - see Fig. 5). With the development of this generalized mathematical model (Ref. 3) is was possible for the first time to investigate this assumption. Various systems have been analyzed (Ref. 1,10) and the results clearly indicate that Lambert's Law is in substantial error for both perfect and imperfect concentrators. In fact, the variations are often such that the use of this assumption for the design of a system could lead to significant problems and/or failures. Figure 6 shows a typical flux distribution on the walls of a cylindrical receiver. The concentrator cannot be isolated and independently optimized from the absorber; they must be studied as interacting components of a total system with the system being optimized from a total system view-point.

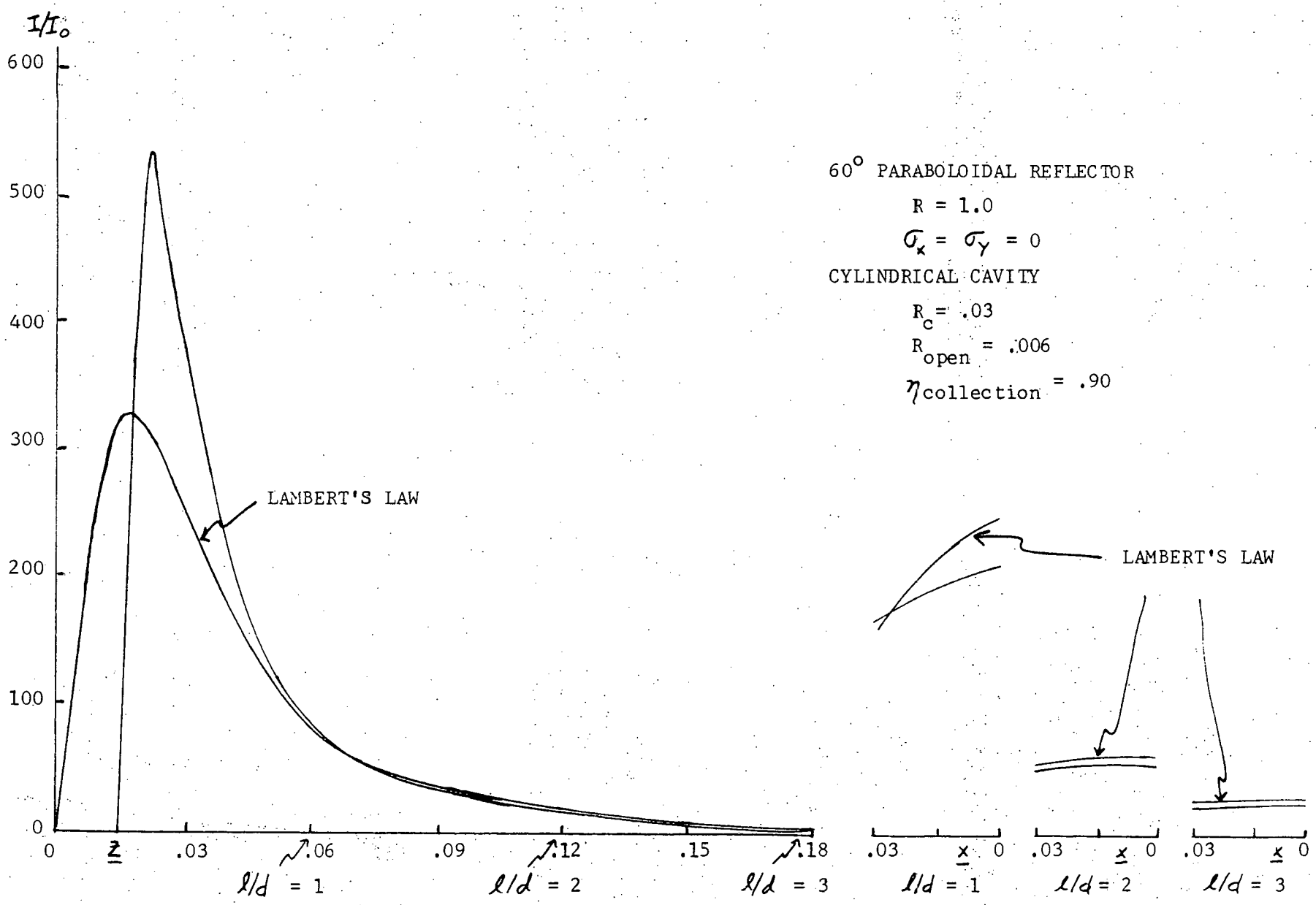

Figure 6. Incident energy flux on the walls of a typical cylindrical cavity for a 60° paraboloidal reflector with $\sigma_x = \sigma_y = 0$.

The next step is the simulation of the cavity absorber system--the intermediate link in the energy transformation between the solar concentrator and the conversion subsystems. Its interface with the solar collector is the solar flux distribution on the cavity wall, as determined above, while its interface with the conversion subsystems is taken at the same physical surface and is described by a specification of the net local heat transfer rate as a function of cavity wall (interface) temperature.

Because of the many variables present in the specification of a cavity configuration, a cavity absorber does not readily lend itself to a generalized design analysis. To date, only specific geometries have been explored. While it is not appropriate to go into specifics in this paper, the results and experience that have been obtained clearly show that the cavity can be a major design problem (Ref. 1,9,10); a very detailed cavity analysis must always be made in order to estimate cavity performance accurately. Furthermore, since the incident flux distribution on the cavity wall is a function of the actual concentrator configuration used and since the cavity wall temperature distribution is a function of whatever connects to the cavity walls (thermal energy storage material (Ref. 9), heat exchanger, etc.) the cavity cannot be studied and optimized independently. A total systems approach must be utilized.

As readily apparent, this solar simulator is not restricted to paraboloidal concentrators with cavity receivers. It is fully applicable to various central receiver systems with the appropraite inclusion of shading and blocking effects in the definition of the concentrator surface. It is also applicable to various distributed systems - e.g., line-focus spherical concentrators (Figure 7 shows the solar flux distribution of a spherical concentrator line-focus system - Ref.11)

MATHEMATICAL SIMULATOR STATUS

The mathematical solar simulator described herein was originally made operational as large FORTRAN IV programs. More recently the original optics programs have been rewritten in APL on the APL-PLUS Scientific Time Sharing Corporation System. As a result of combining the power and versatility of APL with these direct analytical methods, an extremely powerful and versatile interactive mathematical solar simulator has been created.

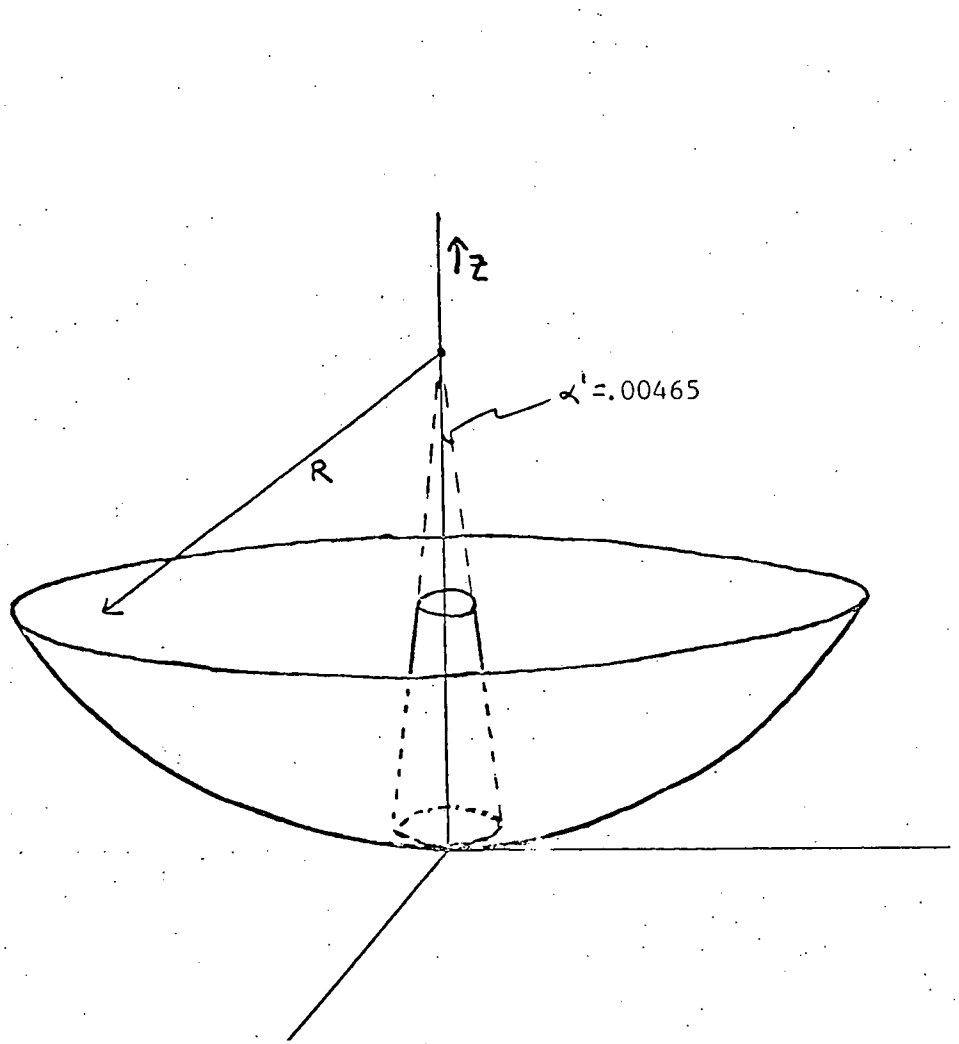

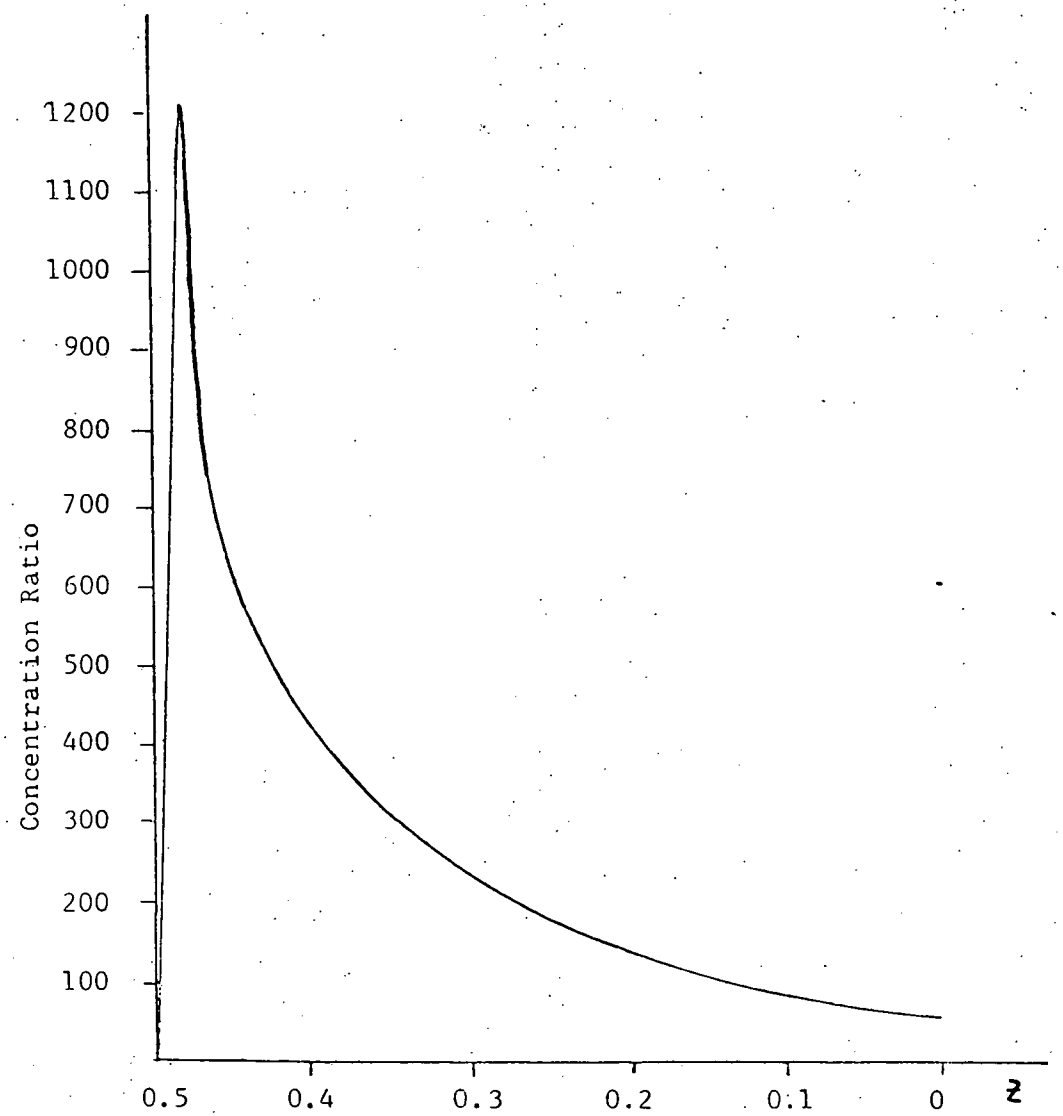

Figure 7. Incident solar flux distribution on the surface of a conical absorber from a perfect 60^{o} line focus spherical concentrator. R = 1.0 ; the paraxial focus is at z = 0.5. Note that the conical absorber is the minimum sized surface that can be used to receive all the reflected solar energy; the half-angle of the cone is the same as that of the sun.

APL-PLUS service is readily available on a nationwide basis; thus, it is quite easy for anyone, even with only limited programming experience, to utilize these existing APL routines - without the numerous difficulties inherent in making large programs operative on different computers.

CONCLUSIONS

The design of a solar-thermal energy conversion system depends on a large number of parameters that relate to the characteristics of the solar concentrator and the absorber. Some of these parameters are readily amenable to experimental determination; others are not. A balanced experimental-mathematical simulation procedure for the solar-thermal subsystem has been described. This procedure has been demonstrated to be capable of quantitative evaluation of the variables critical to the design of a realistic solar-thermal energy conversion system.

The basis for an actual system design cannot be inferred from the specific results presented in this paper. These results have been presented solely to illustrate the power of the tools now available and to indicate problem areas which must be subjected to a thorough parametric investigation for any proposed design. Furthermore, once a design is obtained and reduced to practice, these same simulation tools can be used to evaluate the performance of the hardware.

A mathematical model for analysis of actual solar concentrators has been developed. This solar concentrator model is truly a mathematical solar simulator; thus it is a necessary and indispensable tool in any realistic systems study involving a solar concentrator. Because of the broad scope and generality of this model and the ease of availability through the nationwide Scientific Time Sharing Corporation APL-PLUS Network, its perfection now provides the solar-thermal energy conversion system designer with tools that have been heretofore unavailable. Its use can lead to substantial economies--both in time and in money--in the design, construction, and testing of solar-thermal energy conversion power systems.

References

(1) Schrenk, G., "Solar Collection Limitations for Dynamic Converters," PROC. OF AGARD CONFERENCE, Cannes, France, March 16-20, 1964.

(2) Schrenk, G., Lowi, A., and Wright, G.C., "Analysis of Solar Thermal Energy Conversion Systems," AEROSPACE CORP. REPORT, in preparation.

(3) Schrenk, G., "Final Report - Analysis of Solar Reflectors - Mathematical Theory and Methodology for Simulation of Real Reflectors," AIR FORCE CONTRACT AF04(696)-335, ALLISON DIVISION GMC., EDR 3693 (16 December 1963).

(4) Schrenk, G., "Final Report - Analysis of Solar Reflectors - Mathematical Theory and Methodology for Error Model Synthesis from Experimental Ray Trace Data," AIR FORCE CONTRACT AF04(695)-335, ALLISON DIVISION GMS., EDR 3958 (1 September 1964).

(5) Castle, C. H., TRW Electromechanical Division, private communication, 28 August 1964.

(6) Schrenk, G., and Lowi, A., "Mathematical Simulation of Solar-Thermionic Energy Conversion Systems," PROC. OF THE INTERNATIONAL CONFERENCE ON THERMIONIC ELECTRIC POWER GENERATION, IEE, London, 20-24 September 1965.

(7) Lowi, A., "Radiation Transfer Theory and Methodology for Design of Cavity Type Solar Absorbers," DEPT. OF ENGINEERING REPORT (unpublished), Univ. of California, (10 January 1962).

(8) Wright, C. C., "Development of a Computer Program Subroutine for the Cavity-Absorber Heat Exchanger," AEROSPACE CORP. REPORT A62-1765.36-6 (3 December 1962).

(9) McKinnon, R. A., Turrin, A. D., and Schrenk, G., "Cavity Receiver Temperature Analysis," AIAA SECOND ANNUAL MEETING, San Francisco, California, July 26-29, 1965, AIAA Paper No. 65-470.

(10) Schrenk, G. L., "The Role of Simulation in Solar-Thermal Energy Conversion Systems Development," PROCEEDINGS 1972 SUMMER

SIMULATION CONFERENCE, pp. 833-846.

(11) Schrenk, G. L., "The Role of Simulation in the Development of Solar-Thermal Energy Conversion Systems," PROCEEDINGS 11th INTERSOCIETY ENERGY CONVERSION ENGINEERING CONFERENCE, September 12-17, 1976.

THIS PAGE

WAS INTENTIONALLY

LEFT BLANK

IMAGE GENERATION FOR SOLAR CENTRAL RECEIVER SYSTEMS

Michael D. Walzel
Solar Energy Laboratory
University of Houston
Houston, Texas 77004

ABSTRACT

Computer programs developed at the University of Houston Solar Energy Laboratory involving the calculation of images formed by heliostats comprise an integral part of the system simulation, optimization and design phases for the solar tower method of solar energy collection. Four subroutines are currently available. The routines vary in method, capability, computer time requirements, and accuracy.

Two subroutines can simulate flat polygonal reflectors. A subroutine called FLASH provides an exact analytic result for reflected sunlight. The sun is represented by an analytic function, and an integration is performed over the visible portion of the sun as viewed from selected nodes on an image plane. HCOEF is a subroutine utilizing Hermite polynomials resulting in an analytic function for the image which may be evaluated at any point on the image plane. The Hermite function method is much faster, but less accurate than FLASH.

Two other subroutines can handle arbitrary reflector surfaces and boundaries. Initially a set of central rays from the sun is traced to the image plane for a selected set of nodes in the mirror surface. SUNCONE places a solar image of correct size and power at each ray's impact point. This neglects the size of the mirror element which the ray represents. HFOCUS, a modification of HCOEF, uses the same set of impact

points to find moments for the mirror as required by the Hermite function method. The moments of the image approach their analytic values to an extend dependent upon the number of traced rays.

1.0 INTRODUCTION - IMAGE GENERATION FOR SOLAR CENTRAL RECEIVER SYSTEMS

Fortran subprograms which calculate the flux of sunlight from a heliostat on an image plane comprise that portion of the system simulation package known as image generators. Nested within loops of the calling program, YEAR, these subroutines can be called to compute flux for any heliostat location for any time of the year. Coupled with associated subroutines, image generators provide interception fractions, aiming strategy, and flux maps on a receiver. These outputs are necessary for the simulation, optimization and final performance data needed to design and characterize a solar central receiver system.

Four subprograms named FLASH, HCOEF, SUNCONE and HFOCUS are available for constructing images. The calling structure is devised so that either FLASH, HCOEF or TRACE can be called from YEAR. TRACE is a ray tracing subroutine which calls either SUNCONE or HFOCUS.

A configuration common to all the image generators and every image generated is the relationship between the sun, heliostat and image plane. (Figure 1) The unit normal at the origin of the heliostats' reflecting surface, $\hat{w}$, bisects the angle between a central ray of the sun, $\hat{s}_o$, and the optic axis, $\hat{r}_o$. $\hat{r}_o$ is a unit vector oriented along a line from the center of the heliostat to the origin of the image plane. The orthogonal unit vectors $\hat{u}$ and $\hat{v}$ lie in the plane of the heliostat while $(\hat{x},\hat{y},\hat{r}_o)$ orients the image plane. The distance along $\hat{r}_o$ from the heliostat to the image plane is called the slant range.

The origin of the image plane is located at the center of the receiver. The philosophy of receiver subroutines is to take the intermediate image plane step to allow several receivers to be studied from one set of images. The points on the receiver which require a flux evaluation are projected parallel to the optic axis to a point in the image plane. The value of that flux multiplied by the cosine of the angle of incidence on the receiver results in an adequate evaluation of the receiver flux since the distance of the projection

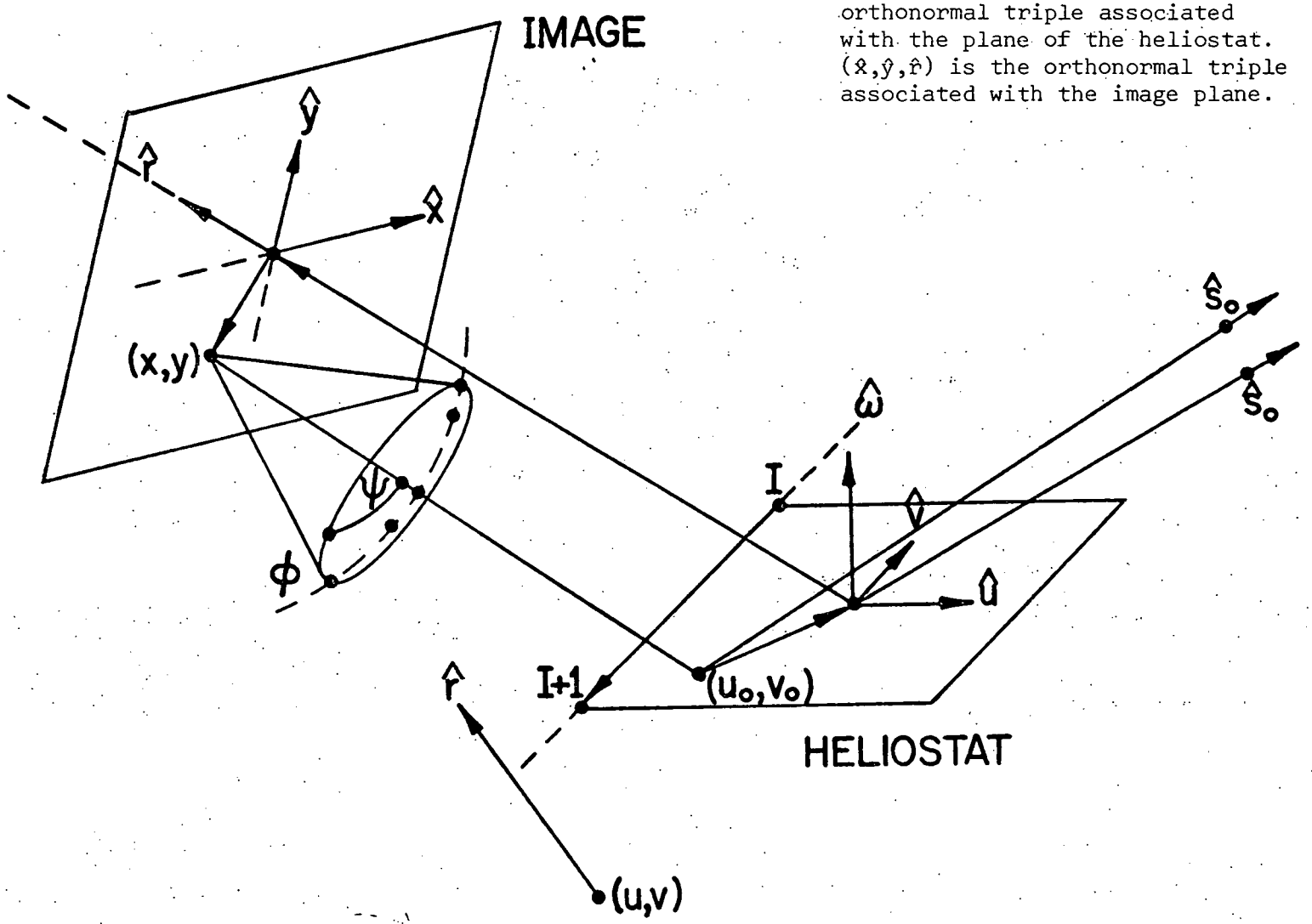

Figure 1. Shows the geometry of the image-forming process. $(\hat{u},\hat{v},\hat{w})$ is the orthonormal triple associated with the plane of the heliostat. $(\hat{x},\hat{y},\hat{r})$ is the orthonormal triple associated with the image plane.

to the image plane is small compared to the slant range.

2.0 FLASH

The method employed by FLASH is based upon an incoming ray formulation (1). An analytic integration is performed over the visible portion of the sun in a flat mirror as viewed from selected (x,y) points on an image plane. (Figure 1) This is the solid angle interval:

$$F(x,y) = \int(\hat{r}_o \cdot \hat{r})\, R(x,y,\hat{r})d\Omega.$$

$F(x,y)$ is the flux at the point (x,y) in the image plane. $R(x,y,\hat{r})d\Omega$ represents the irradiance of the reflected rays at the point (x,y) within the infinitesimal solid angle $d\Omega$ having a direction specified by the unit vector $\hat{r}$. $\hat{r}$ is the direction of a ray from a point (u,v) in the heliostat plane to the point (x,y) under consideration. If we let H denote the luminous region (not shaded or blocked) of the heliostat, then

$$R(x,y,\hat{r}) = \begin{cases} \rho S(\alpha), & \text{if } (u,v) \in H \\ 0, & \text{otherwise} \end{cases}$$

ρ is the coefficient of reflectivity of the heliostat for sunlight. $S(\alpha)$ is a function describing a solar disc. α is the angle measured from the center of the solar disc, and therefore

$$(\hat{r}_o \cdot \hat{r}) = \cos\alpha$$

α_L is the limb angle of the sun and we require

$$S(\alpha) > 0 \quad \text{if} \quad \alpha \leq \alpha_L$$
$$S(\alpha) = 0 \quad \text{if} \quad \alpha > \alpha_L$$

The flux integral then reduces to

$$F(x,y) = \rho\int\cos\alpha\ S(\alpha)\ d\Omega.$$

The region of integration is taken over the intersection of the solar disc and the solid angle subtended by the reflecting region of the heliostat plane as seen from (x,y). α becomes the polar angle of an image oriented spherical coordinate system (α,ϕ,r) with the polar axis parallel to the optic axis $\hat{r}_o$. If we make the following substitutions,

$$d\Omega\cos\alpha = d\phi\ d\alpha\ \sin\alpha\cos\alpha$$
$$= 1/2\ d\phi\ d\Psi$$

where

$$\Psi = (\sin\alpha)^2,$$

the flux integral becomes

$$F(x,y) = \rho/2 \int d\phi \int d\Psi\ S(\Psi).$$

$S(\Psi)$ is conveniently constructed as a polynomial in Ψ.

$$S(\Psi) = \sum_{i=0}^{N} C_i\ \Psi^i$$

We currently fit the solar disc with four constants so

that N = 3 in the summation. The integrand is in a simple form, but the region of integration can become quite complicated. The boundary of the intersection consists of circular sun segments and linear mirror segments. The handling of such arbitrary configurations of the intersection requires more analysis before coding can take place. The reader is directed to References (2) and (3) for further derivations concerning this method.

FLASH has no I/O through arguments of the subroutine. Naturally, all references to the four image generators by the calling program are compatible. This allows the interchange of the subroutines without code modifications in the calling routine. All I/O is managed through group common statements and there are no constants to be initialized within FLASH. The following list reveals the variables input through common statements:

1. Boundary vertices of the flat polygonal reflector given as (u,v) points in the plane of the heliostat
2. Coefficients Ci for the solar brightness distribution
3. Ambient direct beam solar intensity
4. Orthonormal triplets (tower based coordinate system) for the unit vectors $\hat{u},\hat{v}$ and $\hat{x},\hat{y}$
5. Slant range
6. Cosine of the angle of incidence at the mirror plane
7. DELR, the step size in meters between (I,J) nodes on the image plane where a flux evaluation takes place

The output of FLASH consists of a matrix of flux values in watts per square meter. This is currently a 21 x 21 square array representing nodes on the image plane. (Figure 2) The array is returned to a receiver via a group common statement where projections and interpolations take place for the determination of receiver flux values. The step size DELR varies for different locations in the heliostat field such that the angle subtended by the array of nodes is a constant as viewed from positions throughout the heliostat field. Since distant heliostats have larger images than nearby heliostats, a constant DELR for the 21 x 21 array that does not allow a remote image to overspill the nodes would have much less information about smaller images. The variable DELR corrects this situation.

The limits to the capabilities of FLASH allow only images formed by flat polygons to be constructed and allow only one mirror segment per call to be processed

FIGURE 2

Shows a sample heliostat image. At 5.33 hours before noon on the 162nd day after vernal equinox, the sun is almost exactly due east at an elevation of 12.87° for a site at 35° of latitude. At this early morning hour we expect a considerable amount of shading. We have selected a heliostat location one-half a tower height north of the tower. The tower height is 110 meters, the slant distance to the heliostat is 123 meters, and the heliostat is an octagon of width 6.5 meters. The tabular data is flux density in W/m^2 versus x and y coordinates in meters.

	-3.27	-2.86	-2.45	-2.05	-1.64	-1.23	-.82	-.41	0.00	+.41	.82	1.23	1.64	2.05	2.45
	.0	.0	.0	.0	.0	.0	.0	.0	.0	.0	.0	.0	.0	.0	.0
	.0	.0	.0	.0	.0	.0	.0	.0	.0	.0	.0	.0	.0	.0	.0
-3.27	.0	.0	.0	.0	80.2	174.2	187.8	162.2	137.7	99.0	25.6	.0	.0	.0	.0
-2.86	.0	.0	.0	83.2	322.7	506.6	546.9	520.1	492.5	402.2	213.8	19.5	.0	.0	.0
-2.45	.0	.0	51.8	290.6	568.6	742.5	745.6	745.6	743.0	695.5	422.1	133.0	.0	.0	.0
-2.05	.0	26.5	243.4	524.0	728.6	745.6	745.6	745.6	745.6	640.8	384.0	116.2	8.9	.0	.0
-1.64	.8	160.8	466.3	706.6	745.6	745.6	745.6	745.6	670.4	418.3	160.6	17.6	.0	.0	.0
-1.23	11.1	261.4	610.8	745.6	745.6	745.6	745.6	700.5	466.4	187.5	5.6	.0	.0	.0	.0
- .82	11.2	287.8	637.4	745.6	745.6	745.6	726.7	517.0	232.6	21.6	.0	.0	.0	.0	.0
- .41	11.2	287.8	637.4	745.6	745.6	745.6	648.9	343.9	46.3	.0	.0	.0	.0	.0	.0
0.00	11.2	287.8	637.4	745.6	745.6	745.6	608.9	257.3	2.2	.0	.0	.0	.0	.0	.0
+ .41	11.2	287.8	637.4	745.6	745.6	745.6	607.8	251.9	2.2	.0	.0	.0	.0	.0	.0
.82	11.2	269.2	621.3	745.6	745.6	745.6	607.8	251.9	2.2	.0	.0	.0	.0	.0	.0
1.23	1.9	181.4	502.4	730.5	745.6	745.6	607.8	251.9	2.2	.0	.0	.0	.0	.0	.0
1.64	.0	49.2	299.6	588.3	745.6	745.6	608.0	253.5	2.2	.0	.0	.0	.0	.0	.0
2.05	.0	.0	102.4	378.7	651.9	745.6	638.1	318.5	23.3	.0	.0	.0	.0	.0	.0
2.45	.0	.0	.0	167.5	457.6	695.5	709.5	470.0	172.5	.4	.0	.0	.0	.0	.0
2.86	.0	.0	.0	19.5	213.8	402.2	492.5	430.5	212.7	42.5	.0	.0	.0	.0	.0
3.27	.0	.0	.0	.0	25.6	99.0	137.7	162.2	98.6	19.0	.0	.0	.0	.0	.0
	.0	.0	.0	.0	.0	.0	.0	.0	.0	.0	.0	.0	.0	.0	.0
	.0	.0	.0	.0	.0	.0	.0	.0	.0	.0	.0	.0	.0	.0	.0

as determined by the input boundary vertices. However, the polygons may be any shape. If shading and blocking occur, the boundary vertices are changed accordingly by the shading and blocking subroutine. The resulting polygon can be quite different than the original.

FLASH is capable of integrating the flux from a uniform sun, a limb darkened sun or a degraded sun. The choice of suns is determined by the input coefficients to the function describing the solar brightness distribution. The degraded sun is formed by a fine numerical convolution of a guidance error distribution and a limb darkened sun. A least squares fit on this data determines the coefficients of S. The image formed by broadening the solar brightness distribution can represent a population of heliostats within a zone of the field, whereas the image formed by the limb darkened sun represents the flux from one perfectly flat heliostat.

FLASH can also simulate flat canted segmented heliostats. Currently one image is generated for a square segment representative of the actual segments of the heliostat. This image is then shifted within the receiver program according to the aberration associated with each segment. Shading and blocking on a particular segment is taken into account by multiplying the intensity of the representative segment's image by the fraction of the particular segment that is not shaded or blocked.

This approach can give an adequate approximation to the image providing the segment subtends a small angle compared to the sun. An obvious modification to make is calling FLASH for each segment and constructing the image exactly. However, six segments would result in a run time six times as long. The extra computer time may not be worthwhile if the image is formed near the focus of the segments with moderate aberrations and small segments. In this case the representation approach for the segments may perform as well as the exact model.

A detailed description of the tasks performed by the code in FLASH can be obtained by examining a copy of the FORTRAN source as well as a flow chart generated by a processor on the currently available UNIVAC 1108. A user's manual will also describe FLASH and other image generating subroutines when completed. The general program structure of FLASH appears as follows:

```
DO loops over nodes of the image plane (I,J)
  DO loops over boundary vertices
  Summation of sun segments and mirror segments

  FLUX (I,J) is determined

END
```

The primary task of FLASH is to fill the FLUX (I,J) matrix with appropriate values of intensity (W/m^2) and return this information to a receiver program.

FLASH requires about 1995 msec of computer time on the UNIVAC 1108 to generate one image. About half of the nodes on the image plane represented by the 21 x 21 array are non-zero. Nodes having a zero flux value take less time to process. An image will take more or less time depending upon the number of non-zero nodes as well as the number of vertices of the mirror segment and the extent of the complications at the boundary of the intersection of S and H. The overall time required to generate a set of 120 images to represent 120 cells or zones of the heliostat field is on the order of 270 sec or about 4½ minutes. Printing of the flux matrix FLUX(I,J) can be suppressed to save some time in the overall program execution.

The accuracy of FLASH allows its use as a norm for other image generators involving flat polygonal reflectors. There are no internal variables or switches to extend the accuracy of the result. However, any node where flux is evaluated would have the following errors. The analytic fit on the choice of sun, be it uniform, limb darkened for degraded, has some error. There is also no stereographic projection from each (x,y) flux point when shading and blocking occur. These projections are taken parallel to $\hat{s}_o$ and $\hat{r}_o$, respectively. These errors, of course, are not the fault of the mathematical methods employed in FLASH, but are limitations on the model used to represent image formation.

3.0 HCOEF

HCOEF is a subroutine which uses a Hermite function expansion (4) at the image plane to represent an image. In order to make such an expansion, coefficients must be calculated to the desired order for the Hermite polynomials. This is the task performed by HCOEF. This allows an analytic function, F(x,y), to be evaluated at any point on the image plane for the appropriate flux. In contrast, FLASH results in a nodal

representation of F(x,y) which must be interpolated for flux between the nodes.

The expansion in question is one of a convolution integral. The convolution of distributions representing the sun, heliostat and guidance errors gives an excellent representation of the image formation process. By making a good approximation to the convolution, images can be constructed which give good agreement with those produced by FLASH.

The convolution integral can be written

$$F(x,y) = \int_{-\infty}^{\infty}\int M(x_1,y_1)\, S(x - x_1, y - y_1)\, dx_1 dy_1.$$

$$\equiv M*S$$

M is the distribution at the image plane that would result if the sun were a point source. For a flat mirror, this is the projection of the heliostat onto the image plane along $\hat{r}_o$. S is the normalized distribution at the image plane due to the reflection of the solar disc by an infinitesimal mirror. A normalized distribution, G, can be convolved with M and S to produce an image representing a population of heliostats if desired. G represents the distribution of errors in the angle of reflection. In this case, F = M*S*G.

Each of the distributions has a set of moments defined by the following:

$$\mu^f_{i,j} = \int_{-\infty}^{\infty}\int x^i y^j\, f(x,y)\, dxdy$$

where f is either F, M, S or G. The convolution integral defining F(x,y) can be substituted into the moment integral above for F(x,y). After a change of variable and use of binomial formula, the result is

$$\mu^F_{m,n} = \sum_{k=0}^{m}\sum_{l=0}^{n} \binom{m}{k}\binom{n}{l}\, \mu^M_{m-k,n-l}\, \mu^S_{k,l}\ .$$

If G is included, result is

$$\mu^F_{m,n} = \sum_{k=0}^{m}\sum_{l=0}^{n}\sum_{i=0}^{k}\sum_{j=0}^{l} \binom{m}{k}\binom{n}{l}\binom{k}{i}\binom{l}{j} \mu^M_{m-k,n-l}\mu^S_{k-i,l-j}\mu^G_{i,j}$$

In this way, the moments of F can be obtained if the moments of M, S and G are calculated and combined.

The moments of F allow the calculation of the Hermite coefficients. The expansion of F in Hermite polynomials can be written

$$F(x,y) = \sum_{m=0}^{\infty}\sum_{n=0}^{\infty} C_{m,n}(2\pi m!n!)^{-1}\, H_m(x)\, H_m(y)\, e^{-\frac{x^2+y^2}{2}}$$

Due to the orthogonality of the Hermite polynomials, the coefficients $C_{m,n}$ are given by

$$C_{m,n} = \int_{-\infty}^{\infty}\int H_m(x)\, H_n(x)\, F(x,y)\, dxdy$$

If the integration is performed term by term, each term is merely a particular moment of F.

The problem at this point reduces to finding the moments of M, S and G. If they are known, the function F(x,y) can be constructed and evaluated in a straightforward manner. S and G are rotationally symmetric distributions and their shapes are not considered to be functions of time. Thus their moments can be precalculated and are not subject to change for different heliostat shapes, different heliostat locations or different sun positions. M varies for all of the preceding occurrences. For a flat mirror, the moments of M can be calculated in terms of the vertices of its polygonal bounddary which are projected to the image plane parallel to $\hat{r}_o$.

The following list reveals the inputs HCOEF requires. All are introduced via group common statements.

1. Orthonormal triplets (tower based coordinate system) for the unit vectors $\hat{u},\hat{v}$ and $\hat{x},\hat{y}$
2. Boundary vertices of the flat polygonal reflector given as (u,v) points in the plane of the heliostat
3. The number of boundary vertices
4. Slant range
5. Solar limb angle
6. Choice of sun, either uniform or limb darkened
7. Ambient direct beam solar intensity
8. Size of the degrading function G given in milliradians for the one sigma point

There is an internal initialization of the normalized moments of S and G. This involves the calculation of all moments in terms of their ratios to the second moment. For S, this is done for a limb darkened sun and a uniform sun. This choice is controlled by a switch variable. The size of these distributions is controlled by the input limb angle for S and the one sigma point given in radians for G. But the distribution of probability in these functions remains the same when standardized to their sigma, the square root of the second moment. If the guidance errors change for the heliostats or if one requires a different distribution of energy in the solar disc, the precalculated moments of S and G will have to be replaced with the newer values.

The output from HCOEF at the present is just 29 coefficients for the pending expansion, which can be up to sixth order, and for the image plane flux evaluation. The receiver program accepts these in one group common statement and can then calculate flux at desired points in the receiver after a projection along $\hat{r}_o$ to the image plane. Thus the function evaluation takes place in a receiver program. HCOEF has no output to print, but code controlled by a switch variable could be constructed to give image plane output on nodes, like FLASH. The coefficients can also be stored in a permanent file to be used with other receiver geometries if desired.

The restrictions on the capabilities of HCOEF are such that only flat polygons can be processed and only one segment is treated per call. Like FLASH, HCOEF can construct images for different sun models, various degrading functions, flat or canted heliostats with or without shading and blocking. Changing sun models is done with the same switch variable that FLASH uses, choosing a uniform or limb darkened sun. If a different limb darkening function is required, FLASH and HCOEF can adapt by inserting new function coefficients for $S(\Psi)$ and new moments for S, respectively. However, HCOEF has the ability to change the degrading function G by a simple moment calculation and substitution. FLASH must employ a costly numerical convolution on each image, or a new degraded run must be constructed. This involves a fine numerical convolution and least squares fit to require new coefficients for $S(\Psi)$, a much more involved and lengthly process than analytically calculating a few moments for G.

A possible modification of the HCOEF subroutine would be to call it for each segment of a canted heliostat. Currently HCOEF deals with a representative segment as does FLASH. HCOEF is many times faster than FLASH and such a modification might be feasible. Another possible change would be to construct the input boundary vertices so that all segments of a heliostat have their moments calculated together. This would result in one set of coefficients per heliostat for the receiver routine to handle rather than a set for each segment. This would result in a savings in time when one wishes to deal with each segment individually.

The general program structure looks like the following when compared with that of FLASH:

```
┌─DO loop over boundary vertices
│ Calculation of the moments of M
└─

  Calculation of the moments of S and G
  Combination of moments resulting in moments of F
  Calculation of corfficients from the moments of F
  END
```

Note there are no loops for the (I,J) nodes of the image plane as in FLASH, only the loop over the boundary vertices. Also, the combination of moments by the quadruple sum shown earlier is coded explicitly without subscripts. The rotational symmetry of S and G make many of their moments zero, and coding the combination with subscripts and loops would result in many multiplications by zero. These two characteristics of HCOEF increase its speed and efficiency of word usage.

HCOEF requires an average of 17.2 milliseconds of computer time on the UNIVAC 1108. This is for coefficients only, not for function evaluation or image prints. A set of 120 images would therefore require about 2.06 seconds. The overall program execution usually takes 30 to 40 seconds. The extra time is spent in the associated programs which result in receiver flux maps, interception fractions, contours of data, aim points, etc.

Notice that images created by FLASH that cover a majority of the nodes in the image plane will take longer than images which cover fewer nodes. HCOEF, on the other hand, will take same time for either case. More time istaken only if a finer node structure is put on the receiver, and this is time required of the receiver program, whether HCOEF or FLASH is used. Of course, more boundary vertices will increase the run time for HCOEF, but FLASH also has a similar loop.

Figure 3 reveals the kind of accuracy one can expect when using HCOEF (4). The peak flux error of HCOEF compared with FLASH is graphed versus slant range. A square heliostat 6.1 m on a side was used with the slant range varying from 300 m to 1300 m. Different amounts of degrading were employed and fourth and sixth order expansions were produced. Our typical degrading function G has one sigma value of 3 mrad and is a gaussian function. Sixth order expansions are used on all runs. HCOEF can therefore claim a 2% maximum error in peak flux. Usually the greatest error occurs at the peak of the image when HCOEF is used, and thus other regions of the image are better represented.

Proof of this comes when interception fractions are compared to those of FLASH. A .2% maximum error occurs

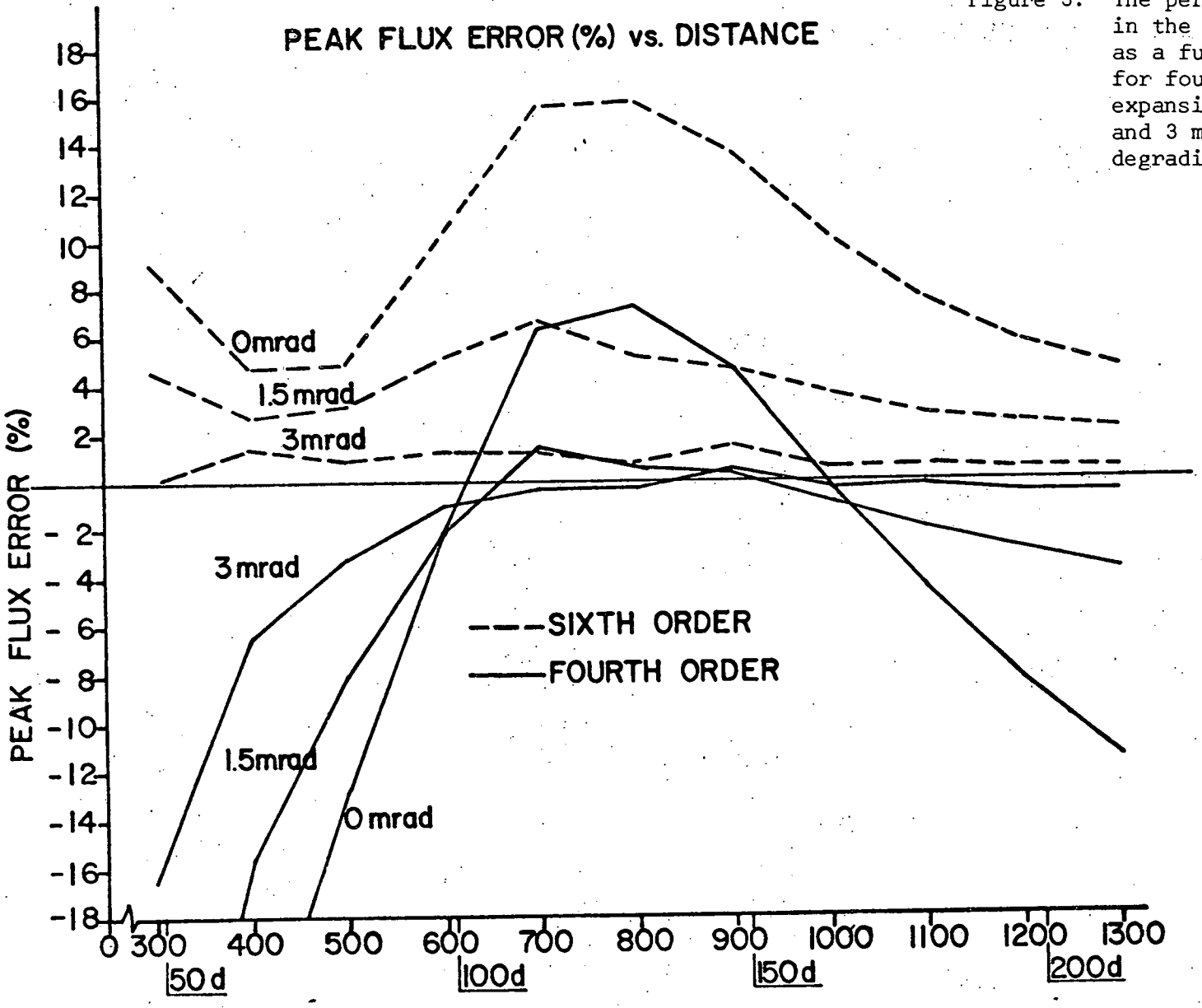

Figure 3. The percentage of error in the peak flux of HCDEF as a function of distance for fourth and sixth order expansions with 0, 1.5, and 3 milli-radius degrading.

for interception fractions in the range of .800 to .999. This is because the expansion in orthogonal polynomials works in the weighted least squares sense, and for Hermite polynomials, the weight function is $e^{+\frac{x^2 + y^2}{2}}$. This weights the periphery of the image more than the central region resulting in good interception fractions and poorer peak flux estimates.

The flux profile on a receiver should not have errors worse than 2% since a great number images are projected to the receiver. The high and low estimates of many projected images should tend to cancel out and make the error much less than 2%.

Figure 4 reveals two things that can be done to increase the accuracy of HCOEF. The amount of degrading can be increased with a gaussian type of function. This tends to make the image more gaussian like and the density function of the Hermite polynomials is gaussian. The approximation is thereby bettered. However, if the simulation does not call for increased degrading or if the function G is not gaussian in nature, the order of the expansion could be increased for more accuracy in the image. Of course, more accuracy would cost more computer time.

The HCOEF model has the same limitations as FLASH in that shading and blocking is considered paraxial to $\hat{s}_o$ and $\hat{r}_o$ respectively. Also the convolution assumes all central rays of the sun from the heliostat to the image plane are the same length. These errors are limitations to the model and cannot be improved by increasing the order of the expansion or the amount of degrading. However, they have only a minuscule effect on the results and can be ignored in practical applications.

4.0 SUNCONE

A third subroutine used to calculate solar flux at the image plane is called SUNCONE. Central rays from the sun are traced from elemental areas in the mirror to the image plane by a subroutine named TRACE. SUNCONE is called by TRACE to project solar discs about the impact points on the image plane. The flux is then evaluated at specified points in the image plane producing a nodal representation of the flux as FLASH does.

Figure 4 shows how the flux of a flat mirror might be represented by SUNCONE. The boundary of this projected

Figure 4. A montage of solar images which would approximate the flux in the image plane as suggested by the SUNCONE subroutine.

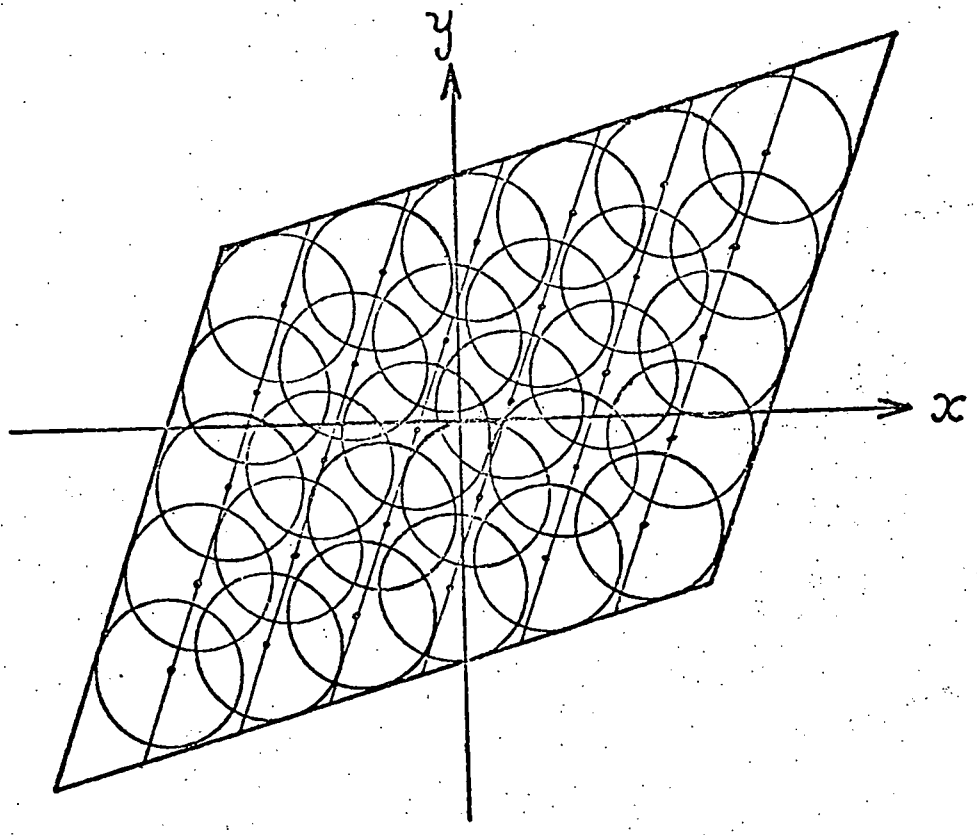

mirror is a parallelogram. Because the mirror is flat, the regular array of nodes in the mirror results in a regular pattern of impact points on the image plane. However, there are not enough rays traced in this particular schematic to give a good representation of the flux. The solar discs are about the same size as the projected elemental areas of the mirror. The idea is to have the elemental areas very small compared to the projected solar discs. In this way, the elemental area can be neglected in the image formation process.

The flux $F(x,y)$ can be evaluated at any point on the image plane using the following equation.

$$F(x,y) = \Delta x \Delta y \cos i \, \rho I_o \sum_{i=1}^{N} S(x - x_i, y - y_i)$$

$\Delta x \Delta y$ = elemental area of the reflector
$\cos i$ = cosine of the angle of incidence of sunlight at the mirror plane
ρ = reflectivity of mirror surface
I_o = ambient direct beam intensity
S = distribution of power in a solar image
x_i, y_i = position of $i^{\underline{th}}$ central ray traced to image plane
N = number of traced rays

The same coefficients derived for the sun for use in FLASH can be used to construct a polynomial in r for the distribution S.

$$S = A + Br^2 + Cr^4 + Dr^6$$

r is the distance away from the center of a projected solar disc at the image plane. Of course S is zero if $r > r_o$, where r_o is the radius of a solar disc at the image plane.

The following list reveals the inputs to SUNCONE, all of which are made through group common statements.

1. Solar limb angle (choice of true limb angle or degraded sun's limb angle)
2. Slant range
3. Traced rays (x_i, y_i)
4. Elemental area $\Delta x \Delta y$ (all are presumed to be the same size, but they could vary)
5. Cosine of incidence angle
6. Ambient direct beam intensity
7. Reflectivity of mirror

In the present design, the coefficients of the function S representing the solar disc are initialized internally. However, these could also come to SUNCONE via a group common statement. This would stabilize the code by not requiring editing and compilation of the source when various sets of coefficients for S are desired.

SUNCONE has no output to print at present although the calling program TRACE can write the matrix of traced rays (x_i, y_i). YEAR, which calls TRACE, can also write a flux matrix like that of Figure 2. SUNCONE outputs this FLUX (I,J) matrix, just as FLASH does, to a receiver program for subsequent projection and interpolation to determine receiver flux patterns. FLUX (I,J) can also be se to permanent storage for later receiver work if desired.

SUNCONE has the added capability of dealing with dished or curved reflectors whereas FLASH and HCOEF could handle only flat polygonal mirrors. Canted segmented heliostats with or without dished segments are also within the capabilities of SUNCONE. SUNCONE is still in a developmental and changing stage, and needs to have shading and blocking included. This can be done by deleting the appropriate traced central rays from elemental areas affected by shading and blocking.

Another possible refinement of SUNCONE would be to require that the solid angle subtended by an elemental area as seen from the image plane always be in a certain proportion to the solid angle of the sun or degraded sun. This would insure an image of adequate quality regardless of the slant range. This would mean that remote heliostats would require less traced rays while nearby reflectors would require more rays. Thus the number of rays traced would be proportional to the reciprocal of the square of the slant range. Once the ratio of run size to elemental area size was defined for a quality image, comparably accurate images for any slant range could be constructed.

The general program structure of SUNCONE appears as follows:

```
    Initialization of constants
┌   DO loops sampling traced rays
|   Restrictions for following loop parameters (window)
|  ┌DO loops sampling image plane nodes
|  |Restrictions on S, i.e. S = 0 if r > r_o
|  |Evaluation of FLUX (I,J)
|  └
└
    END
```

Sampling a great many rays and image plane nodes can greatly increase the run time for a particular image as the structure above reveals. Thus the programmer must pay for increased accuracy with increased run times.

Currently SUNCONE requires an average 2700 msec computer time per image. This image is constructed with 121

rays reflected off a square heliostat with an 11 x 11 square array of nodes centered in elemental areas 1/121 times the area of the heliostat. The 21 x 21 image plane array has more than half of the flux nodes greater than zero. As will be shown in the next section, it is not the ray trace subroutine TRACE which requires so much time, but the loops around the function evaluation in S in SUNCONE. Both SUNCONE and HFOCUS are timed including the TRACE subroutine to arrive at the average CPU time per image. Overall program execution has not been run at this time since SUNCONE is still undergoing modifications. However, due to the time required for one image, image, we expect run times comparable to or greater than that that of FLASH, i.e. $\geq$ 270 seconds for 120 images.

As with most ray tracing routines, SUNCONE seems to be costly in CPU time requirements. But it is an extremely simple program, and increased accuracy is simple to obtain by merely tracing more rays. This seems to be the limiting factor in the use of a ray trace routine. Accuracy is good if enough rays are traced, but enough rays may be too many when CPU time and costs are considered.

5.0 HFOCUS

HFOCUS is a subroutine using the same methods as HCOEF, but now the method is extended to non-flat mirrors of arbitrary shape via a ray trace. The moment acquisition for M is based on a ray trace rather than on the projected boundary vertices of a flat polygonal mirror.

As shown before, the moments of M are obtained using the equation

$$\mu^{M}_{k,l} = \int\int_{-\infty}^{\infty} x^k y^l \, M(x,y) \, dxdy.$$

For a flat mirror, M is just the ambient direct beam intensity inside the projected boundary of the heliostat and is zero outside. The integral needs to be done only over the non-zero portion of M, so a conversion is made to polar coordinates and the integral is done by integrating from one boundary vertex to the next in a counter-clockwise direction. Each moment can be constructed in terms of the boundary vertices of M.

Dished reflectors cannot use the above method. M is the distribution at the image plane if the sun were a point source, and for a curved reflector is no longer

a constant inside the projected boundary and zero outside. Therefore the traced central rays of the sun are used to construct the moments of M. The moment integral becomes

$$\mu^{M}_{k,l} = \sum_{i=1}^{N} x_i^k \, y_i^l \, M(x_i,y_i) \, \Delta x_i \Delta y_i$$

x_i,y_i are the coordinates of the $i^{\underline{th}}$ ray at the image plane

$\Delta x_i \Delta y_i$ is the projected elemental area represented by the $i^{\underline{th}}$ ray

$M(x_i,y_i)$ is the solar intensity reflected by the elemental area

N is the number of rays

$M(x_i,y_i)\,\Delta x_i \Delta y_i$ represents the power reflected reflected by the elemental area, and if all the elemental areas are taken to be equal and the solar intensity is the same for all elements, the moment integral can be written

$$\mu^{M}_{k,l} = M \, \Delta x \Delta y \sum_{i=1}^{N} x_i^k \, y_i^l$$

Since M is required to be normalized for the moment combination with S and G, the moments of M become simply

$$\mu^{M}_{k,l} = \frac{1}{N} \sum_{i=0}^{N} x_i^k \, y_i^l \, .$$

Powers of the x,y coordinates of each ray result in the moments of M. If the elemental areas are not all equal, the $\Delta x_i \Delta y_i$ would stay within the summation and weight each ray according to the area it represents.

The following list shows the inputs required by HFOCUS.

1. Orthonormal triplets (tower based coordinates) for mirror plane unit vector $\hat{u},\hat{v}$ and image plane unit vectors $\hat{x},\hat{y}$.
2. x_i,y_i impact points of traced rays at the image plane
3. Slant range
4. Solar limb angle and sun choice (uniform or limb darkened)
5. Ambient direct beam solar intensity
6. Size of degrading function

Just as HCOEF, the moments of S and G require initialization within HFOCUS.

The outputs from HFOCUS are identical to those of HCOEF. The 29 coefficients go to a receiver program via a group common so the Hermite function expansion can take place for the evaluation of F(x,y). These coefficients can go to permanent storage to construct flux on other receiver if desired. HFOCUS has no output to print at this time, but image plane output

similar to that in Figure 2 could be an option on a switch variable. TRACE, which calls either HFOCUS or SUNCONE, can output the matrix of x_i, y_i traced ray coordinates to print for inspection.

The range of capabilities of HFOCUS is the same as SUNCONE in that HFOCUS is able to handle flat heliostats, canted segmented heliostats and dished heliostats. The possible modifications of codes are the same as SUNCONE. Shading and blocking should be included, and a variable number of traced rays should be considered such that the angle of the elemental area of the mirror remains constant and in a certain proportion to that of the sun. These modifications are really ones to be applied to TRACE, but they affect HFOCUS and SUNCONE.

The general program structure of HFOCUS is as follows.

```
┌ DO loop over traced rays
│ Calculation of moments of M
└

  Calculation of moments of S and G
  Combination of moments resulting in the moments of F
  Calculation of coefficients from the moments of F
  END
```

The structure is identical to that of HCOEF except the loop samples traced rays instead of boundary vertices. Since there are many more rays than boundary vertices, the run time is expected to be somewhat longer for HFOCUS than HCOEF.

HFOCUS requires an average of 64.3 more per image, or about four times as much as HCOEF. This run time includes the tracing of 121 rays. Since these are the same rays used by SUNCONE, the conclusion is that the 2700 msec required for a SUNCONE image is indeed used by the SUNCONE subroutine and not the TRACE subroutine which calls it. Since the TRACE-HFOCUS combination is fairly fast, the number of rays could be increased in TRACE to give better estimates of the moments of M while still being CPU time efficient and cost effective.

Since HFOCUS is four times slower than HCOEF, a set of 120 Hermite image coefficients representing a heliostat field could be generated in about eight seconds. This has not been done yet since further modifications and developments of HFOCUS are taking place. However, overall program execution involving all the associated subroutines should take on the order of 40 to 60 seconds based upon the run times encountered when using HCOEF.

The accuracy of HFOCUS has not been determined to the

same extent as HCOEF, but two types of comparisons are possible. Flat heliostat images can be compared with FLASH and dished heliostat images can be compared to SUNCONE in the following way. An image from SUNCONE and HFOCUS can be constructed for a particular number of traced rays. Then the same images can be constructed for an increased number of rays and compared to the previous images. This technique is analogous to doing a numerical integral and subsequently decreasing the step size until the result no longer changes significantly. In this way HFOCUS can be compared to SUNCONE after they both reach a point where adding rays does not alter the image significantly. Of course, SUNCONE should be a very accurate representation of the image at this point, and considered the standard image just as FLASH is considered standard for flat heliostats.

There are two ways to increase the accuracy of HFOCUS. The number of traced rays can be increased and the order of the Hermite function expansion can be increased. Increasing the order of the expansion is much easier in HFOCUS than in HCOEF since the moments of M are essentially powers of ray coordinates. Increasing the order of expansion in HCOEF involves some long tedious analytic calculations to set up the moments of M in terms of the boundary vertices.

For the reasons given above for ease in increasing the accuracy of HFOCUS and the difference in speed between SUNCONE and HFOCUS, HFOCUS seems to be the most likely candidate for everyday use in construction of images due to curved glass. Another reason for optimism is that focusing tends to decrease the relative size of M at the image plane resulting in a more accurate representation of the image. S and G then become more dominant in the convolution. The image therefore tends to become more like S*G which is much easier for the Hermite functions to fit than the flat-top distribution of M for a flat heliostat.

REFERENCES

(1) Lipps, F.W., "Four Different Views of the Heliostat Flux Density Integral," SOLAR ENERGY, Vol. 18, 1976, pp. 555-560.

(2) Lipps, F.W., and M.D. Walzel, "An Analytic Evaluation of the Flux Density Due to Sunlight Reflected from a Flat Mirror having a Polygonal Boundary," Proceedings of the 1977 Annual Meeting of the American Section of the International Solar Energy Society, Vol. 1, Section 21, June 6-10, 1977, pp. 11-14.

(3) Lipps, F.W., and M.D. Walzel, "An Analytic Evaluation of the Flux Density Due to Sunlight Reflected from a Flat Mirror Having a Polygonal Boundary," to be published in SOLAR ENERGY.

(4) Walzel, M.D., F.W. Lipps and L.L. Vant-Hull, "A Solar Flux Density Calculation for a Solar Tower Concentrator Using a Two Dimensional Hermite Function Expansion," SOLAR ENERGY, Vol. 19, 1977, pp. 239-253.

THE RECEIVER PROGRAMS

Fred W. Lipps
Solar Energy Laboratory
University of Houston
Houston, Texas 77004

ABSTRACT

The CYLN subroutine is designed for the MDAC external cylindrical receiver, but is typical of receiver programs. It generates a set of receiver nodes. Secondly, it incorporates the flux from each cell in the collecter field subject to a variety of options concerning canted heliostats, shading and blocking, aiming strategy, and choice of image generator. Finally, it outputs the flux density map and the various interception factors, etc.

1.0 INTRODUCTION

Many different receiver types can be considered for the central receiver system. There are external (i.e. convex) types, cavity (i.e. concave) types, and for each of these we can have a north field, or an all around field. Concave types include star bodies, pagodas, honeycombs, and various cavities with planar or non-planar apertures. We have studied the following cases:

1. Truncated Sphere
2. Crossed Planes with Flat Top
3. N-Prong Star Bodies
4. Cylinders with Base and Stem
5. 24 Panel Cylinder - CYLN
6. Inclined Flats and/or Aperture
7. True Cavities (in future)

However, currently, only CYLN is available in up-to-date versions.

The CYLN subroutine is utilized in the program environments as shown in Figure 1, which shows the structure of system simulation programs. CYLN has multiple entry points as shown in Table 1.

Table 1. Multiple Entry Structure of CYLN

CALL $CYLN_1$	Generates Receiver Nodes $\{(X,Y,Z,n_x,n_y,n_z,A)_i \mid I = 1...NREC\}$
CALL SAB	Shading and Blocking (Helios.)
CALL FSEG	Shading and Blocking (Segs.)
CALL ANAINT	Image Generator
CALL $CYLN_2$	Incorporates flux from given cell in collector field
CALL $CYLN_3$	Outputs Flux Density Map, Interception Factors, Aims, Aberrations, FSEGS Panel Interception File

2.0 TASKS PROVIDED BY THE SECOND ENTRY

1. Optional Ray Trace for Canted Flat Heliostats
   Location of Segment Centers required.
   Choice of Focal Strategy is provided.
2. Optional Use of Shading and Blocking Input
   A. No shading or blocking.
   B. Normalize total flux from cell by FMIRR or FSEG factors.

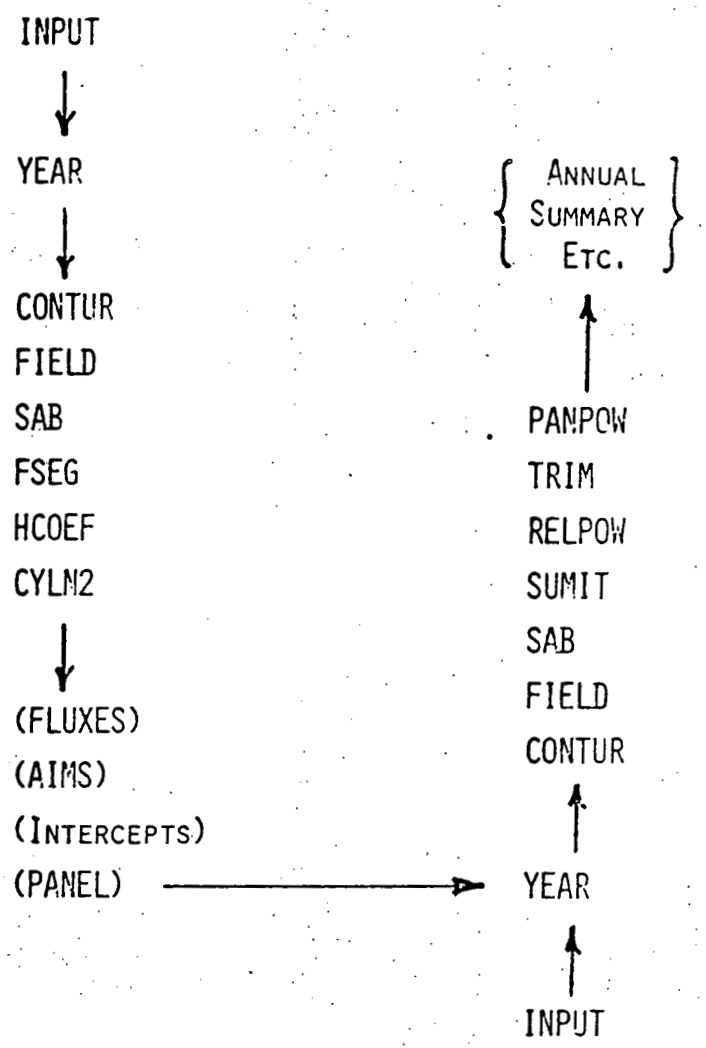

FIGURE 1. STRUCTURE OF SYSTEM SIMULATION

C. SAB included in Image Data Input.

3. Optional Aiming Strategy
   A. No Aiming Strategy = Aim at Belt.
   B. 3 or 5 Point Aims fixed with respect to receiver for all cells.
   C. Hi-Lo optimum, aim for each cell, optimized at specified time.
4. Calculates Cosine of Incidence and Absorption Factor.
5. Evaluates Flux Density Contribution
   A. Interpolation from Image Plane for FLASH
   B. Polynomial Evaluation for HCOEF.
6. Loads Flux Density and PANEL Interception Matrices Separately

The choice of aiming strategy is currently being provided by mapping in the appropriate CYLN version, i.e. CYLN, CLYN3, CYL5, or CYLN2 which is the Hi-Lo optimum. All other options are controlled by input variables located in the INPUT program. See Table 2.

Table 2. Inputs for Receiver Model

ICYLN	=	1	EQUALS 1 to CALL CYLN SUBROUTINE, 0 NOT
JTAPE	=	1	EQUALS 1 TO OUTPUT FILE FOR FINT OR PANEL
LIMB	=		EQUALS 1 TO READ IMAGES, 0 TO USE INTEGRATOR EQUALS 2 TO READ AIM FOR .CYLNSHRD, 3 TO WRITE AIM
NFLAT	=	1	EQUALS NUMBER OF SEGMENTS/HELIOS
NCIRCL	=	24	EQUALS NUMBER OF DIVS FOR CIRCUMFERENCE
IFOC	=	0	EQUALS 1 TO FOCUS, 0 NOT
YUP	=	1.0	FRACTION OF IMAGE RADIUS USED FOR (HI) HI-LO 2 PT AIM
YDN	=	1.0	FRACTION OF IMAGE RADIUS USED FOR (LO) HI-LO 2 PT AIM
ALPHAD	=	.00466	DEGRADED SUN LIMB ANGLE FOR HI-LO AIM IN MRAD
HCYLN	=	25.5	EQUALS HEIGHT OF CYLN IN METERS
RREC	=	8.46	EQUALS RADIUS OF CYLN IN METERS

3.0 SAMPLE OUTPUTS AND TIME INDEPENDENCE OF INTERCEPTION

Table 3 gives a list of CYLN outputs.

Table 3. CYLN Outputs

FIRST ENTRY
- Cell Structure in Receiver
- Coordinates of Nodes

SECOND ENTRY
- Aberration Vectors
- Shift Up and Down for Aiming Point
- Foreshortened Receiver Height and Image Radius

THIRD ENTRY
- Summary of Shift Up
- Summary of Shift Down
- Summary of Image Radius
- Flux Density on Receiver
  - Day, Hour, Rec. Radius
  - Total Receiver Power, Average Flux Density, Concentration Ratio
  - Panel Geometry
  - Flux Density Matrix (See Figure 3.)
  - Panel Power Vector
- Intercepted Power/Cell Versus Cells (See Figure 2.)
- Fraction of Beam Intercepted Versus Cells
- Panel File Print

Figure 1 shows the data transfer via the PANEL file from the initial interception run to the final output run for an annual summary of optimized system performance. The initial run is usually made at equinox noon, so that the interception data is related to equinox noon conditions, however, we assume that interception is time independent.

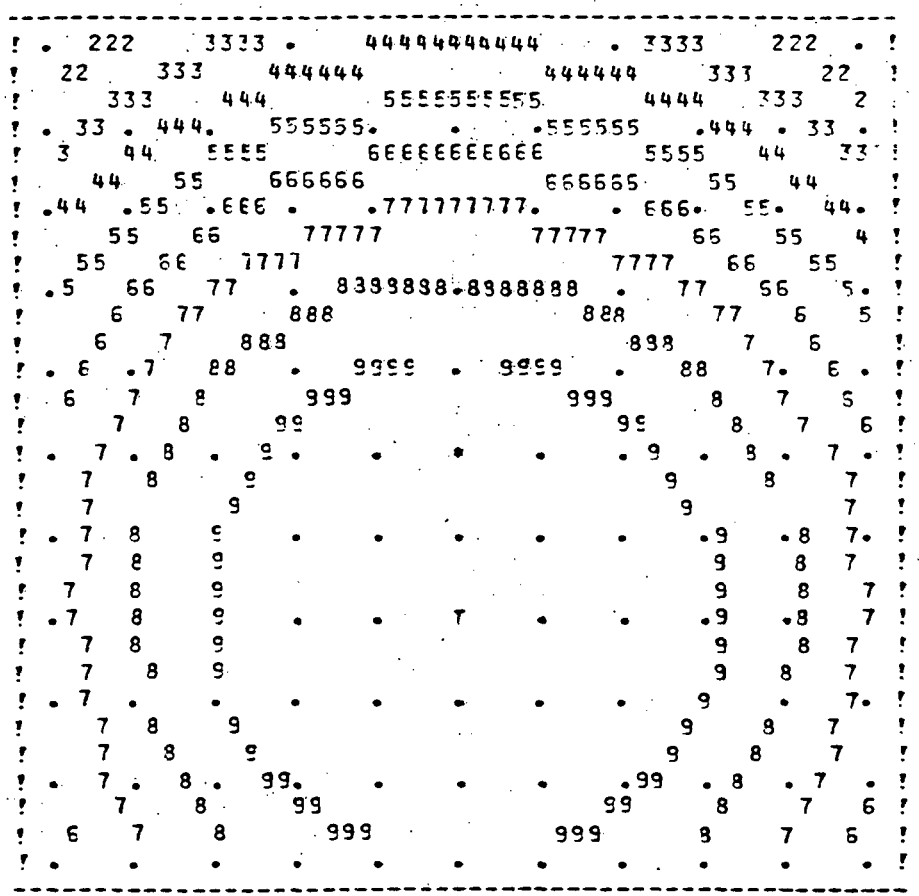

CONTOUR INTERVAL = .050

Figure 2. Contour of Fraction Intercepted.

FLUX DENSITY FOR 2 PT AIM IN W/M2 : UNIVERSITY OF HOUSTON

ON DAY 182 AT .00 HOURS FOR A RECIEVER RADIUS= 8.50

TOTAL RECEIVER POWER FOR 2 PT HI-LO AIM = .8548+09 IN WATTS AVERAGE FLUX DENSITY = .6276+06

PHIA =	.131	.393	.654	.916	1.178	1.440	1.702	1.963	2.225	2.487	2.749	3.011
RRECX=	8.427	7.853	6.744	5.174	3.253	1.109	-1.109	-3.253	-5.174	-6.744	-7.853	-8.427
RRECY=	1.109	3.253	5.174	6.744	7.853	8.427	8.427	7.853	6.744	5.174	3.253	1.109
	.738+05	.844+05	.103+06	.124+06	.152+06	.193+06	.223+06	.249+06	.277+06	.296+06	.317+06	.326+06
	.160+06	.175+06	.203+06	.236+06	.280+06	.344+06	.389+06	.428+06	.468+06	.498+06	.529+06	.543+06
	.282+06	.299+06	.332+06	.380+06	.441+06	.526+06	.588+06	.640+06	.692+06	.733+06	.777+06	.797+06
	.401+06	.417+06	.453+06	.514+06	.591+06	.692+06	.771+06	.836+06	.896+06	.950+06	.100+07	.103+07
	.470+06	.483+06	.522+06	.592+06	.681+06	.796+06	.892+06	.966+06	.104+07	.110+07	.116+07	.120+07
	.462+06	.470+06	.516+06	.592+06	.689+06	.824+06	.935+06	.101+07	.109+07	.117+07	.123+07	.128+07
	.398+06	.400+06	.454+06	.532+06	.637+06	.798+06	.918+06	.985+06	.108+07	.116+07	.123+07	.129+07
	.329+06	.328+06	.385+06	.466+06	.578+06	.760+06	.895+06	.945+06	.104+07	.113+07	.121+07	.128+07
	.308+06	.309+06	.362+06	.446+06	.564+06	.753+06	.879+06	.940+06	.104+07	.112+07	.121+07	.128+07
	.350+06	.355+06	.403+06	.488+06	.609+06	.784+06	.907+06	.978+06	.107+07	.115+07	.123+07	.130+07
	.424+06	.432+06	.474+06	.559+06	.674+06	.825+06	.940+06	.102+07	.110+07	.118+07	.126+07	.131+07
	.473+06	.480+06	.521+06	.598+06	.699+06	.827+06	.933+06	.101+07	.108+07	.115+07	.122+07	.126+07
	.454+06	.458+06	.501+06	.566+06	.644+06	.759+06	.853+06	.909+06	.979+06	.104+07	.110+07	.114+07
	.363+06	.363+06	.410+06	.461+06	.515+06	.619+06	.699+06	.734+06	.801+06	.857+06	.893+06	.933+06
	.237+06	.237+06	.282+06	.319+06	.353+06	.442+06	.503+06	.523+06	.583+06	.627+06	.648+06	.683+06
	.125+06	.126+06	.160+06	.186+06	.207+06	.272+06	.315+06	.327+06	.377+06	.405+06	.416+06	.442+06
	.531+05	.556+05	.754+05	.910+05	.105+06	.144+06	.172+06	.181+06	.210+06	.231+06	.239+06	.254+06
PANEL=	.179+08	.183+08	.205+08	.239+08	.281+08	.346+08	.394+08	.423+08	.461+08	.495+08	.523+08	.545+08

Figure 3. Flux Density Matrix

Heliostat aspect and various focal aberrations cause time dependent interception. Shading and blocking also causes time dependence, however, the main effect of shading and blocking is included by the FMIRR factor, which is evaluated for a good sample of times. The initial run at equinox noon is made without any knowledge of the collector field and hence the no shading and blocking option is necessary. The small amount of shading and blocking which occurs at equinox noon will cause overestimates and underestimates of the interception interception fractions. Heliostat aspect and focal aberrations might cause a significant reduction of interception at early and late hours. We have previously noted that this is not the case for the commercial system with flat uncanted heliostats. We will now present evidence that it is also true for the Pilot plant, which has flat canted heliostats, assuming an MDAC cylindrical receiver. See Table 4.

Table 4a. Fixed Aims

DAY	HOUR	ELEV	$\overline{FINT}$	Worst Cell
AE.	0	55.2	.984*	
SS.	5.70	15.	-.003	-.070 (1,6)
AE.	4.78	15.	.000	-.048 (1,6)
WS.	3.58	15.	+.003	-.039 (6,7)

*Incremental values given below.

Table 4b. Variable Aims

DAY	HOUR	ELEV	$\overline{FINT}$	Worst Cell
AE.	0	55.2	.984	
SS.	5.70	15.	.000	-070 (1,6)*
AE.	4.78	15.	+.003	-036 (1,6)
WS.	3.58	15.	-.005	-032 (6.7)

* + Cases on eastside and - on west as expected for sun in west.

Large aberrations occur at 15° of solar elevation, but they do not contribute significantly to the glass weighted average interception factor $\overline{FINT}$. This is a consequence of the 360° field which always has some cells with a good cos i and the tall cylindrical receiver which can stand appreciable aberrations in the vertical direction. Notice that the worst time dependent losses occur in the north field. The fixed aims case assumes that aims were optimized for equinox noon, whereas the variable aims case optimizes aims continuously. Clearly, variable aims are better, but impractical.

THE SHADING AND BLOCKING PROCESSOR

Fred W. Lipps
Solar Energy Laboratory
University of Houston
Houston, Texas 77004

ABSTRACT

Shading and blocking events reduce the reflective efficiency of a given heliostat due to interference by its neighbors. Shading restricts the incoming rays and blocking restricts the outgoing rays. The shading and blocking subroutine can process any number of events by updating the boundary vector of the heliostat.

1.0 INTRODUCTION

The central receiver system concentrates sunlight by deploying a large number of individually guided heliostates which are aimed at the tower top receiver. The set of heliostats constitutes the collector field, which acts as though it were a very large movable parabola. However, the collector field is segmented and can be regarded as a Fresnel reflector. As in all Fresnel optical systems, we expect interference between the segments. In this case, it is reasonable to call this interference shading and blocking.

Shading occurs when a neighboring heliostat intercepts a ray incoming to the shaded heliostat.

Blocking occurs when a neighboring heliostat intercepts a ray outgoing from the blocked heliostat.

Shading and blocking programs have been increasingly

sophisticated and are now applied in a variety of program environments.

Historical Development

Rectangles	(RECT)	See Reference 1
Regular N-gons	(SAB)	See Reference 2
Polygons	(BOOL)	in planning

Program Environments (See Figure 1.)

YEAR	SAB	CONTUR			for output of fractions.
YEAR	SAB	FSEG	HCOEF	YLN2	for output of flux densities and Interception.
YEAR	SAB	FLASH			for exact images.
RCELL	SABR	PLOTϕ			for optimized field.
LOSS	SABϕ				for LOSS fraction plots.

See Reference 3 for a brief description of programs.

Shading and blocking processors can be classified into two primary types: (1) for single events and (2) for multiple events. The LOSS program utilizes type (1). We are primarily concerned, however, with processors for multiple events. In optimized geometry at midday, multiple events are rare but can occur. On the other hand, for low suns at startup and shutdown, multiple events become very complex and cannot be ignored.

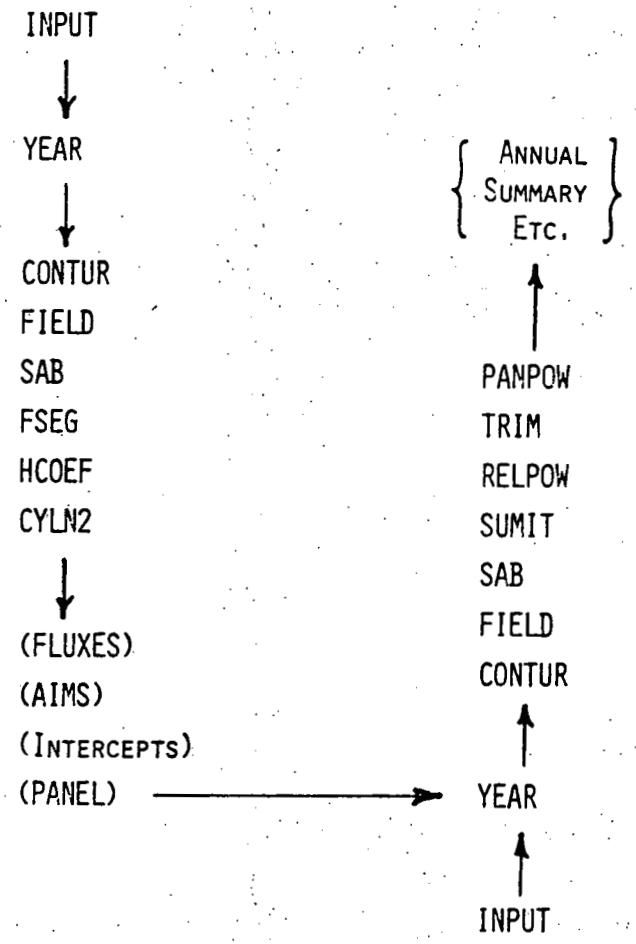

FIGURE 1. STRUCTURE OF SYSTEM SIMULATION

At present we do not have a type (2) processor for round heliostats, although we will be able to handle arbitrary polygons in the near future. Historically, we have progressed from rectangles to regular N-gons to polygons. If necessary, rounds can also be processed but the trigonometric relations will be slow. Figure 2 shows some typical events for rectangular heliostats. These events can be classified by the control variables as shown in Table 1.

Table 1. Loop Control Constants

Centered Shading			Inn	Ordinary			Picture
KA	KB	KC		KA	KB	KC	
3	-1	4	0				
			1	2	0	2	Corner Bite
3	1	2	2	1	1	0	Edge Bite
			3	2	2	0	Bigger Bite, etc.
3	3	0	4	1	3	-2	
			5	2	4	-2	
3	5	2	6	1	5	-4	

When an event occurs, the first corner point to be recomputed is designated by the subscript K. The number of corner points in the boundary is increased by KC. After computing the new corners, control reads the remaining old corners into the updated

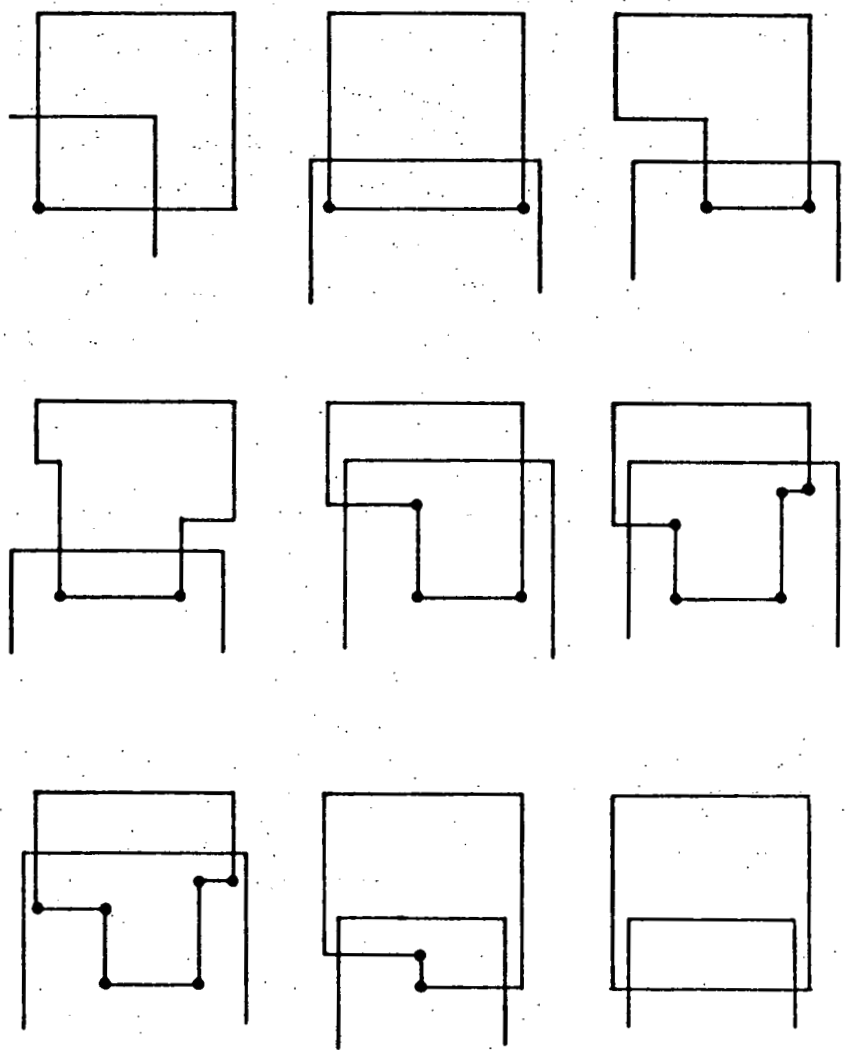

Figure 2. Typical Events for Rectangular Heliostats

boundary vectors SU(K) and SV(K) with the statements

SU(K + KA) = BU(K + KB),

and

SV(K + KA) = BV(K + KB).

The above table shows that various types of events require various combinations of the subscript controls KA, KB, and KC. This part of the program required considerable effort to develop. The program is fast, although not yet optimal. In some cases the boundary vector contracts because KC<0. Fortran V is somewhat inconvenient because we require cyclic vectors, i.e.

BU(K + ICØRN) = BU(K),

and

BV(K + ICØRN) = BV(K).

Figure 3 shows a typical event for an octagon, along with most of the control words which are required. However, the logical structure is more complex in this case. The new boundary points required by this event must be solved for, since they represent the intersection of rather arbitrary straight lines. In fact, the solution for the new points will be no more difficult in the general case of polygons.

The problem of polygons, however, becomes still more sophisticated. One possible approach is suggested below.

BOOLEAN PROCESSOR

Given Polygons X and Y, Compute:

$$Z = X \cap Y$$

Let

$$X \equiv \{(X_{ui}, X_{vi}) | i = 1,2,\ldots N_x\}$$

and similarly for Y and X.

Let

$$X + \Delta_1 \cup \Delta_2 \ldots \cup \Delta_M$$

where

$$\Delta_i \cup \Delta_j = 0 \text{ (area)},$$

so that

$$Z = Z_i \cup Z_2 \ldots \cup Z_M$$

where

$$Z_i = \Delta_i \cap Y.$$

However, this will not be the most efficient approach when many cases will have a null intersection.

2.0 SHADING AND BLOCKING FOR REGULAR N-GONS

Most of our current work relates to squares or octagons, and, consequently, the current SAB subroutines

are based on concepts which are reported in Reference 2.

Table 2. Table of Contents for Reference 2

2.1 TERMINOLOGY

A. Shading is the loss of illumination on a given heliostat due to the interception of incident sunlight by a neighboring heliostat.

B. Blocking is the loss of illumination on the central receiver due to the interception of reflected sunlight by a neighboring heliostat.

C. The Collector Field contains a large number of independently oriented heliostats which are suitably arranged on a flat ground plane.

D. The Central Receiver is a radiant energy absorber which is located at the optical center of the collecter field and is supported by a tower of suitable height.

E. The Boundary Vector is a set of points in the plane of the heliostat which represents the vertices of a plane polygonal region. This region is the effective luminous region of the heliostat.

F. The Sky View seen in the reflecting heliostat from a particular point in the receiver is limited by the neighboring heliostats. The sky view defines the sky version of the shading and blocking projection. This version is used to calculate the flux density receiver at the view point in the receiver.

G. The Receiver View seen in the reflecting heliostat from a point in the center of the solar disk is limited by the neighboring heliostats. The receiver view defines the receiver version of the shading and blocking projection. This version is relatively simple and provides a rapid estimate of heliostat effectiveness.

2.2 THE PURPOSE AND SCOPE OF PROGRAMS

The shading and blocking phenomena play a major role in limiting the effectiveness of the tower top solar concentrator. The arrangement of heliostats in the collector field is optimized to reduce the losses due

to shading and blocking without wasting the incident sunlight unnecessarily. All segmented optical systems suffer from interference between neighboring segments. However, the geometrical situation in the tower top solar concentrator is unusually complex.

The receiver version of the shading and blocking program provides a rapid estimate of heliostat effectiveness. It is not absolutely exact because of umbra and penumbra effects; these errors are very small, however, because of the proximity of the neighboring heliostats. The receiver version provides an initial optimization of the collector field geometry, either by ignoring the influence of receiver efficiency or by estimating the receiver interception factor for a spherical receiver.

The sky version of the shading and blocking program becomes a subroutine to the flux density calculation. This version provides a sterographically exact projection of each neighbor for a given point in the receiver. All of these projections are combined to generate the final boundary vector which represents the sky view.

Both versions of the shading and blocking computer program receive an initial boundary vector and output a final boundary vector. These programs will be general enough to cope with the following geometrical situations:

A. The reflecting surface of the heliostat can be the interior of any regular plane polygon. Input NGON = Number of Sides.

B. Solar tracking is assumed but the heliostat mounting system is arbitrary.

C. The arrangement of heliostats in the plane of the collector field is arbitrary, and any list of neighbors is accepted.

D. The collector field is assumed to be flat but can be inclined or level. The collector field is subdivided into cells which can be located and sized arbitrarily. The inner and the outer boundaries of the collector field are defined by excluding the undesired cells via the input control matrix IGRND.

E. For the sky version, the location of the receiver point R with respect to the optical center O is arbitrary. (See Figure 3.) For the receiver version, the corresponding point is fixed at the center of the solar disk.

F. Although we anticipate the role of guidance errors in degrading the image, we are free to assume perfect tracking for the purposes of the shading and

blocking programs. Shading and blocking calculations are performed for the representative heliostat at the center for each cell in the collector field. The cell structure is assumed for convenience but must sample the geometrical situation adequately.

G. The representative heliostats are assumed to reflect the central ray from the sun to optical center of the receiver. For convenience, we will assume that the neighboring heliostats are parallel, which is not quite perfect tracking, but the error induced in the shading and blocking calculation is very small.

2.3 THE BOUNDARY VECTOR PROCESSOR

The most characteristic aspect of our approach to shading and blocking concerns our use of the plane of the heliostat. Given an orthonormal basis for the heliostat frame, we no longer care what type of mounting system was used and it becomes convenient to introduce (u,v) coordinates for the vertices of the mirror lying in the plane of the heliostat. The set of vertex points determines a polygonal reflecting region. We can write

$$B = \{(u_i, v_i) | i = 1 \ldots NGON\}$$

for the boundary vector so that the processor must generate a new boundary vector every time an event occurs. In short form

$$B_0 \rightarrow B_1 \rightarrow B_2 \ldots \rightarrow B_N ,$$

for N events.

Table 3 summarizes the structure of the SAB subroutines.

Table 3. The Boundary Vector Processor

A. Requirements
- Initial or Std. Boundary Vector
- List of Displacements for Neighbors
- Unit Vectors for Optic Axis and Sun
- Orthonormal Basis for Heliostat

B. Tasks
- Select Highest Boundary Point
- Exclude Neighbors behind Reflector Surface
- Project Neighbor onto Plane of Heliostat
- Exclude Neighbors having Remote Images
- Detect Events (See Figure 4.)
- Calculate New Boundary Points
- Update Boundary Vector

C. Output
- Final Boundary Vector
- Area of Effective Region
- Visibility of Sun by Sun Sensor Print Options

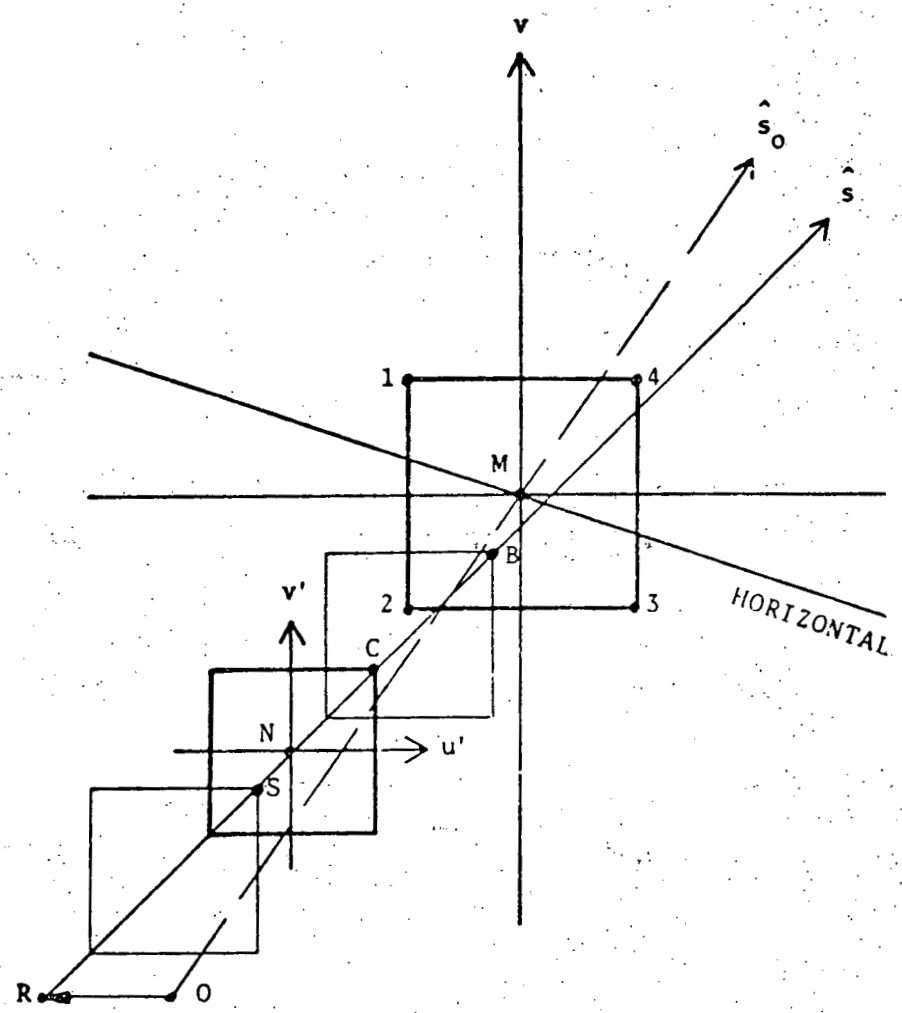

Figure 3. Shading and Blocking Projections Seen in the Heliostat Plane.

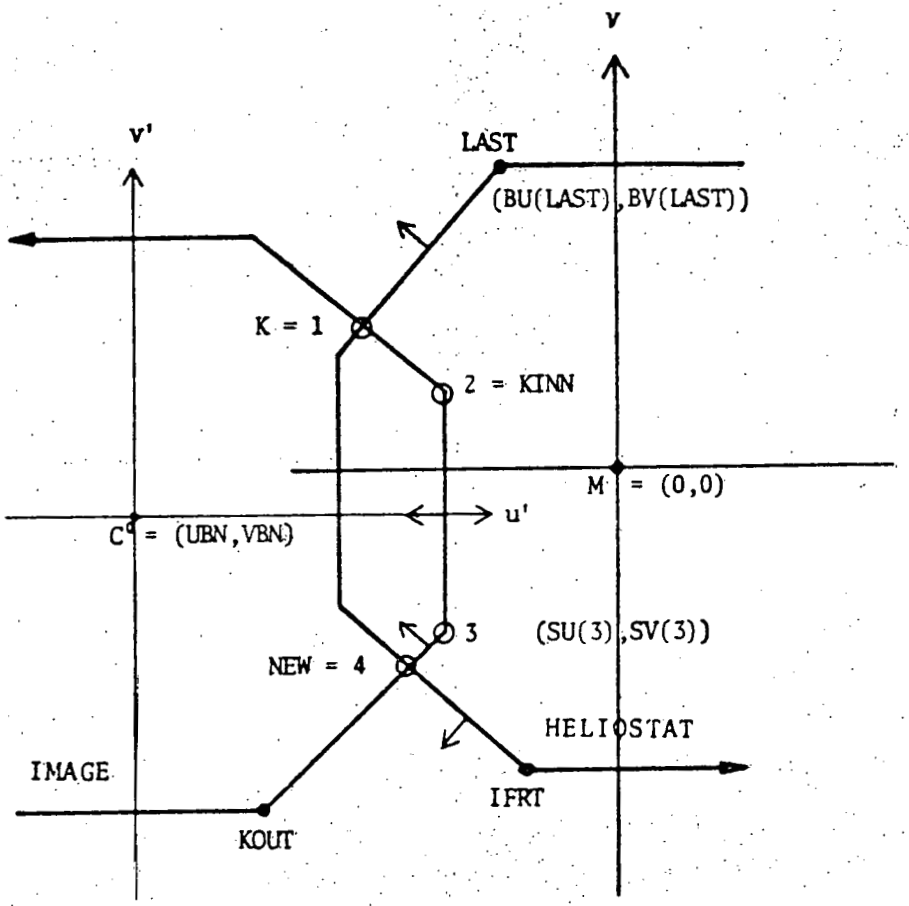

Figure 4. An event showing necessary computer words.

REFERENCES

(1) Shading and Blocking Geometry for Rectangular Mirrors, Technical Addendum 4, p. 239, UH/MDAC Progress Report No. 1 "Solar Thermal Power Systems Based on Optical Transmission" NSF/RANN/SE/GI-39456/PR/73/4.

(2) Generalized Shading and Blocking Programs, Technical Addendum 11, p. 204, UH/MDAC Final Report "Solar Thermal Power Systems Based on Optical Transmission" NSF/RANN/SE/GI-39456/FR/75/3.

(3) SEL/UH Computer Programs Reference Manual for Optical Analysis of Central Receiver Systems.

THIS PAGE

WAS INTENTIONALLY

LEFT BLANK

COLLECTOR FIELD POWER PROGRAM

W. G. Hart
Solar Power Program
Martin Marietta Aerospace
Denver, Colorado 80201

ABSTRACT

This paper describes a computer program that was developed to calculate thermal power reflected into a receiver from a field of heliostats and to determine power losses. Inputs to the program are the geometry of the heliostat, collector field and receiver; alignment and operating times; insolation; mirror reflectivity; reflected flux patterns; and mirror structural deflections as functions of heliostat elevation angle, wind velocity and wind direction. The paper includes examples of reflected flux patterns obtained from radiometer measurements and used as the basis for the reflected flux patterns employed in the program. Mirror structural deflections are calculated by another computer program and have been verified by testing. Example structural deflection data are included in the paper.

The program determines power losses caused by pointing errors, off-axis aberration and heliostat structural deflections. The computation of aberration effects has been verified by comparison of computer results with test data; this comparison is included in the paper. Also included are examples of program outputs showing power losses as a function of time of day and time of year and as a function of wind velocity and direction.

The program is briefly described in terms of a top-level flow chart and major subroutines. Program run time on a CDC 6500 is approximately half a minute for 100 heliostats.

PROGRAM DESCRIPTION

Figure 1 is a top-level flow diagram of the collector field power program. The program first calculates

TOP-LEVEL FLOW DIAGRAM

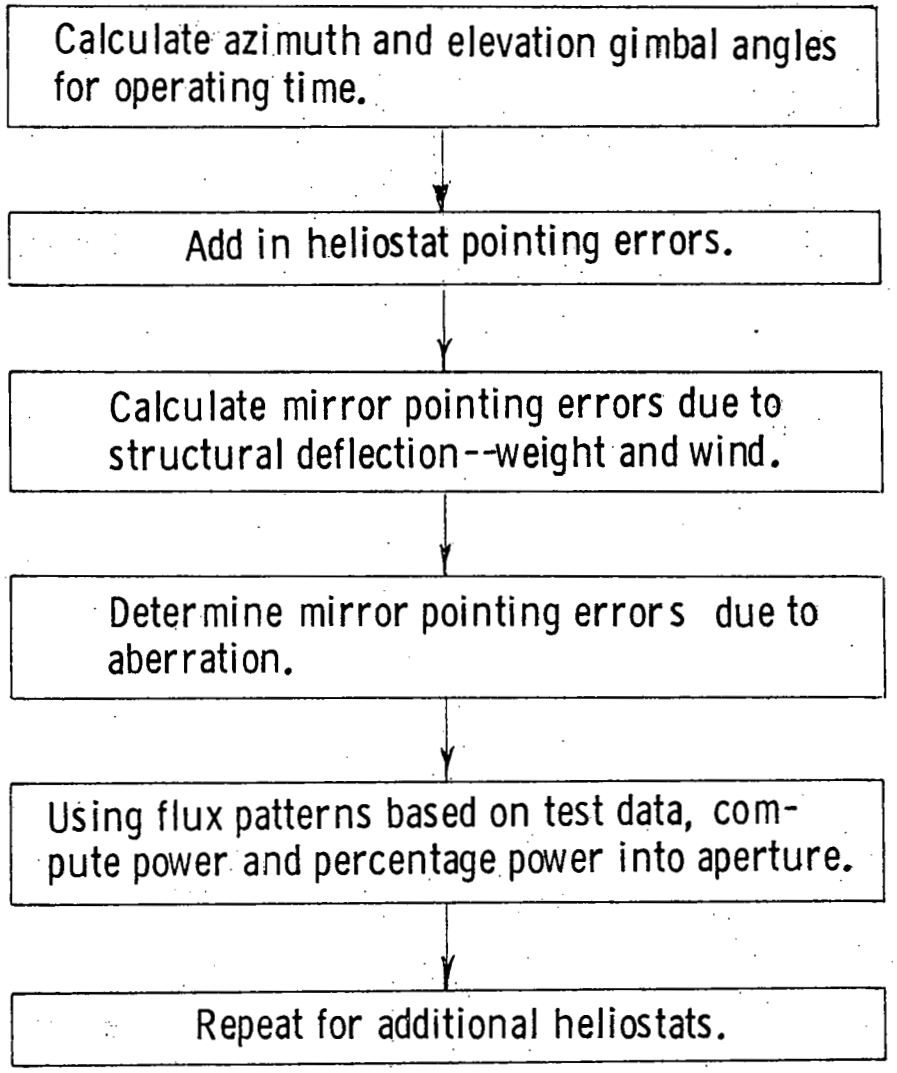

Figure 1

the azimuth and elevation gimbal angles that are required to direct the reflected beam from the heliostat into the aperture of the receiver. Next, pointing errors are computed. Then, using flux patterns based on test data, the program computes the power and the percentage of total reflected power into the receiver. The program calculates the pointing error and the power into the aperture for each mirror on a heliostat and then calculates the totals for the heliostat. The calculations are then repeated for each heliostat in the field, or for a representative group of heliostats.

Heliostat pointing errors affect the whole heliostat, e.g., errors due to the resolution of the device that measures the gimbal angles and errors in the calculation of sun position. The program has normally been run using several different values of pointing error in sequence to determine power loss as a function of pointing error. Then, using information on the statistics of the pointing errors, power losses can be estimated for the field.

Pointing errors due to structural deformation are calculated for each mirror. These pointing errors are calculated using input data defining mirror rotations as a function of elevation gimbal angle and wind velocity and direction.

The program determines mirror pointing errors due to off-axis aberration by first "aligning" each of the mirrors on the heliostat at a selected time of day and time of year--normally noon, vernal equinox. That same relative mirror orientation is then maintained when the heliostat is positioned to center the reflected beam on the target at other times of the day and times of the year. Because of off-axis aberration, the centers of the reflected beams from the individual mirrors spread apart for operating times other than the setup time.

The reflected flux pattern used in the program is a normal distribution chosen to approximately match test data. Power into the aperture is computed by first calculating the projection of the aperture onto a plane perpendicular to the center of the reflected beam and then integrating under the flux distribution within the limits of the projected aperture.

Inputs to the program include the geometry of the heliostat, collector field and receiver; alignment time and operating time; insolation; mirror reflectivity; mirror reflected flux distribution; and mirror structural rotations as functions of heliostat elevation angle, wind velocity and wind direction. Heliostat geometry is input in terms of the location of the center of each mirror with respect to the

center of rotation of the heliostat. The location of each heliostat in the field is specified with respect to a ground reference plane and a vertical line through the center of the aperture. The receiver is defined by tower height, aperture width and height and the slope of the aperture opening with respect to a vertical plane.

Insolation, mirror reflectivity and mirror area are normally combined into a single input constant--the total reflected power from the mirror for normal incidence and reflection.

The program uses a two-dimensional normal distribution to approximate the reflected flux distribution from each mirror. The required input to the program is the diameter of the flux distribution at the point where the intensity has dropped to 1.11% of the peak intensity.

Mirror rotations are input to the program for heliostat elevation angles of 0, 55 and 90 degrees, for wind velocities of zero and 8.94 m/s (20 mph) and for front and back winds.

The primary program outputs are power into the aperture and power losses as functions of operating time, wind velocity and direction and heliostat pointing errors. Other quantities that are computed in the process of generating these primary outputs and that are also printed out include heliostat gimbal angles, cosine loss factors and the locations on the receiver aperture of the centers of the reflected beams. The primary purpose of this program is to determine power losses. Other programs are used to compute the detailed maps of flux distribution inside the receiver that are required for design of the boiler and superheaters.

Major subroutines used in the program include the sun position computation, control algorithm, aberration computation, structural deflection computations, flux pattern determination, aperture projection and flux density integration.

The sun position subroutine calculates the sun vector for the specified time of day and time of year and for the specified site location. The control algorithm determines the mirror normal vector and the azimuth and elevation gimbal angles to center the reflected beam on the target.

To determine the effect of off-axis aberration, the program first solves the control algorithm for each of the mirrors on a heliostat for the specified alignment time--usually noon, vernal equinox. Then the control algorithm is solved for the center mirror for the specified operating time. The unit vector normal to each other mirror is equal to the unit vector

normal to the center mirror corrected for the difference in the alignment angles. The target vector (vector from the center of the mirror to the center of the target) is different for each mirror and can be calculated from the heliostat geometry and the known gimbal angles. The errors in the reflected beams from each mirror (except the center mirror) are computed by solving the vector equations for the reflected beams with the sun vector, mirror normal vector and target vector all known.

To determine pointing errors caused by structural deflections, the program first calculates angle of attack from the wind direction and azimuth gimbal angle. Mirror rotations are determined from the input data for the operating elevation gimbal angle for a wind velocity of 8.94 m/s (20 mph). These mirror rotations are then scaled to account for the actual wind velocity and angle of attack.

The flux pattern used is a normal distribution with a diameter to the ±3 sigma points of 17 mr at the slant range for which the mirror is focused. The program calculates the increase in beam diameter caused by using fixed-focus mirrors at slant ranges not equal to their focal length. The program scales the flux distribution so that the correct total beam power is maintained.

The apparent size of the receiver aperture varies as a function of location in the heliostat field. The program calculates the projection of the aperture on a plane that passes through the center of the aperture and is perpendicular to the reflected ray from the center of the center mirror. Numerical integration techniques are then used to determine the total power being reflected onto the projected aperture.

EXAMPLES OF INPUT DATA

Figure 2 shows an example of mirror rotation data used in the collector field power program. Mirror rotations caused by weight only and by weight plus an 8.94-m/s (20-mph) wind were computed using a space-frame computer program. The rotations due to wind only are calculated by subtracting the weight-only data from the wind plus weight data. The wind-only data are used when it is necessary to scale the rotations for a different wind velocity. The rotations caused by weight are then added back in to obtain the total rotations.

The computer program used to calculate mirror structural rotations was verified by test. A heliostat structure was set up in the structures lab and loads were applied to produce azimuth and elevation torques. Measured deflections of the heliostat structure agreed

EXAMPLE OF MIRROR ROTATION DATA

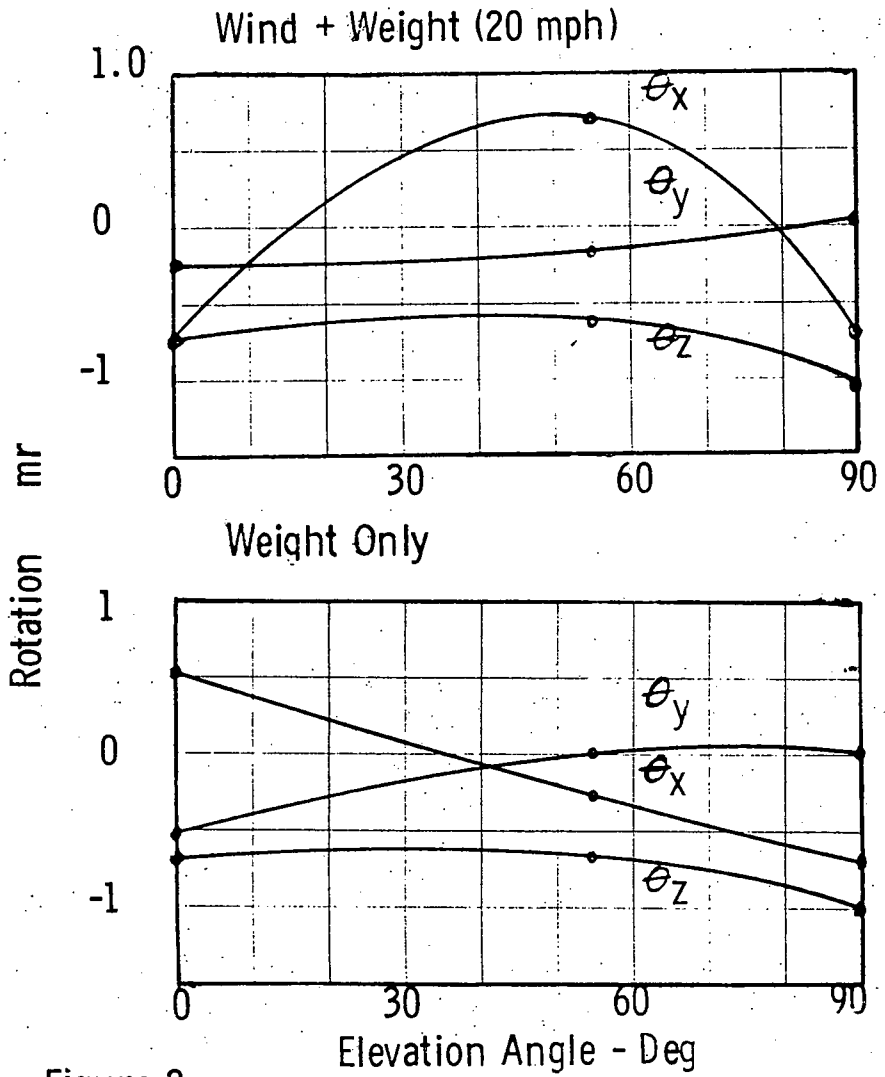

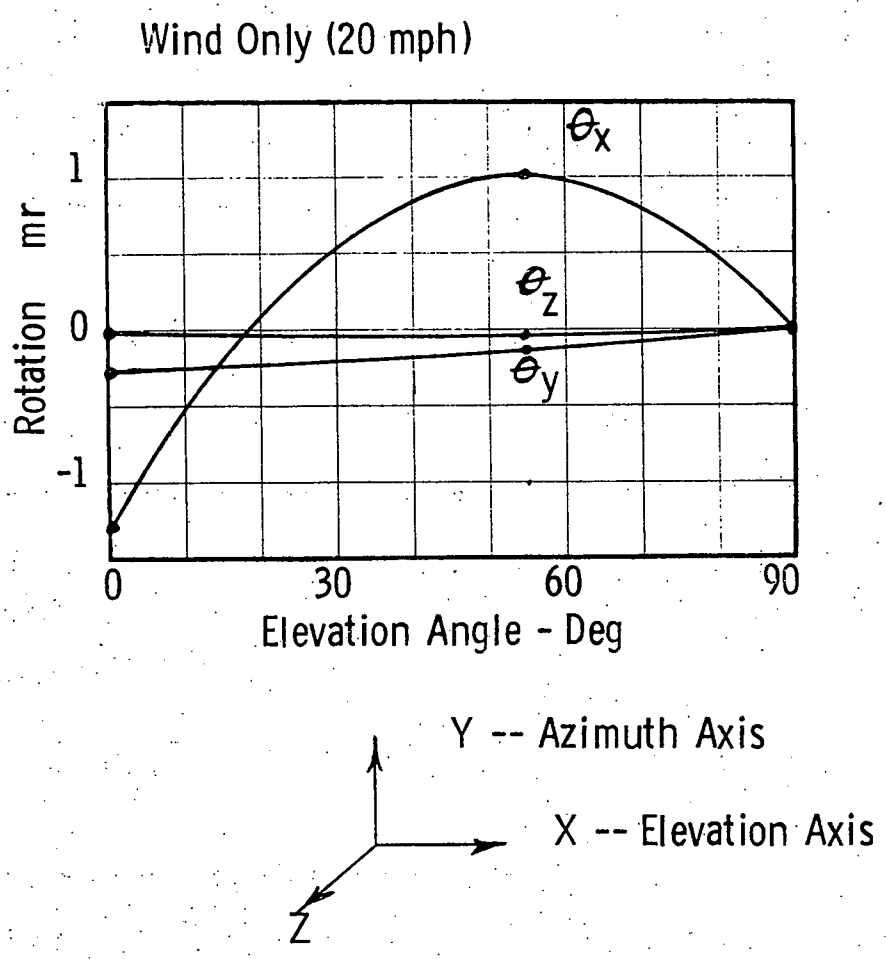

Figure 2

with calculated values within about 15%.

Reflected flux distributions were measured at both Albuquerque and Denver. Measurements were made in Denver using the four heliostats of the subsystem research experiment (shown in Figure 3) and radiometers mounted on a boom as shown in Figure 4. The structure on the left in Figure 4 is a calorimeter that was used to measure total energy into the aperture. Thirteen radiometers were mounted on the boom and flux patterns were determined by sweeping the reflected beam from a test heliostat across the boom and recording the radiometer outputs.

The radiometer outputs as functions of time were converted to functions of distance using the geometry of the test setup and the velocity of the drive motor and the sun.

Example flux patterns from one of the heliostats are shown in Figure 5. It can be seen that a normal distribution provides a good approximation of the test data.

VERIFICATION OF OFF-AXIS ABERRATION COMPUTATION

The technique used to calculate pointing errors of the reflected beams from individual mirrors has been previously described. Verification of this part of the program was accomplished by comparing calculated results with test data.

Patterns of reflected beam centers were available from a test that was run May 29, 1974. Pictures of the reflected beam pattern had been taken at one-hour intervals from 8 am to 3 pm. The computer program was used to calculate and plot the reflected beam centers for the same times using the same geometry as the test setup.

Figure 6 is a picture of the heliostat used in the test. The mirrors were aligned so the reflected beams overlapped at 11 am. Figure 7 shows the reflected beam pattern at 1 pm. (One of the inside mirrors in the row of five is missing in this case.) Covers were placed over the mirrors with an opening in the center of the cover to obtain an approximation to the central ray from the mirror.

Figure 8 shows the computer plot of the target and the centers of the reflected beams for this case. Good general agreement was obtained between the computer results and the test pictures throughout the day.

EXAMPLES OF PROGRAM RESULTS

Examples of program results will be shown for the

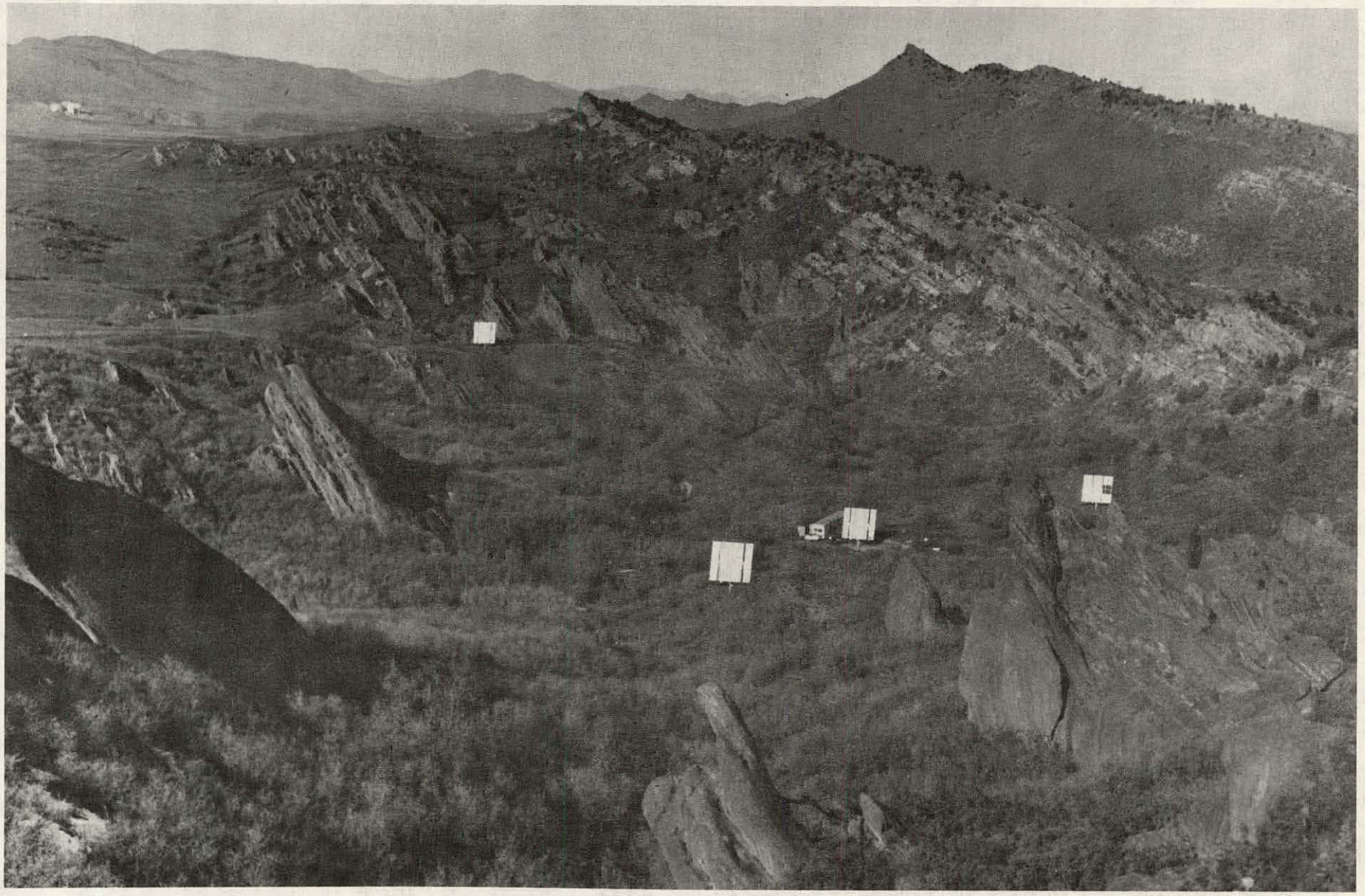

Figure 3 Four Heliostats of Subsystem Research Experiment

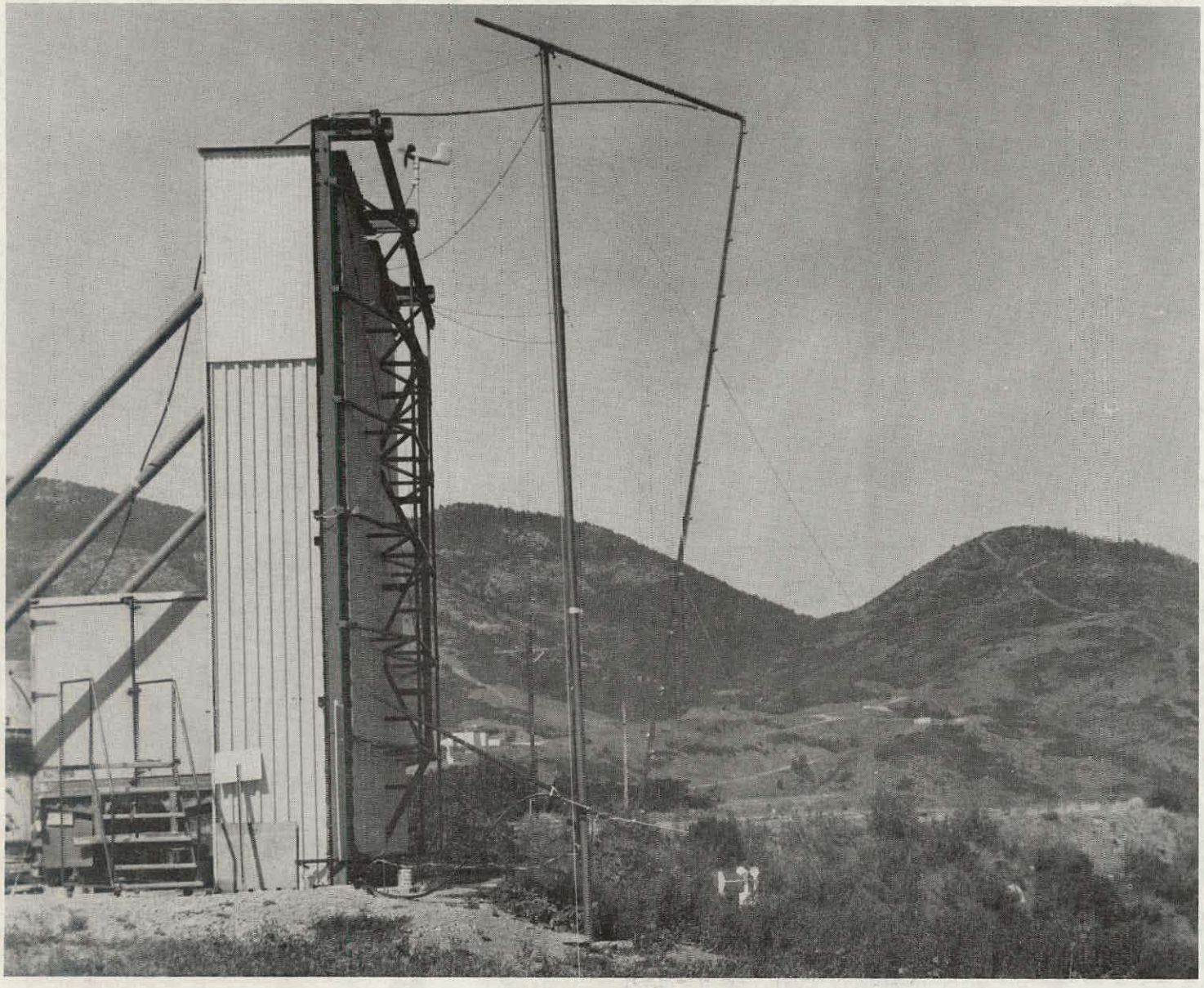

Figure 4 Radiometers Used tc Measure Heliostat Flux Distributions

EXAMPLE FLUX PATTERNS FROM RADIOMETER TESTS

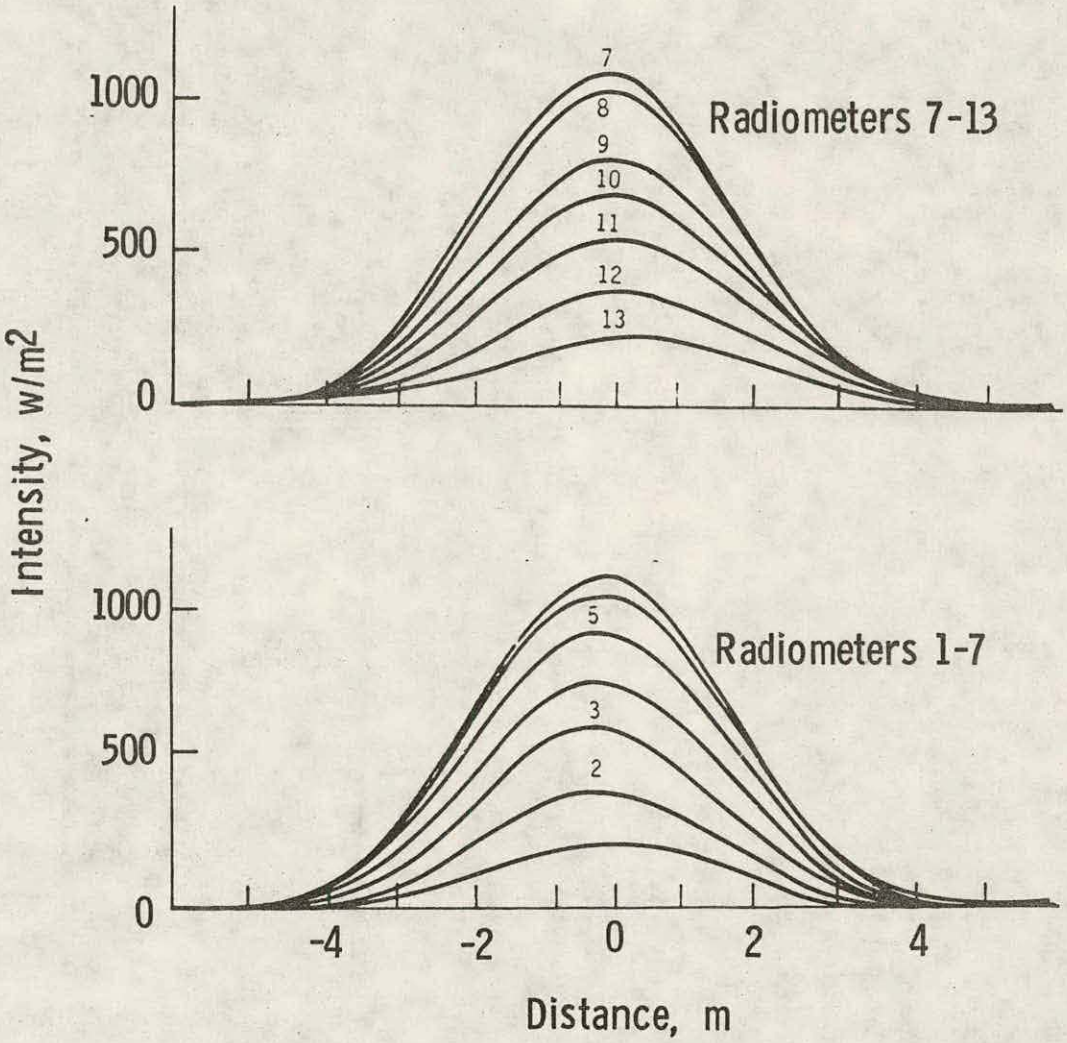

Slant Range = 506 m
Figure 5

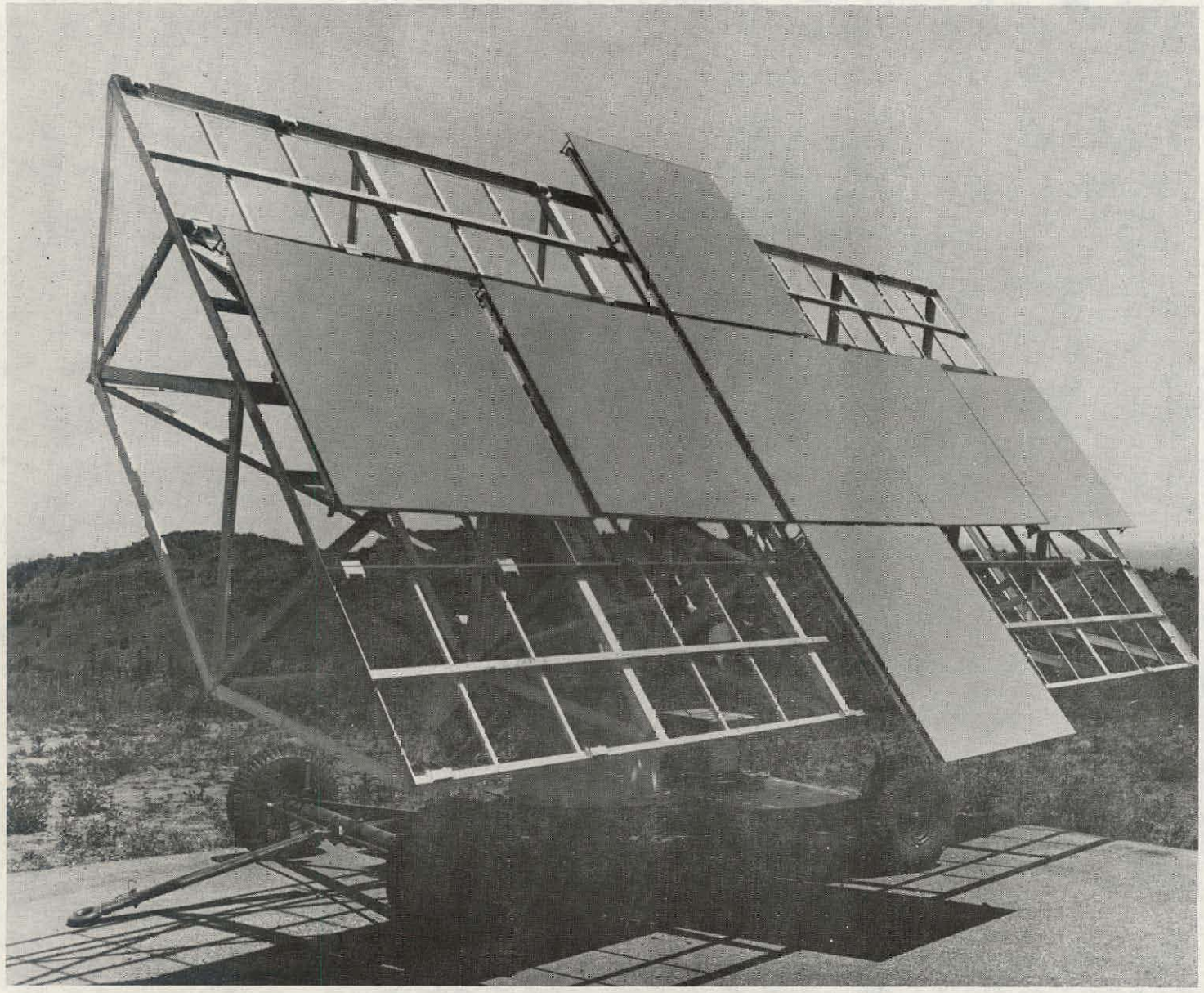

Figure 6 Heliostat Used for Aberration Tests

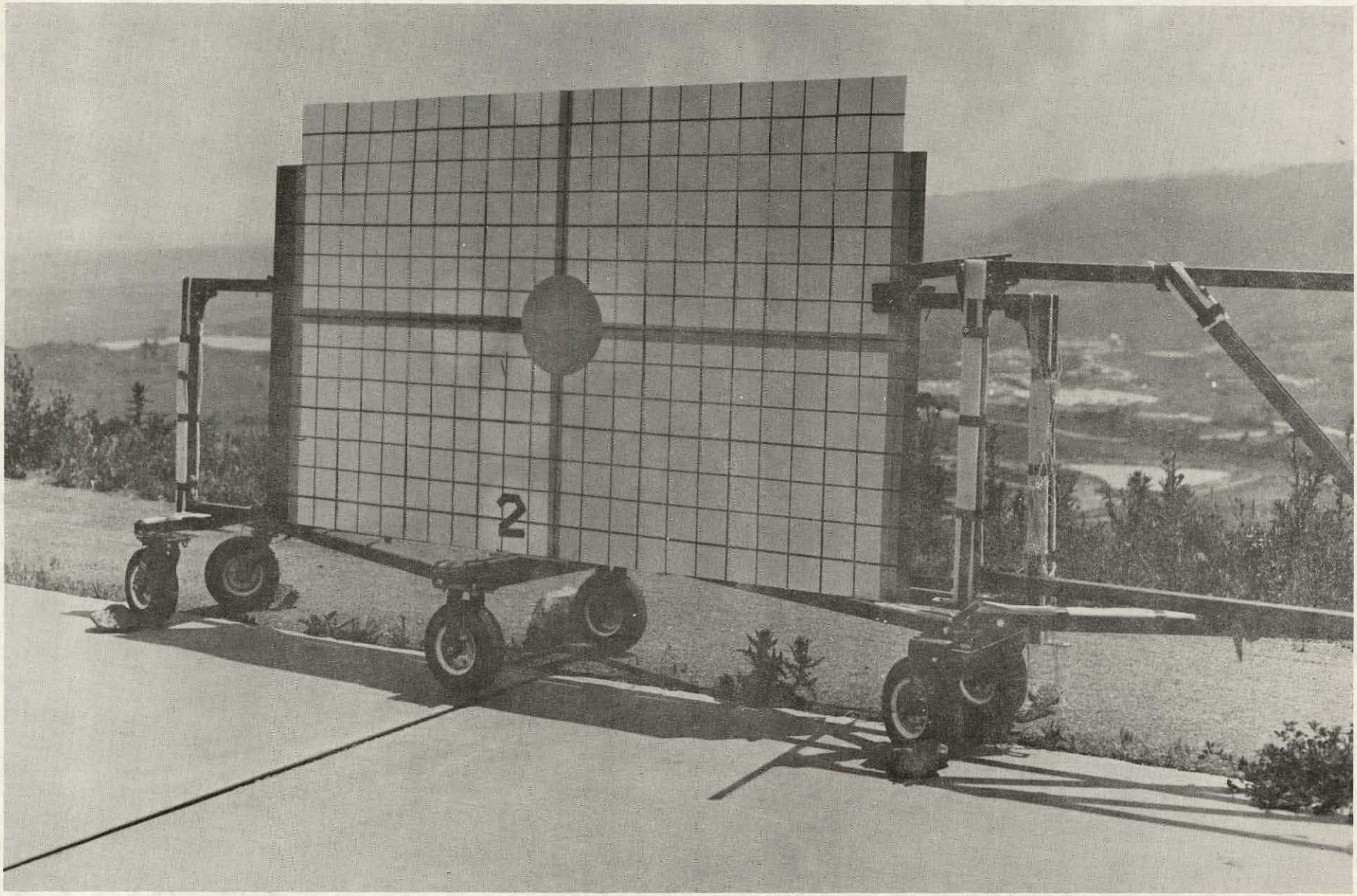

Figure 7 Reflected Beam Pattern at 1 pm (Aligned at 11 am)

COMPUTED BEAM CENTERS FOR COMPARISON WITH TEST RESULTS

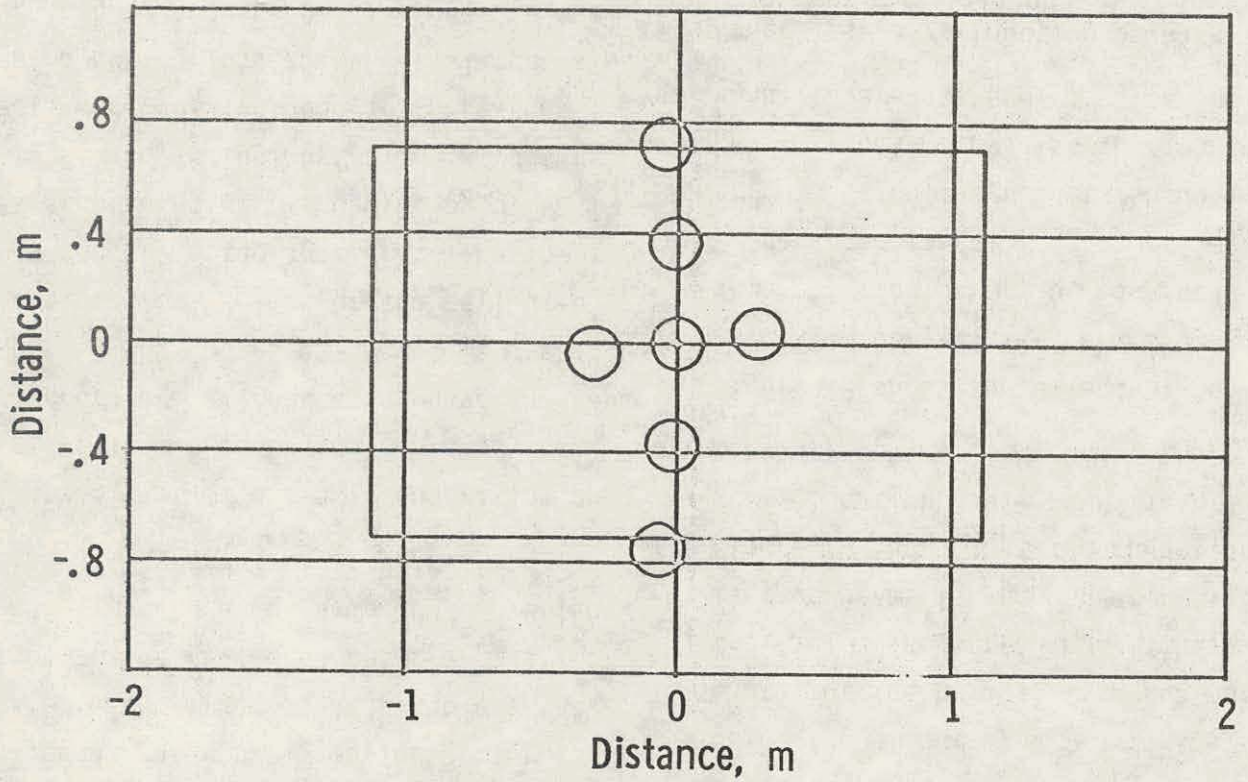

Alignment time: May 29, 11 a.m.
Operating time: May 29, 1 p.m.

Figure 8

Martin Marietta 10-MW pilot plant design. An artist's drawing of the pilot plant is shown in Figure 9. The analytical results shown in the figures that follow were obtained using a tower height of 90 meters, an aperture 7.5 meters square and a field of 1554 heliostats. Each heliostat has nine fixed-focus mirrors 2.13 meters square; each mirror is adjustable in azimuth and elevation so the reflected beams from all of the mirrors on a heliostat can be aligned to overlap at a selected time of day and time of year.

Figure 10 shows the effect of off-axis aberration on the percentage of reflected power that enters the aperture. The mirrors are aligned at noon on the day of vernal equinox, so the losses at that time are caused by spillage due to the size of the reflected beams relative to the projected aperture. The increase in losses at other times is caused by off-axis aberration. Heliostat pointing errors and structural deflection effects were not included in these runs. Also, shading and blocking losses are calculated using another computer program and are not included in the plots shown in Figure 10.

The dashed lines in Figure 10 apply to the total collector field. The solid lines apply to individual heliostats at the three corners on the east side of the collector field; location 1 is the front corner, and location 3 is the back corner.

Figures 11 and 12 are plots showing the projected aperture and the centers of the reflected beams from each of the nine mirrors on the projected aperture. These computer-generated plots are an aid in visualizing the effect of off-axis aberration. They show that, for the heliostat in the northeast corner of the field, the spreading of the centers of the reflected beams is much greater at 6 am than at 6 pm. Figure 10 shows that the power loss for this heliostat (location 3) is significantly greater at 6 am than at 6 pm.

Figure 13 shows the effect of heliostat pointing errors on power loss. The program was run using the same pointing error for each heliostat in the field to generate the plot of power loss versus pointing error. Using the results shown in Figure 13 and the known or estimated distribution of pointing errors, annual average energy loss can be calculated.

Power loss as a function of wind velocity and direction is shown in Figure 14. The program was run using wind velocities of 8.94 m/s (20 mph) and 13.4 m/s (30 mph) and wind directions at 45-degree steps from north. The plots shown were calculated for noon, vernal equinox. The results are similar, but not exactly the same, for other times of day and times of

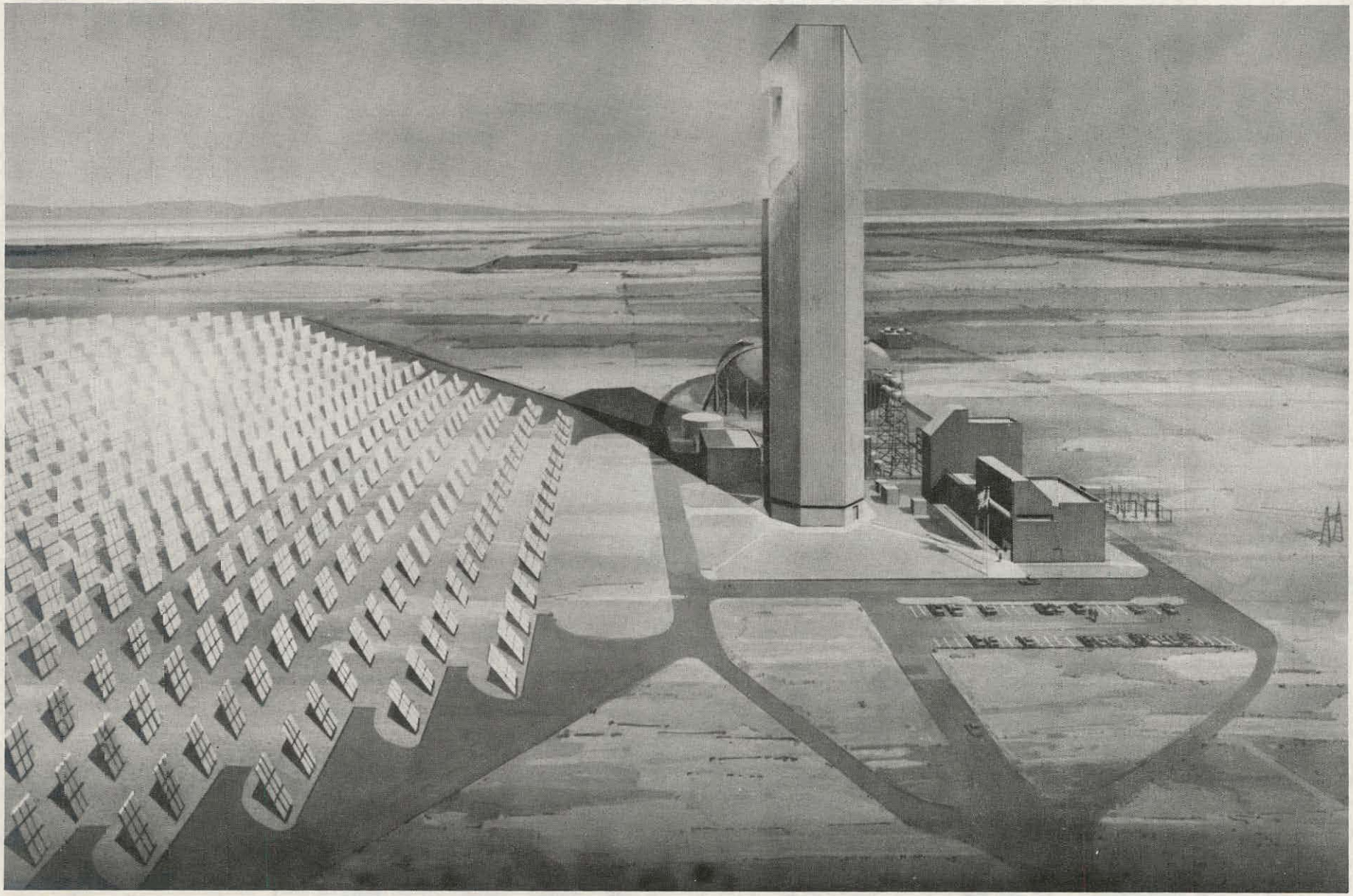

Figure 9 Artist's Drawing of 10-MW Pilot Plant

PROGRAM OUTPUT--EFFECT OF TIME OF DAY AND TIME OF YEAR ON LOSSES

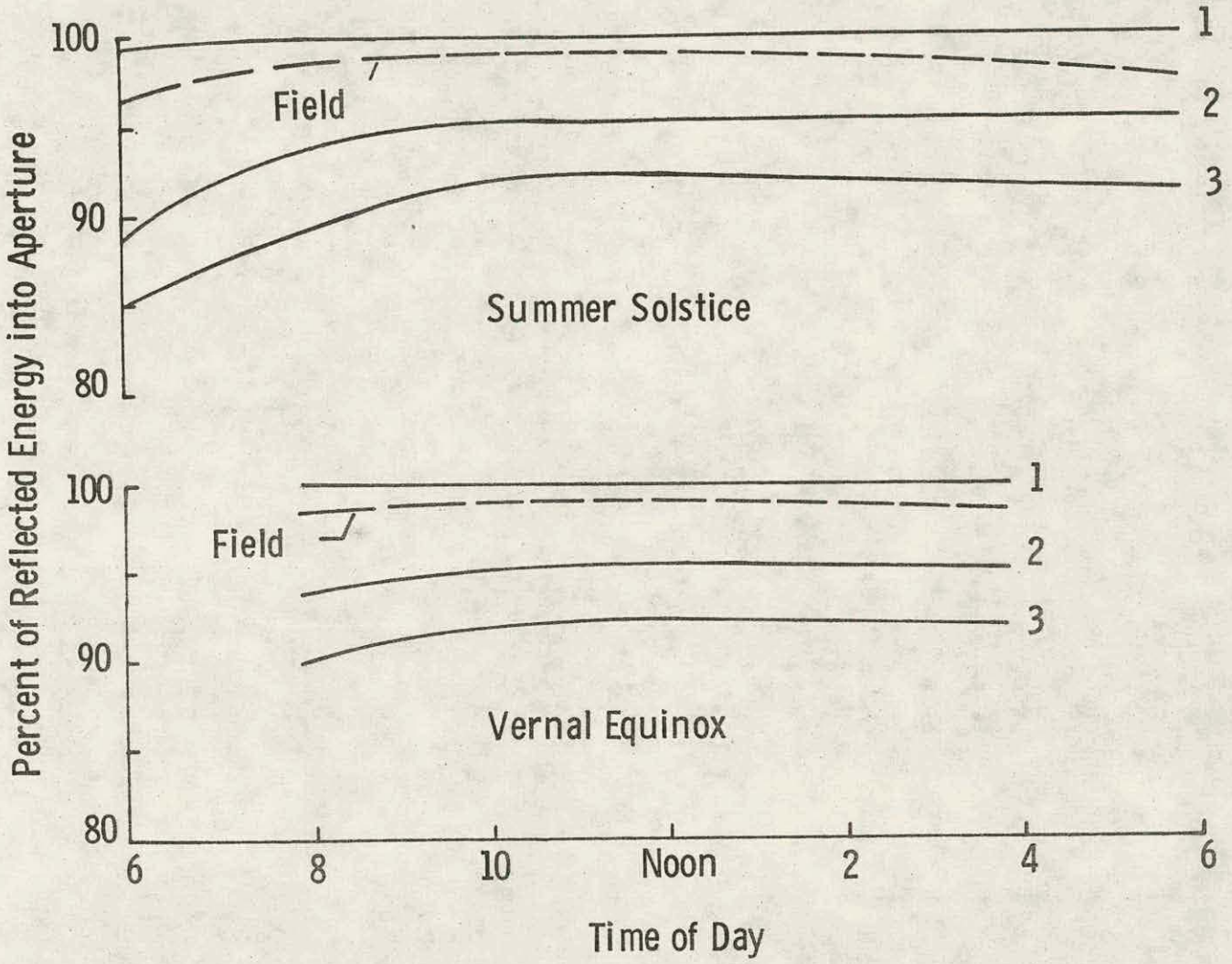

Figure 10

PROGRAM OUTPUT--EFFECT OF OPERATING TIME ON BEAM SPREADING (1)

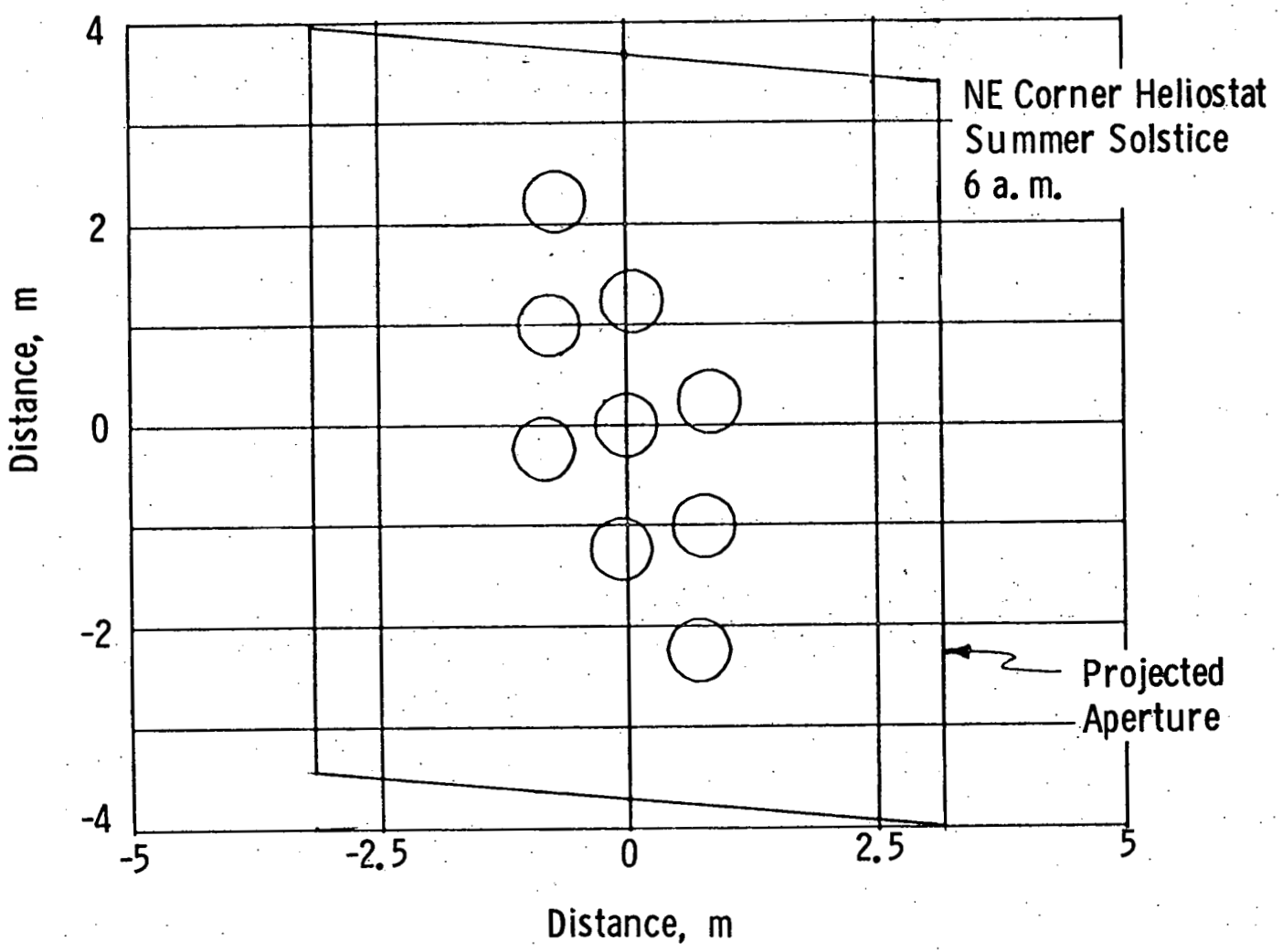

Figure 11

PROGRAM OUTPUT--EFFECT OF OPERATING TIME ON BEAM SPREADING(2)

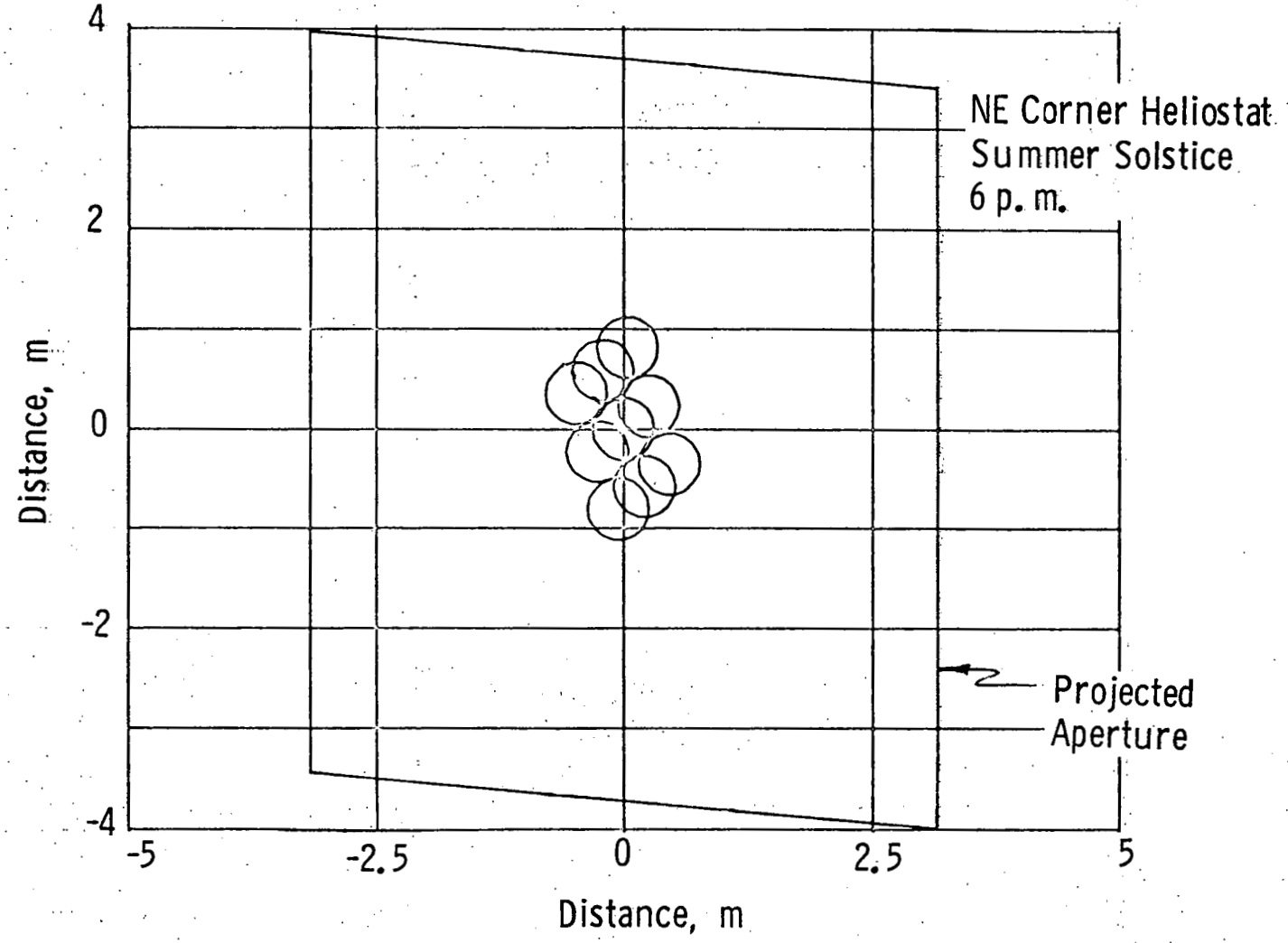

Figure 12

PROGRAM OUTPUT--POWER LOSS AS A FUNCTION OF POINTING ERROR

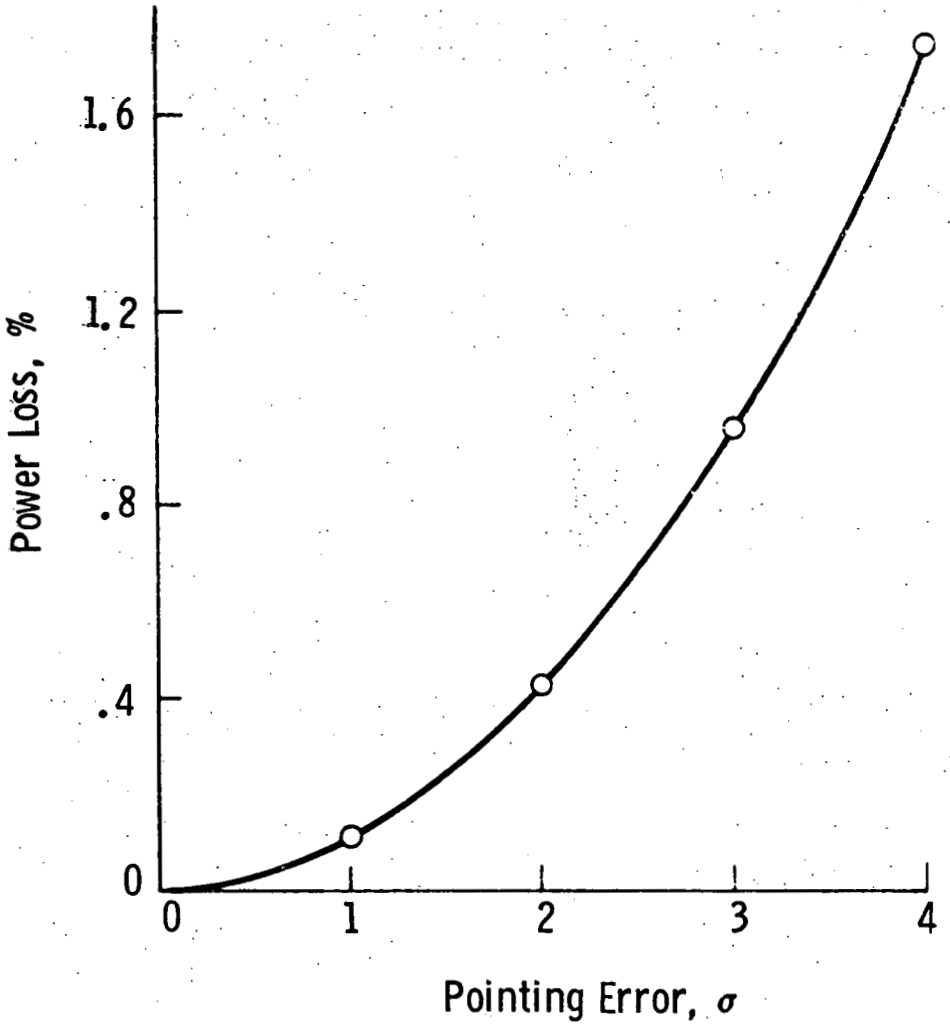

Figure 13

PROGRAM OUTPUT--POWER LOSS AS A FUNCTION OF WIND

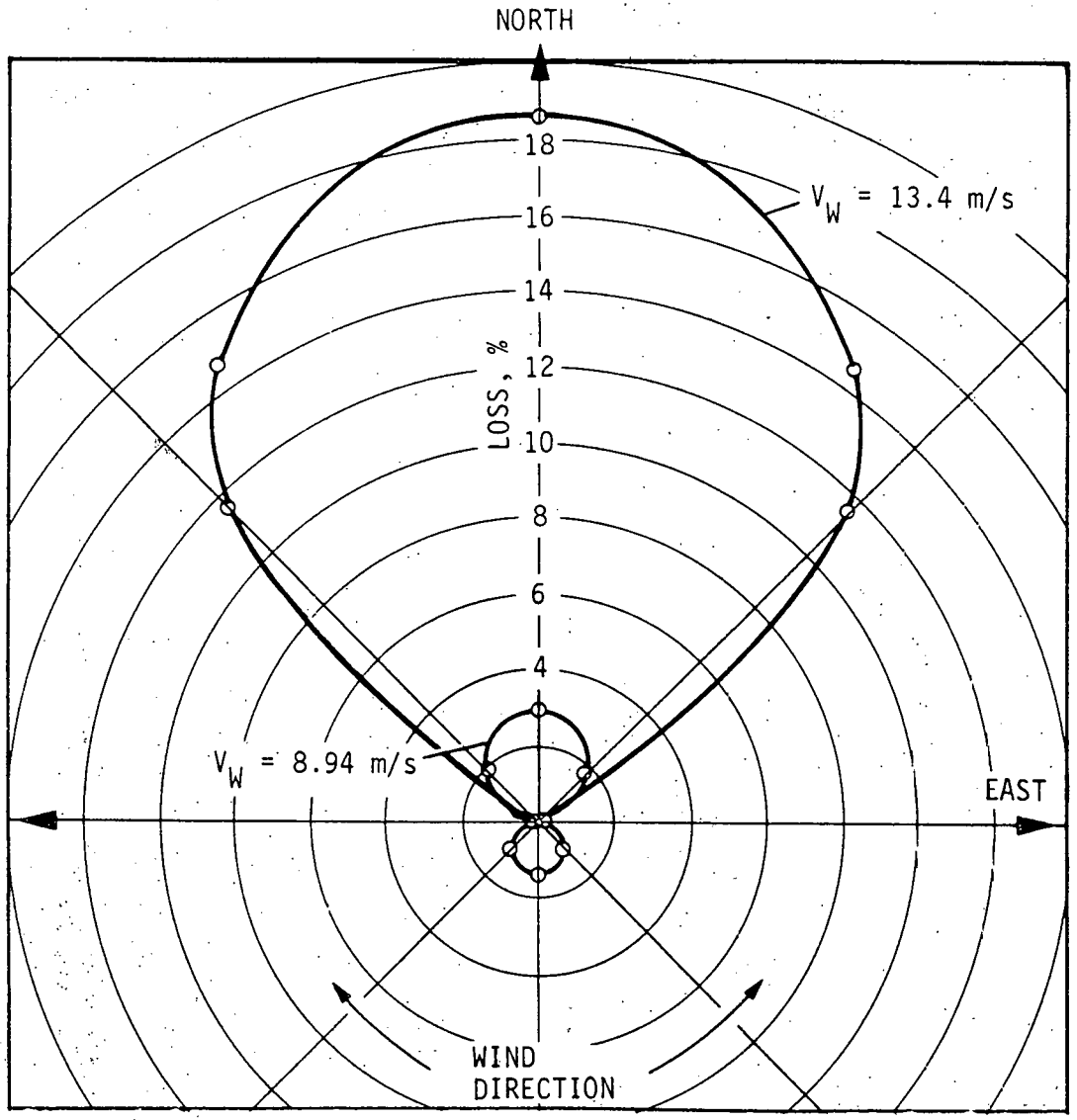

Figure 14

year. Using these results, and statistics on wind velocity and wind direction for the particular plant location, the annual average energy loss due to wind-induced structural rotations can be calculated.

RELATED PROGRAMS

Other computer programs that require considerably more computer run time are used to calculate the flux maps required for receiver design.

The losses due to wind-induced structural rotations shown in Figure 14 were calculated for constant wind velocities. Another computer program developed to model the heliostat drive mechanisms and control feedback loops has been used to determine heliostat response to wind gusts.

A computer program has been developed and used for aligning the mirrors on the heliostats at the Albuquerque Solar Thermal Test facility. That computer program uses subroutines similar to or identical to some of the subroutines used in the collector field power program. Examples are sun position calculation and the control algorithm. The alignment program also calculates mirror rotations caused by weight for the specified alignment time and compensates for those rotations in the alignment procedure.

As stated previously, a structural analysis program is used to calculate the mirror rotations that are input to the collector field power program.

CONCLUSIONS

The collector field power program is a useful tool for determining power losses caused by off-axis aberration, heliostat pointing errors and heliostat structural deflections. The program uses reflected flux patterns based on test data. The computation of beam spreading due to off-axis aberration has been verified by comparison with test data. Heliostat structural deflections due to weight and wind loads that are input to the program have also been verified by testing.

Program run time on a CDC 6500 is approximately 30 seconds for 100 heliostats.

ACKNOWLEDGEMENT

The computer program described in this paper was developed primarily by John W. Evans. Others who contributed to writing and checking out the program include D. E. Buck, D. D. Ostrander, E. G. Page and the author.

SOLAR FLUX DENSITY DISTRIBUTIONS ON CENTRAL TOWER RECEIVERS

M. Riaz and T. Gurr
Department of Electrical Engineering
University of Minnesota
Minneapolis, MN 55455

ABSTRACT

An analytical formulation of the solar flux density distributions produced on the surface of a central tower receiver by large mirror fields is developed which accounts for dispersion, shading and screening effects of mirrors, and for degradation of insolation levels. In the case of symmetrical geometries involving circular mirror fields and vertical cylindrical receivers, a general method of calculation yields closed-form solutions for the concentration ratios in terms of normalized parameters describing the mirror field configuration, the receiver dimensions, the insolation levels, the mirror characteristics, and the time of the day. Aiming strategies of mirror focusing are devised to reshape the insolar flux in accordance with desired distributions. Mirror field asymmetries created by the configuration itself or by operational conditions blanking a portion of the field (due, for instance, to maintenance or cloud cover) are shown to set up flux gradients around the receiver which can be computed using a flux superposition technique. The methodology elaborated in the case of the vertical cylindrical receiver for simplicity and insight of treatment is applicable to many other geometries presently envisioned in receiver studies for solar power tower systems.

Solar Energy, Vol. 19, pp. 185–194. Pergamon Press 1977. Printed in Great Britain

SOLAR FLUX DENSITY DISTRIBUTIONS ON CENTRAL TOWER RECEIVERS

M. RIAZ and T. GURR
Department of Electrical Engineering, University of Minnesota, Minneapolis, MN 55455, U.S.A.

(*Received* 13 *February* 1976; *in revised form* 9 *August* 1976)

Abstract—An analytical formulation of the solar flux density distributions produced on the surface of a central tower receiver by large mirror fields is developed which accounts for dispersion, shading and screening effects of mirrors, and for degradation of insolation levels. In the case of symmetrical geometries involving circular mirror fields and vertical cylindrical receivers, a general method of calculation yields closed-form solutions for the concentration ratios in terms of normalized parameters describing the mirror field configuration, the receiver dimensions, the insolation levels, the mirror characteristics, and the time of the day. Aiming strategies of mirror focusing are devised to reshape the solar flux in accordance with desired distributions. Mirror field asymmetries created by the configuration itself or by operational conditions blanking a portion of the field (due, for instance, to maintenance or cloud cover) are shown to set up flux gradients around the receiver which can be computed using a flux superposition technique. The methodology elaborated in the case of the vertical cylindrical receiver for simplicity and insight of treatment is applicable to many other geometries presently envisioned in receiver studies for solar power tower systems.

INTRODUCTION

Among the various solar thermal conversion systems proposed for large-scale generation of electricity, the central-receiver tower concept of a solar power plant is attracting today a great deal of attention for its promising potentials to conserve fossil fuels, to effect minimal environmental impact, and to become, as a ready technology, cost competitive in the future mix of power generating plants. In this concept, a large field of individually steered Sun-following mirrors or heliostats on two-axis tracking mounts reflects solar radiation to a tower-top receiver or boiler where the concentrated energy is converted to heat in a working fluid for temporary storage and for use in a conventional thermal-electric conversion equipment or in a total energy system[1]. This paper develops an analytical approach for the determination of the solar flux density distributions produced by the large mirror field—the concentrator—on the surface of the central receiver. Serving the function of an optical transmission system, the mirror field essentially is an approximation to the Fresnel equivalent of a parabolic mirror. Although there exists an abundant literature dealing with solar concentrators for such applications as solar furnaces or space power, most of the studies are not directly applicable to the central receiver scheme which is characterized by different constraints, requirements, and operational modes. Typical factors to be accounted for in considering the central receiver concept are the large flux or power levels encountered with the concomitant long optical transmission distances, the shadow effects created by neighboring mirrors which can block the incident and/or reflected radiation, the time-varying nature of the characteristics corresponding to continual changes in Sun altitude during the day, the effects of "blanking" certain zones of the mirror field as a consequence of a partial cloud cover, maintenance, or even malfunction. The mirror field is not so much designed to produce the largest possible concentration of solar energy in a focal zone as is the case, for instance, of a solar furnace; rather its function is to establish controllable concentrations through the use of appropriate time-dependent aiming strategies for focusing (or defocusing) the mirrors in order to reshape the flux density distributions in accordance with receiver design specifications. With such factors and design objectives in mind, this paper develops a methodology for the analysis (and synthesis) of the solar flux density distributions on a central receiver. Using a continuum characterization of the mirror field, the approach which is totally analytical is also general enough to apply to many concentrator-receiver configurations of interest. In the special case of symmetrical arrangements (as exhibited by the vertical cylindrical open receiver), the solutions reduce to closed-form expressions which provide insight into the behavior of the central receiver system and also serve as useful tools in preliminary designs and optimization studies. For detailed analysis of the solar flux produced by specific shapes of mirrors (or blocks of mirrors) placed in defined arrays around the tower, other computer approaches have been developed based on the summation of individual cell contributions[2] or on the use of Monte-Carlo techniques applied to ray trace simulation.

GEOMETRICAL CONFIGURATION

Consider the geometry shown in Fig. 1 in which a mirror M reflects the central ray of the Sun to a fixed focus or aim point F at a height H above horizontal ground. The location of this mirror is given by the angular coordinates (θ_l, β_l) measured with reference to F, θ_l being the distance angle (the linear distance to the tower base B is $R = H \tan \theta_l$) and β_l the azimuth angle referred to north counted positive eastward. The location of a point P on the receiver is specified in terms of the cylindrical coordinates (z_p, r_p, β_r) having F as origin. The orientation of the receiver surface at P is established by the unit normal vector $\bar{n}$, making an angle θ_r to the vertical, with the proviso, however, that it intersects the

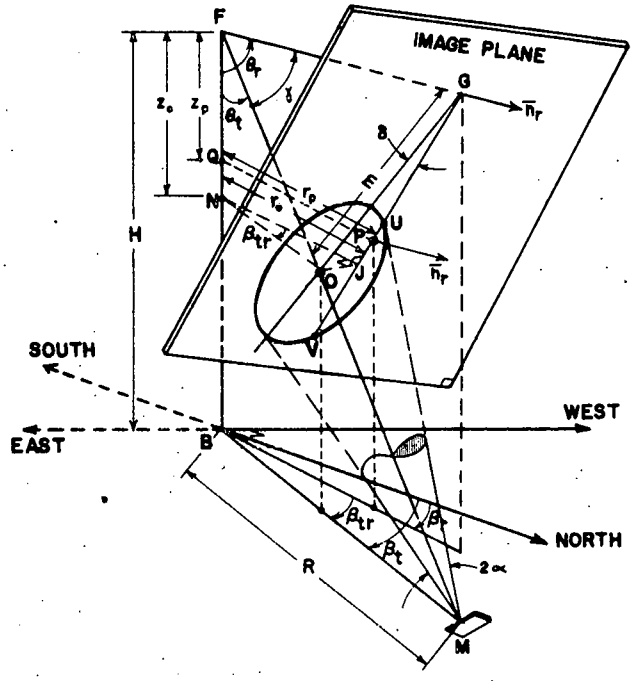

Fig. 1. Geometry of mirror and central receiver.

central vertical line (or tower line) *FB*. This condition imposes restrictions on the shape of receivers to which the analysis directly applies; it does include, however, many surfaces of revolution (around the tower line) such as inverted truncated cones, semi-spheres, cylindrical shells, flat horizontal planes, and combinations of these forms that are considered applicable to various open-type central receiver designs. The tangent plane to the receiver at P will be called the image plane; its intersection with the vertical plane containing the tower line FB and point P will be referred to as the image line GP, where G is the perpendicular projection of F on the image plane and is labeled the image focal point.

The Sun image is the ellipse formed by the intersection of the solar cone of half angle α with the image plane. If the receiver point P is interior to the ellipse, mirror M is said to be active at P; on the other hand, if P is exterior, the mirror is inactive at P. It is shown in the appendix how the size and placement of the ellipse in the image plane can be determined in terms of the specified location parameters for M and P in order to ascertain whether M is active or not at P. The concentrator field region (possibly multiply connected) in which all mirrors are active at P will be referred to as the mirror visibility zone relative to the receiver point P.

DERATING FACTORS

To account for the degradation in concentrator performance due to inherent imperfections in the mirrors and to environmental effects on insolation levels, three derating factors are introduced as intrinsic design parameters to be specified: the dispersion factor k, the mirror utilization factor u, and the degrading factor g imposed on the insolation level.

Dispersion factor k

Although probabilistic models of surface and steering errors and limb darkening effects of solar illumination could be included in the analysis of mirror performance, a constant dispersion factor, possibly field dependent, will be introduced here for simplicity of treatment. A simple definition of k is arrived at by considering a planar mirror of dimensions $L \times L$ located at the (large) distance $T = H \sec \theta_t$ from an image plane. At normal incidence, the total dispersion or spread of the solar image can be expressed as

$$D = 2(\alpha_s + \epsilon_m + \epsilon_{st})T + L = 2\alpha T.$$

The dispersion factor defined as the ratio of the effective reflected solar half angle to the actual Sun disc half angle ($\alpha_s = 4.65 \times 10^{-3}$ rad) is then given by

$$k = \frac{\alpha}{\alpha_s} = 1 + \frac{\epsilon_m + \epsilon_{st}}{\alpha_s} + \frac{L}{2\alpha_s H} \cos \theta_t.$$

Thus errors of the order of ± 1 m rad in steering and surface errors produce an approximate doubling of the solar disc in the case of an infinitesimal mirror; with a finite planar mirror, the dispersion is further increased as indicated by the last term which depends on radial field position and mirror-to-tower length ratio. Because tower height is a function of the square root of the power level, mirror dimensions may also have to be varied as function of power in order to achieve tolerable L/H ratios, especially in the field near the tower. The condition is particularly stringent at low power necessitating unwieldy small planar mirrors. To alleviate this problem, larger but focused nonplanar mirrors can be used to reduce the size of the Sun image and achieve also a modicum of concentration.

In this paper, the dispersion factor k will be assumed to cover a range from 2 to 4, with $k = 1$ representing ideal conditions.

Mirror utilization factor u

This geometric factor provides a measure of the local effectiveness of a mirror area in reflecting solar energy to a central focal point. For an isolated mirror, it is simply the cosine of the incidence angle of sunlight impinging on the mirror surface. For close-packed arrays, shadow effects are produced by neighboring mirrors, blocking the incident sunlight (Sun shading) and/or the reflected light (screening of receiver). For such situations, it has previously been shown[3, 4] that the mirror utilization factor u is equal to the cosine of the Sun zenith angle θ_z when Sun shading predominates (i.e. $u = \cos\theta_z$ when $\theta_t < \theta_z$), and to the cosine of the mirror distance angle θ_t in the case of receiver screening (i.e. $u = \cos\theta_t$ when $\theta_t > \theta_z$). It is significant to note that, in both shadowing cases, the utilization factor is uniquely a function of radial distance and not of azimuth.

Insolation degrading factor g

The reduction in the direct component of the insolation S_0 (a function of Sun angle θ_z) due to air mass, turbidity, and cloud cover effects (which in turn depend on time and geographical location) is lumped in a single factor g which, for convenience, also includes mirror reflectivity and area coverage losses. Thus an effective insolation $S = gS_0$ is introduced as an input design parameter to be specified. For lack of information but mostly for comparison purposes, it will often be appropriate to assign to S_0 a constant value of 1 kW/m².

FLUX DENSITY CALCULATIONS

Taking account of shading and screening effects, the effective area of an incremental mirror located at M in a continuum mirror field can be expressed as

$$dA_m = uR\,dR\,d\beta_{tr} = uH^2 \sin\theta_t \sec^3\theta_t\,d\theta_t\,d\beta_{tr} \quad (1)$$

where u is the pertinent mirror utilization factor. The solar flux reflected by this elementary mirror is $S\,dA_m$, where S is the effective insolation. If the energy density is considered to be uniformly distributed over the elliptical Sun image of area A_z (see (eqn A2)—a reasonable assumption for a geometry involving large target distances—the elementary solar flux density at P can, therefore, be written as

$$dq = \frac{S\,dA_m}{A_z} = \frac{S}{\pi k^2\alpha_z^2}\,u \tan\theta_t \cos\gamma\,d\theta_t\,d\beta_{tr} \quad (2)$$

provided, of course, that the elementary mirror is active at P. In general, the total flux density q at the receiver point P can be obtained by integration over the mirror visibility zone associated with P. Note that q depends only on angle variables (and S) but not on tower height H.

In order to derive analytical closed-form solutions for the flux density distributions, it is necessary to apply eqn (2) to symmetric geometries for both receiver and concentrator mirror field around the central tower. In the case of a vertical cylindrical receiver (discussed in the appendix), the elementary flux density at point P situated at the height H on the receiver (measured from the image focal point G) can be written explicitly in the form

$$dq = \begin{cases} \dfrac{S}{\pi k^2\alpha_z^2}\sin^2\theta_t \cos\beta_{tr}\,d\theta_t\,d\beta_{tr} & (\theta_t \geq \theta_z) \\ \dfrac{S}{\pi k^2\alpha_z^2}\sin^2\theta_t \sec\theta_t \cos\theta_z \cos\beta_{tr}\,d\theta_t\,d\beta_{tr} & (\theta_{tm} < \theta_t < \theta_z). \end{cases} \quad (3)$$

For a circularly symmetric mirror field, the total flux density at a given receiver height h can be obtained by integrating first with respect to β_{tr} so that

$$q = \begin{cases} \dfrac{2S}{\pi k^2\alpha_z^2}\displaystyle\int_{\theta_z}^{\theta_{tM}} \sin^2\theta_t \sin\beta_{tr}\,d\theta_t & (\theta_t \geq \theta_z) \\ \dfrac{2S}{\pi k^2\alpha_z^2}\displaystyle\int_{\theta_{tm}}^{\theta_z} \sin^2\theta_t \sec\theta_t \cos\theta_z \sin\beta_{tr}\,d\theta_t & (\theta_{tm} < \theta_t < \theta_z) \end{cases} \quad (4)$$

in which $\sin\beta_{tr}$ can be derived from $\cos\beta_{tr}$ given in eqn (A15) in terms of h and θ_t. The explicit final expression is, however, complicated so that numerical integration over the visibility zone will be resorted to in obtaining the results presented in the following section.

FLUX DENSITY DISTRIBUTIONS ON VERTICAL CYLINDRICAL RECEIVERS

Mirror visibility characteristics

The mirror field visibility zones for a vertical cylindrical receiver of radius r can be obtained on the basis of eqn (A14) derived in the Appendix. However, for generality, it is desirable to rewrite the equation in a non-dimensionalized form in which lengths on the receiver are normalized with respect to a base length $r_0 = \alpha_z H$ equal to the perfect Sun disc radius at the distance H. Thus, after noting that the reflected Sun disc radius $r_z = \alpha H = k\alpha_z H = kr_0$, eqn (A14) divided by r_0 assumes the normalized form

$$\tilde{h}/k = \csc\theta_t\{(\tilde{r}/k)\cos\theta_t \cos\beta_{tr} \pm [\sec^2\theta_t - (\tilde{r}/k)^2 \sin^2\beta_{tr}]^{1/2}\} \quad (5)$$

where the tilde is a mark denoting per-unit lengths. This equation defines visibility curves which are plots of the intersection points of the Sun ellipses with the image line as function of the relative mirror-to-receiver azimuth angle β_{tr} for various mirror distance angles θ_t and receiver radii $\tilde{r}$. Figures 2(a) and 2(b) are two typical plots, the first illustrating the dependence on θ_t for a fixed $\tilde{r}/k = 3$, and the second the dependence on $\tilde{r}/k$ for a fixed $\theta_t = 50°$. The mirror visibility zone corresponding to a specified location on a receiver of given radius is readily obtained from a plot such as Fig. 2(a). As an illustration, consider the location $\tilde{h}/k = 1.5$ on a receiver having $\tilde{r}/k = 3$: Fig. 2(a) shows that all mirrors located in a region where $\theta_t < 40°$ are inactive at the specified receiver location, while mirrors at a fixed radial distance θ_t greater than 40° are active only within specific azimuthal limits $\pm\beta_{tr}$ (which can be calculated from eqn A15). The maximum azimuthal limits of visibility are

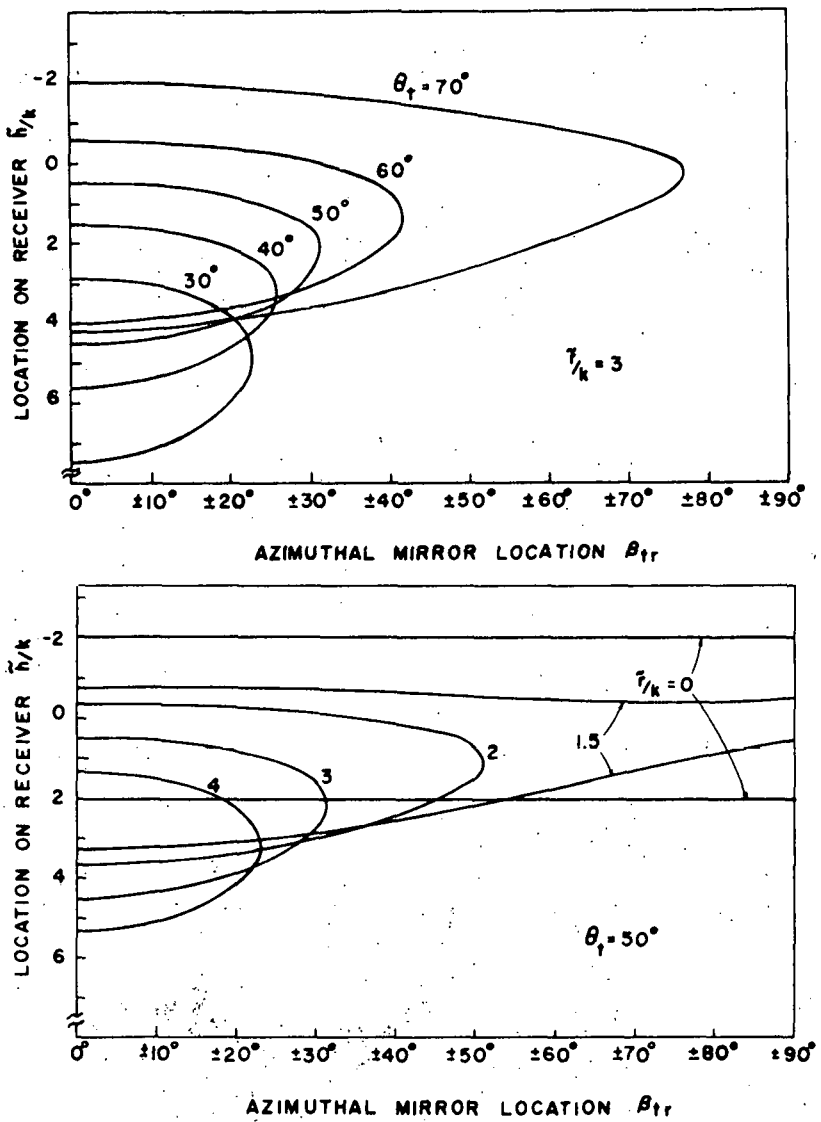

Figs. 2(a,b). Mirror visibility curves.

±90°, while the radial limits are given by the extreme rim angles θ_{tM} and θ_{tm} of the mirror concentrator field.

Single aim-point strategy

Flux density distributions on a vertical cylindrical receiver can be computed by applying the limits of the pertinent visibility curves to the integrals given in eqn (4). A universal set of curves can be derived as shown typically in Fig. 3 yielding the flux distributions under the following stipulations: all the mirrors are located inside a circular ring field with the tower at the center having inner and outer rim angles of θ_{tm} and θ_{tM}; a single-point aiming strategy is adopted so that all mirrors focus on point F; the dispersion factor k is taken to be a constant over the whole mirror field; to achieve maximum solar flux levels, the Sun zenith angle is assumed to satisfy the conditions $\theta_z \leq \theta_{tm}$ (which occurs around local noon) producing a mirror utilization factor $u = \cos\theta_t$ for the whole field which is then dominated by receiver screening effects; finally, a non-dimensional quantity $C = q/S$ representing the local concentration ratio is used in place of the flux density q. Application of these stipulations to eqn (4) yields

$$Ck^2 = \frac{2}{\pi\alpha_s^2}\int_{\theta_{tm}}^{\theta_{tM}} \sin^2\theta_t \sin\beta_{tr}\, d\theta_t (\theta_z \leq \theta_{tm}) \qquad (5)$$

whose integration within the previously determined visibility limits can be represented by the universal curves of Fig. 3 which show the dependency of the concentration ratio upon vertical position on the receiver for various receiver dimensions $\tilde{r}/k$. The plots of Fig. 3 are derived for a mirror field size bounded by $\theta_{tM} = 70°$ and $\theta_{tm} = 30°$. These concentration ratio curves exhibit notable features: An increase in receiver radius $\tilde{r}$ or dispersion factor k is accompanied by a reduction of the solar flux concentration and a linear stretching of the total solar image together with an enlarged tail in the distribution and a shift of the peaks toward lower receiver locations; these changes produce an effective defocusing action. The local concentration ratio C is independent of azimuth and is constant around the cir-

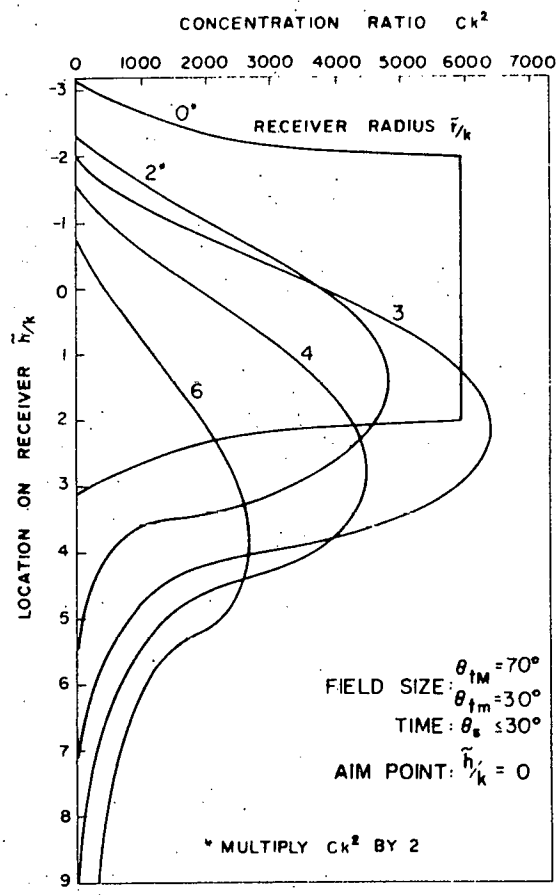

Fig. 3. Concentration ratio distributions. Dependence on receiver dimensions.

cular periphery of the receiver at a fixed height. The total solar flux Q reaching the receiver can thus be expressed by

$$Q = 2\pi r \int q \, dh = 2\pi\alpha_r^2 H^2(\tilde{r}/k) S \int Ck^2 \, d(\tilde{h}/k). \quad (6)$$

To capture all the solar flux reflected by the mirror field, the receiver radius must satisfy the condition $\tilde{r}/k \geq \sec \theta_{tM}$. This means that, with a rim angle of $\theta_{tM} = 70°$, receivers having $\tilde{r}/k < 2.9$ are subjected to a smaller total flux because, being too thin, they do not intercept all the reflected flux. On the other hand, all receivers with $\tilde{r}/k > 2.9$ must intercept the same available total reflected flux. In a previous paper[3], this total flux or power was shown to be equal to

$$Q = 2\pi H^2 S(\sec \theta_{tM} - \sec \theta_{tm}) \quad \text{for} \quad \theta_s \leq \theta_{tm}. \quad (7)$$

The identity resulting from comparing eqns (6) and (7), namely

$$(\tilde{r}/k) \int Ck^2 \, d(\tilde{h}/k) = \sec \theta_{tM} - \sec \theta_{tm}$$

can serve as a means of checking the accuracy of the universal curves, since the integral on the left-hand side is given by the area under the concentration ratio curve for any given $\tilde{r}/k$ (greater than $\sec \theta_{tM}$).

Multiple aiming strategies

With a single aim-point strategy of mirror focusing, the distributions illustrated in Fig. 3 exhibit rather high peak-to-average flux density ratios which are not suited to meet normal boiler design requirements. To flatten the flux distributions, it is necessary to resort to multiple aiming strategies by which various rings of mirrors concentric to the central tower—the $\Delta\theta_t$ bands—aim at different focal points along the center line of the receiver. Figure 4 presents the concentration ratio contributions of various $\Delta\theta_t$ mirror bands when all the mirrors in the entire field are aimed at one focal point so that the sum of all these individual band contributions produces the curve of Fig. 3 corresponding to the same set of parameters. When a particular ring of mirrors is reaimed at a new focal point, its flux contribution on the receiver maintains the original distribution in shape, magnitude, and azimuthal symmetry though shifted vertically by the identical distance through which the focal point has been displaced. This preservation of the shape of the contributing flux distribution is a valid approximation here when one considers the large distances between mirrors and receiver compared to the dimensions of the receiver. Thus by applying selectively multiple aiming strategies to different bands of mirrors, the solar flux density distributions can essentially be reshaped to meet desired specifications. A typical illustration of a possible strategy that will produce a trapezoidal flux density distribution is shown in Fig. 5.

Asymmetrical mirror fields

This section examines the effects of asymmetrical mirror fields on the flux density distributions under the

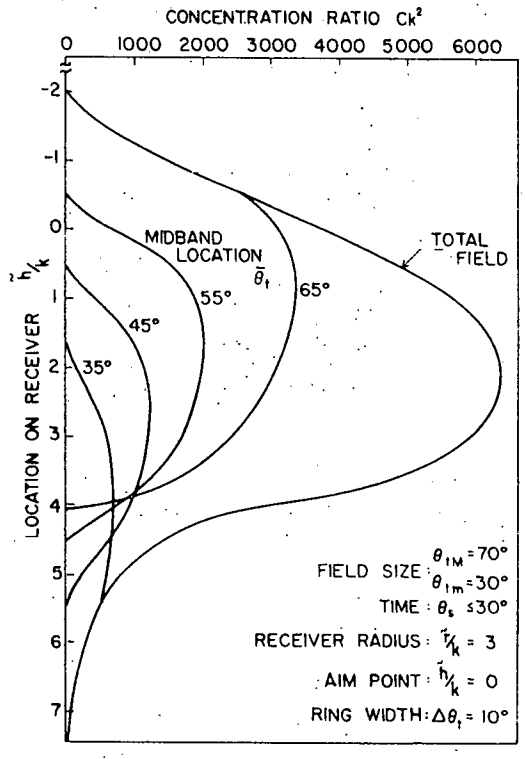

Fig. 4. Concentration ratio distributions. Circular ring contributions.

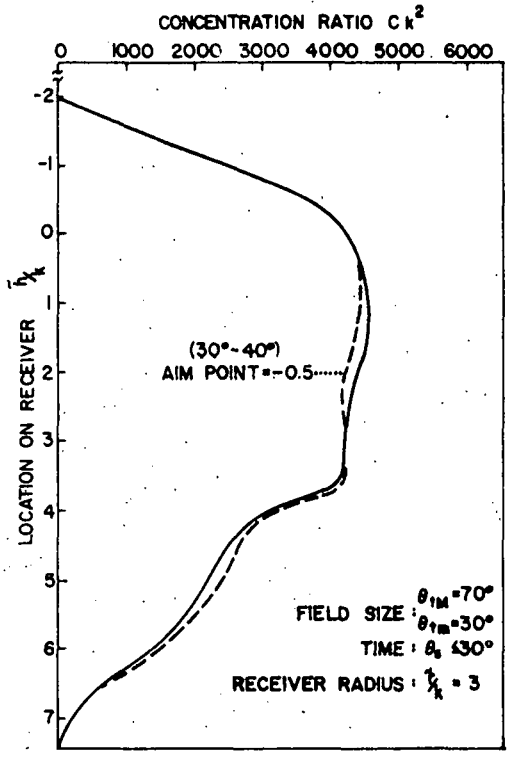

Fig. 5. Concentration ratio distributions. Multiple aim-point strategies.

$\Delta\theta_t$ Ring	Aim point $\bar{h}/k$
30°–40°	−1 (and −0.5)
40°–50°	+2
50°–55°	+2
55°–60°	−1.5
60°–70°	0

single-aim point focusing strategy. Asymmetrical fields can be encountered in various situations, normal or even abnormal: the actual mirror field may indeed not be circular; the tower may be displaced from the center (normally southward to improve mirror area utilization); portions of the mirror field may become ineffective due to a cloud cover or maintenance or perhaps malfunction. With asymmetry in the mirror field, the solar flux density distributions around the cylindrical receiver are no longer uniform but exhibit azimuthal gradients which must be taken into account in the receiver design or in the establishment of new focusing strategies to reduce their magnitudes. To render the analysis mathematically tractable, the field asymmetry to be considered here will be established by effectively removing a sector from the original circularly symmetrical mirror field. Thus, having previously examined the symmetrical contributions of $\Delta\theta_t$ bands, we turn here to the contributions of $\Delta\beta_t$ wedge segments upon the flux distributions. A wedge segment is identified by its width $\Delta\beta_t$ and by its bisecting radius vector of relative azimuth $\bar{\beta}_{tr} = \bar{\beta}_t - \beta_r$ measured with respect to a reference β_r on the receiver (absolute azimuth is $\bar{\beta}_t$ measured with respect to north where $\beta_r = 0°$); mirrors inside this wedge are, therefore, within the azimuthal limits $\bar{\beta}_{tr} - (\Delta\beta_t/2) \le \beta_{tr} \le \bar{\beta}_{tr} + (\Delta\beta_t/2)$, the radial limits still being $\theta_{tm} \le \theta_t \le \theta_{tM}$. Figure 6 illustrates the flux contributions of 15° wedge segments for the set of parameters indicated. Because $\bar{\beta}_{tr}$ represents a relative azimuth angle, the curves in Fig. 6 can be interpreted either as showing the contributions produced at one receiver location β_r by various 15° wedges located $\pm\bar{\beta}_{tr}$ away, or as giving the distributions at various receiver locations due to a single wedge segment situated at $\bar{\beta}_t$. For the chosen parameters, wedges of mirrors in the field range $75° \le \bar{\beta}_{tr} \le 90°$ are inactive at the receiver and thus do not appear in the figure. By superposing the above individual contributions of wedges, positively in the presence of active wedges and negatively in the case of removal of wedges, the flux density distributions created by various asymmetrical, though circular, mirror field configurations can readily be obtained. As an example, consider the original circular field which, for one reason or another, finds its effective area coverage reduced by one quarter; assume that the 90°-noncontributing sector is located due north of the central tower so that it is bounded by the limits $-45° < \beta_t < 45°$. For this field configuration and for the given parameters, the concentration ratio characteristics are shown in two equivalent sets of plots, one as a function of receiver height with receiver azimuth as parameter (Fig. 7a), the other exhibiting the dependency upon azimuth at various heights on the receiver (Fig. 7b). Both figures show the flux distributions to be symmetrical with respect to the north-facing image line at $\beta_r = 0$ where the minimum flux levels occur. Figure 7(a) indicates that the receiver zone where $|\beta_r| > 120°$ (facing due South) experiences the original total fluxes produced by the circular mirror field; the reason is that the 90°-northern sector is simply inactive in

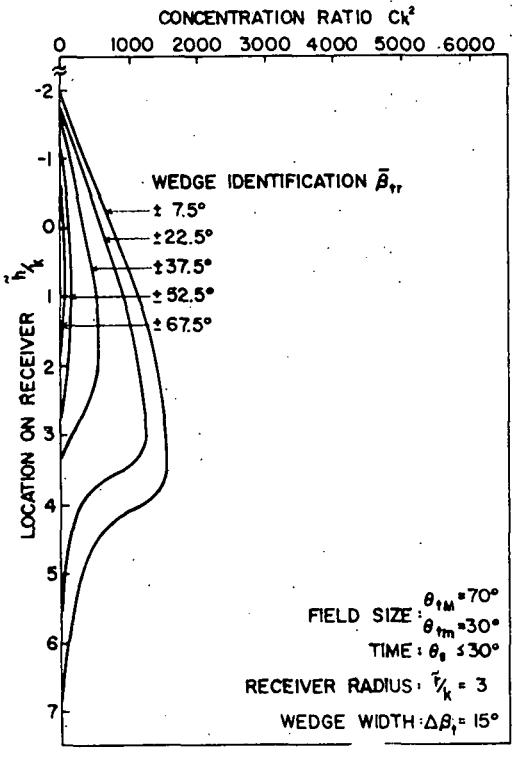

Fig. 6. Concentration ratio distributions. Wedge segment contributions.

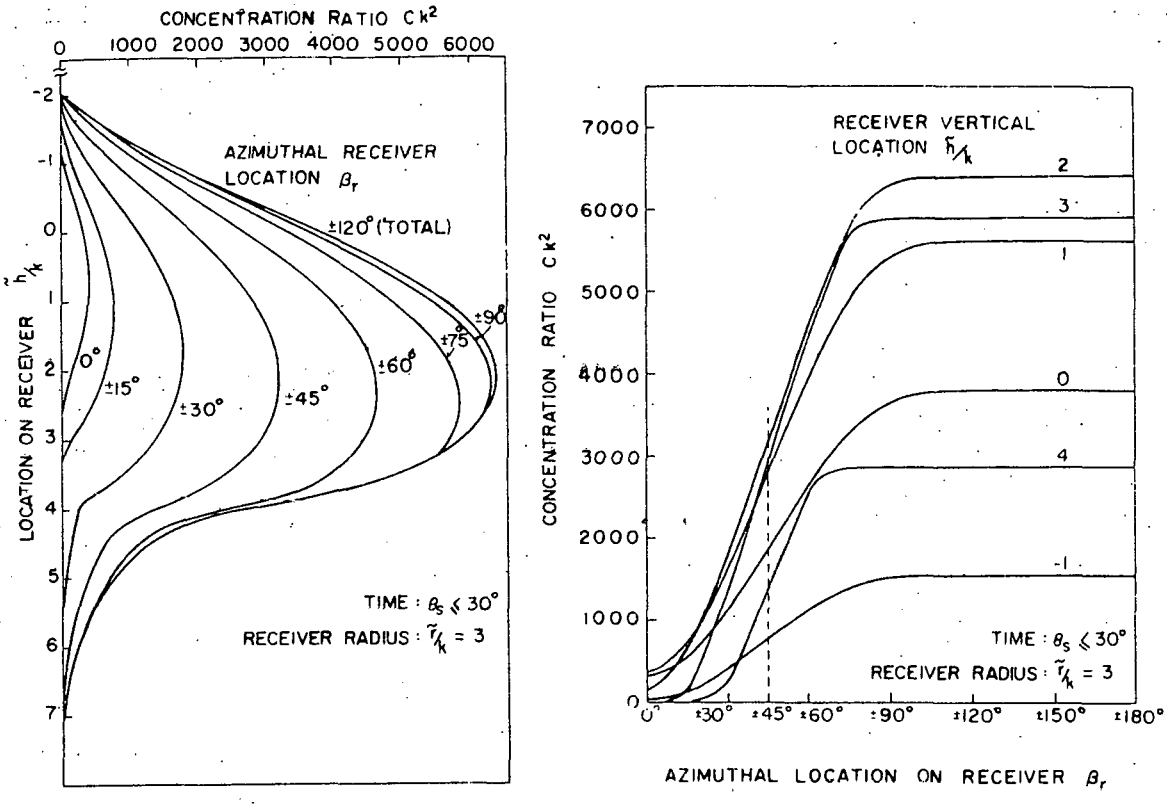

Fig. 5(a.b). Azimuthal dependence of concentration ratios produced by Asymmetrical mirror field. Size: $\theta_{iM} = 70°$; $\theta_{im} = 30°$. Non-contributing sector: $-45° < \beta_r < 45°$.

this southern receiver zone. Figure 7(b) shows that the azimuthal flux gradient at a fixed height on the receiver is approximately constant and that the 50 per cent flux levels occur at $\beta_r = \pm 45°$. The high flux density gradients observed here are obviously the result of the extreme asymmetry assumed for the mirror field. Nevertheless, the example is not atypical of the type of severe problems that could be encountered in central receiver operation. To alleviate the problem and develop a more symmetrical flux density distribution around the receiver from an inherent asymmetrical field may require off-axis strategies of mirror focusing.

Time effects

Thus far, the Sun zenith angle θ_s was assumed to satisfy the condition $\theta_s \leq \theta_{im}$ which occurs (if at all) around noon and provides for maximum flux density levels. At a different time when $\theta_s \geq \theta_{im}$, the mirror field experiences shading effects which lower these flux levels. The computation of the concentration ratios is now based on using the complete eqn (4) in which the shading effect clearly appears as the reduction factor $\rho = \sec\theta_i \cos\theta_s$ whenever $\theta_i < \theta_s$. The concentration ratio distributions resulting from a low Sun on the horizon of $\theta_s = 65°$ are illustrated in Fig. 8 for a receiver having $\tilde{r}/k = 3$ and a circularly symmetric mirror field (having $\theta_{im} = 30°$ and $\theta_{iM} = 70°$) focusing at one central point. Shown are the $\Delta\theta_i$ band contributions and the total flux density distributions. By comparing Figs. 4 (for which $\theta_s \leq 30°$) and 8, it can be seen that a $\Delta\theta_i$ band contribution of a selected midband location ($\bar{\theta}_{in} < \theta_s$) in Fig. 8 can be approximated by multiplying the corresponding distribution in Fig. 4 by the constant factor $\sec\bar{\theta}_{in}\cos 65°$ which is less than unity. In Fig. 9, a similar reduction in the contributions of 15° wedges can be observed for $\theta_s = 65°$ when compared to the distributions of Fig. 5 obtained when $\theta_s \leq 30°$. Using such techniques, the daily time effects as they translate into changes in Sun angle θ_s can be accounted for in the determination of the time-varying solar flux density distributions and hence in the establishment of aiming strategies designed to control these distributions.

CONCLUSIONS

The solar flux density distributions produced on the surface of a central tower receiver by large mirror fields have been determined using an analytical formulation that accounts for dispersion, shading and screening effects, and insolation degradation. Simple closed-form solutions for the concentration ratios effective at the receiver have been obtained in the case of symmetrical geometries involving circular mirror fields and vertical cylindrical receivers. The significance of such solutions which are presented as universal curves with dimensionless parameters is that they can readily be used to study the effects of changes in system parameters such as mirror field geometry, receiver dimensions, mirror characteristics, time of the day, and insolation level. Furthermore, the universal curves have demonstrated their usefulness in the establishment of mirror aiming strategies for reshaping the solar fluxes on the receiver to achieve desired and controllable distributions. Finally,

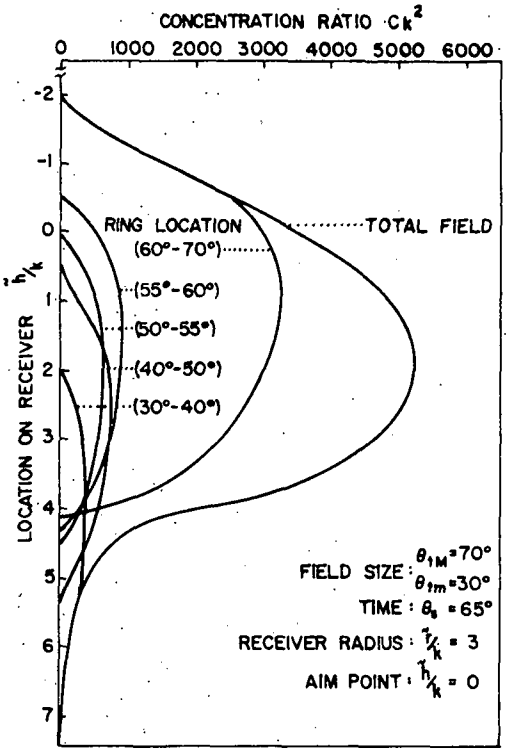

Fig. 8. Concentration ratio distributions. Time effects on ring contributions.

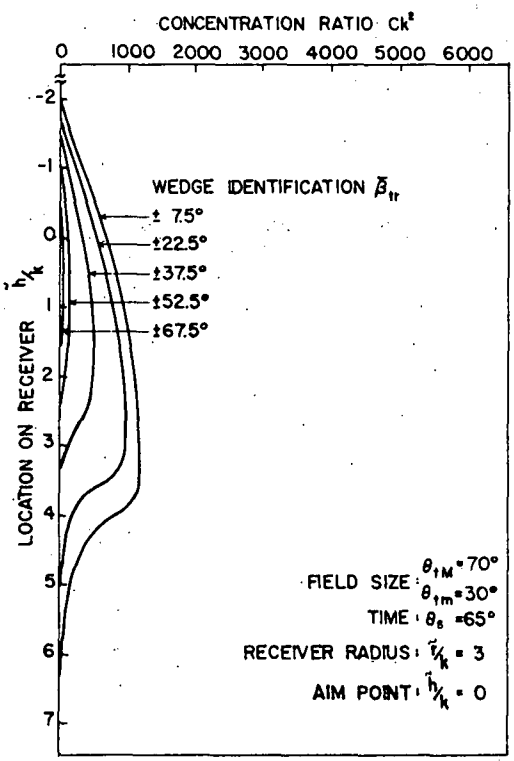

Fig. 9. Concentration ratio distributions. Time effects on wedge contributions.

asymmetries in the mirror field created by design or by operational conditions (for instance, maintenance or cloud cover which effectively blanks a whole region) have been shown to produce flux gradients around the receiver which can be evaluated by superposing the flux contributions of pertinent segments of the mirror field.

The flux density calculations detailed here in the context of cylindrical receivers for simplicity of treatment and insight afforded by the closed-form results can further be applied to many other concentration-receiver configurations subject to this proviso: the whole mirror field most focus on a vertical tower line where the receiver surface normals also intersect. Thus, the mathematical analysis may readily be extended to cover receivers having surfaces of revolution (about the tower line) such as inverted truncated cones, semispheres, half vertical cylindrical shells, flat horizontal planes, as well as combinations of such shapes. However, special considerations must be given to open receivers with reentrant surfaces and cavity receivers which produce partial blocking of the incoming solar flux. Off-axis or azimuthal aiming strategies of mirror focusing also require further study.

Acknowledgement—The research on which this paper is based has been supported by ERDA under Contract No. E(11-1)-2699[5].

NOMENCLATURE

- a semi-major axis of elliptical Sun image
- b semi-minor axis
- A_e area of ellipse
- A_m mirror effective area
- C concentration ratio = q/S
- H tower height
- R distance of mirror to tower base
- T distance of mirror to focal point F
- r radius of cylindrical receiver
- r_0 normalizing length = $\alpha_s H$
- h distances on receiver image line
- k dispersion factor = α/α_s
- $\bar{n}_r$ unit vector normal to receiver
- Q total solar power or flux reaching the receiver
- q solar flux density
- S effective insolation
- g insolation derating factor
- u mirror utilization factor
- α_s Sun disc half angle ≅ 4.65 m rad
- α effective reflected Sun cone half angle
- β azimuth angles measured with respect to north positive eastward
- θ_t mirror distance angle
- θ_s Sun zenith angle
- δ profile angle in image plane
- γ incidence angle on image plane
- ϵ_m mirror surface contour error
- ϵ_s steering or pointing error
- ρ shading parameter = sec θ_t cos θ_s($\theta_t < \theta_s$)

REFERENCES

1. L. L. Vant-Hull and A. F. Hildebrandt, Solar thermal power system based on optical transmission. *Solar Energy* **18**, 31 (1976).
2. F. W. Lipps, An analytical integration of the solar flux density due to rectangular mirrors. *ASME* Paper 74-WA/Sol-10 (1974).
3. M. Riaz, A theory of concentrators of solar energy on a central receiver for electric power generation. *ASME Journal of Engineering for Power* **98**, 375 (1976).
4. Solar Power Array for the Concentration of Energy. Semi-Annual Progress Report, NSF Grant GI-41019. Sheldahl, Inc., University of Minnesota, and Foster Wheeler Corp., Report No. NSF/RANN/SE/GI-41019/PR/74/2 (1974).

5. T. Gurr and M. Riaz, Heliostat Array Analysis (Solar Power Array for the Concentration of Energy). Technical Report covering Task 4a No. COO-2699-1 under ERDA Contract No. E(11-1)-2699 (1975).

APPENDIX

SUN IMAGE ON RECEIVER PLANE DUE TO A SINGLE MIRROR

General case of inclined image plane

In this appendix the size and placement of the solar image in the image plane are found in terms of specified location parameters for the mirror M and receiver point P. The object of the exercise is to determine the conditions for which mirror M is active at P. Referring to Fig. 1, this condition is satisfied when P is inside the ellipse and, therefore, located between points U and V representing the intersection of the ellipse with the image line.

The center O of the ellipse which is the piercing point of the tower line or cone axis MF on the image plane is defined in terms of the cylindrical coordinates (z_0, r_0, β_r) referred to the focal point F as origin. The incidence angle of the tower line MF with respect to the image plane is denoted by γ. The major axis of the ellipse is oriented along the line OG which makes a profile angle δ with respect to the image line. The lengths of the semi-minor and semi-major axes are respectively

$$b = r_s \sec\theta_t \qquad a = b\sec\gamma = r_s \sec\theta_t \sec\gamma. \tag{A1}$$

where $r_s = \alpha H = k\alpha_s H$ is the radius of the reflected circular solar image on an image plane at normal incidence located a distance H from the mirror. Thus the area of the sun ellipse is

$$A_s = \pi ab = \pi k^2\alpha_s^2 H^2 \sec^2\theta_t \sec\gamma \tag{A2}$$

Implicit in these relations is the justified assumption that receiver and Sun image dimensions are small compared to the tower height H; consequently, the distance MO is approximated as $H\sec\theta_t$.

To evaluate the profile and incidence angles δ and γ in terms of the location parameters specifying M and P, it is convenient to examine a profile view of the image plane as shown in Fig. A from which the following relations are readily derived

$$h = GP = z_p\sin\theta_r - r_p\cos\theta_r$$

$$FG = z_p\cos\theta_r + r_p\sin\theta_r$$

$$= z_0\cos\theta_r + r_0\sin\theta_r$$

$$GJ = z_0\sin\theta_r - r_0\cos\theta_r$$

The right triangles NJO and FNO yield

$$OJ = r_0\tan\beta_{tr} \quad \text{and} \quad ON = r_0\sec\beta_{tr} = z_0\tan\theta_t$$

so that $r_0/z_0 = \tan\theta_t\cos\beta_{tr}$ where $\beta_{tr} = \beta_t - \beta_r$ is the relative azimuth angle between mirror and receiver point. Similarly, the right triangles FGO and FNO yield

$$OF = FG\sec\gamma = z_0\sec\theta_t.$$

These relations can now be used to express γ and δ in terms of the location parameters as follows

$$\cos\gamma = \frac{FG}{FO} = [\cos\theta_r + (r_0/z_0)\sin\theta_r]\cos\theta_t$$

$$= \cos\theta_r\cos\theta_t + \sin\theta_r\sin\theta_t\cos\beta_{tr} \tag{A3}$$

$$\sin\delta\sin\gamma = \frac{OJ}{OG}\times\frac{OG}{OF} = \frac{OJ}{OF} = \frac{r_0}{z_0}\cos\theta_t\tan\beta_{tr}$$

$$= \sin\theta_t\sin\beta_{tr} \tag{A4}$$

$$\cos\delta\sin\gamma = \frac{GJ}{OJ}\times\frac{OG}{OF} = \frac{GJ}{OF}$$

$$= [\sin\theta_r - (r_0/z_0)\cos\theta_r]\cos\theta_t$$

$$= \sin\theta_r\cos\theta_t - \cos\theta_r\sin\theta_t\cos\beta_{tr} \tag{A5}$$

$$\tan\delta = \frac{\sin\theta_t\sin\beta_{tr}}{\sin\theta_r\cos\theta_t - \cos\theta_r\sin\theta_t\cos\beta_{tr}}. \tag{A6}$$

The intersections of the solar ellipse with the image line at U and V can be obtained by solving simultaneously the corresponding equations of the ellipse and image line. Using x–y axes coinciding with the principal axes of the ellipse, these equations are

$$\begin{cases} (x^2/a^2) + (y^2/b^2) = 1 \\ y = (m - x)\tan\delta \end{cases}$$

where

$$m = OG = FG\tan\gamma = (z_p\cos\theta_r + r_p\sin\theta_r)\tan\gamma. \tag{A7}$$

Eliminating y gives the quadratic equation

$$x^2 - a^2 + (a^2/b^2)(m - x)^2\tan^2\delta = 0$$

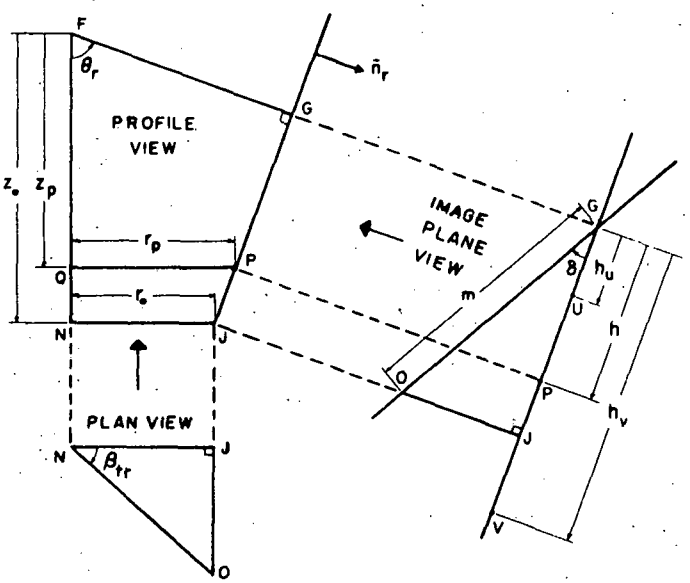

Fig. A. Views of image plane tangent to receiver at P.

whose solutions are the projections of U and V measured from O along the major axis. To find the distances $h_u = GU$ and $h_v = GV$ measured from G along the image line, define the new variable $x' = m - x$ so that $h = x' \sec \delta$ and solve the quadratic equation in x', namely

$$[1 + (a^2/b^2)\tan^2 \delta]x'^2 - 2mx' + m^2 - a^2 = 0.$$

The result is

$$h_{u,v} = \sec \delta \frac{m \pm a[1 + \tan^2 \delta(a^2 - m^2)/b^2]^{1/2}}{1 + \tan^2 \delta(a^2/b^2)} \quad \text{(A8)}$$

with the plus sign associated with V, the minus with U. A negative h_u means that the image focal point is between U and V.

The mirror M will be active at the receiver point P (located at $h = GP$) when the condition $h_u \le h \le h_v$ is met.

Special case of vertical cylindrical receiver

The previous results simplify considerably when applied to the special case of an open receiver having the shape of a cylinder of radius r whose axis coincides with the vertical tower line FB. Not only are image line and plane vertical, but the image focal point G is at the same altitude H as the central focal point F above ground. More significantly, because the vertical cylindrical receiver imposes the constraint $\theta_r = 90°$ on the image plane orientation, all the previous relations can now be written explicitly in terms of the location parameters.

The incidence and profile angles are given by the simpler expressions

$$\cos \gamma = \sin \theta_t \cos \beta_{t,r} \quad \text{(A9)}$$

$$\tan \delta = \tan \theta_t \sin \beta_{t,r} \quad \text{(A10)}$$

which can be further written in these equivalent forms

$$\sin \gamma = \sqrt{A} \cos \theta_t \cos \beta_{t,r};\ \tan \gamma = \sqrt{A} \cot \theta_t \quad \text{(A11)}$$

$$\sin \delta = \frac{1}{\sqrt{A}} \tan \theta_t \tan \beta_{t,r};\ \cos \delta = \frac{1}{\sqrt{A}} \sec \beta_{t,r}$$

where

$$A = 1 + \sec^2 \gamma \tan^2 \delta = 1 + \sec^2 \theta_t \tan^2 \beta_{t,r} \quad \text{(A12)}$$

The location of the center O of the solar ellipse formed in the vertical image plane can be defined by the lengths of these line segments

$$m = OG = r \tan \gamma = r\sqrt{A} \cot \theta_t \quad \text{(A13)}$$

$$OJ = r \tan \beta_{t,r}$$

$$JG = r \cot \theta_t \sec \beta_{t,r}$$

Finally after noting that

$$a/b = \sec \gamma;\quad b = r_s \sec \theta_t;\quad m = r \tan \gamma,$$

the general expression (A7) for the distances $h_{u,v}$ between the image focal point G and the intersections U, V of the ellipse with the image line can be reduced as follows

$$h_{u,v} = \frac{\sqrt{A} \cos \beta_{t,r}}{A}\left[r\sqrt{A} \cot \theta_t \pm r_s \sec \theta_t \csc \theta_t \sec \beta_{t,r} \times \left(A - \frac{r^2}{r_s^2}\cos^2 \theta_t A \cot^2 \theta_t \tan^2 \theta_t \sin^2 \beta_{t,r}\right)^{1/2}\right]$$

$$= \csc \theta_t [r \cos \theta_t \cos \beta_{t,r} \pm (r_s^2 \sec^2 \theta_t - r^2 \sin^2 \beta_{t,r})^{1/2}]. \quad \text{(A14)}$$

It is important to recognize the simplicity of the final result from which the visibility zones are readily obtained. In particular, corresponding to a specified position h on the receiver, the azimuthal visibility limits for a ring of mirrors located at a distance angle θ_t are given by

$$\cos \beta_{t,r} = \frac{1}{r \sin \theta_t}[-h \cos \theta_t \pm (h^2 + r^2 - r_s^2 \sec^2 \theta_t)^{1/2}]. \quad \text{(A15)}$$

Resumen—Una formulación analítica de las distribuciones de densidad de flujo solar producidas por grandes campos de espejos en la superficie de una torre central receptora, es desarrollada incluyendo efectos de dispersión oscurecimiento de los espejos debido a sombras y degradación de los niveles de aislamiento. En el caso de geometrías simétricas que involucran campos circulares de espejos y receptores cilíndricos verticales, un método general de calculo permite obtener expresiones analíticas para los radios de concentración en función de los parámetros normalizados que describen la cofiguración del campo de espejos, las dimensiones del receptor, los niveles de aislamiento, las características del espejo, y la hora del dia. Estrategias de orientación para enfoque de los espejos son desarrolladas a fin de modificar el flujo solar de acuerdo a las distribuciones deseadas. Se demuestra que asimetrías en el campo de los espejos creadas por la configuración misma o por eliminación parcial del campo debido a condiciones operacionales (por ejemplo, debido a mantenimiento o cielo nublado) producen gradientes de flujo alrededor del receptor que pueden ser calculados usando una técnica de superposición de flujos. La metodología elaborada para el caso de un receptor vertical cilíndrico es aplicable por simplicidad e intuición de tratamiento a muchas otras geometrías actualmente consideradas para sistemas de torres solares.

Résumé—Une méthode analytique pour la détermination de la densité du flux solaire produit par un large champ de mirroirs sur la surface d'un capteur placé sur une tour centrale est dévelopée en tenant compte des effets de dispersion, d'ombres des mirroirs, et de la dégradation des niveaux du rayonnement solaire. Dans le cas de géométries symétriques comprenant des champs circulaires de mirroirs et de capteurs cylindriques verticaux, une méthode générale de calcul permet d'obtenir des expressions analytiques pour la concentration qui est évaluée à partir de paramétres normalisés représentant la configuration du champ des mirroirs, les dimensions du capteur, le niveau du rayonnement solaire, les caractéristiques des mirroirs, et l'heure du jour. Des stratégies d'orientation pour la focalisation des mirroirs sont déduites afin de redistribuer le flux solaire selon des profiles désirés. Les asymétries du champ des mirroirs établies par des configurations particulières ou par des conditions d'ópération éliminant une partie du champ (causées, par example, par des réparations ou par le passage de nuages) produisent des changements de la densité du flux sur la périphérie du capteur qui peuvent être évalués par un procédé de superposition des flux. La méthode dévelopée ici en détail pour le cas d'un capteur cylindrique vertical par raison de la simplicité du raisonnement et de l'analyse peut aussi être appliquée à d'autres géométries de capteurs qui sont actuellement considérées dans les études de tours centrales solaires.

THIS PAGE

WAS INTENTIONALLY

LEFT BLANK

A THEORY OF CONCENTRATORS OF SOLAR ENERGY ON A CENTRAL RECEIVER FOR ELECTRIC POWER GENERATION

M. Riaz
Assoc. Professor
University of Minnesota
Minneapolis, Minnesota

ABSTRACT

The modeling of the performance of large-area solar concentrators for central receiver power plants is formulated using a continuum field representation of ideal heliostat arrays that accounts for two governing factors: the law of reflection of light rays imposes steering constraints on mirrors orientations; the proximity of mirrors creates shadow effects by blocking the incident and/or reflected solar radiation. The results of a steering analysis which develops the space-time characteristics of heliostats and of a shadow analysis which determines the local effectiveness of mirrors in reflecting solar energy to a central point are combined to obtain in closed analytical form the global characteristics of circular concentrators. These characteristics which appear as time profiles for mirror orientations, for effective concentration areas (i.e, reflected solar flux), and for concentration ratios establish theoretical limits of performance against which actual or realistic solar power systems can be compared and assessed.

Reprinted from ENGINEERING FOR POWER, Vol. 98, No. 3, July 1976

M. R. Riaz
Assoc. Professor,
Department of Electrical Engineering,
University of Minnesota,
Minneapolis, Minn.

A Theory of Concentrators of Solar Energy on a Central Receiver for Electric Power Generation

The modeling of the performance of large-area solar concentrators for central receiver power plants is formulated using a continuum field representation of ideal heliostat arrays that accounts for two governing factors: the law of reflection of light rays imposes steering constraints on mirror orientations; the proximity of mirrors creates shadow effects by blocking the incident and/or reflected solar radiation. The results of a steering analysis which develops the space-time characteristics of heliostats and of a shadow analysis which determines the local effectiveness of mirrors in reflecting solar energy to a central point are combined to obtain in closed analytical form the global characteristics of circular concentrators. These characteristics which appear as time profiles for mirror orientations, for effective concentration areas (i.e., reflected solar flux), and for concentration ratios, establish theoretical limits of performance against which actual or realistic solar power systems can be compared and assessed.

Introduction

Several methods are under consideration for converting solar radiation to electricity at levels commensurate with conventional power generating plants. The conversion process is either direct, utilizing photovoltaic cells [1][1] or solar-thermal, typically employing concentrating solar collectors to raise the temperature of a working fluid operating a heat engine [2–5]. The impetus for tapping the abundant and nondepleting, albeit intermittent and dilute, energy of the sun stems from the possibilities solar power plants offer to conserve fossil fuels, to impact minimally the environment, and to compete economically in the existing mix of power generating plants.

This paper is an attempt to develop some of the basic physical and theoretical performance characteristics underlying solar-thermal power systems. It is confined, however, to the study of a generic concept of particular interest known today as the central receiver system [3–5]. This system consists of a large field of heliostats (mirrors) that collects the solar radiation, concentrates it on a receiver (located at the top of a central tower) which, acting as a boiler, raises a fluid to high temperatures and pressures compatible with modern power generating plants. The analysis postulates an ideal model for the heliostat arrays which assumes that the mirrors are perfectly flat with unity reflectivity, perfectly steered to redirect sunlight to the central receiver, and may be placed in any desired field configuration around the central tower. A continuum field approach is adopted to describe the ideal heliostat arrays as a function of location and time of the day. Two fundamental considerations govern the space-time characteristics of the mirror field: (*a*) the steering relations needed to satisfy the constraint of the reflection law of light rays, that is the equality of incidence and reflection angles; (*b*) the presence of neighboring mirrors which creates the possibility of blocking the incident and/or reflected solar radiation. Steering and shadow analyses are therefore performed to determine the local properties of the mirror field. The integrated properties of the whole ensemble of heliostats, i.e., the concentrator, are then derived in closed analytical form for a circular field with the tower at the center. The principal results are presented as time profiles for mirror steering angles, for effective concentration areas (or, equivalently reflected solar flux), and for concentration ratios (which depend upon receiver geometry). The ideal characteristics of circular concentrators establish theoretical upper limits of performance against which actual or realistic systems can be evaluated with the introduction of suitable derating factors to account for such effects as steering errors, mirror size and reflectivity, area coverage and geometry, and solar insolation.

[1] Numbers in brackets designate References at end of paper.

Contributed by the Solar Energy Division and presented at the Winter Annual Meeting, Houston, Texas, November 30–December 5, 1975 of THE AMERICAN SOCIETY OF MECHANICAL ENGINEERS. Manuscript received at ASME Headquarters July 14, 1975. Paper No. 75-WA/Sol-1.

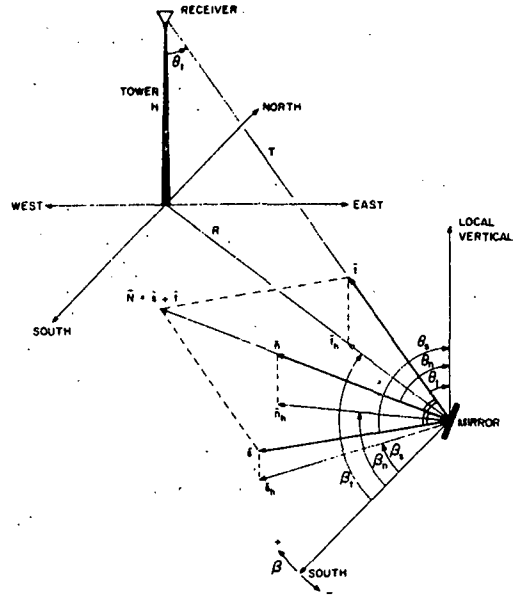

Fig. 1 Geometrical configuration of unit vectors associated with sun, tower, and mirror

Mirror Steering Analysis

Fundamental Steering Relations. The geometrical configuration of a steered planar mirror at a given instant of time and a given location with respect to the central tower is illustrated in Fig. 1. The fundamental steering relation for the mirror is obtained as a result of satisfying the constraint imposed by Euclid's law equating the angles of incidence and reflection of light rays on a planar mirror.

Let the sun's position be determined at a given instant of time by the unit vector **s** pointing *toward* the sun or, more precisely, the center of its disk. Let the location of a given mirror with respect to the targeted top of the tower be represented by the unit vector **t** (directed positively from mirror to tower). The orientation of the mirror, specified by its unit normal (outward) vector **n**, is then given by

$$\mathbf{n} = \frac{\mathbf{s} + \mathbf{t}}{|\mathbf{s} + \mathbf{t}|} \tag{1}$$

in order to satisfy Euclid's law, namely that

$$\mathbf{n} \cdot \mathbf{s} = \mathbf{n} \cdot \mathbf{t} \tag{2}$$

These relations can be written conveniently in terms of the resultant vector $\mathbf{N} = \mathbf{s} + \mathbf{t}$ as

$$\mathbf{n} = \mathbf{N}/N \tag{3}$$

and

$$\mathbf{n} \cdot \mathbf{s} = \mathbf{n} \cdot \mathbf{t} = N/2 \tag{4}$$

If the vectors **n** and **s** are specified, then the tower vector **t** is derived from

$$\mathbf{t} = 2(\mathbf{n} \cdot \mathbf{s})\mathbf{n} - \mathbf{s} \tag{5}$$

Equation (1) constitutes the basic steering relation for a mirror defining its orientation as a function of time (because of the sun's time-varying position **s**) and space (because of the specific location of the mirror with respect to the tower). Equation (2) giving the cosine of the incidence angle is an important parameter of mirror behavior which will be referred to as the incidence factor k_i.

The apparent diurnal motion of the sun relative to a given spot on the earth can be obtained from well-known trigonometric calculations in terms of three specifying parameters—the area location, the day of the year, and the time of the day—which can be defined by the following three angles:

λ = latitude (positive in Northern hemisphere)

δ = declination (positive in the summer for Northern hemisphere)

τ = time angle (positive in the afternoon, measured from local apparent noon)

The sun position vector **s** can be described by two angle components: a zenith angle θ_s measured from local vertical, and a horizontal azimuth angle β_s measured from true South and counted positive in the westerly direction. The zenith angle at any time of the day is given by

$$\cos\theta_s = \sin\lambda \sin\delta + \cos\lambda \cos\delta \cos\tau \tag{6}$$

and the azimuth angle by either

$$\cot\beta_s = \frac{\sin\lambda \cos\tau - \cos\lambda \tan\delta}{\sin\tau} \tag{7}$$

Nomenclature

A_i = actual concentrator area
A_c = receiver area
A_r = effective concentrator area
a_r = per-unit effective concentrator area = $A_r/\pi H^2$
C = concentration ratio = A_r/A_c
D = per-unit distance between two parallel mirrors (referred to mirror width)
E = offset tower distance angle from center of circular concentrator field
H = tower height
i = unit local vector pointing EAST
j = unit local vector pointing NORTH
k = unit vector pointing to local zenith (vertical)
n = unit mirror vector (outward normal)
s = unit sun vector (toward sun)
t = unit tower vector (toward receiver)
N = resultant vector **s** + **t**
N = magnitude of **N**
k_d = derating factor
k_i = incidence factor $\mathbf{n}\cdot\mathbf{s} = N/2$
k_g = ground utilization factor = $1/D_p$
k_m = mirror area utilization factor
k_0 = overall area utilization factor = $k_g k_m$
k_s = shading (sun) factor = $\cos\theta_s$
k_t = screening (tower) factor = $\cos\theta_t$
q = parameter = $\cos\theta_s/\cos\theta_t$
L = per-unit length of mirror
W = width of mirror (unity)
R = distance of mirror to tower base
T = distance of mirror to receiver
P_i = solar power at receiver
S = solar constant
X = top exposure of mirror
Y = side exposure of mirror
x_m = shadow length (perpendicular to mirror horizontal edge)
y_m = shadow skew (parallel to mirror edge)
β_n = azimuth orientation of mirror
β_s = azimuth orientation of sun
β_t = azimuth orientation of mirror location with respect to tower
β_d = azimuth orientation of separation distance between two parallel mirrors
θ_n = mirror tilt angle (from horizontal)
θ_s = sun zenith angle
θ_t = mirror-tower distance angle
η = concentrator efficiency = A_r/A_i
ρ = receiver dimension
δ = declination
λ = latitude
τ = time angle
ω_s = sun apparent velocity
σ = sun disk angle

Subscripts

s = sun
t = tower
n = mirror normal
M = maximum (rim)
m = minimum
p = mirror profile view
f = mirror front view
h = projection of vector on horizontal plane

or

$$\sin\beta_s = \sin\tau\frac{\cos\delta}{\sin\theta_s} \tag{8}$$

It is convenient to indicate the sun's hourly position by combining the pair of angles (θ_s, β_s) in quasi-polar plots as illustrated in Fig. 2. The plots are symmetrical with respect to the North-South axis. Fig. 2 shows sun paths corresponding to the summer and winter solstices, and the equinoxes; also shown are equivalent polar plots in the $\tan\theta_s$, β_s plane. The sun's apparent velocity $\omega_s = d\tau/dt$ is 15 deg per hr or 7.2722×10^{-5} radian per s.

As indicated in Fig. 1, the location of a given mirror is specified by the unit vector **t** pointing from the mirror to the top of the tower (assumed to be a point at a height H from horizontal ground). Again, it is convenient to describe this unit vector by two angle components: a zenith angle θ_t corresponding to a radial distance $R = H\tan\theta_t$ relative to the base of the tower, and a horizontal azimuth angle β_t measured with respect to South, positively westward.

Finally, the mirror orientation, defined by the outward normal unit vector **n**, is also described by a zenith angle θ_n (also equal to the tilt profile angle with respect to the horizontal plane) and a horizontal azimuth angle β_n from South.

The three vectors **s**, **t**, and **n** subject to the steering constraint are shown in Fig. 1 with their associated pairs of angular orientations. The components of these three unit vectors can be expressed in a local cartesian coordinate system defined by the triad of unit vectors **i**, **j**, and **k** pointing toward East, North, and the local vertical, respectively. Specifically, these components are

$$\left.\begin{aligned} s_i &= -\sin\theta_s \sin\beta_s \\ s_j &= -\sin\theta_s \cos\beta_s \\ s_k &= \cos\theta_s \end{aligned}\right\} \; Sun\ (a)$$

$$\left.\begin{aligned} t_i &= -\sin\theta_t \sin\beta_t \\ t_j &= -\sin\theta_t \cos\beta_t \\ t_k &= \cos\theta_t \end{aligned}\right\} \; Tower\ (b) \tag{9}$$

$$\left.\begin{aligned} n_i &= -\sin\theta_n \sin\beta_n \\ n_j &= -\sin\theta_n \cos\beta_n \\ n_k &= \cos\theta_n \end{aligned}\right\} \; Mirror\ (c)$$

The magnitude of the resultant vector $\mathbf{N} = \mathbf{s} + \mathbf{t}$ is then

$$N = \sqrt{2}[1 + \cos\theta_s \cos\theta_t + \sin\theta_s \sin\theta_t \cos(\beta_t - \beta_s)]^{1/2} \tag{10}$$

The orientation of the mirror can be obtained using equation (1) in terms of sun and mirror location angles with the result that the angular mirror tilt is given by

$$\cos\theta_n = \frac{1}{N}(\cos\theta_s + \cos\theta_t) \tag{11}$$

or equivalently,

$$\tan\theta_n = \frac{[\sin^2\theta_s + \sin^2\theta_t + 2\sin\theta_s \sin\theta_t \cos(\beta_t - \beta_s)]^{1/2}}{(\cos\theta_s + \cos\theta_t)} \tag{12}$$

and the mirror azimuthal orientation is

$$\tan\beta_n = \frac{\sin\theta_s \sin\beta_s + \sin\theta_t \sin\beta_t}{\sin\theta_s \cos\beta_s + \sin\theta_t \cos\beta_t} \tag{13}$$

or equivalently

$$\frac{\sin(\beta_n - \beta_t)}{\sin(\beta_n - \beta_s)} = -\frac{\sin\theta_s}{\sin\theta_t} \tag{14}$$

Finally, the incidence factor is given by

$$k_i = \mathbf{n}\cdot\mathbf{s} = N/2 \tag{15}$$

where N is computed from equation (10). Equations (10)–(15) will serve as the starting relations from which the properties of heliostat arrays are to be derived.

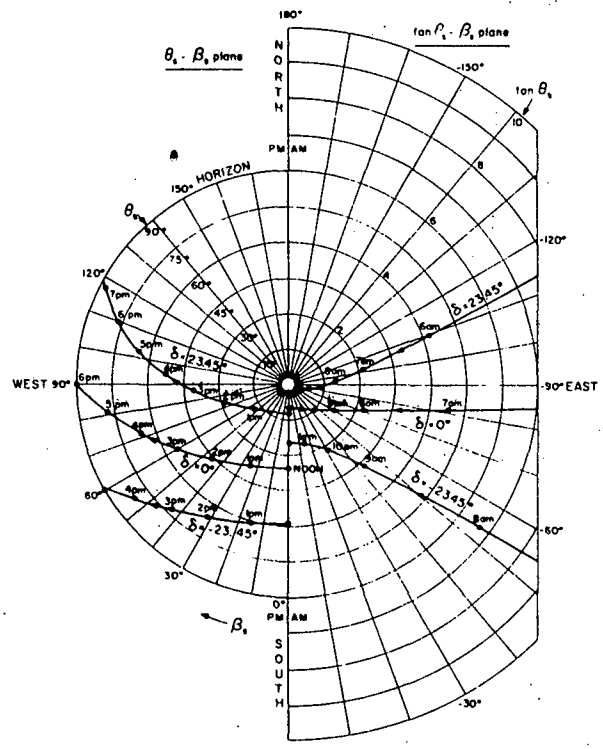

Fig. 2 Polar plots of sun's hourly position (λ = 35 deg N)

In order to develop an understanding of the space-time characteristics of ideal mirrors subject to the above steering equations, it is helpful to consider the heliostat arrays as a continuum field and to view this mirror field first as a function of space at fixed times and then as a function of time for fixed positions.

Space Mapping of Mirror Orientations. Consider a fixed instant of time of day which specifies the sun vector **s** in terms of its zenith angle θ_s and azimuth angle β_s, and examine corresponding field space distributions of mirror orientations. A mapping of these distributions can be conveniently visualized by introducing two sets of loci:

(*a*) loci of constant azimuthal orientations (constant β_n lines);

(*b*) loci of constant tilt (constant θ_n lines).

A typical set of polar plots of these loci in the $\tan\theta_t$, β_t plane is shown in Fig. 3. The plots are symmetrical about a line representing the projection $\mathbf{s}_h$ of the sun vector **s** in the horizontal plane. For convenience of plotting, all azimuth angles are shown as relative angles, namely $\beta_{ts} = \beta_t - \beta_s$ and $\beta_{ns} = \beta_n - \beta_s$, thereby producing a mapping that is a function of a single parameter—the sun zenith angle θ_s. (If absolute azimuth angles are to be exhibited, simply rotate the plots by the specified sun azimuth angle β_s.)

The simplest mapping occurs when the sun is at zenith ($\theta_s = 0$) because then $\beta_n = \beta_t$ and $\theta_n = \theta_t/2$, signifying that constant β_n loci are radial lines intersecting at the origin (where the tower is located), and that the constant tilt lines form concentric circles with centers at the origin. For other values of θ_s, the loci become distorted as shown in Fig. 3 for the case where θ_s = 45 deg. However, they possess interesting properties. For instance, constant β_n lines are made up of portions of hyperbolas intersecting at a singular point located at $\theta_t = \theta_s$ and $\beta_t = \beta_s + 180$ deg (or $\beta_{ts} = 180$ deg). This particular point shall be referred to as the *node* of the mapping. A specific hyperbolic locus defined by a fixed angle $\beta_{ns} = \beta_n - \beta_s$ has its major axes tilted at an angle $-\beta_{ns}$ with respect to the

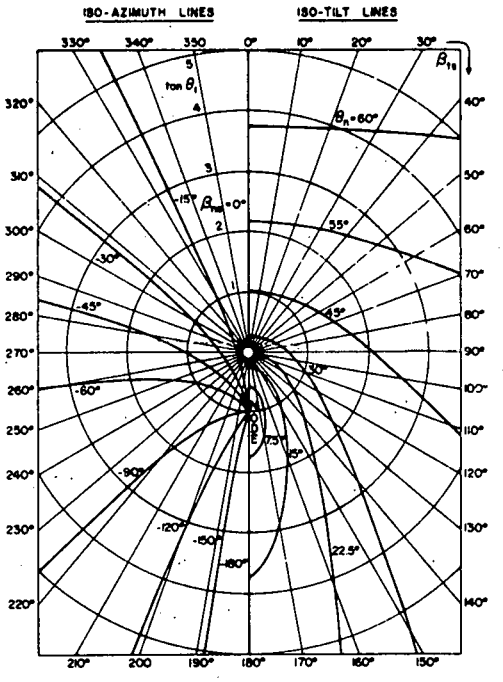

Fig. 3 Mirror field distribution (θ_s = 45 deg)

xy axes. The constant θ_n or isotilt lines are quartic curves which form closed paths only when $\theta_n \leq 45$ deg $- (\theta_s/2)$. At the node, $\theta_n = 0$ deg so that this nodal mirror (in fact, the only one) is horizontal.

Since the node constitutes a singular characteristic point defining the mirror field distribution at a given time, the time-variation of the distribution can be visualized by observing the motion of this node. The path of the node is in fact identical to that of the sun as shown in Fig. 2. The complete distribution can be obtained by superimposing the pertinent mapping (for a given θ_s) on Fig. 2 such that node and sun position coincide.

Time Profiles of Mirror Orientations. The time evolution of mirror orientation for a fixed location specified by θ_t, β_t can be derived from equations (11) and (13) after expressing the solar angles θ_s and β_s in terms of the time angle τ using equations (6) and (8) so that

$$\cos\theta_n = \frac{1}{N}(\cos\theta_t + \sin\lambda \sin\delta + \cos\lambda \cos\delta \cos\tau) \quad (16)$$

in which

$$N = \sqrt{2}[1 + \cos\theta_t(\sin\lambda\sin\delta + \cos\lambda\cos\delta\cos\tau) + \sin\theta_t\sin\beta_t\cos\delta\sin\tau + \sin\theta_t\cos\beta_t(\sin\lambda\cos\delta\cos\tau - \cos\lambda\sin\delta)]^{1/2}$$

and

$$\tan\beta_n = \frac{\sin\theta_t \sin\beta_t + \cos\delta \sin\tau}{\sin\theta_t \cos\beta_t + \sin\lambda \cos\delta \cos\tau - \cos\lambda \sin\delta} \quad (17)$$

As illustrations, Figs. 4 and 5 show time profiles of angular orientations for a ring of seven mirrors located 30 deg apart in the Eastern quadrants at a constant radial distance from the tower expressed by θ_t = 60 deg (because of symmetry, only the eastern half of the field is considered); the chosen day is the equinox (δ = 0 deg) and the latitude is λ = 35 deg N. It is of interest to note that the mirror situated at θ_t = 60 deg, β_t = 120 deg is close to a node of the field distribution occurring about 8:30 a.m. (τ = −52.4 deg) at the location θ_t = 60 deg and β_t = 113.8 deg, and thus exhibits at that time very large time rates of change of angular orientations; this will be a characteristic feature of mirrors in the vicinity of a passing node. In general, time profiles of angular velocities and accelerations can be derived from the orientation time profiles; they provide useful information regarding the controls and torques required for steering action.

Shadow Analysis

The performance of ideal heliostat arrays is to a large measure governed by the effects of shadows cast by neighboring mirrors. Two types of shadows can render a mirror (or portions of its surface) ineffective: (1) a mirror can be shaded from the sun by an adjacent mirror which effectively blocks the incident light rays; (2) a mirror, though in sunlight (i.e., unshaded), can be screened from viewing the top of the tower by a neighboring mirror which effectively blocks the reflected rays. To distinguish between these two shadowing possibilities, the first shall be referred to as *shading* and the second as *screening*. To analyze the shadowing effects of neighboring mirrors, the shadows produced by a single mirror on the horizontal surface are first examined as a function of space and time; such horizontal shadows can be viewed as defining the "footprints" of a mirror. The analysis is confined to rectangular (or square) shaped mirrors having an edge (i.e., two corners) placed on the ground which is assumed to be horizontal.

Mirror Shadow "Footprints." Consider a single rectangular mirror of unit width (W = 1) and length L at a field location specified by θ_t and β_t. At a given instant of time specified by the sun's position angles θ_s and β_s, the mirror orientation angles θ_n and β_n are determined by the steering equations. The shading and screening footprints have the shape of parallelograms as illustrated in the plan view of Fig. 6(a). In order to determine the exact size of these

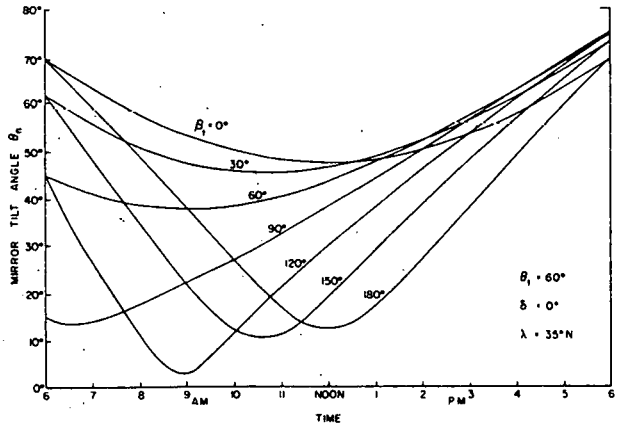

Fig. 4 Time profile of mirror tilt angle

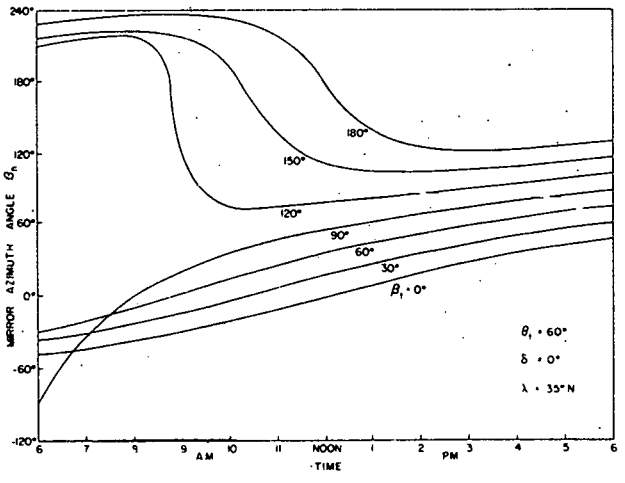

Fig. 5 Time profile of mirror azimuth angle

parallelograms, two special views of the mirror are introduced: a side (or profile) view of the mirror (Fig. 6(*b*)), and a front (or face) view of the mirror (Fig. 6(*c*)). Projecting the sun zenith angle θ_s in the normal plane to the mirror results in a sun profile angle θ_{sp} given by

$$\tan\theta_{sp} = \tan\theta_s \cos(\beta_n - \beta_s) \tag{18}$$

In the front view, the sun angle θ_s appears as the front angle θ_{sf} given by

$$\tan\theta_{sf} = \tan\theta_s \sin(\beta_n - \beta_s) \tag{19}$$

The two corner points of the parallelogram of sun shade represent "piercing points" on the horizontal surface of sun rays passing through the upper corners of the mirror in a direction antiparallel to the sun vector **s**. In the frame of reference of the mirror, a piercing point is at a distance x_{ms} perpendicular to the mirror horizontal edge given from inspection of Fig. 6(*b*) by

$$x_{ms} = \cos\theta_n + \sin\theta_n \tan\theta_{sp} = \cos(\theta_n - \theta_{sp})/\cos\theta_{sp}$$
$$= \cos\theta_n + \sin\theta_n \tan\theta_s \cos(\beta_n - \beta_s) \tag{20}$$

This distance will be referred to as the sun shadow length. The skew length or lateral displacement of the piercing point parallel to the mirror edge is found from Fig. 6(*c*) to be

$$y_{ms} = \sin\theta_n \tan\theta_{sf} = \sin\theta_n \tan\theta_s \sin(\beta_n - \beta_s) \tag{21}$$

It is desirable to express the position of piercing points in a fixed coordinate system in the horizontal plane defined by East-North xy axes. The components x_{0s} and y_{0s} of the piercing points along these new axes can be derived from the components x_{ms} and y_{ms} in the mirror frame by performing a rotation of axes involving the mirror azimuth angle β_n. Thus,

$$\left.\begin{aligned} x_{0s} &= x_{ms}\sin\beta_n - y_{ms}\cos\beta_n \\ y_{0s} &= x_{ms}\cos\beta_n + y_{ms}\sin\beta_n \end{aligned}\right\} \tag{22a}$$

or

$$\left.\begin{aligned} x_{0s} &= \cos\theta_n \sin\beta_n + \sin\theta_n \tan\theta_s \sin\beta_s \\ y_{0s} &= \cos\theta_n \cos\beta_n + \sin\theta_n \tan\theta_s \cos\beta_s \end{aligned}\right\} \tag{22b}$$

Following a similar process, the corner or piercing points of the screening shadow of the tower (interpreted as the shadow produced by a fictitious light source at the top of the tower) can be obtained by simply interchanging the subscripts s and t. Thus, the tower shadow length becomes

$$x_{mt} = \cos\theta_n + \sin\theta_n \tan\theta_t \cos(\beta_n - \beta_t) \tag{23}$$

while the tower shadow skew is

$$y_{mt} = \sin\theta_n \tan\theta_t \sin(\beta_n - \beta_t) \tag{24}$$

However, because the piercing points are established by lines parallel to the **s** and **t** unit vectors which are in turn related by the steering equations, the sun and tower shadows are not independent of one another. Specifically, equation (2) yields

$$\begin{aligned} \mathbf{n}\cdot\mathbf{s} &= \cos\theta_s \cos\theta_n + \sin\theta_s \sin\theta_n \cos(\beta_n - \beta_s) \\ &= \cos\theta_s\, x_{ms} = \mathbf{n}\cdot\mathbf{t} \\ &= \cos\theta_t \cos\theta_n + \sin\theta_t \sin\theta_n \cos(\beta_n - \beta_t) \\ &= \cos\theta_t\, x_{mt} = \frac{N}{2} \end{aligned} \tag{25}$$

so that

$$\frac{x_{mt}}{x_{ms}} = \frac{\cos\theta_s}{\cos\theta_t} = q \tag{26}$$

Furthermore, using equation (14):

$$\frac{y_{mt}}{y_{ms}} = -\frac{\cos\theta_s}{\cos\theta_t} = -q \tag{27}$$

Because of the significance of the quotient $\cos\theta_s/\cos\theta_t$, it is denoted by the parameter q. Equations (26) and (27) which summarize the results of the shadow footprint analysis can be interpreted as follows:

(*a*) The parameter q uniquely characterizes the relative extent of shadows for the sun shade and tower screen: when $q < 1$, (i.e. $\theta_t < \theta_s$), the sun shade is larger than the tower screen; if $q > 1$, (i.e. $\theta_t > \theta_s$), the reverse situation holds.

(*b*) The normal to the horizontal edge of the mirror at its corner *bisects* the sun and tower line shadows produced in the horizontal plane by the tilted side edge of the mirror. Thus, while the horizontal projections of the three basic vectors ($\mathbf{n}_h$, $\mathbf{t}_h$, and $\mathbf{s}_h$) do not satisfy the equality of incidence and reflection angles, this equality property is recovered in the edge shadows.

(*c*) The skewing of the two parallelogram shadows occurs in opposite directions (from the normal to the horizontal mirror edge) which are determined by the sign of the relative angle $\beta_n - \beta_s$ (or $\beta_n - \beta_t$).

(*d*) Shadow computations need be performed for only one type of shadow, the other being derived from it by simple scaling with the parameter q.

Shadows Cast on Adjacent Parallel Mirrors. Consider next a neighboring mirror of identical dimensions ($1 \times L$) and orientation (θ_n, β_n) located at a per-unit distance D (between center) from the original shadowing mirror; the separation distance between mirror centers has an orientation specified by the azimuth angle β_d measured as usual from South. This parallel mirror may be partially shaded from the sun and/or screened from the tower; the "union" of shade and screen areas constitutes the total shadow whose "complement" area is the exposed or available area of mirror. To obtain this exposed area, it is again convenient to examine a side (or profile) view of the mirrors as well as a plan (or top) view.

In a side view, the mirrors appear to be separated by the profile distance

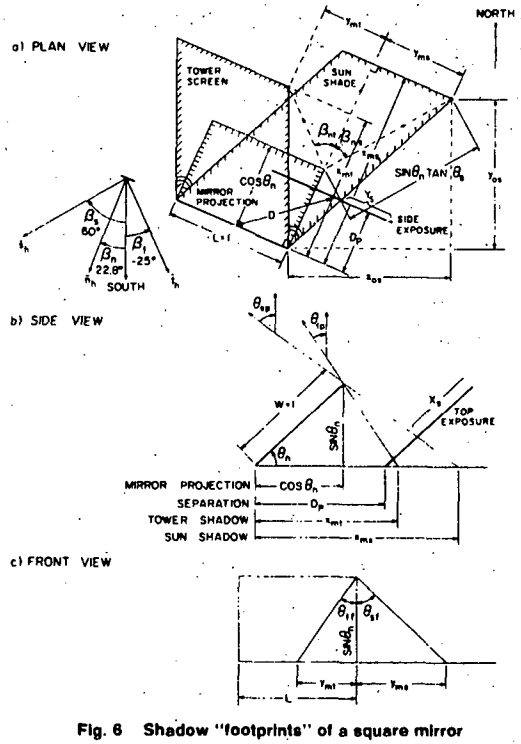

Fig. 6 Shadow "footprints" of a square mirror

$$\left[\begin{aligned} \theta_s &= 60\text{deg} \quad \theta_t = 45\text{deg} \quad \theta_n = 44\text{deg} \\ \beta_s &= 60\text{deg} \quad \beta_t = -25\text{deg} \quad \beta_n = 22.8\text{deg} \end{aligned} \qquad q = 0.7\right]$$

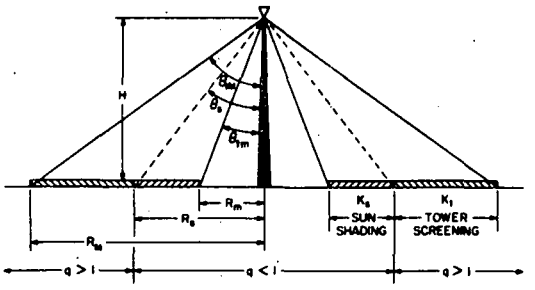

Fig. 7 Distribution of mirror utilization factors in a circular ring concentrator

$$D_p = D\cos(\beta_n - \beta_d)$$

As seen from Fig. 6(*b*), the exposed top distance for the case of sunshading is

$$X_s = \begin{cases} D_p/x_{ms} & \text{for } D_p < x_{ms} \\ 1 & \text{for } D_p \geq x_{ms} \end{cases} \quad (28)$$

while in the case of tower screening it is

$$X_t = \begin{cases} D_p/x_{mt} = X_s/q & \text{for } D_p < qx_{ms} \\ 1 & \text{for } D_p \geq qx_{ms} \end{cases} \quad (29)$$

The side exposure distance (for either sun or tower) can be obtained from the geometry of Fig. 6(*a*) as

$$Y = D\frac{\sin(\beta_d - \beta_r)}{\cos(\beta_n - \beta_r)} \text{ for } |Y| \leq L \text{ and } X < 1 \quad (30)$$

in which $\beta_r = \tan^{-1} x_0/y_0$ is the azimuth angle of the edge shadow line. If either $X \geq 1$ or $|Y| \geq L$, the mirror is fully exposed. For simplicity, the subscripts s or t have been dropped by not referring specifically to either sun or tower shadows.

The final step in the determination of the effective mirror area used for reflecting the solar radiation to the central receiver must account for the incidence factor k_i. The effective area is simply the available or exposed area times k_i.

Utilization Factors. Utilization factors are introduced to provide some localized measures of effectiveness of mirror field coverage. They are defined in the context of top mirror exposures (X type) as illustrated by the profile view of two parallel mirrors in Fig. 6(*b*). Side exposures (Y type) cannot occur in the case of close-packed arrays of mirrors.

Ground Area Utilization Factor k_g. This is simply the inverse of the per-unit profile separation distance D_p. Clearly $D_p \geq 1$ to avoid overlap of mirrors when placed in the horizontal position; $D_p = 1$ means that the horizontal parallel mirrors are just touching.

Mirror Area Utilization Factor k_m. This factor represents the top exposed per-unit length X (or, more precisely, the least of X_s or X_t) which is equal to

$$k_m = \begin{cases} D_p/x_m & (D_p < x_m) \\ 1 & (D_p \geq x_m) \end{cases} \quad (31)$$

Overall Area Utilization Factor k_0. This is simply the product $k_g k_m$, that is

$$k_0 = \begin{cases} 1/x_m & (D_p < x_m) \\ 1/D_p & (D_p \geq x_m) \end{cases} \quad (32)$$

Incidence Factor k_i. As usual, this is equal to the cosine of the incidence angle or

$$k_i = \mathbf{n}\cdot\mathbf{s} = \cos\theta_s\, x_{ms} = \mathbf{n}\cdot\mathbf{t} = \cos\theta_t\, x_{mt} = \frac{N}{2} \quad (33)$$

Effective Shadow Factor. This factor is a measure of the total effectiveness of a mirror in reflecting solar power to a central point; it is equal to the product $k_0 k_i$.

Three situations can be encountered:

(*a*) A mirror which does not experience shading or screening has an effective utilization factor equal to the incidence factor k_i.

(*b*) In the case of sun shading, the maximum utilization factor is given by the shading factor

$$k_s = \frac{1}{x_{ms}}(\mathbf{n}\cdot\mathbf{s}) = \cos\theta_s \quad (34)$$

(*c*) In the case of tower screening, the maximum utilization factor is given by the screening factor

$$k_t = \frac{1}{x_{mt}}(\mathbf{n}\cdot\mathbf{t}) = \cos\theta_t \quad (35)$$

It is important to stress the significance of these simple-looking results. In the presence of either shading or screening, the effective mirror utilization factor is a function of only the cosine of the appropriate zenith angle (θ_s or θ_t) but not of azimuth angles or mirror orientation. (This is in contrast to the case of an isolated mirror for which the utilization factor is the incidence factor k_i, a function of both θ_s and θ_t as well as β_s and β_t.) When $\theta_t < \theta_s$ ($q < 1$), $k_s < k_t$, so that sun shading overlaps the tower screening and, as such, predominates. Conversely, when $\theta_t > \theta_s$ ($q > 1$), $k_t < k_s$, signifying the predominance of tower screening over sun shading.

Concentrator Analysis

Configuration of Concentrator Model. To develop the theoretical characteristics and performance limits of an ideal array of heliostats, the following model of the concentrator is postulated:

(*a*) The mirrors constitute infinitesimal close-packed arrays all arranged at any instant of time so as to satisfy the steering equations while reflecting maximum solar flux without shadowing effects. The mirrors can be viewed as small concentric ribbons surrounding the node and coinciding with the isotilt lines of the field distribution. In order to achieve full exposure with maximum field coverage, the ribbons are separated by the smallest distances compatible with avoiding shading and screening.

(*b*) The concentrator is assumed to have the shape of a circular ring with the tower of height H at the center. The outer radius is $R_M = H\tan\theta_{tM}$, where θ_{tM} is the rim angle of the concentrator; the inner radius is $R_m = H\tan\theta_{tm}$. The geometry of the concentrator is illustrated in Fig. 7.

(*c*) The land is taken to be horizontal with no obstructions anywhere in the field. In particular, the blocking effects of the central tower are ignored.

(*d*) The days are considered to be cloudless.

(*e*) Because of the close-packed configuration of mirrors, no side exposure (Y type) to sun or tower is possible; only top exposure (X type) matters.

Mathematical Model of Concentrator. Since shading and screening effects are differentiated by the value of the parameter q, it is appropriate as shown in Fig. 7 to divide the concentrator field into two regions separated by a circle of radius $R_s = H\cos\theta_s$ which passes through the node (at the azimuth angle β_n): inside this circle ($q < 1$) sun shading dominates, while outside it ($q > 1$) tower screening is the governing feature. If the node occurs inside the circular hole ($\theta_s < \theta_{tm}$), the whole concentrator experiences tower screening effects; on the other hand, with the node outside ($\theta_s > \theta_{tM}$), the concentrator is influenced by sun shading. The total effective concentrator area A_r which intercepts at a given time (i.e., given node location) the maximum solar flux and redirects it to the central receiver without shadowing effects can now be obtained in closed form by integrating a circular differential ring element of area dA subjected to the reduction $k_s = \cos\theta_s$ if located in the shading zone and to the reduction factor $k_t = \cos\theta_t$ in the

screening zone. The ring element area is given by

$$dA = 2\pi RdR = 2\pi H^2 \sin\theta_t \sec^3\theta_t d\theta_t$$

Depending upon the location of the node with respect to the concentrator, three expressions for its total effective area A_r can be obtained by integration:

(a) Node *inside* concentrator ($\theta_s \le \theta_{tm}$):

$$A_r = 2\pi H^2 \int_{\theta_{tm}}^{\theta_{tM}} \sin\theta_t \sec^2\theta_t d\theta_t = 2\pi H^2(\sec\theta_{tM} - \sec\theta_{tm}) \quad (36a)$$

(b) Node *on* concentrator ($\theta_{tm} < \theta_s < \theta_{tM}$):

$$A_r = 2\pi H^2\left[\int_{\theta_{tm}}^{\theta_s} \sin\theta_t \sec^3\theta_t \cos\theta_s d\theta_t + \int_{\theta_s}^{\theta_{tM}} \sin\theta_t \sec^2\theta_t d\theta_t\right]$$

$$= \pi H^2(2\sec\theta_{tM} - \cos\theta_s \sec^2\theta_{tm} - \sec\theta_s) \quad (36b)$$

(c) Node *outside* concentrator ($\theta_s \ge \theta_{tM}$):

$$A_r = 2\pi H^2 \int_{\theta_{tm}}^{\theta_{tM}} \sin\theta_t \sec^3\theta_t \cos\theta_s d\theta_t$$

$$= \pi H^2(\tan^2\theta_{tM} - \tan^2\theta_{tm})\cos\theta_s \quad (36c)$$

Since the concentrator total area $A_i = \pi H^2(\tan^2\theta_{tM} - \tan^2\theta_{tm})$, a concentrator area efficiency defined as $\eta = A_r/A_i$ can be evaluated as

$$\eta = \begin{cases} 2(\sec\theta_{tM} + \sec\theta_{tm})^{-1} & (\theta_s \le \theta_{tm}) \quad (a) \\ \dfrac{2\sec\theta_{tM} - \cos\theta_s\sec^2\theta_{tm} - \sec\theta_s}{\sec^2\theta_{tM} - \sec^2\theta_{tm}} & (\theta_{tm} < \theta_s < \theta_{tM}) \quad (b) \\ \cos\theta_s & (\theta_s \ge \theta_{tM}) \quad (c) \end{cases} \quad (37)$$

For convenience and generality, it is desirable to express the concentrator effective area in a per-unit dimensionless form by using as normalizing base the area πH^2 of a circle of radius equal to the tower height. In this per-unit system, equations (36) become

$$a_r = \begin{cases} 2(\sec\theta_{tM} - \sec\theta_{tm}) & (\theta_s \le \theta_{tm}) \quad (a) \\ 2\sec\theta_{tM} - \cos\theta_s\sec^2\theta_{tm} - \sec\theta_s & (\theta_{tm} < \theta_s < \theta_{tM}) \quad (b) \\ (\tan^2\theta_{tM} - \tan^2\theta_{tm})\cos\theta_s & (\theta_s \ge \theta_{tM}) \quad (c) \end{cases} \quad (38)$$

It is worth emphasizing that, because the shading and screening factors are not functions of azimuth angles, the integrated effects expressed by the concentrator effective per-unit area a_r and the area efficiency η are also independent of these angles and are only functions of radial distances.

Ideal Performance Characteristics of Circular Concentrators. To simplify the presentation of the characteristics, the concentrator is taken here to be a full circle (i.e., with no central hole or $\theta_{tm} = 0$ deg) of rim angle θ_{tM}.

Plots of the ideal concentrator area efficiency η as a function of size for various sun zenith angles are given in Fig. 8. The curve for the vertical sun at $\theta_s = 0$ corresponds to the well-known ideal characteristics of a Fresnel mirror; in this case, only tower screening occurs. With an oblique sun, the efficiency is further reduced due to sun shading effects ($\theta_t < \theta_s$) which are added to the tower screening effects.

Plots of effective per-unit concentrator area a_r versus sun zenith angles θ_s for various field sizes θ_{tM} are given in Fig. 9. It is interesting to note the flat nature of the effective area over a wide range of sun angles; this flatness is due to the combined effects of shading and screening when $\theta_s < \theta_{tM}$. In fact, in that region all curves are essentially displaced from one another, exhibiting identical absolute droops given by

$$a_r|_{\theta_{s=0}} - a_r|_{\theta_s} = \cos\theta_s + \sec\theta_s - 2 \quad (\theta_s \le \theta_{tM})$$

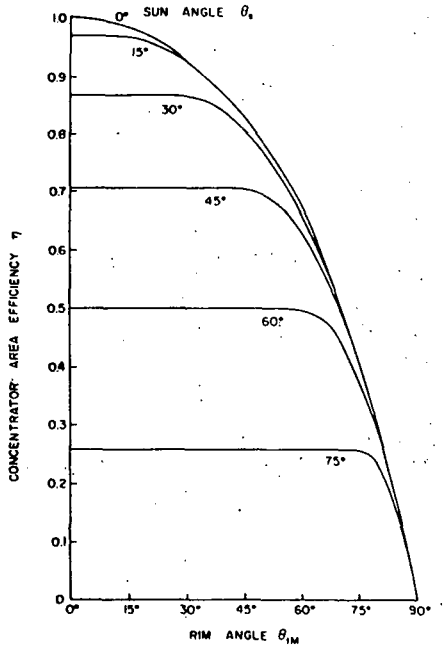

Fig. 8 Concentrator area efficiency characteristics

In the regions where θ_s exceeds θ_{tM} (i.e., when the node is outside the field of the concentrator), the curves drop rapidly as indicated due to the predominating sun shading effects on the whole concentrator.

The abscissa of the characteristic curves of Fig. 9 can also be viewed as representing time since zenith angle θ_s and time are known for any given day. For example, in Fig. 10, effective concentrator area-time profiles are plotted for a given size concentrator ($\theta_{tM} = 70$ deg) for various days of the year. It is significant to note the rather small change in maximum output effective area (occurring at noon) that takes place over a year. Again, it is stressed that these characteristics are independent of azimuth angles. The im-

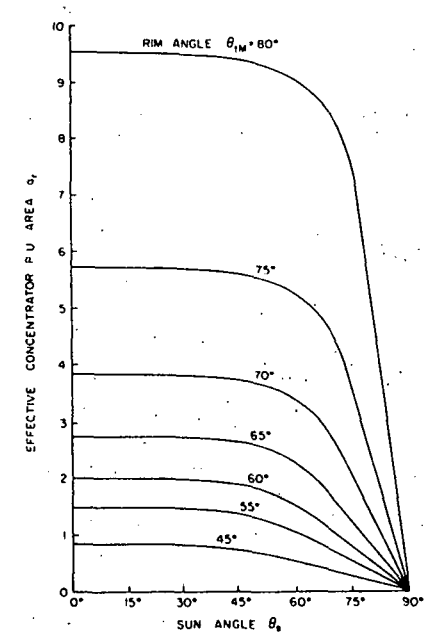

Fig. 9 Effective concentrator area characteristics

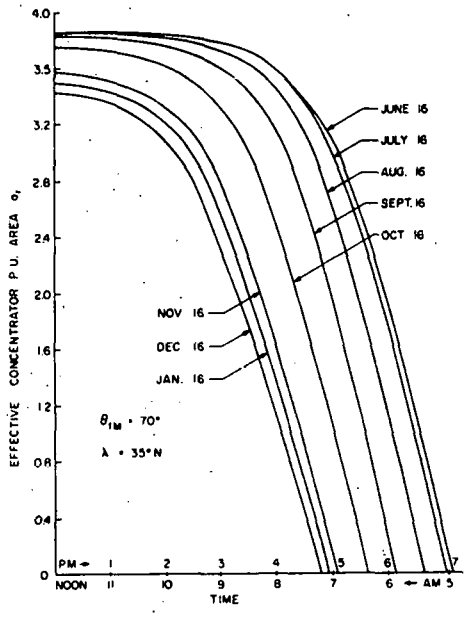

Fig. 10 Daily time profile of effective concentrator area

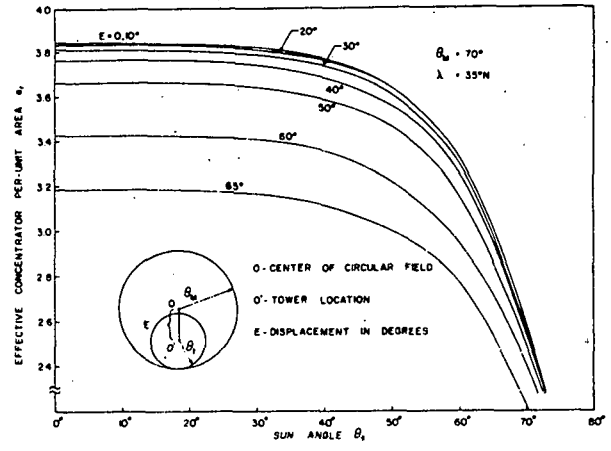

Fig. 11 Characteristics of tower offset

portance of these curves is that they can readily be translated into reflected solar power profile curves, once the pertinent solar constant S is introduced as a multiplier. If, as a base, the solar constant is taken to be equal to 1kW/m^2, then a_r can also be interpreted as an effective output power density referred to the base area πH^2. The total solar power reflected to the receiver is then $a_r \pi H^2$kW (H expressed in meters.) However, to obtain accurate power profiles, complete and detailed insolation data must be used, expressing S as a function of θ_s (or time).

Effect of Tower Offset. So far in the model of the concentrator, it has been assumed that the tower is located at the center of the circular field. It is of interest to examine the effect of placing the tower anywhere in the field. Suppose that the tower is located at an angle E (in degrees) or at a distance H tan E from the center of the circular field (azimuth again plays no role). The analysis can be performed in the same manner as in the case of the central tower except that the integrations must be performed numerically. Fig. 11 gives plots of a_r versus θ_s for various offset angles E (in the case of a circular field of rim angle θ_{tM} = 70 deg). Interestingly enough, the reduction in output effective areas due to the tower offset is small; even when the tower is close to the rim of the field (at 65 deg), the reduction in a_r is about 17 percent.

Ideal Concentration Ratios. A geometric concentration ratio can be defined as the area of the effective concentrator divided by the area of the receiver, assuming that all solar energy reflected by the heliostat array reaches the receiver. Clearly the shape and size of receiver will affect this concentration ratio. Three specific receiver geometries are considered here: a semisphere, a horizontal flat circular disk, and an inverted truncated cone. The minimum size of receiver placed on top of the central tower at a height H is determined by the complete interception of the sun ray cone of angle σ (σ = 9.3 mrad) reflected by the far-field mirrors located at the rim of the concentrator (at θ_{tM}). Table 1 summarizes the results of the analysis and indicates the concentration characteristics of the three receivers for three possible rim angles of interest. A comparison of the ideal concentration ratios for the three types of receivers is also illustrated in Fig. 12 which shows the superiority of the conic receiver for large rim angles of the concentrator.

The product of concentration ratio C by the solar constant S yields a measure of the average solar flux density available at the receiver. Again it is important to recognize that the flux density distribution is not a function of azimuth angles around the receiver surface.

Conceptual Design

As an application of the theory developed and an illustration of the orders of magnitude involved, a conceptual design for a 500 MW (thermal) solar power plant is sketched based on the following simplifying assumptions and specifications:

1 The design point is defined by a power level $P = 500 \times 10^6$W to be achieved at noon (τ = 0 deg) at equinox (δ = 0 deg) for a site located at λ = 35 deg N (i.e., this means that the solar zenith angle θ_s = 35 deg).

2 The ring-shaped circular concentrator has a rim angle θ_{tM} =

Table 1 Concentration characteristics for three receiver geometries

Receiver			Flat Horizontal Disc		Semi-Sphere		Frustum of Cone
Minimum Radius r_0			$\frac{\sigma H}{2}\sec^2\theta_{tM}$		$\frac{\sigma H}{\cos^2\theta_{tM}(1+\cos\theta_{tM})}$		$\frac{\sigma H}{\cos^2\theta_{tM}}$ (length)
Area A_c			$\frac{\pi}{4}\sigma^2 H^2 \sec^4\theta_{tM}$		$\frac{2\pi\sigma^2 H^2}{\cos^2\theta_{tM}(1+\cos^2\theta_{tM})^2}$		$\pi\sigma^2 H^2 \sec^2\theta_{tM}$
Concentration Ratio $C = A_r/A_c$			$\frac{4}{\sigma^2} a_r \cos^4\theta_{tM}$		$\frac{1}{2\sigma^2} a_r \cos^2\theta_{tM}(1+\cos\theta_{tM})^2$		$\frac{1}{\sigma^2} a_r \cos^2\theta_{tM}$
θ_s	θ_{tM}	R_M/H	σ/H	C	σ/H	C	C
0°	65°	2.15	0.026	4000	0.015	5700	5600
0°	70°	2.75	0.04	2400	0.020	4700	5200
0°	75°	3.73	0.07	1200	0.029	3500	4400

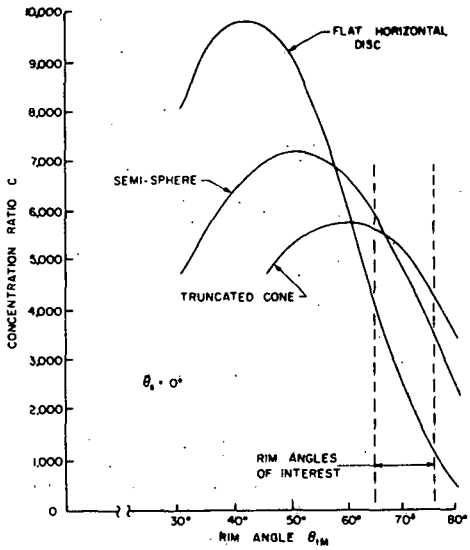

Fig. 12 Ideal concentration ratios for three receiver geometries

70 deg and a central hole with $\theta_{tm} = 30$ deg.

3 The central receiver has the geometry of a truncated cone.

4 The direct component of the insolation (disregarding the diffuse component) is taken to have a value $S = 800 W/m^2$ at noon and normal incidence.

5 A derating factor of $k_d = 0.72$ is assumed to account for loss of mirror area coverage of 0.85 and for a mirror reflectivity of 0.85.

6 A maximum angular spread of the reflected light beam at the outer rim is assumed to be $\sigma_M = 2.5\sigma$ where the multiplying factor is to account for the finite width of mirrors and for steering errors.

Since the expression for the power available at the receiver is given by

$$P = \pi H^2 a_r k_d S$$

(where $a_r = 3.53$ from equation (38*b*)), the tower height is found to be equal to

$$H = \left[\frac{P}{\pi a_r k_d S}\right]^{1/2} = \left[\frac{500 \times 10^6}{\pi \times 3.53 \times 0.72 \times 800}\right]^{1/2} = 280 \text{ m}$$

With the knowledge of the tower height, the overall sizing of the solar power plant can be completed as summarized in Table 2.

Table 2 A 500 MWt solar power plant

POWER LEVEL	$P = 500$ MW
TOWER HEIGHT	$H = 280$ m
CONCENTRATOR LAND DIMENSION	$A_L = 1.78$ km^2 ($R_M = 770$ m; $R_m = 162$ m)
EFFECTIVE CONCENTRATOR AREA	$A_r = 0.87$ km^2
CONCENTRATOR AREA EFFICIENCY	$\eta = 0.49$
TOTAL MIRROR AREA	$A_m = 1.50$ km^2
CONCENTRATION RATIO	$C = 800$
RECEIVER MAIN DIMENSION	20 m
RECEIVER AVERAGE FLUX DENSITY	640 kW/m^2

Conclusions

The principal results of the analysis of the ideal solar concentrator developed in this paper can be summarized as follows:

(*a*) A fundamental theory of solar concentrators for central receiver power plants has been formulated in terms of a continuum field model of ideal heliostat arrays. The analytical results derived from this ideal model are inherently simple and, more importantly, provide the physical basis underlying the central receiver concept of solar power concentration.

(*b*) A steering analysis has yielded the space-time characteristics of heliostat arrays in the form of field mappings exhibiting iso-tilt lines and iso-azimuth lines, and of time profiles of mirror orientations. The notion of a *node* for the mirror field distribution coinciding with the sun's hourly path is extremely useful in describing the properties of heliostat arrays.

(*c*) A shadow analysis has been performed for rectangular mirrors showing the relationship between sun shading and tower screening. Two key parameters defining the utilization factors $\cos\theta_s$ for sun shading and $\cos\theta_t$ for tower screening express the local effectiveness of mirrors in reflecting solar energy.

(*d*) The ideal global characteristics of circular concentrators have been derived from the preceding steering and shadow analyses as closed-form expressions for effective concentrator areas (or, equivalently, reflected solar flux), concentrator efficiencies, and concentration ratios (which are dependent upon the choice of receiver geometries). From these expressions, dimensionless curves have been obtained to characterize the behavior of large-area concentrators and to establish theoretical limits of performance against which actual or realistic systems can be compared. With the ideal model providing a best performance benchmark, the base design of a solar power plant can proceed with the introduction of correction terms or derating factors accounting for such effects as steering errors, mirror size and reflectivity, area coverage and geometry, solar insolation, cloud cover, and wind loads, to cite a few.

(*e*) A major feature of the ideal solar plant characteristics is their unique dependency on just two parameters: the sun zenith angle θ_s (i.e., the time of day) and the size of concentrator. As a corollary, the characteristics do not depend upon azimuthal orientations. In particular, the solar flux density at a given time is uniformly distributed around the receiver. (This would not be the case had shadowing effects been ignored.)

(*f*) Although the present model has emphasized a circular field configuration with the tower at the center, it can readily be adapted to the study of more complex geometrical configurations. The added complication is that integrations must now be performed numerically. A specific study of this type has shown that offsetting the tower away from the center of a circular field does not substantially alter the ideal characteristics of the concentrator. The analysis of square, elliptical, or other shaped fields (including multiply-connected fields containing holes or regions without mirrors) can be performed using the present formulation.

Acknowledgments

This research was supported by the National Science Foundation RANN Program under grant No. GI-41019. The author is especially indebted to Dr. D. E. Anderson of Sheldahl, Inc. for his substantial contributions and to Mr. T. Gurr for his assistance in the computation of the reported results.

References

1 Cherry, W. R., "The Generation of Pollution-Free Electrical Power From Solar Energy," JOURNAL OF ENGINEERING FOR POWER, TRANS. ASME, Series A, Vol. 94, No. 2, Apr. 1972, pp. 78–82.

2 Meinel, A. B., and Meinel, M. P., "Large-Scale Thermal Conversion of Solar Energy (abstract)," *American Geophysical Union, EOS Trans.*, Vol. 52, 1971, p. 814.

3 Baum, V. A., Aparasi, R. R., and Garf, B. A., "High Power Solar Installations," *Applied Solar Energy*, Vol. 1, No. 1, Jan.–Feb. 1957.

4 Francia, G., "Pilot Plants of Solar Steam Generating Stations," *Solar Energy*, Vol. 12, 1968, pp. 51–64.

5 Hildebrandt, A. F., Haas, G. M., Jenkins, W. R., and Colaco, J. P., "Large-Scale Concentration and Conversion of Solar Energy," *American Geophysical Union, EOS Trans.*, Vol. 53, No. 7, July 1972, pp. 684–692.

DISCUSSION

L. L. Vant-Hull[2]

The author's paper develops the usual steering relations and shadow geometries for heliostats in a central receiver array, but then goes on to analyze the properties of the sun and tower shadows in a very clear and useful manner. In particular, the relations between the sun and tower shadows expressed through his parameter "q" are instructive as is the concept of the nodal point.

The concentrator analysis, which results in maximum realizable energy reflected toward the receiver provides a useful algorithm for field scaling relations, etc. It provides a much more realistic upper limit to the energy one can collect from a specified area than the zero-order limits of $S^* \cos\theta_z^*$ ground area, or S^* mirror area, because now the effects of incidence angle and shading are recognized through the efficiency factor η. For a specific time, one now has the tools to lay out a field of mirrors and compute the reflected power using only a hand calculator. However, the algorithm requires that no light ever bypass the mirrors and does not allow for edge shadows. Thus at a time other than the design instant, the performance will suffer unless the heliostat locations are continually changed, which is not very practical, in general. In particular, this analysis provides no guide for locating the heliostats in the field or for optimizing the heliostat field.

A parallel effort in which the same problem has been programmed in detail on a Univac 1108 allows us to generate data similar to that of Fig. 10 for a specified nonuniform heliostat distribution. After evaluating numerous arrays with mean rim angles of about 70 deg at a latitude of 35 deg north, we have obtained two arrays, one designed for best summer (and annual) performance, and a second designed for best performance on winter mornings and afternoons (to minimize variations in peak power to the receiver). In Fig. 13 we show the diurnal behavior of these fields in comparison to Fig. 10. (*WS* and *SS* refer to winter solstice and summer solstice, while *EQ* refers to equinox. The curve marked "Riaz" has been generated by reducing values of a_r obtained from Fig. 10 by 0.85 as suggested by Riaz to account for loss of mirror area coverage.)

The summer perturbed array has a reflector area 49 percent of the ground area and the tower is in the center of the field. At noon, the reflector effectiveness varies from 82 to 62 percent with the solar elevation as a result of the average value of the angle of incidence (0.87–0.83) and of shading and screening (0.94–0.80). Because of the lower solar evaluation in the winter, the winter perturbed array has a reflector area only 34 pecent of the field area, and its noontime effectivity varies from 76 to 66 percent over the year. The tower is located 45 deg south of the field center in this case, to take advantage of the more normal angle of incidence in the north field in the winter.

The general congruence between these results is heartening. The major reason for the lower values for our fields is that considerable sunlight is bypassed at all times so that excessive shading will not occur as the solar azimuth changes. e heliostat cost predominates, so every effort is made to maximize the efficient use of the mirrors. In conclusion, it appears that intelligent use of the author's algorithm will aid greatly in the design and analysis of central receiver heliostat field arrays.

[2]Solar Energy Laboratory, University of Houston, Houston, Texas.

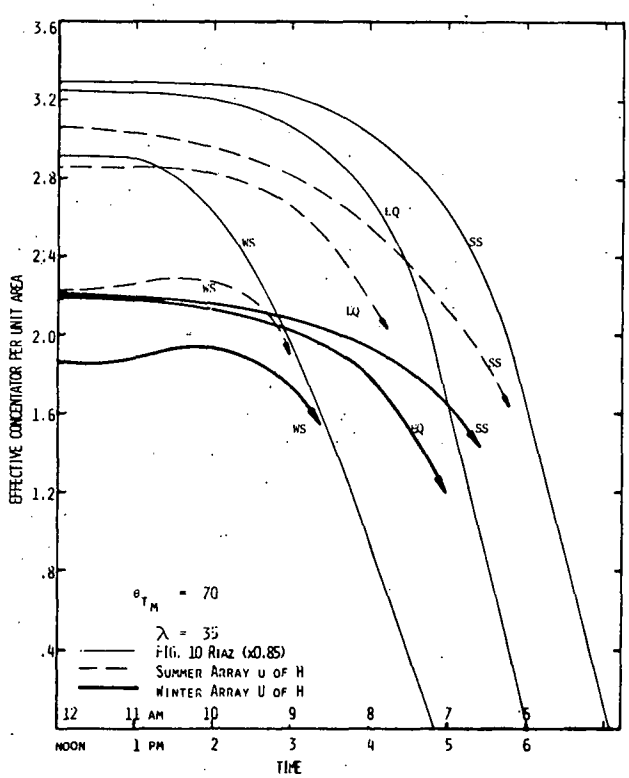

Fig. 13

L. Melamed[3]

Several independent analyses of real-world 40 MW_t Central Receiver Systems have indicated an optimum cost effective unit heliostat size of about 6-m dia. Although the author's derivations based on a continuum field representation are mathematically attractive, they may not be useful for a discrete (quantized-type) reflector field. A tacit acknowledgement of this is suggested in the author's own analysis of a 500 MW_t plant in which 740,000! mirrors (of 1 M^2 area) are stipulated; this is virtually a "continuum" of mirrors. The near-impracticality of this approach arises from the requirements of 740,000 individual tracking systems. It would have provided a stronger argument for the validity of the sample calculation had a mirror area of 25 → 30 M^2 been chosen as the elemental heliostat. Presumably, discarding the continuum field representation for a discrete (quantized) field would require numerical integration since closed-form integration could not be accomplished. It is not clear to me whether the analysis as presented would require any major modification in this case. One question that troubles me is the following: In the presented continuum field analysis, the reflector is postulated to consist of iso-tilt concentric ribbons, consisting of infinitesimal close-packed mirrors. The author's analysis postulates that shading effects are independent of azimuth angles. If a discrete-heliostat concentric collecting ribbon be substituted for the infinitesimal array, will shadowing still be independent of azimuth angle of the individual heliostats within a given ribbon?

Author's Closure

The author wishes to thank the discussers for their pertinent questions and valuable comments which add considerably to the paper.

[3] Program Manager, Solar Thermal Branch, United States Energy Research and Development Administration, Washington, D.C.

It is gratifying to find in Vant-Hull's discussion a computational confirmation of the general theory developed in the paper as well as an estimation of the extent to which the "best" performance characteristics of the idealized concentrator exceed those of an actual heliostat field. Indeed, the stated purpose of the paper was to establish analytically those theoretical limits of performance against which realistic heliostat arrays can be compared and assessed; the comparison and assessment now provided by Vant-Hull for his specific configurations of optimized heliostat arrays in effect answer some of the queries posed by Melamed with regard to real-world heliostats. For the paper did not address the admittedly important problem of designing optimum cost-effective heliostat arrays in terms of actual size, siting, and separation of mirrors in the field; rather, it was mainly concerned with determining the maximum possible reflected solar power or flux available at the central receiver. This maximization of the solar flux reflected from close-packed heliostat arrays "requires that no light ever bypass the mirrors and does not allow for edge shadows." Under these conditions, the reflected solar flux is only a function of radial distance, even though the shadowing of mirrors and the lengths of the shadows depend on both radial distance and azimuth angle; thus, for a radially symmetric mirror field in the form of a ring concentric to the central tower, the total flux impinging on the receiver is constant for all directions.

As is also pointed out, maximum reflected flux can be realized only if the mirror configuration is continually adjusted as a function of time to conform with the ribbon-like distributions discussed in the paper. An interesting scheme by which this adjustment can be simply mechanized is to mount rows of mirrors on a rotating platform. The rotation of the platform about a central axis controls azimuthal orientations; the mirrors can be moved in ganged fashion to control their tilt angles. Although the mirrors are arranged in rectilinear rows and columns (approximating the theoretical ribbon configuration), they need not be coplanar but may exhibit a "toe in" at initial alignment to focus on the receiver. In addition to the ganged motion, second-level adjustments can be incorporated to correct periodically the tilt and rotation of a given mirror in order to reduce excessive steering errors. A detailed description of such turntable heliostat arrangements for a central tower receiver system can be found in a recent United States Patent No. 3,924,604 dated December 9, 1975. The size of turntables can range from 10 to 100 m in diameter. Small turntables of about 10 m in diameter can be equipped with some 70 individual mirrors of 1 m^2 area mounted in a ganged fashion without incurring excessive steering errors; a 500 MWt solar power plant would then require the steering controls of only 22,000 such turntables needed to cover this *field in close-packed hexagonal arrays (not a million-and-a-half* mirrors!). Large turntables of about 60 m to 100 m in diameter can accommodate larger mirrors of, say, 5–20 m^2 area, but now each mirror will require a second level of steering control.

It should be emphasized that if the design objective is to always redirect the maximum sunlight to the central receiver, the row-to-row spacing between mirrors on a specific turntable corresponds to the shortest shadow length $|\min(\max x_m, x_m)|$ encountered in a year. In this respect, the northern half of the field provides for a greater mirror utilization, thereby allowing the use of larger row-to-row spacings in that zone; furthermore, the uncorrected steering errors are smaller in this northern zone, allowing use of larger turntables. The main point of this discussion is to indicate the feasibility of configuring a heliostat field that will effectively collect some 90 percent (the packing factor for circular turntables in closed-packed hexagonal arrays) of the maximum solar energy available over all seasons of the year, thereby almost reaching the performance limits derived in the paper on the basis of a continuum mirror field. Unquestionably, reducing the total mirror area means a reduction in mirror costs, but with a concomitant diminution in solar flux collection of the kind exhibited in Fig. 13. The trade-off considerations required to optimize the sizing of a collector-receiver system for a central tower solar power plant are clearly beyond the scope of the present investigation.

COMPUTER SOFTWARE PACKAGE FOR THE OPTICAL ANALYSIS OF CENTRAL RECEIVERS AND HELIOSTAT FIELDS

Presented by: Dr. E. J. McBride
Systems Engineer
Black & Veatch Consulting Engineers
Kansas City, Missouri 64114

ABSTRACT

Black & Veatch Consulting Engineers has developed, using internal funds, a computer software package for analysis of central receiver solar power plants. This software package was written in APL-PLUS, an interactive language, and is implemented on the Scientific Time Sharing System. This software package has three fundamental capabilities, as follows.

1. To calculate, for a single time point, a flux map on a given receiver geometry.
2. To calculate, for a single time point, the performance of a heliostat field. This performance, which is calculated as a function of position in the field, includes the cosine of the angle of incidence, the losses attributed to shadowing and blocking, and the cleanly redirected power.
3. To calculate, for any given time period, the integrated average performance of a heliostat field. This performance, which is calculated as a function of position in the field, includes average insolation, average insolation-weighted cosine of the angle of incidence, and insolation-and-cosine-weighted shadow and block efficiency.

This package is highly flexibile with regard to heliostat field parameters such as ground cover, field shape, and heliostat array pattern and orientation. Because the software package is written in an interactive language and because the hardware is extremely fast, a user can generate dozens of runs in a single day. Because the APL-PLUS language is interactive, and because it is so condensed, a programmer can make major changes to the codes in a short time.

BLACK & VEATCH CONSULTING ENGINEERS

Computer Software Package for the Optical Analysis of Central Receivers and Heliostat Fields

1.0 INTRODUCTION

Black & Veatch has been involved in study, design, and construction activities in connection with solar power for about four years. During this period, using internal funds, a computer software package with the capability to analyze central receivers and heliostat fields with diverse design characteristics was developed for design, performance, and cost calculations. Those personnel responsible for selecting the analysis techniques to be used examined the published descriptions of similar software packages. They attempted to select and combine analytic techniques so as to yield a software package with high flexibility, ease of use, ease of modification, and low operating cost. This paper describes that software package.

2.0 HARDWARE AND LANGUAGE

The Black & Veatch optical analysis codes are written in APL-PLUS, a language which is the property of the Scientific Time Sharing Corporation. The codes are executed on an Amdahl 470 computer. Using this combination, a single analyst can easily generate results from dozens of computer runs in a single day.

2.1 Language

APL-PLUS utilizes a large number of primitive operators and, as such, can perform with a single statement a calculation which would require a large number of FORTRAN statements. Because the language is condensed, and because the system is interactive, it is not difficult for a programmer to generate and debug, in one day, a program which would require hundreds of FORTRAN cards and the considerable associated checkout time.

2.2 Hardware

The computer on which this package is executed is an Amdahl 470, a computer with a cycle time of 29 nanoseconds. This computer is owned by Scientific Time Sharing Corporation and is located in Bethesda, Maryland. Black & Veatch uses a solely dedicated terminal facility for the execution of these codes. The terminal is a thirty character per second Xerox 1700 Communication terminal with an Omnitec accoustic coupler.

3.0 CAPABILITIES

The software package has the capability to perform three basic types of analyses. They are single time point flux maps, single time point heliostat field performance, and integrated time average heliostat field performance.

3.1 Flux Maps

This package can generate flux maps on the following receiver geometries.

- o Horizontal plane at any height
- o Vertical plane with any orientation
- o Right circular cylinder with vertical axis
- o Right circular cylindrical cavity with a downward-facing circular aperture
- o Right circular cylindrical cavity with a side facing circular or rectangular aperture

The software gives the user the option of viewing the standard error of the flux map. For the cavity geometries, the program input and output are stored in a file for later use by a detailed cavity analysis software package.

3.2 Field Performance

For a heliostat field and a target and for a single time point, as a function of position in the field, the software package can generate the following data

- o Cosine of the angle of incidence
- o Shadow-block efficiency
- o Cleanly redirected power

The software permits multiple runs for a single field-target combination. This permits the user to enter only an additional day and time and eliminates the need for repetition of the possibly complex heliostat field data.

3.3 Average Field Performance

This package can generate for a heliostat field and target and for a given interval of time, as a function of position in the field, the following data

- o Average insolation. This is calculated by finding the time integral of the insolation and dividing by the time interval.
- o Average cosine of the angle of incidence, weighted by insolation. This is calculated by finding the time integral of the product of the cosine of the angle of incidence and the insolation, and then dividing that integral by the time integral of the insolation.
- o Average shadow-block efficiency, weighted by the product of insolation and the cosine of the angle of incidence. This is calculated by finding the time integral of the product of insolation and cosine of the angle of incidence and shadow-block efficiency, and dividing that integral by the time integral of the product of the insolation and the cosine of the angle of incidence.

4.0 FLEXIBILITIES AND CONSTRAINTS

This software package has the following flexibilities and constraints.

4.1 Target Points

There may be any number of target points. Each portion of the heliostat field may aim at any designated target. An option exists to aim each portion of the field at its nearest target.

4.2 Focussing Strategy

There are several options for focussing strategy. Only one focussing strategy may be selected; it must apply to the entire field. These options are as follow.

- o Flat mirrors.

- o Parabolic mirrors with slant range equal to focal length.
- o Mirrors which are perfectly focussed for the time point in question; i.e., there are no off-axis aberrations at this time point.
- o Mirrors which are perfectly focussed for some time and target point; neither of which is required to be the time and target being analyzed. If this option is selected, there must be only one target point for which the mirrors are perfectly focussed; although there may be any number of target points being analyzed.

The first option, flat mirrors, is treated as a degenerate case of the fourth option. This is accomplished by making the perfect focussing target point a very large distance from the heliostat field.

The off-axis aberrations of the second option are treated by finding, in closed form, the size and shape of the image on the target plane; and then selecting locations from within this image using Monte Carlo techniques.

The third option is most easily treated as a degenerate case of the second option. This is accomplished by setting the mirror size equal to zero.

The fourth option is treated by finding, at the perfect focus time, the sagittal and transverse curvatures of the mirror surface. Then, for the time point under analysis, the curvatures in the new sagittal and transverse planes are calculated. This permits the calculation, in closed form, of the image size and shape on the target plane. From which point the calculation proceeds as for the second option.

4.3 Heliostat Size and Shape

This code will analyze heliostats of any size and shape. Only one shape and size may be used for the entire field. Options exist for square, rectangular, or circular mirrors. Heliostats of an arbitrary shape are treated by analyzing an oversized square array of ones and zeros, with ones wherever there is mirror surface, and zeroes wherever there is not.

4.4 Heliostat Field Shape

This code will analyze a heliostat field of any size and shape. Options exist for rectangular and circular fields.

The option for a circular field will analyze a field which can be described by two radii and two azimuths. The rectangular and circular options may be used only when the field has a uniform ground cover and when all portions of the field aim at the nearest target and when the orientation (discussed in 4.7) of the heliostat array pattern (discussed in 4.6) is constant throughout the field.

Heliostat fields with arbitrary shape are treated by analyzing an extra-large heliostat field with a rectangular shape. This extra-large field is broken into a rectangular array of small cells. A ground cover of zero is used to denote areas of this extra-large field in which there are no heliostats.

4.5 Ground Cover

This code will analyze variable ground cover. The ground cover may vary in any manner througnout the field. The variation in ground cover may be expressed as a function of x and y or as a function of radius and azimuth or may be input as a tabular function.

For variable ground cover, the code requires the ground cover at the center of each cell of the extra-large field (discussed in 4.4) and uses that constant ground cover throughout that cell. Where the variation in ground cover can be expressed in closed form, the calculation of those ground covers can be performed internally; otherwise they are entered in tabular form.

4.6 Heliostat Array Pattern

The heliostats may be arrayed, on the ground, in four different ways: square, rectangular, hexagonal close-packed, or rhombic. For a rectangular array, the long side to short side ratio is required. For rhombic, both the long side to short side ratio and angle from the long side to the short side are required. Only one array pattern may be used in a field.

4.7 Heliostat Orientation

The heliostat array pattern may be oriented three ways. The long side of the array pattern may be at a fixed angle from north. The long side of the array pattern may be at a fixed angle from a radial line. The long side of the

array pattern may be oriented as a tabular or closed form function of position in the field.

4.8 Screening

This code will consider shadowing only, blocking only, shadowing and blocking, or neither.

Shadowing and blocking are treated in closed form. The calculation is performed by considering the overlay of the heliostat binary matrix (discussed in 4.3) with that of adjacent heliostats. All heliostats within five array pattern unit cells are considered. An interesting feature of APL-PLUS is that it automatically recognizes that an array is binary and allots only one storage bit per variable, thereby permitting calculations of this nature to be performed with very little core space. Further, the calculations employ Boolean algebra and are very rapid.

4.9 Reflectivity

Reflectivity is a single value for the field, independent of angle of incidence.

4.10 Solar Disk

The solar disk is modelled as a circle, of diameter 9.3 milliradians, with uniform radiation intensity.

Alternative solar models can be incorporated with little effort.

4.11 Insolation

The insolation is calculated, as a function of solar elevation and date, using the ASHRAE model. It is possible to override this model, with any numerical value, following the internal calculation.

4.12 Slope and Track Errors

Slope and track errors are treated identically. Each is assumed to be a random variable, in two independent perpendicular directions, with a Gaussian distribution. The user input for each error is the standard deviation, in milliradians, of the probability distribution. These values are constant across the field.

4.13 Units

This code uses SI units. Distances are in meters, power is in megawatts, and fluxes are in kilowatts per square meter.

5.0 EXAMPLES

An example of each of the three types of analysis is presented and explained. Because of format considerations, these examples are not true copies of computer output, but have been retyped.

5.1 Flux Map

An input summary and an output from a flux map run are shown. This case is described as follows.

- The heliostat field is a 90° sector to the north of the tower. The inside and outside radii are 37 and 115 m. The uniform ground cover is .3125 and the array pattern is rectangular. The short-side to long-side ratio is 0.8 and the long sides are in a north-south direction.
- The heliostats are square, 6.096 m on a side. All heliostats aim at the single aim point and are perfectly focussed at that aim point.
- The analysis is at solar noon on December 21; while the heliostats are perfectly focussed at solar noon on September 21.
- The target is a cylindrical cavity, with a height of 1.524 m and a radius of 1.454 m. The aperture is a north-facing square, .75 m on a side, with the bottom edge even with the base of the cavity. The single aim point is the center of the aperture.
- The flux maps are self-explanatory.

INPUT SUMMARY FOR RUN OF FLUXMAPS, WSID BVFLUX
RUN MADE AT 11:21:39 AM 7/12/77

o THE 1 AIM POINT IS LOCATED AT X=0, Y=8.69, Z=44.5
HELIOSTATS ARE SUPER-SMART.
THE SUPER-SMART AIM POINT COORDINATES ARE: 0.000, 8.69, 44.50.

o HELIOSTAT FIELD IS A STRIP OF INNER RADIUS 37, OUTER RADIUS 115, BETWEEN 315° AND 45°.
IT IS DIVIDED INTO 6 CELLS ALONG A RADIAL COORDINATE, AND INTO 8 CELLS ALONG AN AZIMUTHAL COORDINATE.
THE UNIFORM GROUND COVER RATIO IS 0.3125.
HELIOSTATS AIM AT NEAREST AIM POINTS.

o HELIOSTATS ARE 10 FACET BY 10 FACET ARRAYS
THE HELIOSTAT FACE ARRAY IS 6.096 METERS SQUARE.
THE ACTUAL HELIOSTAT AREA IS 37.161216 SQUARE METERS.
THE MAXIMUM PROJECTED HELIOSTAT DIAMETER IS 8.619744 METERS.

o THE HELIOSTAT ORIENTATION IS UNIFORM, WITH A CELL ANGLE OF 0° CW FROM Y AXIS.

o THE HELIOSTAT ARRAY PATTERN IS RECTANGULAR, WITH A UNIT CELL WIDTH TO LENGTH RATIO OF 0.8.

o THE FIELD IS LOCATED AT LATITUDE 35.5°.

o SCREENING TESTS PERFORMED: BLOCKING AND SHADOWING.

o SLOPE ERROR = 0.65 MILLIRADIANS, TRACK ERROR = 0.65 MILLIRADIANS.

o APPROXIMATELY 10000 RAYS TRACED.

o MIRROR REFLECTIVITY IS 82 PER CENT.

o THE TIME POINT UNDER TEST IS DEC. 21 AT 12:00.

o THE SUPER SMART TIME POINT IS SEP. 21 AT 12:00.

o THE CAVITY IS A RIGHT CIRCULAR CYLINDER PERPENDICULAR TO THE GROUND, OF RADIUS 1.454 METERS, HEIGHT 1.524 METERS CENTERED AT X=0, Y=7.236, Z=44.887.
THE CAVITY WALL MAP HAS 12 AZIMUTHAL AND 5 VERTICAL ZONES.
THE CEILING IS MAPPED INTO 10 BY 10 ZONES.
THE APERTURE IS RECTANGULAR, 0.75 METERS WIDE, HEIGHT 0.75 METERS.
THE APERTURE IS CENTERED AT X=0, Y=8.69, Z=44.5.
ITS OUTWARD NORMAL IS 0° CW FROM NORTH.

OUTPUT SUMMARY FOR FLUXCAVITY**11:25:43 AM 7/12/77
EXACTLY 9978 RAYS TRACED
TOTAL POWER WAS 2.150 MEGAWATTS
1.196 MW ENTERED THE APERTURE
.950 MW MISSED THE APERTURE

MAP OF THE INCIDENT FLUX (KW/SQ METER) ON THE CAVITY WALL IS:

METERS ABOVE BASE OF CAVITY	° CW FROM NORTH											
	15	45	75	105	135	165	195	225	255	285	315	345
1	0	0	60	146	98	59	65	84	160	77	0	0
1	0	0	35	46	8	1	5	13	53	41	0	0
1	0	0	7	1	0	0	0	0	1	10	0	0
0	0	0	0	0	0	0	0	0	0	0	0	0
0	0	0	0	0	0	0	0	0	0	0	0	0

CEILING FLUX MAP (KW/SQ METER) IS:

NORTH

	0	0	0	3	0	0	0	0	0	0	
	0	8	48	69	79	71	82	28	8	0	
	10	51	150	171	145	145	181	138	59	10	
E	64	163	260	219	194	229	209	219	153	66	W
A	143	265	237	265	227	288	313	227	206	161	E
S	153	158	242	270	209	278	257	224	186	178	S
T	122	201	158	183	199	224	204	161	158	82	T
	33	110	150	138	138	191	135	161	104	23	
	0	46	74	74	82	120	99	89	61	0	
	0	0	23	38	43	61	59	15	0	0	

SOUTH

5.2 Field Performance

An input summary and an output for a field performance run are shown. This case is described as follows.

- The field is an irregular shape. It is described by constant ground covers, as shown, within each 10 m by 10 m cell of the field.
- The heliostat array pattern is rhombic. The heliostats are arranged at the corners of a diamond. The diamond is 8 units in an east-west direction and 6 units in a north-south direction. The distance between nearest heliostats is 10 units.
- The heliostats are circular, 2.134 m in diameter. All heliostats aim at the single aim point, 32.5 m above the center of the heliostats. Each heliostat has its focal length equal to its slant range.
- The time point is 11:30 a.m., solar time, on June 21.

- o POWERCELL shows, for each cell, the power (kilowatts) cleanly redirected.
- o COSANGIND shows, for each cell, the cosine of the angle of incidence.
- o SBFRAC shows, for each cell, the fraction of incident power which was cleanly redirected.

INPUT SUMMARY FOR RUN OF FIELDPOWER, WSID BVFIELDPOWE
RUN MADE AT 10:23:12 AM 6/20/77

- o THE 1 AIM POINT IS LOCATED AT X=0, Y=0, Z=32.5.
- o HELIOSTAT FIELD IS A MATRIX OF 9 CELLS ALONG N-S AXIS BY 8 CELLS ALONG E-W AXIS.
  CELLS ARE 10 METERS NS BY 10 METERS EW.
  THE FIELD IS CENTERED AT X=0, Y=5.
  THE GROUND COVER RATIOS FOR THE FIELD ARE:

		0.55	0.51	0.51	0.55		
0.47	0.60	0.61	0.59	0.59	0.61	0.60	0.47
0.51	0.60	0.67	0.67	0.67	0.67	0.60	0.51
0.57	0.66	0.71	0.70	0.70	0.71	0.66	0.57
0.67	0.72	0.76			0.76	0.72	0.67
0.73	0.80	0.80			0.80	0.80	0.73
0.74	0.80	0.80	0.80	0.80	0.80	0.80	0.74
	0.80	0.80	0.80	0.80	0.80	0.80	
			0.80	0.80			

HELIOSTATS AIM AT NEAREST AIM POINT

- HELIOSTATS ARE CIRCULAR, WITH 10 FACETS ACROSS THE DIAMETER.
  THE HELIOSTAT FACE ARRAY IS 2.134 METERS SQUARE.
  THE ACTUAL HELIOSTAT AREA IS 3.577 SQUARE METERS.
  THE MAXIMUM PROJECTED HELIOSTAT DIAMETER IS 2.134 METERS.
- THE HELIOSTAT ORIENTATION IS UNIFORM, WITH A CELL ANGLE OF 0° CW FROM Y AXIS.
- THE HELIOSTAT ARRAY PATTERN IS RHOMBIC. THE LONG-SIDE TO SHORT-SIDE RATIO OF IS 1.2, AND THE ANGLE FROM LONG SIDE TO SHORT SIDE IS 53.1° CW.
- THE FIELD IS LOCATED AT LATITUDE 33°.
- SCREENING TESTS PERFORMED: BLOCKING AND SHADOWING.
- SLOPE ERROR = 0 MILLIRADIANS, TRACK ERROR = 6 MILLIRADIANS.
- APPROXIMATELY 1000 RAYS TRACED.
- MIRROR REFLECTIVITY IS 88 PER CENT.
- THE TIME POINT UNDER TEST IS JUN. 21 AT 11:30.

POWERCELL

0	0	39	36	36	38	0	0
33	43	45	43	43	44	42	32
37	42	50	51	50	49	43	35
40	48	54	54	54	53	48	40
45	53	58	0	0	57	52	47
52	58	61	0	0	58	56	47
50	58	59	60	59	58	54	45
0	54	57	57	57	54	50	0
0	0	0	55	52	0	0	0

COSANGIND

.000	.000	.925	.925	.920	.908	.000	.000
.923	.936	.945	.947	.940	.926	.906	.884
.934	.951	.965	.970	.963	.944	.918	.891
.940	.963	.982	.991	.983	.958	.926	.895
.940	.965	.988	.000	.000	.963	.927	.892
.931	.955	.977	.000	.000	.951	.916	.883
.914	.955	.950	.957	.948	.925	.896	.867
.000	.933	.916	.918	.911	.893	.871	.000
.000	.000	.000	.882	.875	.000	.000	.000

SBFRAC

.000	.000	.975	.975	1	.987	.000	.000
.975	.975	1	1	1	1	1	1
.987	.950	1	1	1	1	1	1
.950	.975	1	1	1	1	1	1
.925	.975	1	.000	.000	1	1	1
.975	.975	1	.000	.000	1	.975	.937
.950	1	1	1	1	1	.962	.900
.000	.962	1	1	1	.975	.925	.000
.000	.000	.000	1	.950	.000	.000	.000

TOTAL POWER CLEANLY REDIRECTED FROM THE FIELD IS 2.744 MEGAWATTS.

5.3 Average Field Performance

An input summary and an output for an average field performance run are shown. This case is described as follows.

- o The sampling times and days were chosen to represent an annual average between 8 a.m. and 4 p.m., solar time.

- The heliostat field is square with a ground cover of 0.7. The heliostat array pattern is as was described in the previous example.
- The heliostats are circular, with a diameter of 2.134 m. Each heliostat is aimed at the single target, 37.5 m above the center of the heliostats. Again, slant range equals focal length.
- SUN shows the average insolation, in kW/m^2.
- SUN x COSINE shows the average product of insolation and the cosine of the angle of incidence.
- SUN x COSINE x SBFRAC shows the average product of insolation and the cosine of the angle of incidence and the shadow-block efficiency.
- COSINE shows SUN x COSINE divided by SUN.
- SBFRAC shows SUN x COSINE x SBFRAC divided by SUN x COSINE.

INPUT SUMMARY FOR RUN OF ANNCELLEFFD, WSID BVACED
RUN MADE AT 11:17:24 AM 6/10/77

- HOURS OF SAMPLING WERE 8:30 AM, 9:30 AM, 10:30 AM, 11:30 AM.
  THE DAYS SAMPLED WERE JUL. 22, SEP.22, NOV.22.
- THE 1 AIM POINT IS LOCATED AT X=0, Y=0, Z=37.5.
- HELIOSTAT FIELD IS A MATRIX OF 12 CELLS ALONG N-S AXIS BY 12 CELLS ALONG E-W AXIS.
  CELLS ARE 10 METERS NS BY 10 METERS EW.
  THE FIELD IS CENTERED AT X=0, Y=0.
  THE UNIFORM GROUND COVER RATIO IS 0.7.
  HELIOSTATS AIM AT NEAREST AIM POINTS.
- HELIOSTATS ARE CIRCULAR, WITH 10 FACETS ACROSS THE DIAMETER.
  THE HELIOSTAT FACE ARRAY IS 2.134 METERS SQUARE.
  THE ACTUAL HELIOSTAT AREA IS 3.577 SQUARE METERS.
  THE MAXIMUM PROJECTED HELIOSTAT DIAMETER IS 2.134 METERS.

- o THE HELIOSTAT ORIENTATION IS UNIFORM, WITH A CELL ANGLE OF 0° CW FROM Y AXIS.
- o THE HELIOSTAT ARRAY PATTERN IS RHOMBIC. THE LONG-SIDE TO SHORT-SIDE RATIO OF A UNIT CELL IS 1.2, AND THE ANGLE FROM LONG-SIDE TO SHORT-SIDE IS 53.1° CW.
- o THE FIELD IS LOCATED AT LATITUDE 33°.
- o SCREENING TESTS PERFORMED: BLOCKING AND SHADOWING.
- o SLOPE ERROR = 0 MILLIRADIANS, TRACK ERROR = 6 MILLIRADIANS.
- o APPROXIMATELY 5000 RAYS TRACED.
- o MIRROR REFLECTIVITY IS 100 PER CENT.

SUN x COSINE

.834	.835	.835	.832	.826	.814	.799	.779	.757	.734	.712	.691
.836	.839	.841	.839	.833	.821	.804	.781	.755	.730	.705	.682
.836	.841	.845	.845	.840	.826	.808	.781	.752	.722	.695	.670
.833	.840	.846	.848	.844	.832	.809	.778	.744	.711	.682	.656
.827	.834	.841	.845	.842	.829	.804	.769	.731	.696	.665	.639
.815	.823.	.829	.833	.830	.816	.788	.750	.711	.675	.645	.620
.800	.805	.809	.810	.804	.788	.759	.722	.684	.650	.622	.600
.781	.783	.783	.779	.770	.751	.723	.688	.654	.624	.599	.579
.759	.757	.753	.746	.732	.712	.685	.655	.625	.599	.577	.559
.736	.732	.724	.713	.697	.676	.651	.625	.599	.576	.557	.541
.714	.707	.697	.684	.667	.646	.623	.600	.578	.558	.540	.526
.698	.684	.672	.658	.641	.622	.601	.530	.560	.542	.527	.514

SUN
.8659

SUN x COSINE x SBFRAC

	.564	.615	.636	.654	.658	.635	.618	.636	6627	.609	.564	.511
	.568	.614	.657	.693	.689	.698	.675	.674	.665	.632	.584	.527
	.579	.628	.670	.718	.722	.730	.722	.710	.685	.641	.589	.530
	.569	.633	.694	.729	.738	.737	.733	.719	.688	.651	.610	.548
	.607	.634	.695	.734	.751	.742	.724	.709	.687	.657	.623	.579
	.642	.681	.718	.744	.744	.748	.731	.703	.673	.649	.622	.587
	.869	.702	.725	.730	.730	.725	.712	.692	.657	.630	.603	.574
	.653	.685	.700	.712	.706	.691	.690	.662	.638	.612	.579	.544
	.626	.646	.661	.674	.674	.664	.650	.636	.612	.585	.554	.511
	.571	.596	.615	.634	.637	.531	.621	.605	.587	.560	.534	.493
	.538	.552	.582	.604	.617	.695	.581	.574	.558	.540	.510	.481
	.496	.526	.554	.574	.574	.555	.543	.533	.532	.515	.491	.458
COSINE	.968	.965	.965	.961	.954	.941	.922	.900	.874	.848	.822	.798
	.965	.969	.971	.969	.962	.949	.928	.902	.873	.943	.814	.788
	.965	.972	.976	.976	.970	.956	.938	.902	.868	.834	.802	.774
	.962	.970	.977	.979	.975	.961	.934	.899	.859	.821	.787	.758
	.955	.963	.971	.976	.973	.958	.928	.888	.844	.803	.768	.738
	.942	.950	.957	.961	.958	.942	.910	.866	.821	.780	.745	.716
	.924	.930	.934	.935	.929	.910	.877	.834	.790	.751	.719	.692
	.902	.904	.904	.900	.889	.867	.834	.795	.756	.721	.692	.668
	.877	.875	.870	.861	.846	.822	.791	.756	.722	.692	.666	.646
	.851	.845	.836	.823	.805	.781	.752	.722	.692	.666	.644	.625
	.825	.816	.805	.789	.770	.746	.720	.698	.667	.644	.624	.608
	.801	.790	.777	.760	.740	.718	.694	.670	.647	.626	.608	.698

SBFRAC

.677	.736	.761	.786	.797	.780	.774	.816	.828	.829	.793	.789
.680	.731	.782	.825	.827	.849	.840	.863	.880	.867	.829	.772
.692	.747	.793	.844	.859	.881	.894	.909	.811	.887	.848	.791
.683	.754	.820	.860	.874	.886	.906	.924	.924	.915	.895	.835
.734	.760	.826	.869	.892	.894	.901	.923	.939	.945	.937	.905
.787	.828	.866	.894	.897	.917	.928	.937	.947	.962	.965	.946
.836	.873	.897	.902	.907	.920	.937	.953	.961	.969	.969	.957
.837	.875	.894	.914	.917	.920	.955	.962	.974	.961	.966	.941
.824	.853	.877	.903	.920	.833	.949	.972	.979	.977	.960	.915
.775	.815	.850	.689	.914	.933	.953	.968	.980	.971	.958	.910
.746	.781	.885	.888	.926	.920	.932	.957	.967	.969	.943	.913
.715	.769	.824	.878	.895	.898	.908	.919	.951	.951	.933	.891

6.0 COSTS

The following are representative computer costs, to Black & Veatch, of the three different types of analysis. These costs include CPU charges and time-sharing connect charges.

- o Flux Map - $ 65
- o Field Performance - $ 10
- o Average Field Performance - $100

These costs will vary with the complexity of the heliostat field data. The costs given here are conservative and represent fairly complex heliostat field data.

Since this software package was developed with Black & Veatch funds and is considered proprietary, it has not been made available to outside users, but has only been used on Black & Veatch projects. Consequently, the total cost including Black & Veatch engineering setup time and recovery of development costs has not been determined.

These costs would be developed for prospective users of the software package.

7.0 CONCLUSIONS

Black & Veatch has developed a computer software package for the optical analysis of central receivers and heliostat fields. This package is highly flexible with regard to heliostat field parameters such as ground cover, field shape, and heliostat array pattern and orientation. Because the software package is written in an interactive language and because the hardware is extremely fast, a user can generate dozens of runs in a single day. Because the APL-PLUS language is interactive, and because it is so condensed, a programmer can make major changes to the codes in a short time.

THIS PAGE

WAS INTENTIONALLY

LEFT BLANK

CIRCUMSOLAR RADIATION DATA FOR CENTRAL RECEIVER SIMULATION

Arlon Hunt, Donald Grether, and Michael Wahlig
Lawrence Berkeley Laboratory
University of California
Berkeley, California 94720

ABSTRACT

The circumsolar measurement project is being carried out to provide data to assess the effects of circumsolar radiation on the operation of solar thermal conversion systems using concentrating collectors, especially central receiver systems. Four circumsolar telescopes have been constructed and are providing detailed intensity vs. angle profiles of the solar and circumsolar region, as well as other solar and climatological data. These measurements have been underway for more than one year at several locations. The current program emphasis is on reducing the data and making it available to groups analyzing the performance of central receiver systems. In most highly concentrating solar systems, the size of the receiver is determined by the ray bundle originating from the most distant heliostat. If the bundle size is calculated by using the solar disc, it is clear that some fraction of the circumsolar radiation will fall outside the receiver aperture. The results of this project provide the detailed type of input data for central receiver simulation codes that are necessary for determining these losses, optimizing the receiver or field size, and determining the distribution of stray flux due to circumsolar radiation.

INTRODUCTION

Circumsolar radiation refers to the light that has its apparent origin in the region of the sky around the sun. The term solar aureole is often used to describe easily observable or characteristic occurrences of circumsolar radiation. The phenomenon can easily be observed by using a finger or nearby object to block the direct sunlight from entering the eye and examining the light that streams around the occulting object.

Circumsolar radiation is caused by the scattering of light by small particles in the earth's atmosphere. The aerosol particles may be composed of ice crystals or water droplets in thin clouds. They may be dust or sea salt particles, smoke or fumes, photochemical pollutants, sulfuric acid droplets, solid particles with a water mantel, flocks formed of a loose aggregates of smaller particles, or any of a large variety of solid, liquid or heterogeneous materials that are small enough to be air borne. The amount and character of circumsolar radiation vary widely with geographic location, climate, season, time of day and observing wavelength. Some of the more striking cases can be observed in the presence of high, thin cirrus clouds.

Under some circumstances these aerosols can cause a significant fraction of the solar flux to be deviated to angles of several degrees or more. Solar energy conversion techniques using high concentration ratios, such as the central receiver concept, only collect light from the solar disc and a small portion of the circumsolar region. Pyrheliometers, the instruments normally used to estimate the direct solar radiation, typically have a field of view of 5-6°. The pyrheliometer measurement includes a large portion of the circumsolar radiation and thus overestimates the amount of direct sunlight that would be collected by a concentrating system. The detailed angular distribution of the circumsolar radiation is important, as it affects the radiant energy distribution on the surface of the receiver in solar thermal power plants.

In the next section the operation of the telescope is described and sample data are given. The following material includes a discussion of the effect of circumsolar radiation on the losses of a solar power plant, presents 16 standard profiles for use with a simulation program, and describes the reduced data base that will be available to general users.

CIRCUMSOLAR TELESCOPE

The basic instrument was designed and fabricated at LBL and consists of a "scanning telescope" that is mounted on a precision solar tracker. A digital electronics system provides control for the tracking and scanning mechanisms. A photograph of three instruments near completion is shown in Fig. 1. The design has been described in more detail elsewhere.[1] The telescope uses as its basic optical element an off-axis mirror of 7.5 cm-diameter and 1-m focal length. A fused silica window protects the mirror from the environment. The mirror forms an image of the sun and sky around it on a plate to the side of the telescope

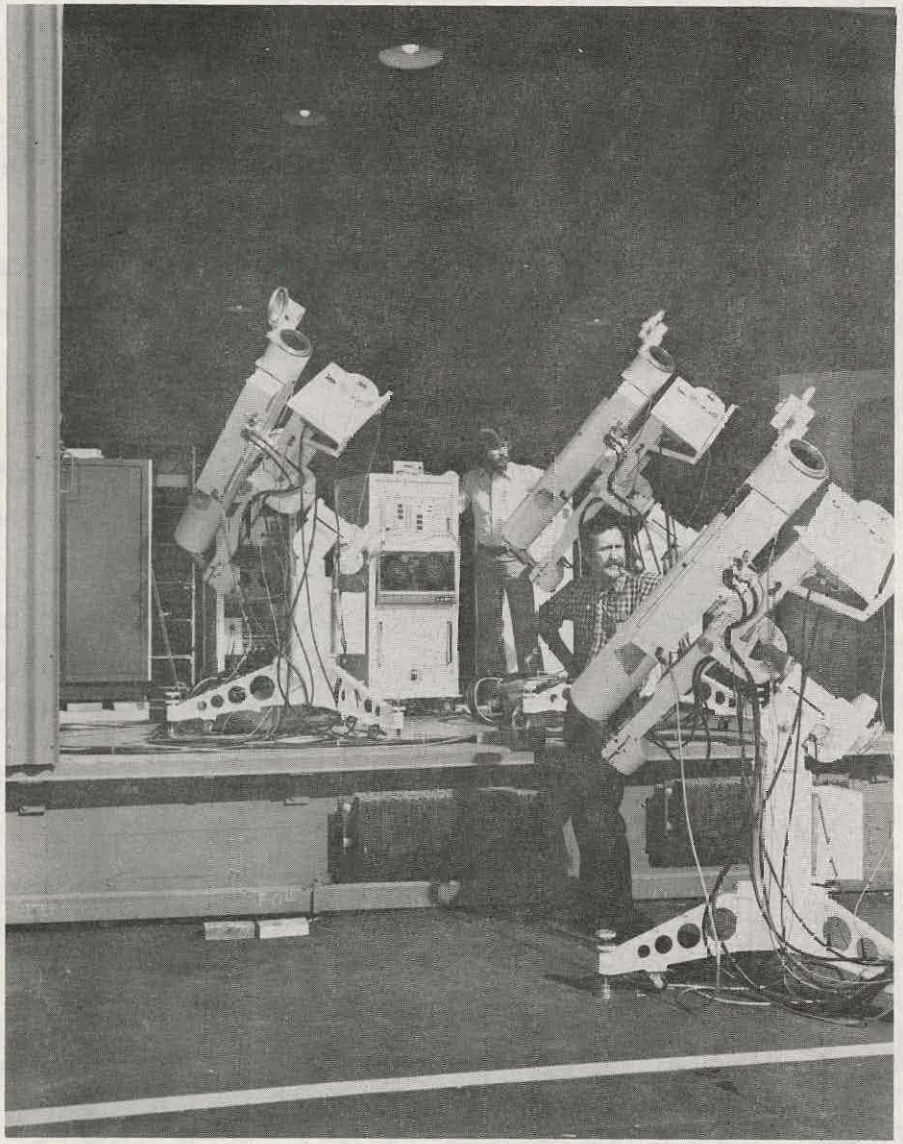

Fig. 1. The circumsolar telescopes nearing completion.

axis. A small hole in this plate, the detector aperture, defines the angular resolution (1/20 of the solar diameter, and the amount of light passing through the aperture into the detector assembly constitutes the fundamental measurement. In the detector assembly the light is mechanically chopped, optically filtered, and focused onto a pyroelectric (thermal) detector. This type of detector was chosen for its uniform wavelength response in the 0.3 to 2.5 μm region and its wide dynamic range.

The telescope scans through a 6^{o} arc with the sun at the center and measures the brightness of the solar and circumsolar radiation as a function of angle. The instrument scans in declination so that at sunrise and sunset it travels nearly parallel to the horizon and at noon it moves in a vertical plane.

Each 6^{o} scan requires one minute of time. The brightness is digitized every 1.5' or arc. Within 0.5^{o} on either side of the sun an aperture of size 1.5' of arc is used, and outside this region the aperture is increased to 5' or arc. A set of measurements consists of one scan at each of 10 "filter" positions". There are eight optical filters, one open (or "clear") position, and one opaque position. The opaque position is used to monitor the detector noise. The absolute de-

termination of the normally incident flux (within 2.5° of the sun center) is provided by an active cavity radiometer.[2] This device is self-calibrating and has an accuracy of 0.5%. This pyrheliometer is provided with a matched set of filters that rotate synchronously with those on the scanning telescope. Thus the telescopes produce an absolute measurement of the normally incident flux along with the detailed solar profile in eight wavelength bands. Two pyranometers are used, one mounted in the conventional horizontal position, and one tracking the sun.

The telescopes are capable of unattended operation for up to a week, although they typically receive a daily inspection during the work week. During the night the solar trackers run backwards and automatically initiate operation at the beginning of each day. The data is recorded on magnetic tape and processed at the laboratory's computer center.

Four of these circumsolar telescopes have been constructed. Three of them have been making measurements automatically fifteen hours each day for approximately one year at the following locations: Albuquerque, New Mexico (5 MW_{th} test site), Ft. Hood, Texas (planned site for demonstration of a solar total energy system), and China Lake, Ca.

Figure 2 shows a computer-plotted graphical display of a clear filter scan made by SCOPE 1 at Berkeley at 12:50 hours on May 20, 1976. The brightness is integrated from the center to the edge of the sun and from there to the end of the scan to give the intensities of the direct and circumsolar radiation respectively. The ratio of circumsolar to solar radiation is then calculated and is given at the top of the graph (C/S =). The normal incidence measurement provided by the pyrheliometer (NI =) is also indicated. This particular scan is for a slightly hazy day, with a circumsolar to solar ratio of 5.5% and a normal incidence value of 811 W/m^2.

Figures 3 to 6 display the time dependence of various parameters of the solar radiation for two separate days. These measurements were taken by SCOPE 2 which is located at Albuquerque, New Mexico. The total losses that would be experienced by a highly concentrating collector due to circumsolar radiation can be calculated by integrating the product of the normal incident radiation and the circumsolar to solar ratio. If the collector system fills the receiver with the solar disc, the total integrated losses for the day in Fig. 3 and 4 would be equal to 1.2%. Figures 5 and 6 illustrate a day that probably had a blue sky slightly

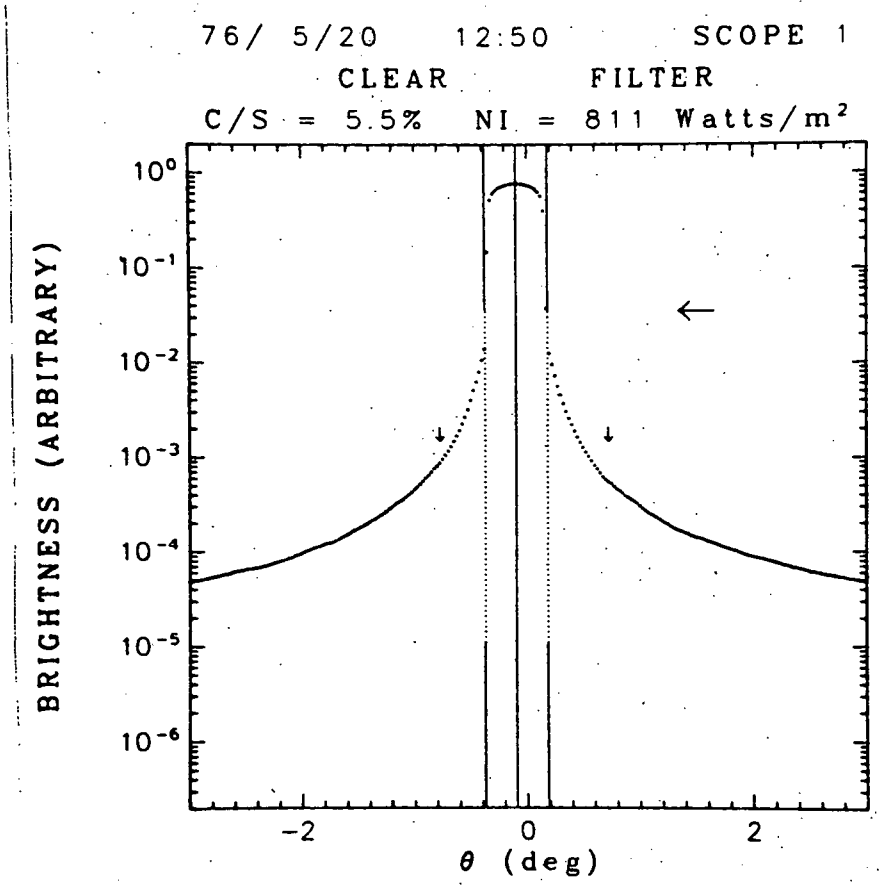

Fig. 2. Computer-plotted graphical display of a clear filter scan made by SCOPE 1 at Berkeley at 1250 hours on May 20, 1976. The dots are the individual scan digitizations. The scan started at +3, as indicated by the large horizontal arrow, crossed the sun near 0^{o}, and ended at -3^{o}. The small vertical arrows indicate the angles where the aperture was switched from 5' of arc to 1.5' of arc, and then back again.

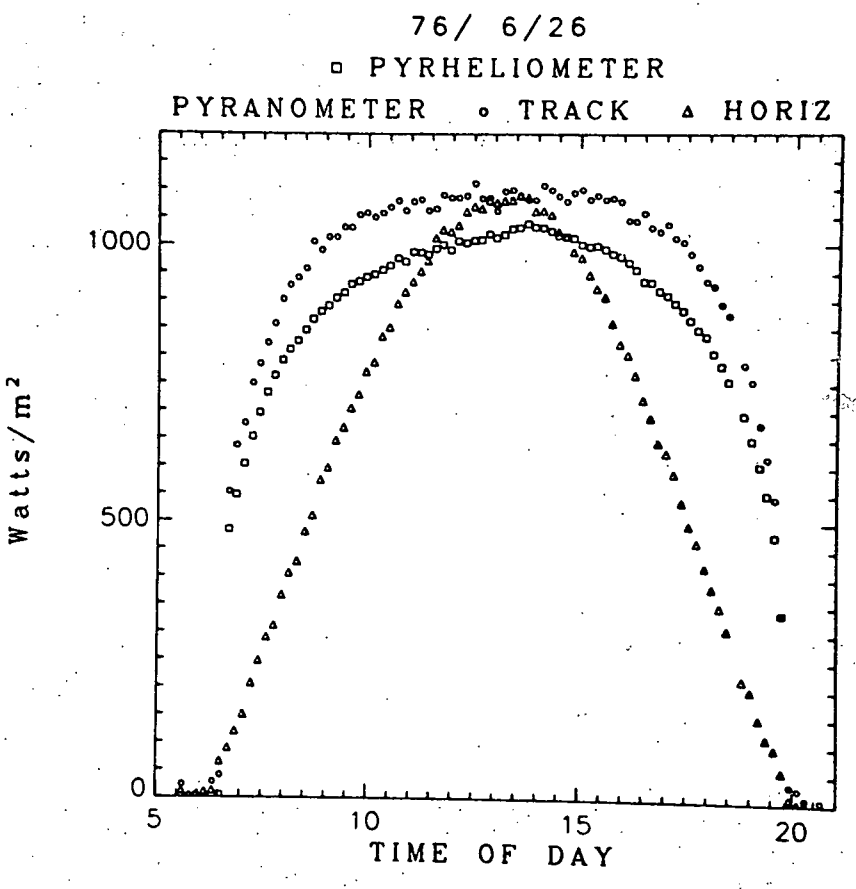

Fig. 3. The time dependence of various parameters of the solar radiation on June 26, 1976 in Albuquerque, New Mexico showing the normal incidence readings from the pyrheliometer (□), and the total radiation readings from the horizontal pyranometer (Δ) and from the sun tracking pyranometer (○).

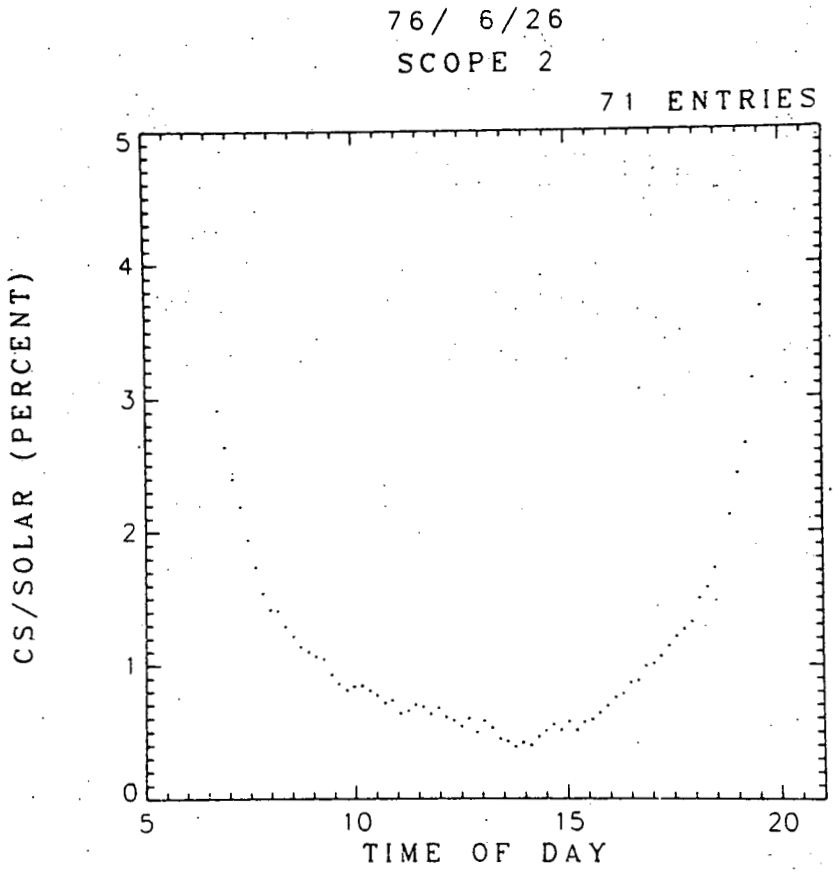

Fig. 4. Illustrating the ratio of circumsolar to solar radiation for the same day as in Fig. 3.

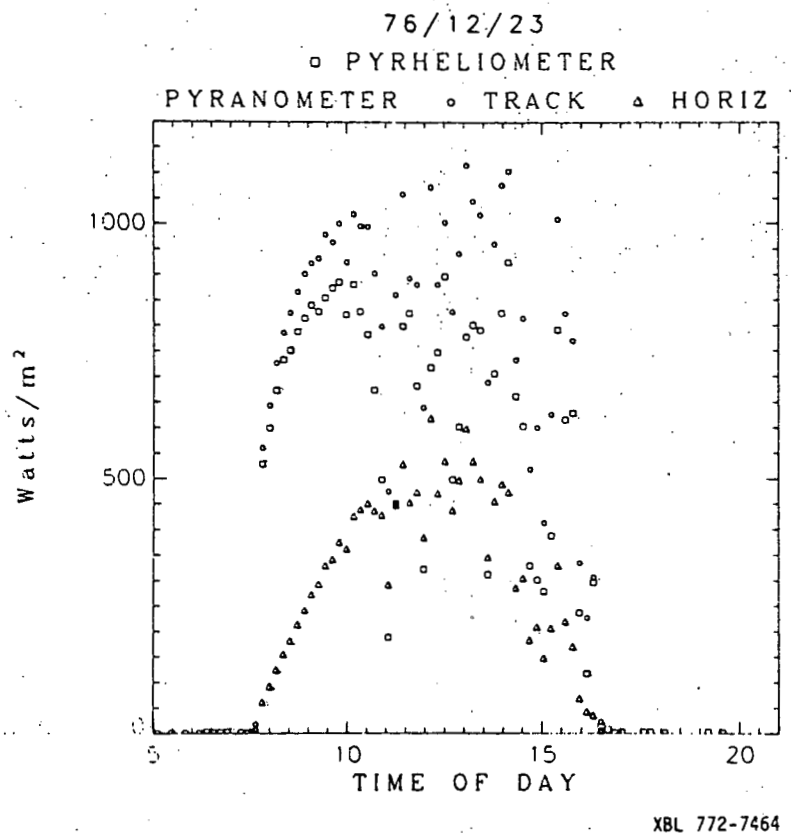

Fig. 5. The time dependence of various parameters of the solar radiation on December 23, 1976 in Albuquerque, New Mexico showing the normal incidence readings from the pyrheliometer (□), and the total radiation readings from the horizontal pyranometer (Δ) and from the sun tracking pyranometer (0).

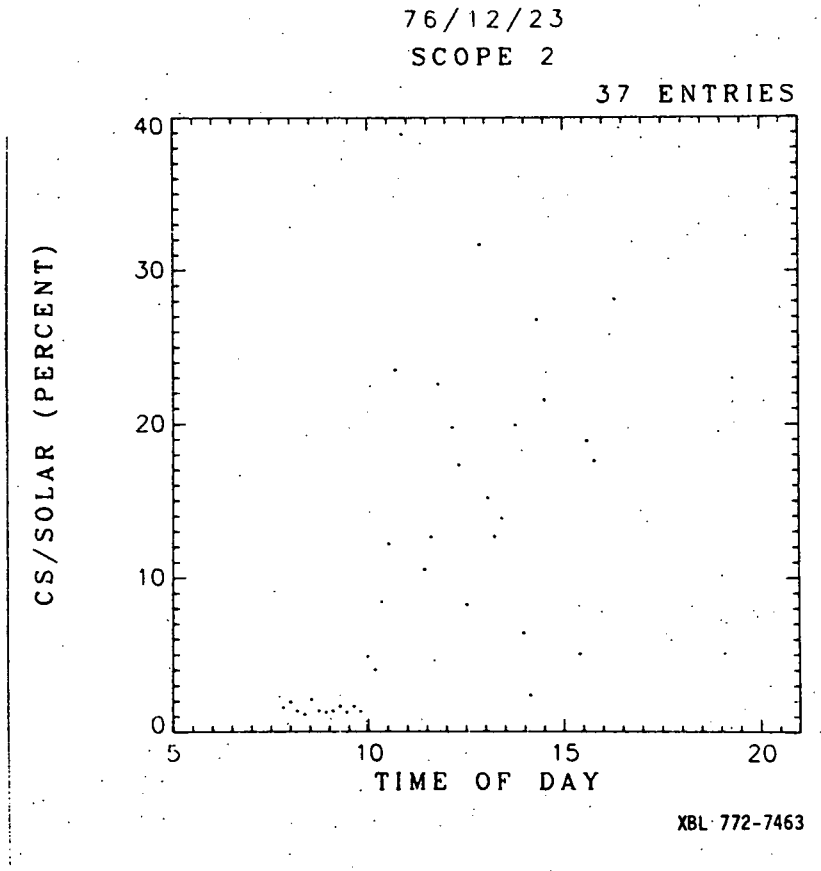

Fig. 6. Illustrating the ratio of circumsolar to solar radiation for the same day as in Fig. 5.

whitened by cirrostratus cover. (Note the difference in scale for the circumsolar graphs in Figs. 4 and 6). The normal incidence readings are moderately high throughout the day. The circumsolar to solar ratio is low early in the morning but from 10 a.m. onward its average is very high (many points are above the top of the graph). The pyrheliometer data indicates sufficient flux for plant operation most of the day but the integrated amount of circumsolar radiation for the whole day is calculated to be over 17%. Thus the errors in utilizing pyrheliometer data for this kind of day would be considerable.

It is anticipated that solar power plants will be operated whenever the solar input exceeds the radiative losses from the receiver. In order to accurately assess the effects of circumsolar radiation for a given location and type of collector, it is necessary to determine the potential losses by an optical simulation procedure combined with a knowledge of circumsolar radiation throughout the year for various viewing apertures and minimum thresholds of normally incident flux. In the next section two sets of data are presented to determine the impact of circumsolar radiation on various solar collection systems.

DETERMINING LOSSES DUE TO CIRCUMSOLAR RADIATION

There are several ways to estimate the effect of circumsolar radiation on a concentrating solar collector. The least ambiguous method is to use measured radial intensity profiles of the sun in conjunction with an optical simulation code. By using the code with and without the circumsolar component, the fractional energy loss from the system due to that particular profile can be determined. If this is done for a variety of profiles with varying ratios of circumsolar to solar radiation, and the frequency of occurrence and corresponding normal incident flux is known, the overall effect can be determined. This procedure is being carried out for several large heliostat fields with the set of profiles shown in Figure 7 and 8. The profiles are plotted in two sets of 8; one set is selected from data taken at Albuquerque, New Mexico and the second set from Ft. Hood, Texas. The corresponding ratios of circumsolar to solar-plus-circumsolar, values of normal incident flux, and times of occurrences are given in table I. The values of circumsolar radiation for these profiles vary over a considerable range. It should be pointed out that these profiles are meant to represent the range of possible profiles; they do not occur with equal frequencies nor do they typically have comparable

Table I
Selected Circumsolar Profiles

C/(C+S)(%)	NI(W/m^2)	STD Time	Date-site*
0.8	953	11:56	76/8/7-A
1.0	714	9:54	76/8/25-FH
2.7	918	11:29	76/11/20-FH
2.9	794	15:10	76/11/22-FH
3.5	948	11:19	76/12/14-A
5.7	747	15:59	76/12/29-FH
8.9	802	9:39	77/1/25-A
10.6	781	14:32	76/12/29-FH
14.6	802	12:57	76/12/14-A
20.4	639	11:06	77/1/25-A
29.4	468	10:14	76/12/14-A
40.0	347	14:11	76/12/29-FH
47.1	291	10:12	77/1/25-A
52.6	298	10:56	76/12/29-FH
58.7	87	13:17	76/12/29-FH
69.2	85	13:06	77/1/25-A

*Site code, A for Albuquerque, New Mexico, FH for Ft. Hood, Texas

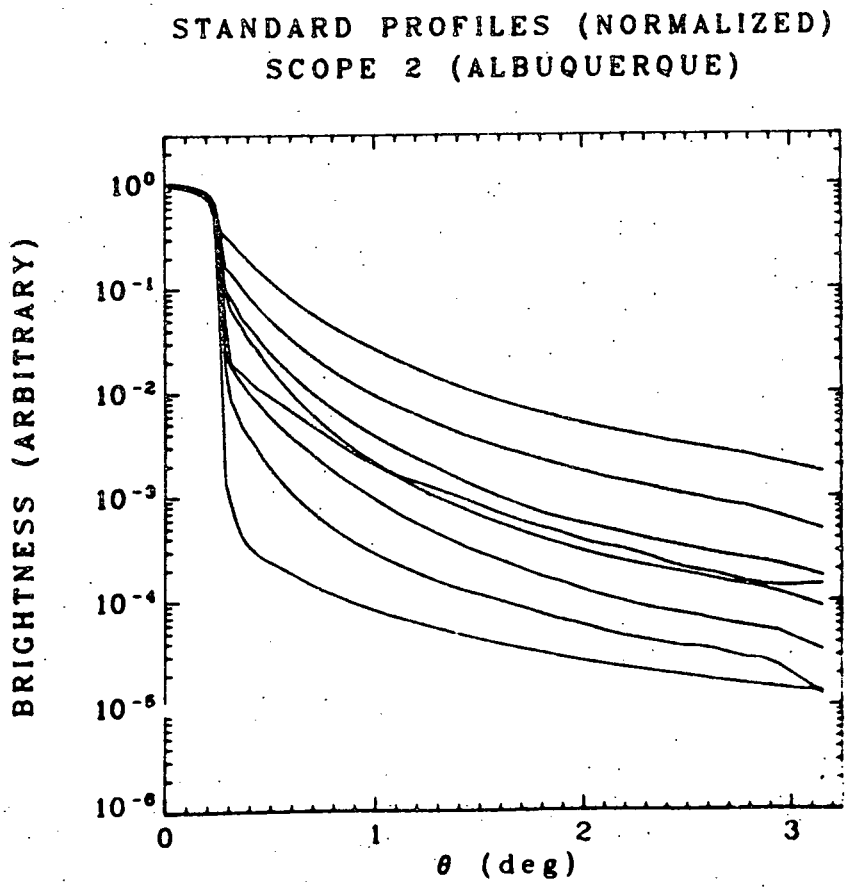

Fig. 7.
Standard solar and circumsolar profiles, selected from Albuquerque, New Mexico.

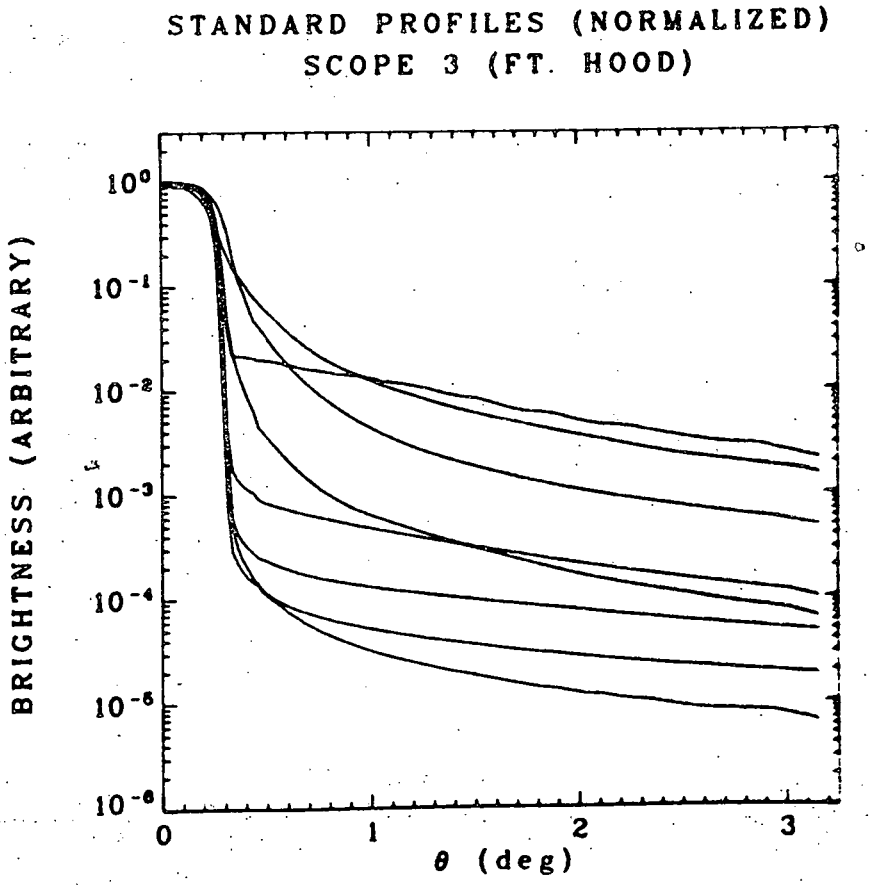

Fig. 8.
Standard solar and circumsolar profiles, selected from Ft. Hood, Texas.

values of normally incident flux.*

The approach discussed above is useful in determining the sensitivity of a solar power plant to the effects of circumsolar radiation. In order to determine the actual monthly losses that would be experienced over the course of a year, measurements must be performed at that site for the corresponding period of time. Once these measurements are in hand, the losses can be determined by sorting all the profiles that occur at that site into one of the 16 standard types. If the fractional energy loss corresponding to each of the 16 profiles known, the measured profile can be weighted with the corresponding value of normal incident flux. These losses then can be tallied and compared to the total plant output for the desired period of time.

The original data base for the telescopes represents a very large amount of data. To put the data into a more manageable form a reduced data base has been generated that contains a subset of the original data. This includes the white light profiles, the pyrheliometer and pyranometer data, the spectral pyrheliometer data, certain indicative information including date, time, solar angle, etc., and some derived data, including true normal incident flux, circumsolar to solar ratio, pyrheliometer errors, etc. This reduced data base is produced in the form of one magnetic tape per year per telescope and will be available to interested users in the future.

*Detailed numerical values for these profiles are available from LBL on computer punch cards.

CONCLUSION

The LBL circumsolar telescopes have completed over one year of nearly continuous measurements at several locations. The resulting set of measurements represents one of the most intensive and extensive characterizations of the effect of the atmosphere on the solar intensity profile. In order to evaluate the effect of circumsolar radiation on solar energy collection systems, the data are being treated in a number of ways. A sensitivity analysis of large central receiver systems, utilizing a selected set of intensity profiles will indicate whether a substantial fraction of the circumsolar radiation is lost from the plant. Since plant performance estimates are based on pyrheliometer measurements that include the circumsolar component it is likely that available normal incidence data should be corrected, or more accurate measurements performed. The amount of the correction will depend on location and season as well as plant design, but the available data from the circumsolar telescopes indicate the

errors are from a few percent to nearly ten percent. Since it is not yet clear how to extrapolate the data to new locations, long term measurements of the circumsolar radiation are still necessary to determine the magnitude and seasonal variations of the effect at locations with substantially different climatic conditions than those already explored.

ACKNOWLEDGEMENTS

The able assistance of Stephen Kanzler in many parts of this project is gratefully acknowledged. We also thank all the people, too many to mention, who have cooperated in setting up and running the telescopes at their respective locations.

REFERENCES

(1) Donald Grether, Jerry Nelson, and Michael Wahlig, Measurement of Circumsolar Radiation, Proceedings of the Society of Photo-optical Instrumentation Engineers, 68, 41, (1975).

(2) R. C. Willson, Active Cavity Radiometer, Appl. Opt. 12, 810 (1973).

THIS PAGE

WAS INTENTIONALLY

LEFT BLANK

A STRATEGY FOR CALCULATIONS OF OPTICAL CONCENTRATION DISTRIBUTIONS FOR FIXED MIRROR SYSTEMS

Dr. John D. Reichert
Director, Crosbyton Solar
Power Project
Texas Tech University
Lubbock, Texas 79409

ABSTRACT

A method of calculation of optical concentration distributions, developed and implemented for the Crosbyton Solar Power Project, is described. The concept examined by this implementation is the Solar Gridiron, sometimes called FMDF (Fixed Mirror-Distributed Focus), differing from the Tower/Heliostat in that the concentrator is a large, fixed spherical segment mirror. The only tracking element in the Solar Gridiron is a receiver/boiler suspended in the mirror bowl. A crucial feature for the thermal/fluid performance of this receiver is the non-uniformity of the optical concentration over the receiver surface. The fluid flow strategy for the boiler must be mated for advantage to the input power profile of the distributed focus.

In order to develop and confirm the fluid flow strategy and the thermal absorption and transfer, it is necessary to determine the input optical power profile accurately as a function of position on the receiver and location of the sun with respect to the fixed axis of the mirror bowl. In the spherical segment bowls, certain sharp structure (concentration peaks and caustics) is present and it is of interest to determine this behavior accurately for purposes of thermal stress analysis as well as for the heat transfer analysis.

INTRODUCTION

It is a pleasure to be invited to this workshop as a visitor with the background of another perspective on optical concentration calculations. I am very

impressed by the quality and level of effort on the adaptive optics concepts which are evident at this workshop. The Solar Gridiron concept upon which I have been working lacks the romance of fully adaptive optics, so my discussion will be briefly presented with due apology to the romantically inclined.

The choice between adaptive optics and fixed optics may be illustrated with the old story of Archimedes' optical defense of the harbor of Syracuse against Roman attack. In the story, Archimedes had the defending army polish its shields to a bright mirror finish and then deployed his soldiers in densely-packed fashion around the concave rim of the harbor, shields in hand. The story does not indicate whether shading and blocking features were properly analyzed, but it does describe the duty of each soldier to orient his shield to direct the sun's rays upon the sails of the Roman war galleys. Here the story divides into two versions. In the more romantic version the sun brightly shone and the Roman sails brightly burned. In the competing account, the sun was overcast and the morning gray, so that the defenders reverted to the older (fossil fuel) technology of catapulting balls of flaming pitch onto the Roman decks. The versions converge at the end to conclude with the vision of a saved citizenry happily watching the Roman ships burn.

Archimedes was killed during a later, successful, Roman invasion as he sat upon the beach drawing geometric figures in the sand. There is a legend that he was, at the time, absorbed in the development of an alternate Fixed Shield Strategy which I would now like to describe. In this approach the highly polished shields would be staked into place, lashed to spears planted in the ground. The advantage: fewer soldiers would be required and those available could be deployed on other missions, such as manning the fossil fuel catapult backup system. The disadvantage: a crew of volunteers would have to be appointed to man a decoy or, possibly, a tug galley to lead the Roman fleet into the focal zone. Though this "fixed mirror" scheme might involve some sacrifice, it could amount to considerable savings when it came time to pay the soldiers. The choice between the two alternatives might well come down to the number of soldiers that Syracuse could raise or afford to pay.

Even though Archimedes' later, untested, strategy may have lacked a certain element of romance, those of us who live on the Staked Plains of Texas can take some thrill from the spear stakes in the story. We have had to become accustomed in the past, due to the economic and climatic realities of our territory, to obtaining a large share of our romance vicariously.

The adaptive optics approach featured in this workshop and so well described by the other speakers involves shading and blocking features which have received a great deal of careful attention and analysis. The fixed mirror of the Solar Gridiron concept also undergoes shading, which is relatively easy to analyze, but is not subject to the blocking feature. The emphasis of the analysis, therefore, has been placed upon accurate mapping of the optical concentration in the distributed focus region. I would like to describe one of the formulations that I have used for the problem. The formulation is rather general and may prove to be useful for concentration mapping on fixed receivers mounted on towers.

THE OPTICAL APPROACH

A method of analysis has been developed which allows the optical concentration to be computed at any point $\vec{q}$ in the vicinity of a reflector surface. The point $\vec{q}$ is understood to lie on a surface oriented as indicated by a local unit surface normal $\hat{b}$ and the distant source is taken to be of finite angular extent. Figure 1 gives a sketch of relevant geometry and notation. The solid angle of the sun viewed directly from a point on the earth is Ω_s and infinitesimal patches of area on the receiving, reflector, and solar disc surfaces are

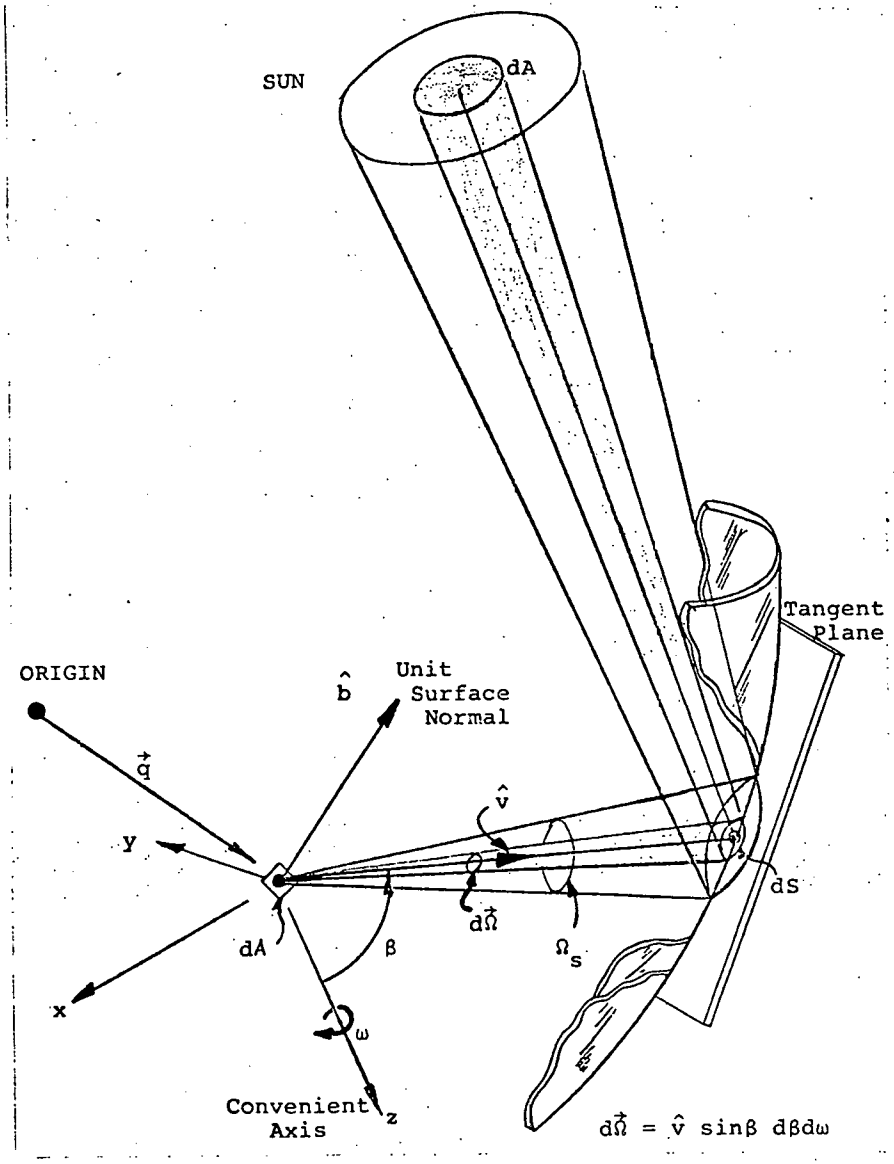

Figure 1. Generalized Mirror Geometry

labeled. Light received at $\vec{q}$ through $d\vec{\Omega}$ is subtended by infinitesimal patches of area on the reflector, and ultimately, on the sun disc.

If, for preliminary considerations, the input from the sun is modeled as being of uniform density in solid angle, then the differential of optical concentration, measured in "suns", received through $d\vec{\Omega}$ is proportional to $d\Omega/\Omega_s$:

$$dC(\vec{q},\hat{b}) = \hat{b}\cdot\frac{d\vec{\Omega}}{\Omega} = (\hat{b}\cdot\hat{v})\,\frac{d\Omega}{\Omega_s} \qquad (1)$$

where the unit vector $\hat{v}$ indicates the direction of the solid angle differential and

$$\Omega_s = 4\pi(\sin\frac{\sigma}{2})^2 \qquad (2)$$

where σ is the angular radius of the sun viewed from the earth, approximately 0.265°. The total concentration at $\vec{q}$ for a surface oriented with direction $\hat{b}$ is obtained by adding up all contributions:

$$C(\vec{q},\hat{b}) = \frac{1}{\Omega_s}\iint_{\Omega_M}\hat{b}\cdot d\vec{\Omega} \quad . \qquad (3)$$

The region of integration, Ω_M, is the solid angle of the sun when viewed in the reflector. For a concentrating reflector the solid angle, Ω_M, subtended by the sun as viewed in the reflector may be hundreds of times larger than the solid angle, Ω_s, of the sun viewed directly. Except for a cosine weight factor, Eq. (3) simply indicates that the concentration is essentially the ratio Ω_M/Ω_s.

The basic formula shown in Eq. (3) is extremely general and can be used as the starting point for computation of concentration distributions for any reflector or reflector array. The complexity of the problem is hidden in the range of integration, Ω_M. For a heliostat array, for example, the shading and blocking, as well as the facet shapes and locations, must be considered in order to determine the region Ω_M. In the Solar Gridiron, the blocking feature is absent, but a multiple reflection feature is added. Light can be used which has bounced from the reflector several times, as indicated in Figure 2.

It should be emphasized that the Solar Gridiron is not a point focus concept, but a distributed focus concept. The multiple bounce radiation is part of what those desiring a point focus would call a "spherical aberration" effect. From the Solar Gridiron, distributed focus, viewpoint a point focus would be an undesirable effect resulting from "parabloidal aberration", the failure of a paraboid to adequately represent a spherical segment. In short, a distributed focus is essential for good heat transfer and, in the Solar Gridiron, "spherical aberration", is the mechanism for achieving the distributed focus.

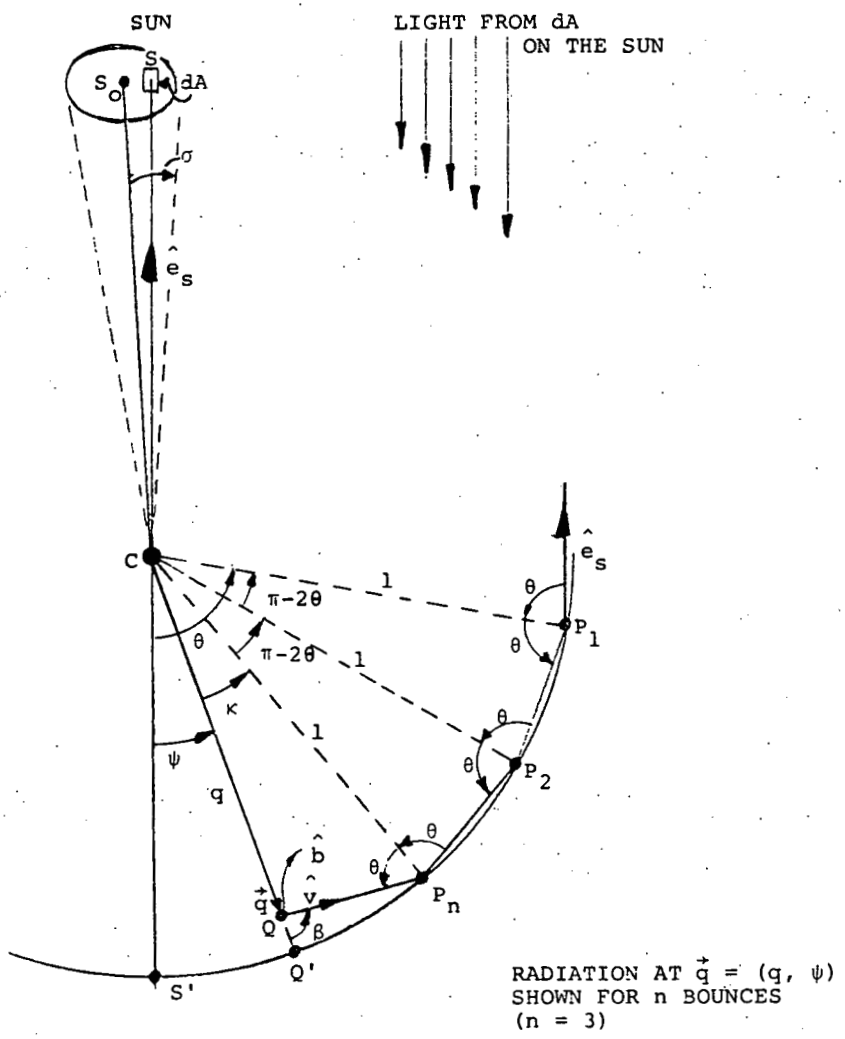

Figure 2. Hemispherical Dish Multiple Reflection Geometry

To deal with multiple reflections, it is simplest to modify the form of Eq. (3) slightly. Light in a differential of solid angle will always consider the reflector to be locally flat; i.e., will reflect repeatedly as if from the local tangent planes. Thus Eq. (3) may be used in the presence of multiple reflections in the mirror by separating and adding the contributions from light that has reflected n times:

$$C(\vec{q},\hat{b}) = \sum_n R^n C_n(\vec{q},\hat{b}) = \frac{1}{\Omega_{Sn}} \sum_n R^n \iint_{\Omega_{Mn}} \hat{b}\cdot d\vec{\Omega}. \qquad (4)$$

The solid angle Ω_{Mn} is the apparent size of the sun as viewed in the mirror with radiation that has reflected n times. A reflection coefficient R has been included in Eq. (4) to account for reflective losses. The factor R must be kept inside the integral if one wished to include angle of incidence dependence.

Similarly, if the wavelength dependence of the reflectivity is of interest, one must add an integral over $W(\lambda)\, d\lambda$ to the form shown in Eq. (4), where $W(\lambda)$ is a spectral density weight. If one wishes to use an effective sun size σ_n, depending upon the number of reflections, to represent mirror imperfections, then Ω_s should be expressed:

$$\Omega_s = 4\pi\left(\sin\frac{\sigma_n}{2}\right)^2 \qquad (5)$$

and included inside the summation shown in Eq. (4). The

"self-evident" derivation of Eq. (1) relied upon modeling the sun as being of uniform density in solid angle. The ability to include limb darkening effects, apparently sacrificed to provide a trivial derivation, can be recovered in a way to be mentioned later.

In order to perform the integration indicated in Eq. (4) the integral can be parameterized using any convenient axis, as indicated in Figure 1:

$$C_n(\vec{q},\hat{b}) = \frac{1}{\Omega_s}\int\int_{\Omega_{Mn}} (\hat{b}\cdot\hat{v})\,\sin\beta d\beta d\tilde{\omega}\ ,\ \hat{b}\cdot\hat{v} > 0 \text{ only} \qquad (6)$$

If a cartesian coordinate system (x,y,z) is selected with origin at $\vec{q}$, then

$$\tilde{v} = \begin{pmatrix} \sin\beta\cos\tilde{\omega} \\ \sin\beta\sin\tilde{\omega} \\ \cos\beta \end{pmatrix} \text{ and } \hat{b} = \begin{pmatrix} b_x \\ b_y \\ b_q \end{pmatrix} \text{ where } b_q \equiv b_z \ . \qquad (7)$$

The restriction to positive values of the dot product in Eq. (6) is the requirement that only light impinging from one side (the "outside" of the receiver or probe) is of interest at the field point.

If the mirror shape is extremely difficult to describe analytically or bears stochastic errors, then one might divide the mirror surface into cells for interrogation by a numerical integration code. On the other hand, for simply describable surfaces such as spherical segments, cylindrical surfaces, parabloids, and so forth, it is desirable to proceed analytically. For this purpose the mirror shape and the desired region of integration may be described in terms of Mirror Structure Relations.

As an example, the spherical segment mirror of the Solar Gridiron will be briefly considered. Although the integrand shown in Eq. (6) is particularly smooth and convenient for integration, it is difficult to describe the solid angle Ω_{Mn} in terms of the variables β and $\tilde{\omega}$. One way to describe Ω_{Mn} is to consider integration over variables other than β and $\tilde{\omega}$.

Consider a mirror which is a segment of a sphere of radius R with center at C as illustrated in Figure 2. [Normalized units are used so that R = 1.] Light from an element of area dA on the sun enters the dish as a plane wave front from direction $\hat{e}_s$. Such light, striking the dish at zenith θ bounces n times and comes to the field point $\vec{q}$ from direction $\hat{v}$. The field point is located by spherical coordinates: q, the distance from C, and ψ, the zenith from the " sun axis", S'C. The "outward normal" $\hat{b}$ associated with an element of area dA at $\vec{q}$ may or may not lie in the plane of the figure.

For convenience, the angle β employed as a parameter in Eq. (6) will be measured as the zenith angle of $\hat{v}$ with respect to the axis QC passing through the field point $\vec{q}$ from C. It is desired to obtain the geometrical connection relating β, θ, and ψ. Using Figure 2, one can

deduce that

$$K = (\theta-\psi) - (n-1)(\pi-2\theta) \quad \text{and} \quad \beta = K + \theta. \tag{8}$$

Eliminating K from these relations,

$$\beta = 2n\theta - \psi - (n-1)\pi. \tag{9}$$

Using the Law of Sines in the triangle CQPn, one obtains

$$q \sin\beta = \sin\theta \tag{10}$$

so that

$$\left(\frac{d\theta}{d\beta}\right)_q = q\,\frac{\cos\beta}{\cos\theta}\,. \tag{11}$$

Using the Mirror Structure Relations (9) and (10) along with Eq. (11), a change of integration variables may be accomplished in Eq. (6):

$$C_n(\vec{q},\hat{b}) = \frac{1}{\Omega_s}\int\!\!\int_{\Omega_{CM}} (\hat{b}\cdot\hat{v})\left|\frac{\cos\theta\,\sin\theta}{q\sin\psi[\cos\theta-2nq\cos\beta]}\right|\sin\psi\,d\psi\,d\omega \tag{12}$$

where $\omega \;\tilde{\omega}-\pi$. Now the differential $\sin\psi\,d\psi\,d\omega$ in Eq. (12) may be interpreted as an element of solid angle $d\Omega_{CM}$, measured from the center C of the sphere. The angle ψ, the field point zenith is measured from the S'CS line which varies inside a cone of angular radius σ as S is swept over the face of the sun. Alternatively, as illustrated in Figure 3, ψ may be interpreted as the zenith of the sun axis S'CS measured from the line Q'C passing through the field point. Noticing now that $\Omega_s^{-1}\sin\,d\psi d\omega$ performs an average over positions on the sun, one can recover limb darkening effects by weighting the average with a brightness function $B(\psi,\omega)$.

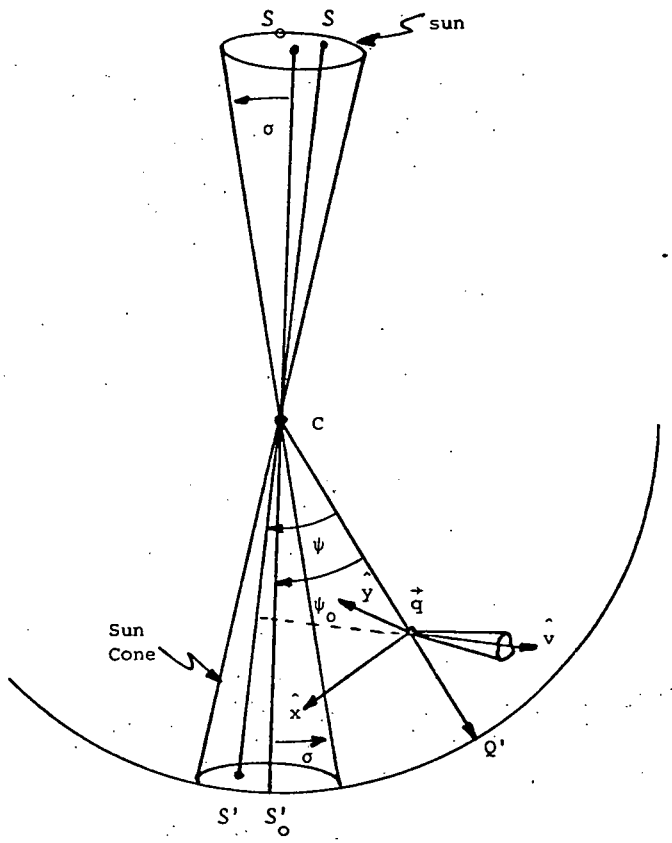

Figure 3. Generalized Receiver Geometry and Sun Cone.

The "principal sun axis" is the line $S_o'CS_o$ passing through the center of the sun disc. The cone generated by S'C, shown in Figure 3, is called the "sun cone". The integral in Eq. (12) can be interpreted as an average over the solid angle of the sun cone of the quantity:

$$C_{nP}(\vec{q},\hat{b}) \equiv (\hat{b}\cdot\hat{v})\left|\frac{\cos\theta \sin\theta}{q\sin\psi[\cos\theta-2nq\cos\beta]}\right| \qquad (13)$$

The quantity shown in Eq. (13) must be the "n bounce concentration produced at the field point q by a point sun at infinity". This interpretation is correct and can be confirmed by direct derivation. This point sun concentration is, itself, a useful approximation because the angular size of the actual sun is so small. It should be noted, however, that the denominator can vanish in the distribution shown in Eq. (13) so that caustic infinities are present in the point sun distribution. Although these singularities are integrable, the properties of this expression make Eq. (12) difficult to handle numerically.

A convenient integration policy is to integrate the form shown in Eq. (6), obtaining the integration limits from the (ψ,ω) range appropriate for Eq. (12). The mirror rim and its shadow and the restriction $\hat{b}\cdot\hat{v} > 0$, are expressed in terms of ψ,ω, and θ and then the structure relations, Eqs. (9) and (10), are used to determine the integration region in $(\beta,\tilde{\omega})$ appropriate for Eq. (6). The integration region is folded and considerable complexity is involved in accomplishing the determination of the proper region of integration with the generality required to handle all cases of interest. Since brevity was promised in the introduction and since the basic strategy of the approach has been exposed, further details (available in Vol. II of the February 1977 Interim Technical Report to ERDA on the Crosbyton Solar Power Project), will be suppressed and I will conclude by showing some results.

EXAMPLES OF OPTICAL CONCENTRATION DISTRIBUTIONS ON CONICAL RECEIVERS IN THE SOLAR GRIDIRON

In order to illustrate the power of the optical method described above, several figures are included showing computed concentration distributions on a conical receiver suspended in a spherical segment mirror as illustrated in Figure 4. One of the integrations in Eq. (6) was performed analytically and one with a high speed computer. The axis of symmetry of the cone passes through the center C of the spherical segment and, for the cases shown, is perfectly aligned so that the axis also passes through the center of the solar disc.

In Figure 5 the dotted curve shows the point sun concentration (in "suns") from Eq. (13) for a conical receiver of angular radius $\psi_o = 0.5^o$. The continuous

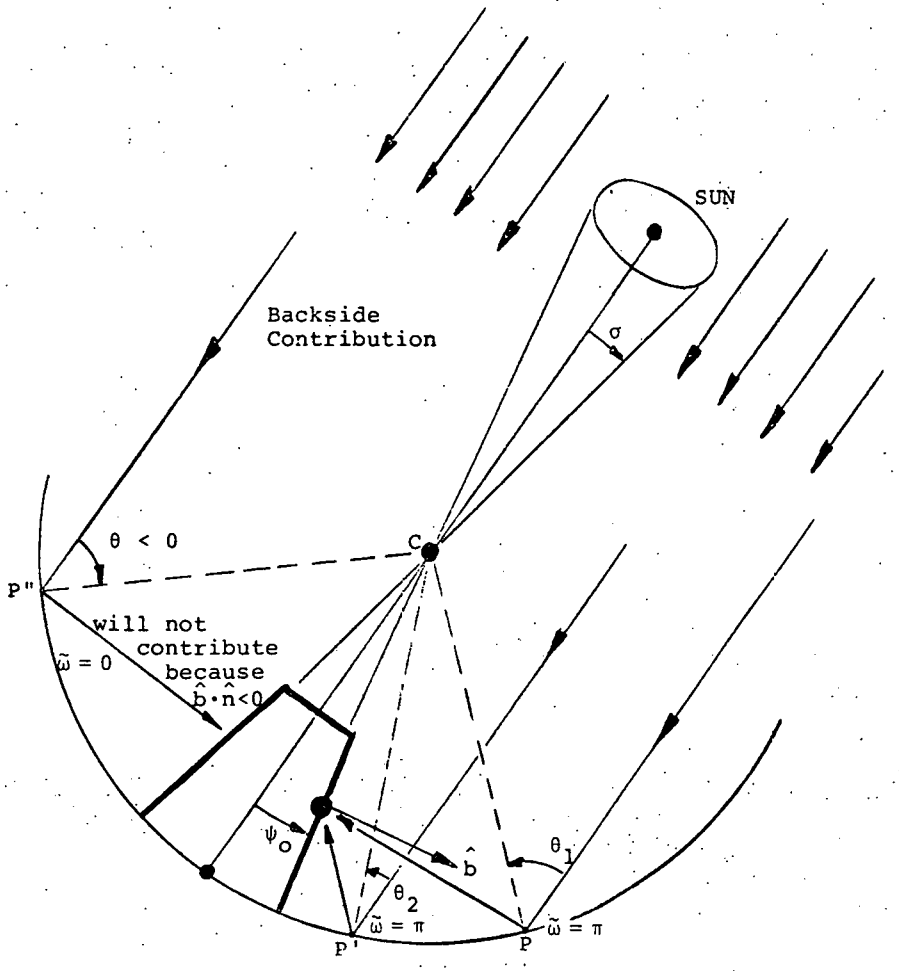

Figure 4. Multiple Contributions to the Single Bounce Concentration

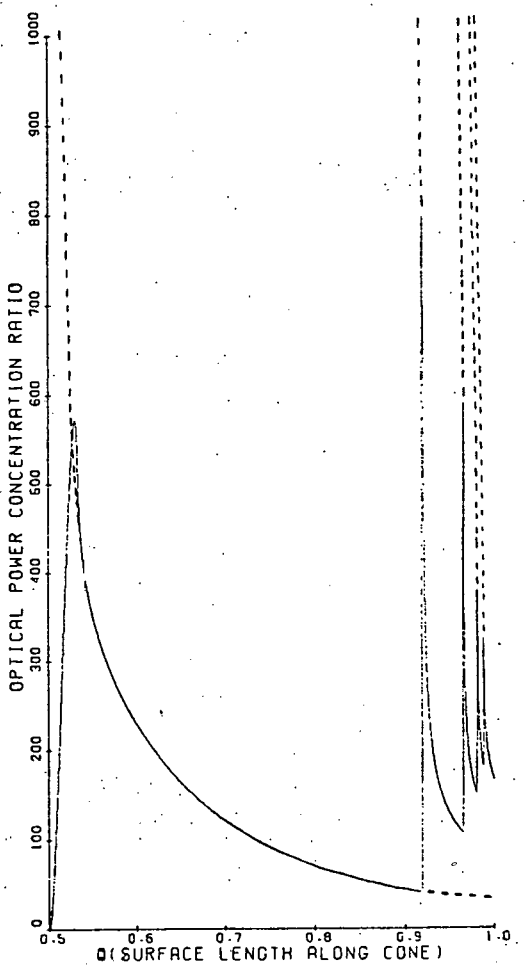

Figure 5. Symmetric Concentration Distribution on Receiver With $\psi_o=\sigma=0.5^0$, R=1.0, $\theta_{rim}=90^0$.

curve shows the concentration for a finite sun of angular radius $\delta = 0.5^{o}$ from Eqs. (4) and (6). The abscissa is the distance q (as a fraction of the sphere radius) of the field point on the conical surface from the center C of the spherical segment. This coordinate is illustrated in Figure 6. The infinities in the point sun distribution locate the caustics which are converted to large peaks in the finite sun distribution. No light is received on the interval of q from 0 to 0.5. The very sharp structure for $q > 0.9$ results from multiple bounce radiation. Very little total power is under these peaks, as one can see in the integrated distribution shown in Figure 7.

The rim angle θ_{rim} is 90^{o} for these figures, indicating a full hemisphere and the reflectivity, R = 1.0. The inclination I of the sun with respect to the dish symmetry axis is zero for this case, indicating that the symmetry axis passes through the center of the sun. There is complete azimuthal symmetry of the distribution around the barrel of the cone for this configuration. Figures 8 and 9 show details of the single bounce and double bounce peaks from Figure 5, illustrating the accuracy and resolving power of the procedure. The accuracy is to five or six significant figures in the concentration and is essentially exact for the idealized, perfect mirror surfaces assumed.

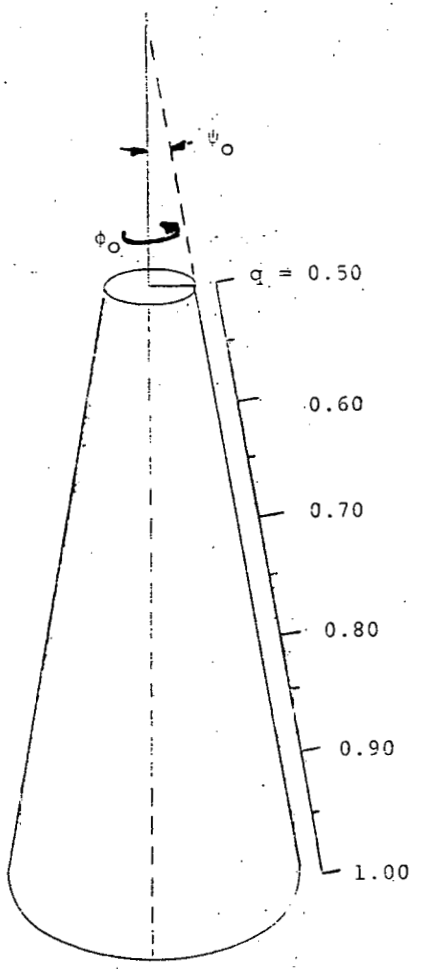

Figure 6. Geometry of Conical Absorber

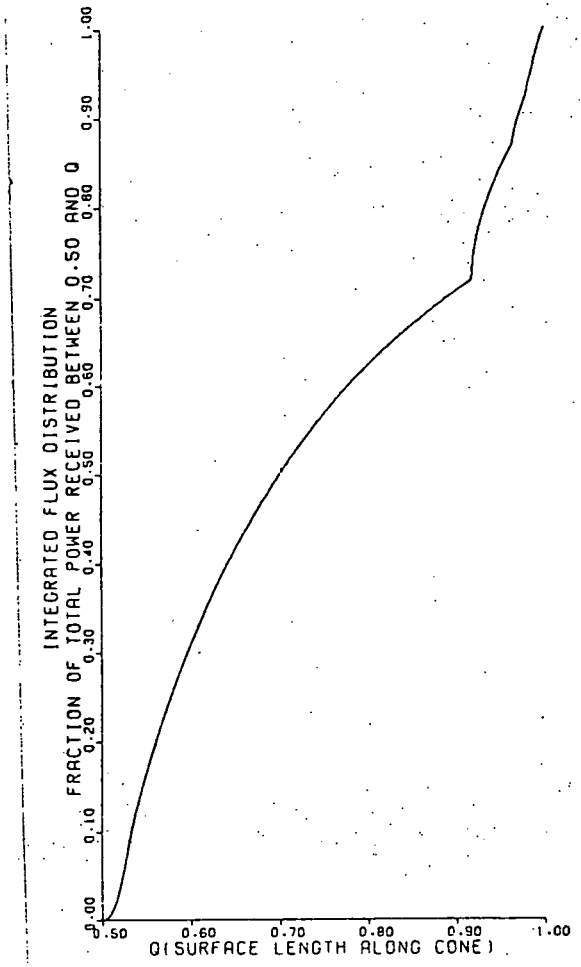

Figure 7. Integrated Flux Distribution as Function of Position on Receiver With $\psi_o=\sigma=0.50^0$, R=1.0, $\theta_{rim}=90^0$.

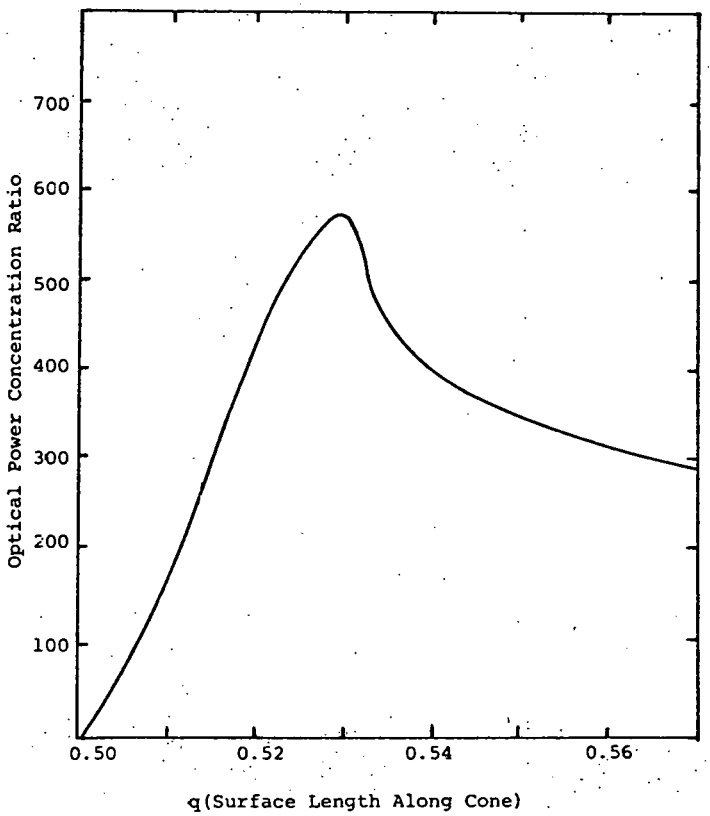

Figure 8. Detail of n=1 Peak.

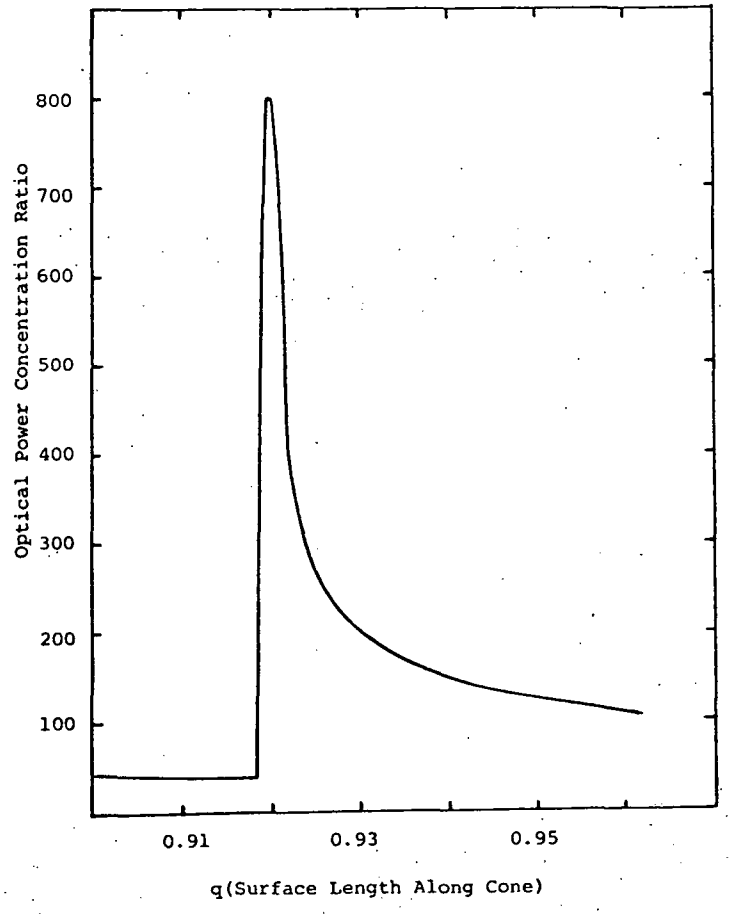

Figure 9. Detail of n=2 Peak.

The final fourteen figures, Figures 10-23, show the concentration distributions for sun inclinations of 30° and 60° from the symmetry axis of the dish. The rim angle of the dish is 60° for these cases, providing an included angle of 120° of arc for the bowl. Figures 10-16 show the distribution for $I = 30^{\circ}$ at seven values of the azimuth ϕ_o around the barrel of the conical receiver. The azimuth $\phi_o = 0$ corresponds to the brightest side of the receiver, the side closest to the dish symmetry axis, and $\phi_o = 180^{\circ}$ locates the azimuth of the opposite side. Figures 17-23 show the distribution at the same seven azimuth slices for a sun inclination of $I = 60^{\circ}$ from the symmetry axis. The distribution is identically zero at $\phi_o = 180^{\circ}$, Figure 23, because when $I = 60^{\circ}$, the axis of the aligned cone passes through the mirror rim and there is, therefore, no mirror surface supporting contribution at this azimuth.

For these figures, perfectly aligned "matched receivers" were considered. A "matched receiver" has angular radius ψ_o equal to the effective sun angular radius, σ. The sun angular radius σ illustrated is approximately twice as large as the actual sun. Such enlarged suns are considered in an effort to partially account for stochastic mirror imperfections and irregularities. We call this the "effective sun size" approach.

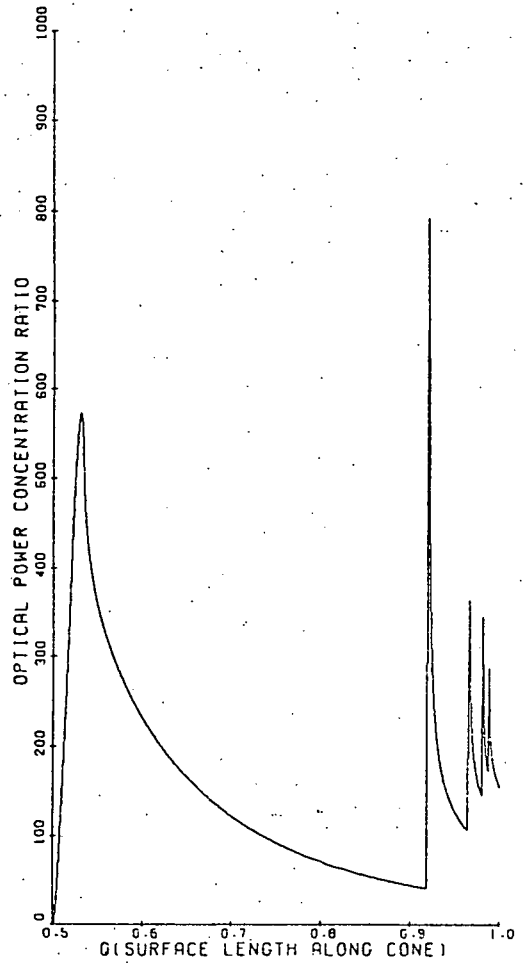

Figure 10. Concentration Distribution at $\phi_o=0$ With $\psi_o=\sigma=0.5^0$, R=1.0, $\theta_{rim}=60^0$, and Solar Inclination $=30^0$.

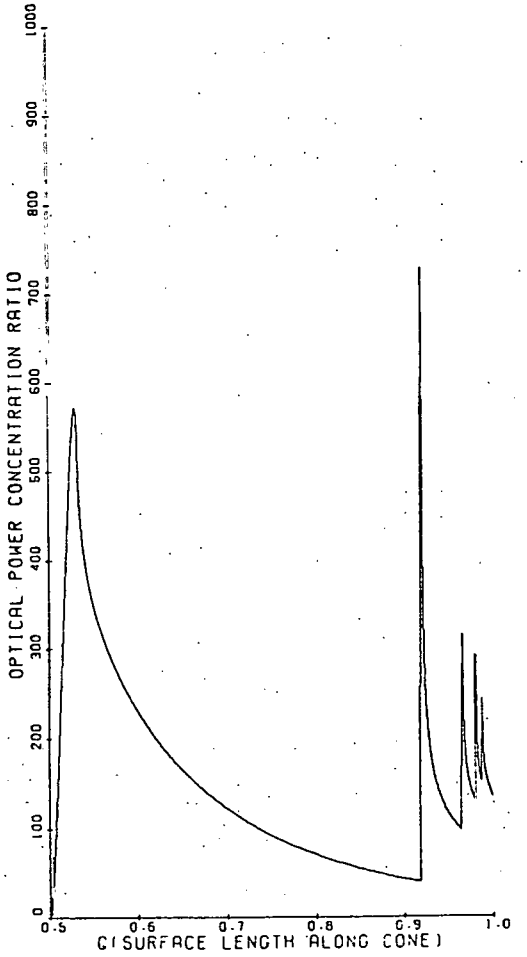

Figure 11. Concentration Distribution at $\phi_o=30^0$ With $\psi_o=\sigma=0.5^0$, R=1.0, $\theta_{rim}=60^0$, and Solar Inclination = 30^0.

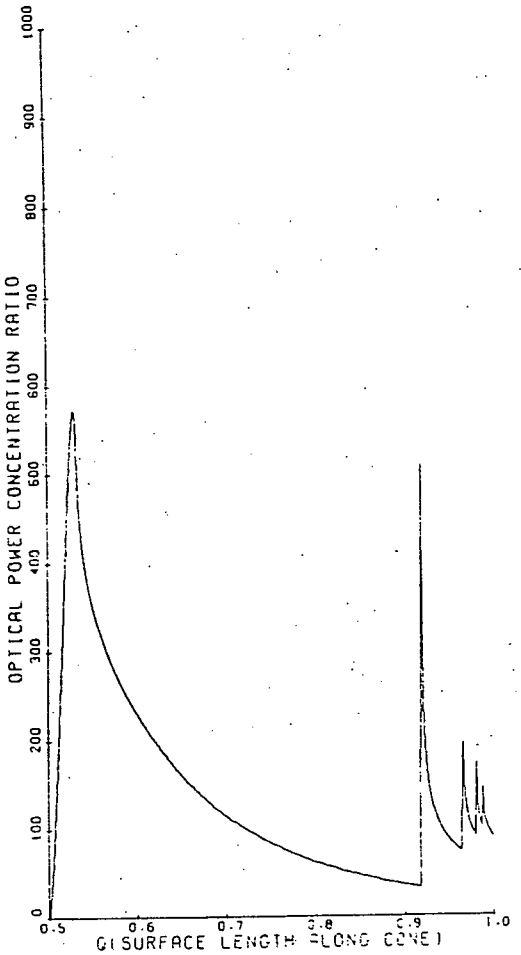

Figure 12. Concentration Distribution at ϕ_o=60° With ψ_o=σ=0.5°, R=1.0, θ_{rim}=60°, and Solar Inclination = 30°.

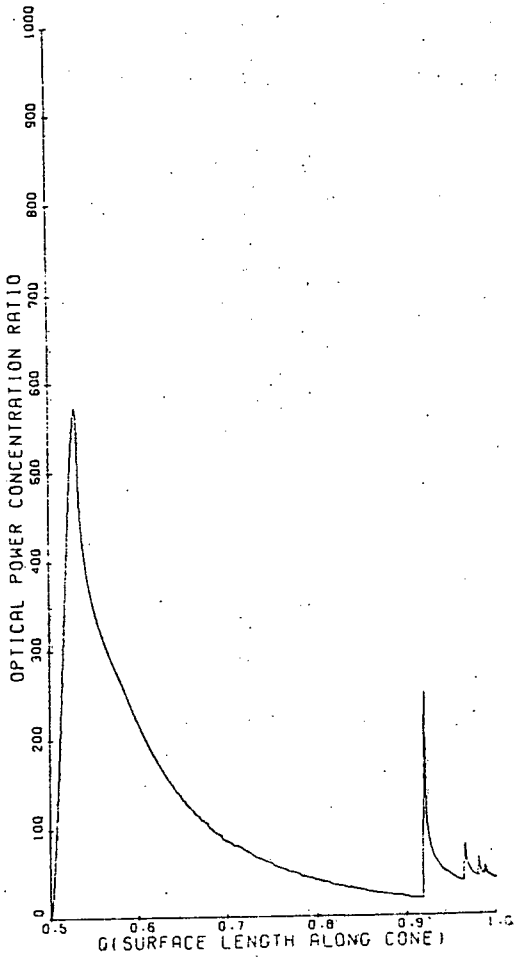

Figure 13. Concentration Distribution at ϕ_o=90° With ψ_o=σ=0.5°, R=1.0, θ_{rim}=60°, and Solar Inclination = 30°.

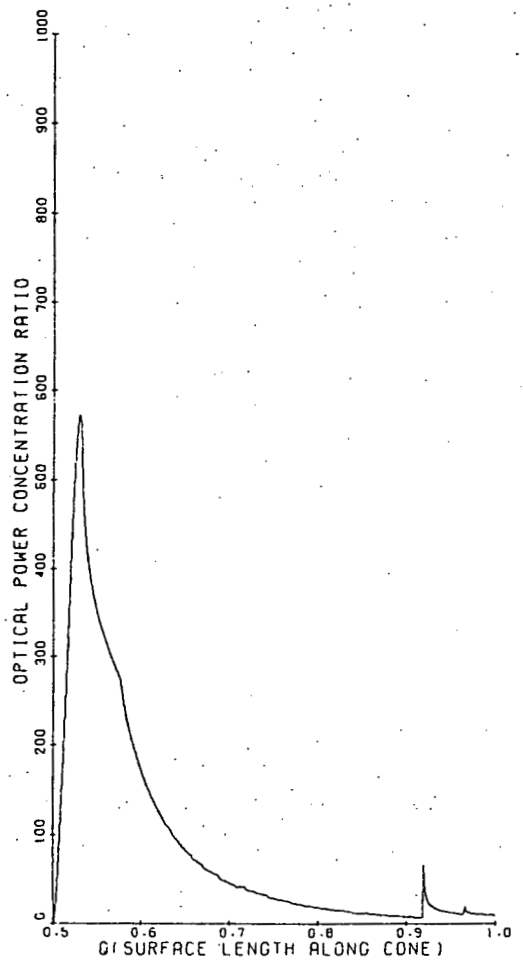

Figure 14. Concentration Distribution at ϕ_o=120° With ψ_o=σ=0.5°, R=1.0, θ_{rim}=60°, and Solar Inclination = 30°.

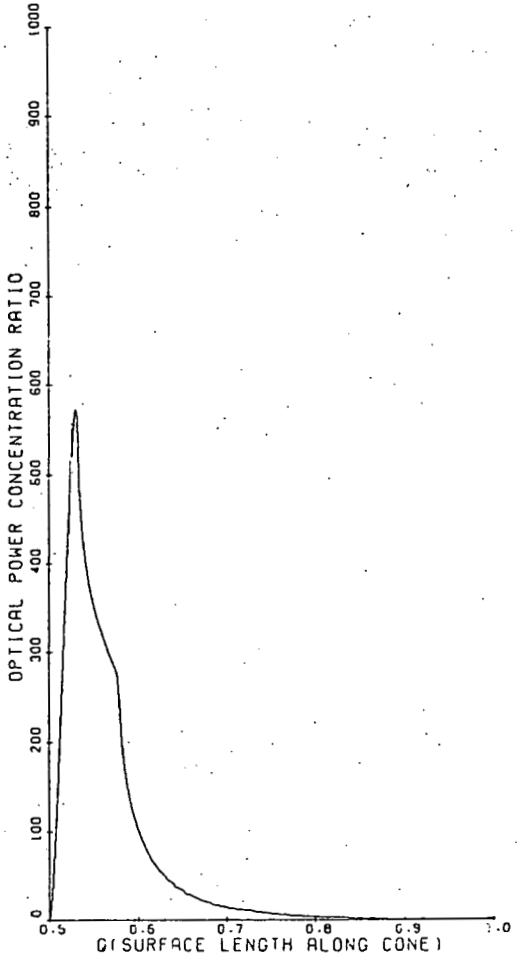

Figure 15. Concentration Distribution at ϕ_o=150° With ψ_o=σ=0.5°, R=1.0, θ_{rim}=60°, and Solar Inclination = 30°.

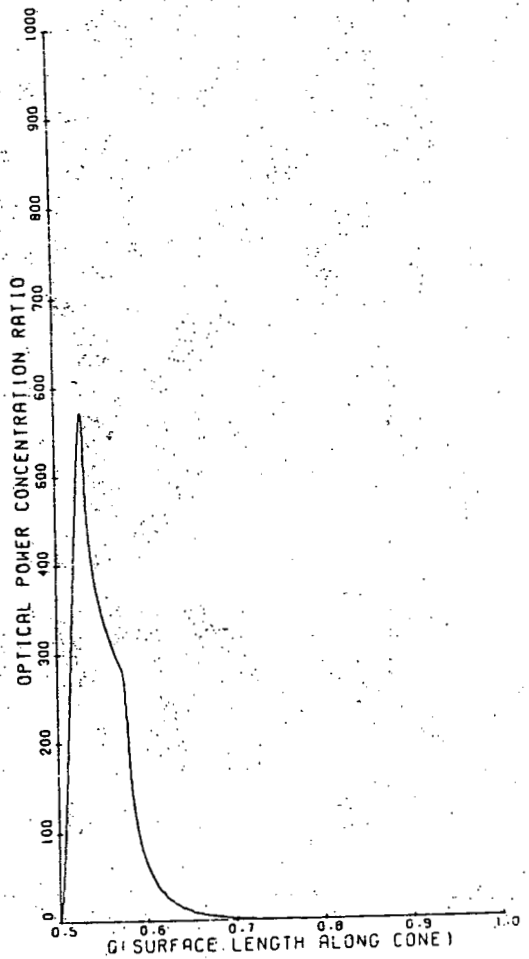

Figure 16. Concentration Distribution at ϕ_o=180°. With ψ_o=σ=0.5°, R=1.0, θ_{rim}=60°, and Solar Inclination = 30°.

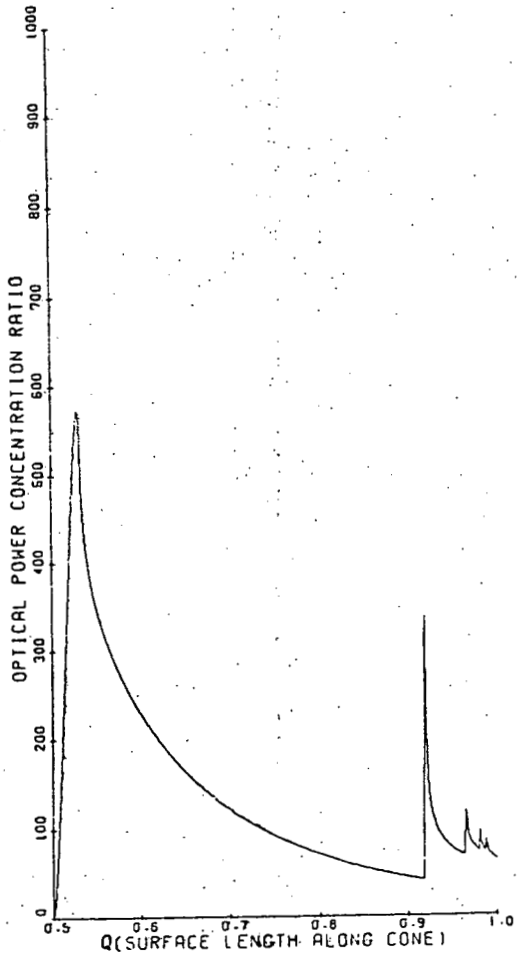

Figure 17. Concentration Distribution at ϕ_o=0° With ψ_o=σ=0.5°, R=1.0, θ_{rim}=60°, and Solar Inclination = 60°.

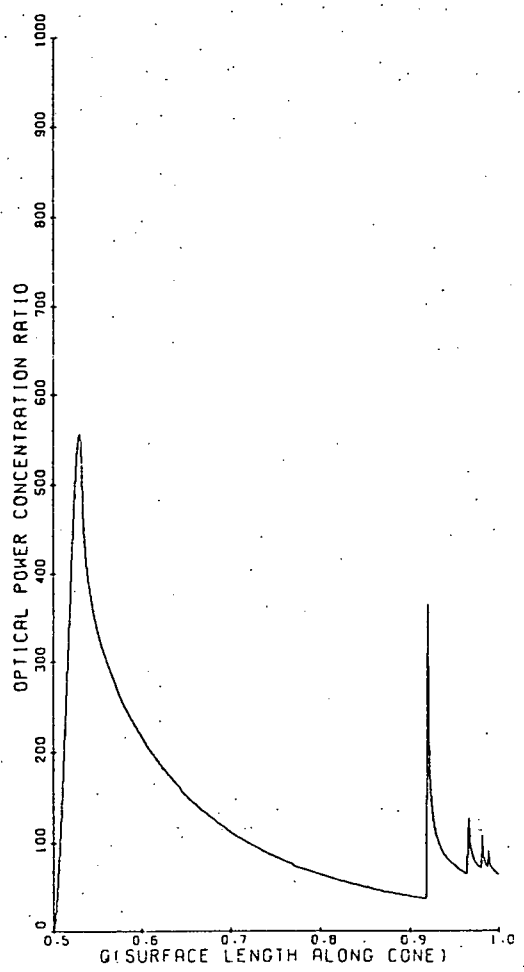

Figure 18. Concentration Distribution at ϕ_o=30° With ψ_o=σ=0.5°, R=1.0, θ_{rim}=60°, and Solar Inclination = 60°.

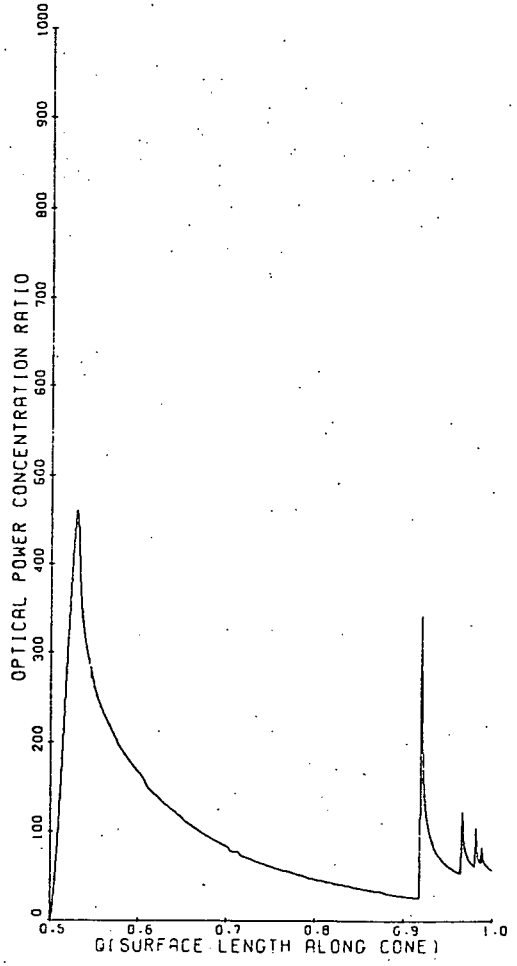

Figure 19. Concentration Distribution at ϕ_o=60° With ψ_o=σ=0.5°, R=1.0, θ_{rim}=60°, and Solar Inclination = 60°.

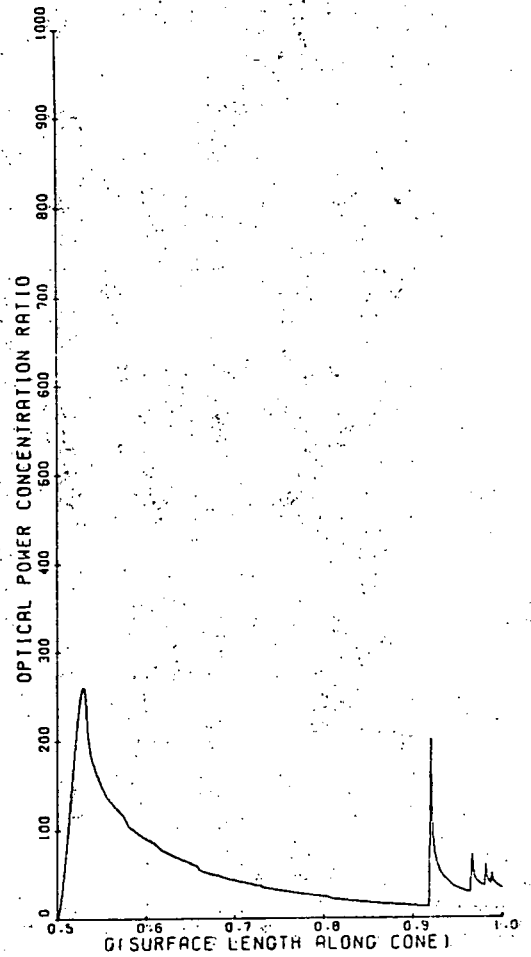

Figure 20. Concentration Distribution at ϕ_o=90° With ψ_o=σ=0.5°, R=1.0, θ_{rim}=60°, and Solar Inclination = 60°.

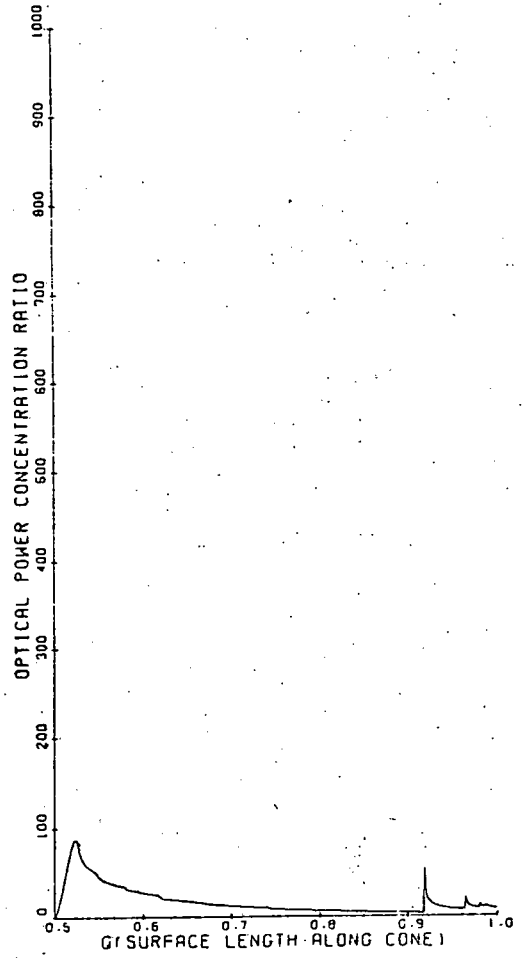

Figure 21. Concentration Distribution at ϕ_o=120° With ψ_o=σ=0.5°, R=1.0, θ_{rim}=60°, and Solar Inclination = 60°.

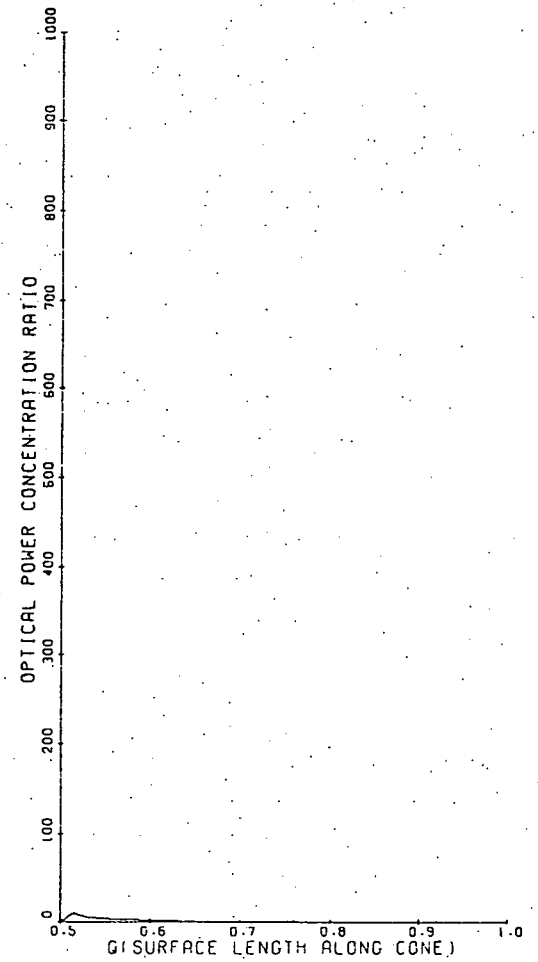

Figure 22. Concentration Distribution at ϕ_o=150° With ψ_o=σ=0.5°, R=1.0, θ_{rim}=60°, and Solar Inclination = 60°.

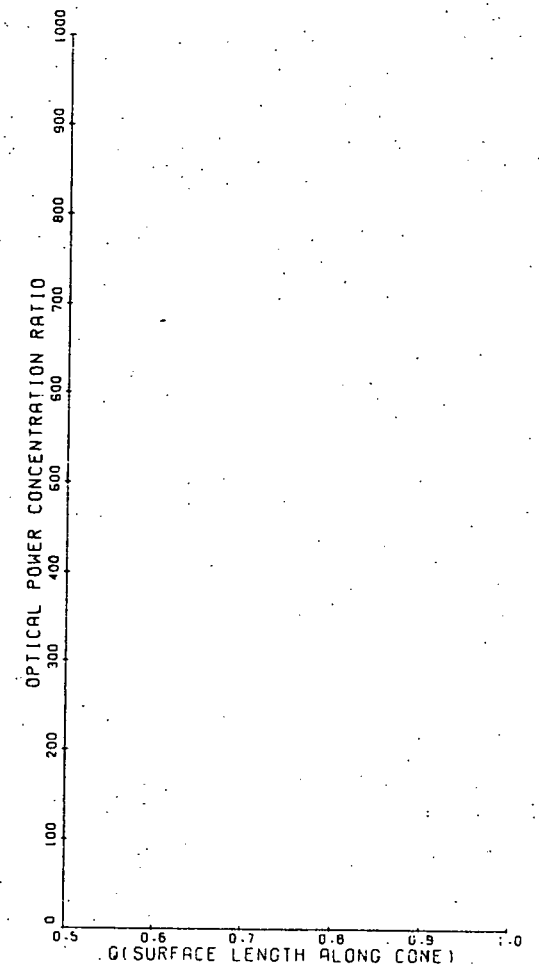

Figure 23. Concentration Distribution at ϕ_o=180° With ψ_o=σ=0.5°, R=1.0, θ_{rim}=60°, and Solar Inclination = 60°.

CONCLUSION

The calculational approach which has been illustrated here has proved to be useful in our Solar Gridiron problem. Highly streamlined versions of good accuracy have been developed for production runs to analyze receiver thermal performance on hourly, daily, and annual bases. There is perhaps a chance that these ideas may be useful for some of the adaptive optics computations. At least, this is the approach I am familiar with and would use.

It has been a pleasure to be included here, to have a chance to tease a little and to learn of the excellent work you fellows have done. We all have some interesting and romantic problems to work on and it is a great privilege to enjoy the discussions of this workshop.

Conf-770850--1

HELIOS: A COMPUTATIONAL MODEL FOR SOLAR CONCENTRATORS*

F. Biggs and C. N. Vittitoe
Sandia Laboratories, Albuquerque, New Mexico 87115

ABSTRACT

The HELIOS computer code calculates the power concentrated by a field of individually guided heliostats and the resulting flux density (watts/cm^2) falling upon an arbitrary target grid. The problem has individual subroutines for each task in order to incorporate options for a variety of facet shapes, heliostat designs, field layouts, and tower-receiver apertures, and to facilitate additions and code improvements. HELIOS evolved concurrently with the construction of the Solar Thermal Test Facility (STTF) at Sandia Laboratories and has been used extensively by the STTF engineers to analyze questions on safety, performance, design trade-offs, and tower protection engineering. Comparisons of HELIOS results with measurements have given good agreement.

HELIOS calculates the "sun position" and uses it to establish alignment geometries. Atmospheric attenuation effects are included. Measured angular-distributions of incoming photons (sunshapes) and effects of aureole scattering are incorporated. Nondeterministic factors such as sun-tracking errors and facet-surface errors are described statistically and combined with the sunshape by numerical convolution. Shadowing and blocking are included. Several output choices are available, including graphical display of flux density distributions, of shadowing and blocking and of sunshape.

Some of the modeling in HELIOS and samples of results will be described.

*This work supported by the U.S. Energy Research and Development Administration.

INTRODUCTION

The computer program HELIOS calculates the power concentrated by a field of individually guided heliostats and the flux density (W/cm^2) falling upon an arbitrary target grid. The program evolved over the past two years concurrently with the construction of the Solar Thermal Test Facility (STTF) at Sandia Laboratories in Albuquerque, NM. We worked closely with the STTF engineers and as new questions arose, options were added to the code to answer them and to present the solutions in a convenient form.

It became clear early in the code development that the priority of questions to be answered changed with time. An early priority was performance predictions but soon safety analyses took top priority. Later the emphasis shifted more to design trade-off studies, then to an analysis of calibration and alignment effects and to general parameter studies. This required us to adopt a philosophy of constructing a usable computer program quickly using approximations where necessary, then to improve upon them as the needs were identified. Moreover, it was necessary to structure the program with individual subroutines for each major task to facilitate the addition of new options for an everchanging variety of facet shapes, heliostat designs, field layouts, and target-grid specifications.

As HELIOS continued to evolve, there were fewer new kinds of questions to answer and the emphasis shifted from adding new capabilities to improving existing ones, streamlining the code, and documentation work. We are still in the latter phases of the project. A users guide is now available (Ref. 1) and a report giving the development of the model is in progress (Ref. 2). Preliminary versions of HELIOS have now been distributed to several agencies outside Sandia Laboratories.

The remainder of this report is organized as follows: (1) an overview summarizes the important functions of the model, (2) some of the statistical optics are examined, (3) a more detailed description of the computer code is given emphasizing the input parameters, and finally (4) some examples of auxiliary programs are presented.

MODEL DESCRIPTION

Figure 1 shows a schematic drawing of a central-receiver solar-collector system emphasizing the important elements. Three heliostats are shown on a small hill to illustrate that the ground may not be level. There are, of course, more than three heliostats in the usual collector field but these will be adequate to illustrate

the main ideas of the model including shadowing and blocking.

From the time a photon leaves the sun until it reaches the receiver aperture, it is subjected to many effects. HELIOS is designed to simulate these effects and to determine the consequences of them on the performance of the collector system. We now give an overview of the model organizing the discussion in roughly the order a photon encounters the system.

We first go through the system to define a few special terms, then go back through it describing effects and how HELIOS simulates these effects. The "central ray" from the sun originates from the center of the solar disk. The "sun position" is the direction (azimuth and elevation) of the incoming central ray. Each heliostat consists of one or more reflecting surfaces called "facets". Figure 1 shows 9 facets for convenience in drawing. The heliostat is guided so that a central ray from the sun will reflect from the center of the "reference facet" (center facet) to intersect the "aim point". The distance from a heliostat reference-facet to the aim point is called the "slant range" for that heliostat and the path followed by a reflected central ray is called the "slant-path". The facets also have slant-ranges, these may differ slightly from the corresponding heliostat slant-range. The "target-grid" is a grid of points at which HELIOS calculates the "flux density" in watts per cm^2.

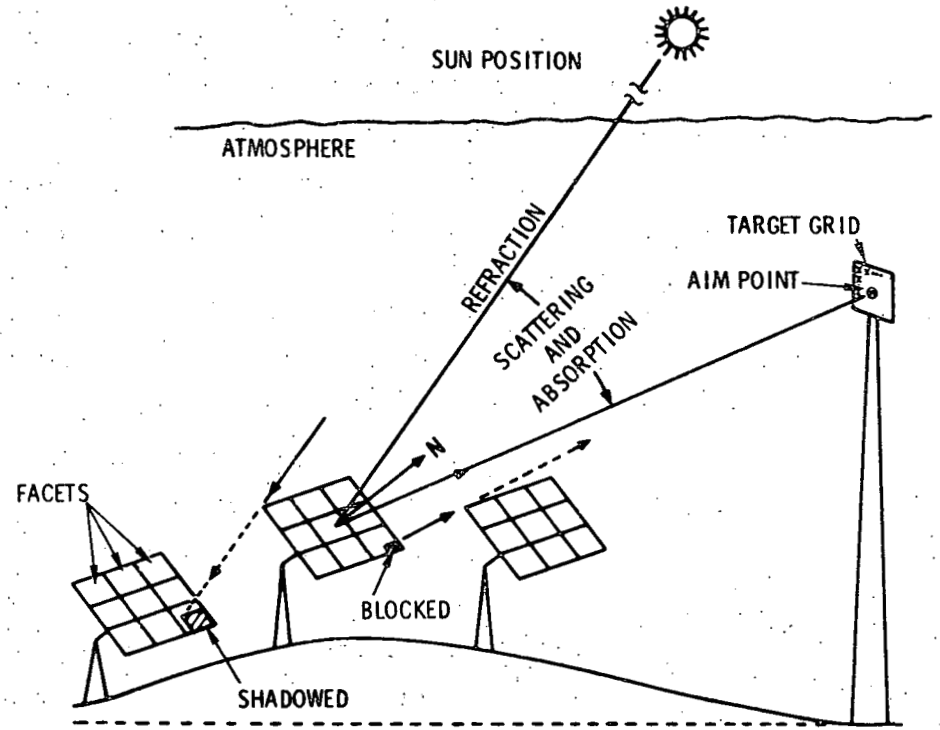

Figure 1. A schematic drawing of a central-receiver solar-collector system showing a three-heliostat portion of the collector field.

The central ray does not follow a straight path through the atmosphere but is curved by refraction. HELIOS

determines the sun position (actually apparent sun position) that corrects for atmospheric refraction. This information is subsequently used by the code to help establish alignment geometries for the heliostats.

Photons are incident on the atmosphere, not as a collimated beam of light but with an angular distribution of directions, called the "sunshape", about the central ray. The solar disk subtends an angle of approximately 10 mrad as viewed from the earth. As sunlight traverses the atmosphere scattering (aureole scattering) broadens the sunshape. This is especially evident during hazy atmospheric conditions. HELIOS uses sunshapes that are measured at the collector site.

As sunlight traverses the atmosphere, it is attenuated by absorption and scattering. Several models of the atmosphere are available to determine insolation at the site and to calculate absorption losses along the slant paths from each heliostat to the tower receiver. Measured values of solar insolation can also be used as input.

Each heliostat is aligned by rotation about two axes. The alignment is calculated so that the central ray reflecting from the center of the reference facet (center facet) will intercept the aim point. Since the alignment rotations may cause displacements of the reflecting surface, the alignment calculation is iterated until the calculation is based on the correct final position of the reflecting surface.

The facets are prealigned with respect to the heliostat frame to obtain the desired focal properties for the heliostat. Figure 1 shows 9 facets per heliostat for simplicity in drawing; however, zone-A heliostats of the STTF have 25 facets. It is, of course, possible to have only one facet per heliostat. A common "prealignment" option is designated as "on axis" where the facets are set so that light incident and reflected at a zero angle of incidence would come to a focus at a distance from the heliostat equal to its slant range. In this option, the total heliostat surface approximates a paraboloid of revolution as closely as is possible by the prealignment of facets. Another option is obtained by specifying a date and time of day from which HELIOS calculates an apparent sun position and then uses it to determine the prealignment conditions that will permit central rays to reflect from the center of each facet to intercept the aim point at the specified time. The prealignment information is stored and used in subsequent calculations.

Several options are available for specifying facet shapes, among these are flat, spherical, paraboloidal, and some surface shapes obtained from stress-analysis calculations. If the shape is specified to be paraboloidal, a focal length equal to the slant range is used. In the present stress-analysis options a facet center pull-down distance is used to adjust the focal properties of the facet. HELIOS uses an optimization routine to find the value of the pull-down parameter that maximizes the flux density in the solar image projected on the target grid for each facet.

As shown schematically in Figure 1, a heliostat may be partially shadowed from the sun by another heliostat or a heliostat may block light that is reflected from another one. These effects are calculated by HELIOS and options are available to display the results graphically.

The aim point is used for heliostat guidance calculations. It would usually be placed at the center of the receiver aperture for most performance calculations, but it would be someplace else for purposes of simulating a standby mode of operation. Separate aim points for different heliostats can be specified if desired. This would be necessary for some shapes of receiver apertures. Aim points are also used in the prealignment calculations but these are specified separately from those used in the simulation "run-time" calculations. The run time consists of a date and time of day which is used by HELIOS to calculate the corresponding apparent sun position which it then uses to determine the heliostat alignment geometry.

The target grid is shown in Figure 1 to coincide with the receiver aperture and centered on the aim point. Although this is a common arrangement for performance calculations, the specification of the target grid is independent of the aim point; it can be placed anywhere. It may be positioned on the tower to simulate spillage effects in order to answer questions on tower-protection engineering. The target grid is shown as rectangular in Figure 1, but options are available for it to be spherical, cylindrical, or an arbitrary shape to be specified by the user. Currently, the code is set up to calculate the flux density (W/cm^2) at 121 points (on an 11 by 11 grid) on the target grid. It also calculates the radiant power obtained by integrating over the target grid.

When the computer calculates heliostat alignments, it does so to machine accuracy whereas the sun-tracking mechanism can guide the heliostats to within some (much more course) error tolerance. A similar effect occurs

in the prealignment of facets. There are also many other nondeterministic factors that degrade the performance of the system. The facet shapes vary about their designed shapes because of manufacturing tolerances, because of temperature effects, and even because of changes in gravity loading as the heliostat tracks the sun. Turbulent wind-loading may cause the facets to vibrate. There is a non-specular component to the reflection of sun light. These nondeterministic factors degrade the average performance of the solar collector. It is important to include them in a model that simulates the behavior of the system.

HELIOS subdivides each facet into an integration mesh. It then calculates a contribution to the flux density at each of the target grid points from one of these integration-mesh areas. The program then cycles over the integration mesh of the facet to obtain the facet contribution. It cycles over the facets of the heliostat and finally over the heliostats of the field.

Figure 2 shows one block of the integration mesh within a facet. The incident central-ray from the sun lies along vector I. The cone drawn about I depicts the angular distribution of incoming sun rays (sunshape). The vector N shows the nominal direction of the normal for this element of surface and the cone drawn about N

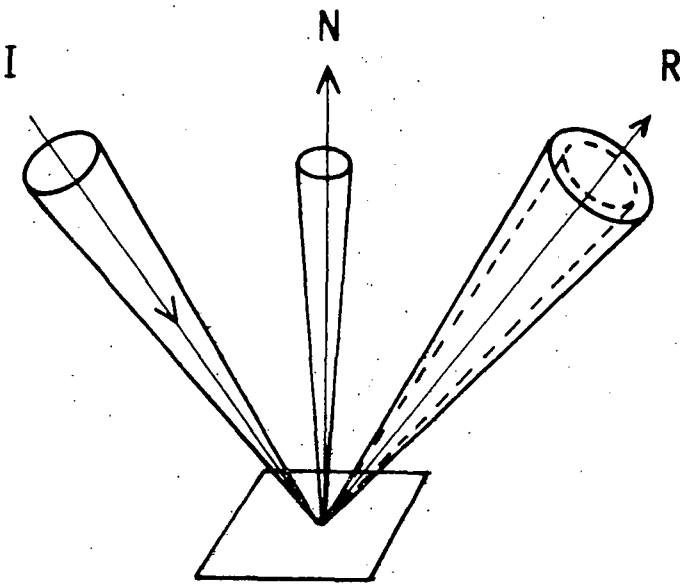

Figure 2. The broadening of the effective sunshape due to uncertainty in the direction of the reflecting-surface normal.

depicts the nondeterministic nature of the direction of this surface-normal due to the uncertainties mentioned above. If the surface normal were known to lie along N (no uncertainty) then the reflected sunshape would be as shown by the dotted cone about the reflected central ray R. With uncertainties in the direction of the surface normal, the reflected cone is spread out (on the average) as indicated by the solid cone drawn about R. We call this the "effective sunshape". The effective sunshape is projected onto the target grid to obtain the average contributions to the flux density at each

of the target-grid points.

The distribution of directions of the surface normal is mapped into a distribution of directions of reflected rays about R and combined numerically with the reflected sunshape using the two-dimensional fast Fourier transform to obtain the effective sunshape. This characterizes the distribution of reflected sun-rays when averaged over time and reflecting surface.

AN ILLUSTRATION

As an illustration of the use of HELIOS, we examine the flux-density pattern on the Martin Marietta one Megawatt Receiver that is produced by the 78 heliostats of zone A of the STTF. We also analyze some of the factors that cause this flux-density pattern to change with time.

The shadowing projection of Figure 3 is convenient for showing the heliostat arrangement. The 78 heliostats and the tower are projected onto a plane through the base of the tower and perpendicular to the central ray from the sun at noon on March 21. This is, therefore, a veiw of the collector field and tower from the south at an elevation of 55 degrees.

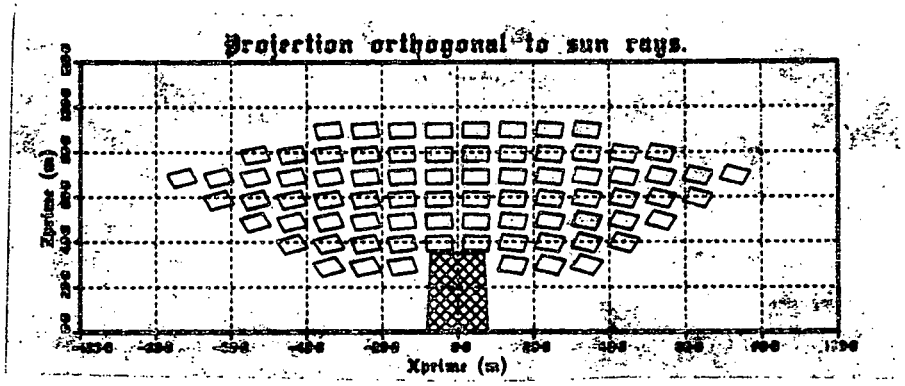

Figure 3. The tower and 78 heliostats of zone A of the STTF. This is a projection on a plane through the base of the tower and perpendicular to the central ray from the sun at noon on March 21. The xprime axis is horizontal.

The 1-m by 1-m receiver aperture on the tower faces north, it is centered at an altitude of 44.5 m above the base of the tower, and is inclined downward 20° from the vertical. The prealignment of facets is for noon of March 21. This means that the facets are prealigned with respect to the heliostat frame so that central rays from the sun reflect from the center of each facet to intercept the aim point while in the geometry of Figure 3, i.e., at noon on March 21. We assume an insolation of 800 W/m^2 and a facet reflectivity of 0.8 for this example.

Figure 4 shows the sunshape (dotted curve), the error cone (dashed curve), and the resultant effective sunshape (solid curve). A circular-normal error-cone of

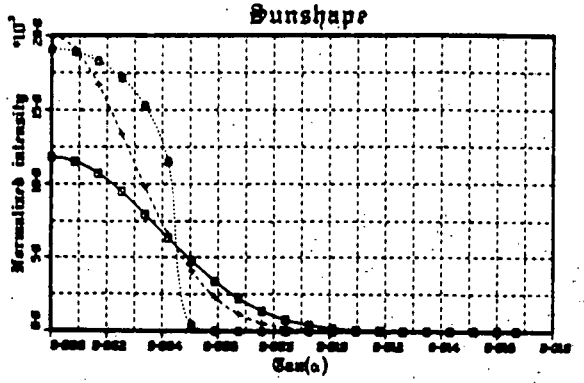

Figure 4. The sunshape (dotted curve), the error cone (dashed curve) and the effective sunshape (solid curve).

dispersion equal to 2 milliradians is used. The sunshape is one that was measured in Albuquerque, NM at 1 PM on June 25, 1976.

Figure 5 shows flux density (W/cm^2) patterns on the receiver aperture. Part a corresponds to 8 AM and part b to noon, both are for March 21. The peak flux density at noon is about 300 watts/cm^2 (3750 suns) and the integral of the flux density over the 1-m by 1-m aperture is 1.36 MW which corresponds to 1700 suns when averaged over the aperture. Thus the average flux density is a little less than half the peak value. At 8 AM (part a) the peak value of the flux density is about 120 watts/cm^2 (1500 suns) and the power intercepted by the aperture is 0.66 MW. This gives an

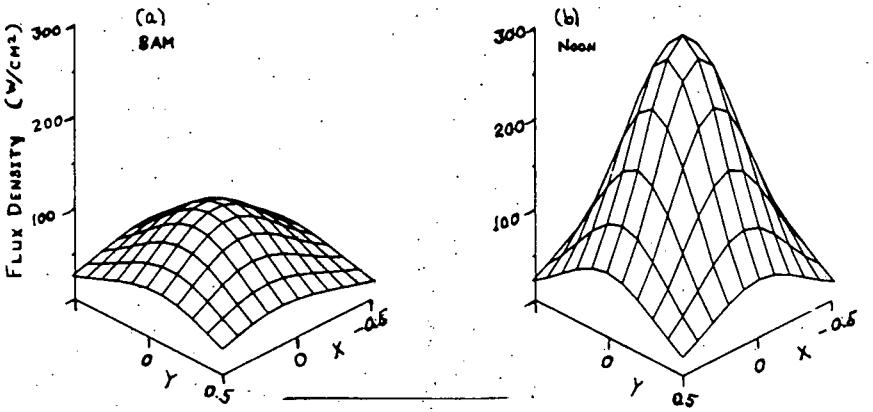

Figure 5. Flux-density patterns on the 1-m tower receiver aperture from the 78 heliostats of zone A of the STTF on March 21. The prealign time is noon of March 21.

average of 66 Watts/cm^2 (825 suns) over the aperture which is a little more than half the peak value. There is, therefore, a significant flattening out of the flux density pattern between the noon and the 8 AM results.

Let us take a more detailed look at the reasons for the differences between these two flux density patterns. The total collector area for the zone A field is $A = (1.22)^2(25)\ (78) = 2902\ m^2$. If this area were normal to the central ray from the sun, it would intercept a power of $P = AQ = (2902\ m^2)\ (800 W/m^2) = 2.32$ MW where $Q = 800\ W/m^2$ is the insolation. Of course, the area A is not all perpendicular to the sun's rays but

is effectively reduced by the "cosine effect". Shadowing and blocking together with other factors also contribute to losses in the power collected. It is of interest to use results from HELIOS to compare the loss factors corresponding to the two flux-density patterns of Figure 5.

The first row of Table 1 gives the cosine-effect loss factors for the two run-times. The number in parenthesis in the 8 AM column is the ratio of the 8 AM value to the corresponding noon-time value. Thus the cosine-effect loss-factor at 8 AM is 88% of its value at noon. The reflected power (neglecting shadowing and blocking) is given in the next row. This is the product of the total collector area A = 2902 m^2, times the insolation (800 W/m^2), times the reflectivity $\rho = 0.8$, times the cosine-effect loss-factor from the first row. The next row gives the shadowing and blocking loss factors, multiplying these by the numbers in the row above gives the effective reflected power. However, not all the effective reflected power is intercepted by the receiver-aperture. There is a spillage loss-factor which is given in the next to the last row of the table. At 8 AM, only 49% of the effective reflected power intercepts the aperture to give a collected power of 0.66 MW. At noon, 80% of the effective reflected power intercepts the aperture giving a collected power of 1.36 MW.

Table 1 - Loss factors for performance of the 78 heliostats of zone A of the STTF with the 1-m by 1-m Martin Marietta 1 MW receiver and using a circular-normal error-cone of dispersion equal to 2 milliradians. Pre-alignment time is noon of March 21. The run times listed below are also for March 21. The facet reflectivity is $\rho = 0.8$ and $P = (2902\ m^2)\ (800\ W/m^2) = 2.32$ MW. The numbers given in parenthesis in the 8 AM column are ratios of the loss factor at 8 AM to its value at noon.

	Run Times	
	8 AM	Noon
Cosine-effect loss-factor = $< \cos i >$	0.84 (0.88)	0.96
Reflected power neglecting shadowing and blocking loses = $P\rho < \cos i >$	1.56 MW	1.78 MW
Shadowing and blocking loss-factor	0.87 (0.91)	0.96
Effective reflected power	1.36 MW	1.71 MW
Spillage loss-factor	0.49 (0.61)	0.80
Collected power	0.66 MW	1.36 MW

Note that the loss factor that changes most between the noon and 8 AM run-times is the spillage loss-factor (the smallest of the numbers in parenthesis of the 8 AM column). In order to illustrate how heliostat-size astigmatic-aberrations contribute to the spillage loss factor, we use some more HELIOS results.

Consider the flux-density patterns resulting from only the four corner facets of heliostat #18 of the zone A field. This heliostat is in the bottom row of heliostats shown in Figure 3 and just to the left of the shadow of the tower. Figure 6 shows the flux density pattern in part a for a run time of 11 AM and in part b for a run time of 3 PM. The prealignment of facets and the run times in this example are different from those used in the previous results but the concepts to be illustrated are the same. These four facets are assumed to be aligned on-axis (zero angle of incidence). This is approximately the situation in part a of Figure 6 where the angle of incidence is only 3 degrees. The target grid is centered on the Martin Marietta one-Megawatt receiver-aperture but we have enlarged it to 2.5-m in order to show more of the spillage pattern and to better illustrate the effect of astigmatic aberrations. The 1-m by 1-m receiver aperture would occupy a 4-block by 4-block square in the center of the target grid shown in the figure.

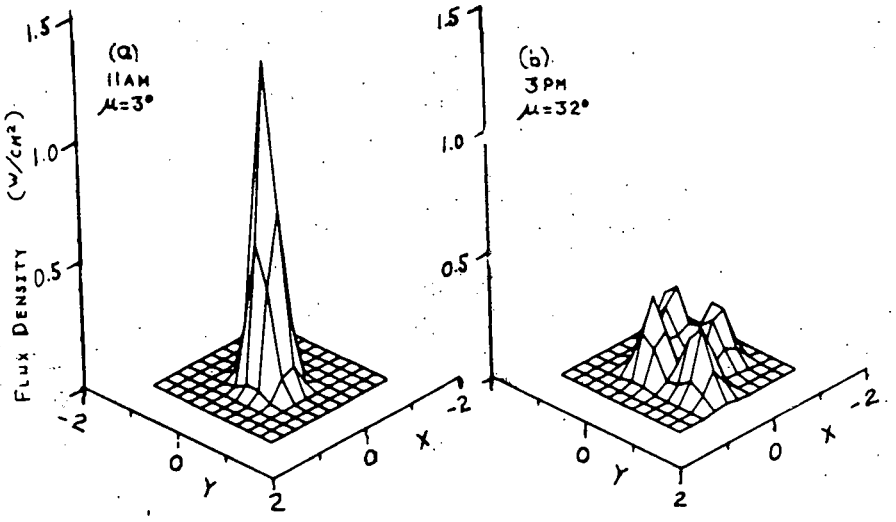

Figure 6. Flux-density patterns from the four corner facets of heliostat #18. In part a, the run time is 11 AM on March 21 and in part b the run time is 3 PM on March 21. The facets are prealigned on-axis.

The heliostat alignment in both parts of Figure 6 is such that the center facet would project a solar image centered on the aim point (the center of the target grid here). If all the facets of the heliostat were used in the calculation, the flux-density pattern in part a of Figure 6 would be similar in shape but more intense by a factor of about 25/4 = 6.25. In part b, however, the individual peaks would no longer be resolved but a generally smeared out pattern would be obtained.

This illustrates the major reason for the change in the spillage loss-factors between the a and b parts of Figure 5. Of course, in Figure 5, the flux patterns are for the 78 heliostats of zone A of the field. The extent of the astigmatic aberrations changes from one heliostat to another because of the different geometric relationships between each heliostat and its prealignment conditions. HELIOS is designed to facilitate such parameter studies as these.

CODE ORGANIZATION AND INPUT CAPABILITY

In keeping with the conference objective of providing a description of the computer code for specialists and potential users, we now concentrate upon the code input as a means of further indicating the capabilities of HELIOS. The discussion should convince you that use of HELIOS is easy and is reasonable for many types of problems.

The basic flow chart is given in Figure 7. The LOCK and NTLOCK parameters allow calculation of the energy flux pattern in two emergency situations, (1) the sun continues across the sky after motors have been locked by a power failure, or (2) the sun continues across the sky after an emergency caused the motors to slew toward the storage position.

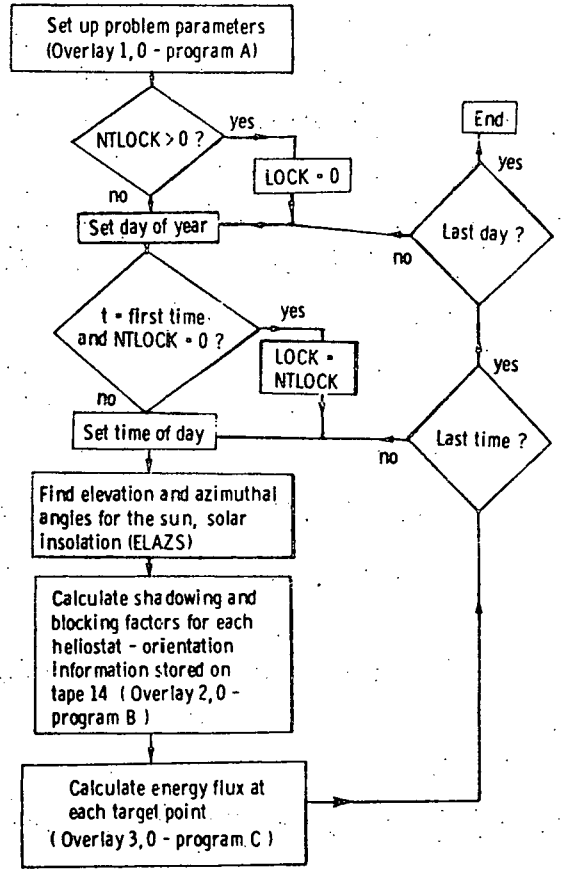

Figure 7. HELIOS Flow Chart

Program A is further subdivided in Figure 8 where controlling subroutines are identified by parenthesis. DATA1 sets the default values appropriate for the Solar Thermal Test Facility at Sandia Laboratories. INDATA accepts all the input variables. This subroutine should be studied by prospective users to increase

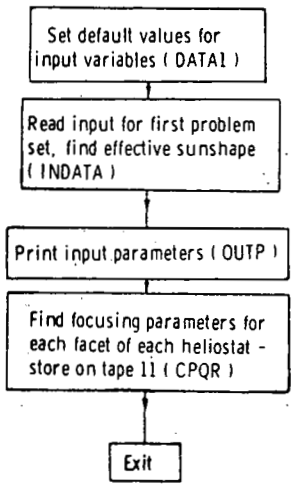

Figure 8. Program A Flow Chart

understanding of code capabilities and to identify possible errors in input data.

The HELIOS input data are separated into seven groups: problem- and output-type data, sun-parameter data, receiver data, facet data, heliostat-positioning data, time data, and atmospheric data. Each set is characterized by a group number NGRUP. As each new problem is encountered, new data need only be read in for groups with data differing from the previous problem. Hence, each set of data may be discussed separately from the other groups. Each of the data groups is now examined briefly with mention of decisions to be made for each group.

Figure 9 gives the group 1 input. Do you want print out for each facet, or for each heliostat, or only for the heliostat field? Are graphs to be generated? Which shadowing and blocking options are to be used? Do you want rapid calculation with less accuracy or improved accuracy with extended computer time? Is a new heliostat distribution to be input or is the STTF default distribution sufficient? Is the propagation loss between mirror and receiver to be included?

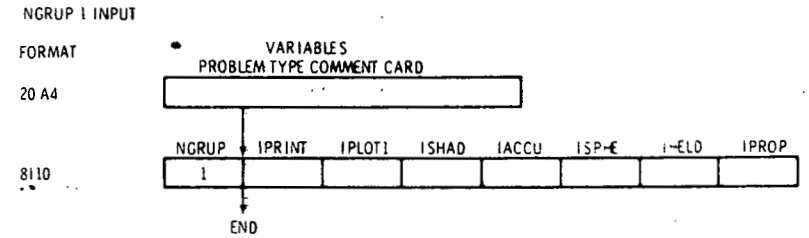

Figure 9. Group 1 input flow chart.

Group 2 data control the effective sunshape. The parameters in Figure 10 determine the sunshape, error cone, and effective sunshape. They also allow solar insolation as an input variable. The sunshape may be inserted via parameters or as a table of values.

The receiver data are input as group 3 in Figure 11. They specify the number of target points, printing options, target orientation, target shape, receiver latitude, coordinates of the target center, of the

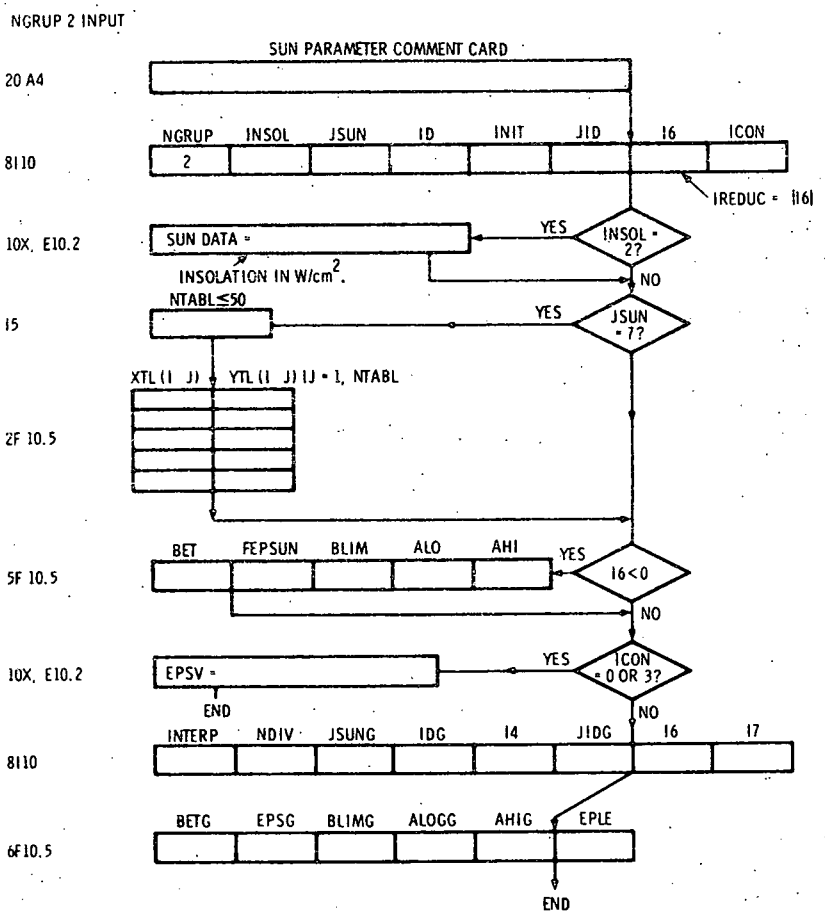

Figure 10. Group 2 input flow chart.

aim point, and of the prealignment point, and effective tower dimensions for shadowing calculations.

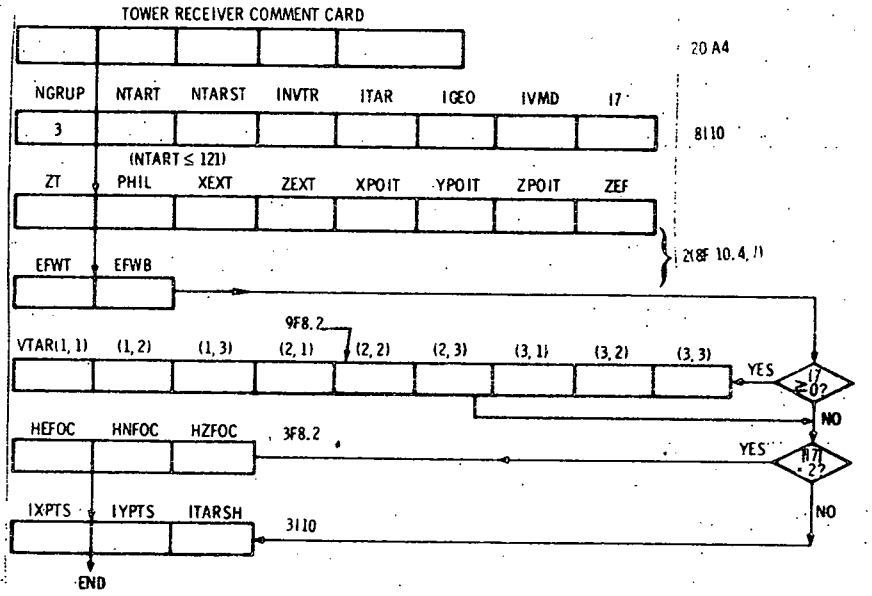

Figure 11. Group 3 input flow chart.

Figure 12 gives the flow chart for the facet data. How many facets are on each heliostat? Are the facets circular or square? How many subdivisions of the facet are to be taken along each edge? What is the surface shape? If a shape resulting from stress analysis is to be used, what is the radius of a stressed ring or disk, and what is Poisson's ratio for the stressed material? What is the facet dimension? Reflectivity? Distribution on the heliostat?

The facet distribution on the heliostat is given in Figure 13. The U3 axis completes the right handed coordinate system. The coordinate of the facet centers

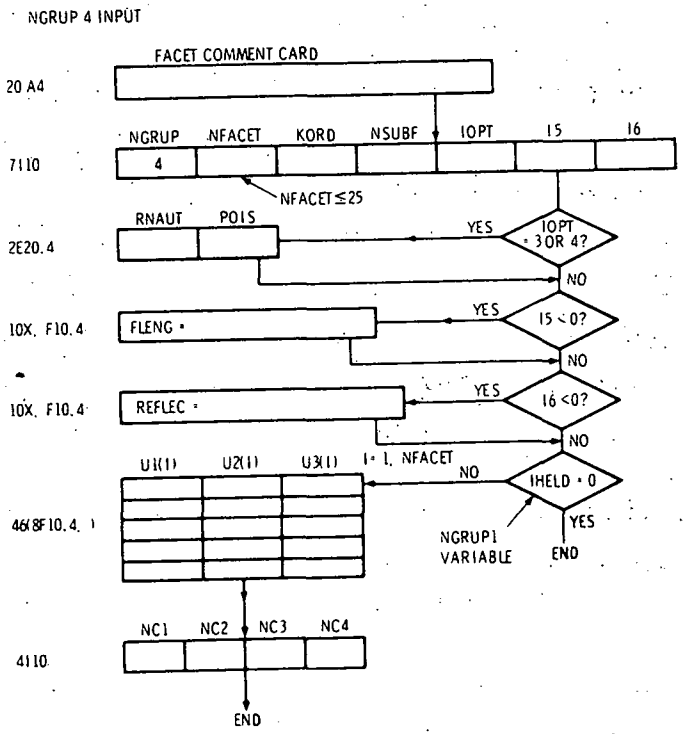

Figure 12. Group 4 input flow chart.

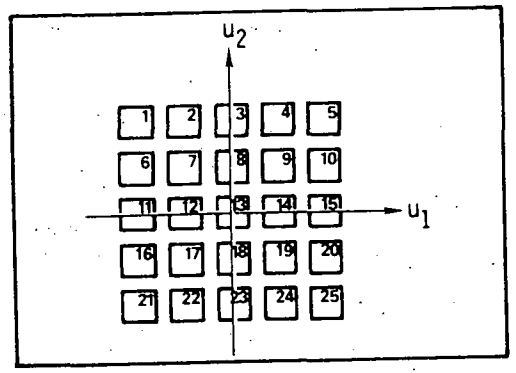

PLANE PROJECTION OF FACET ARRAY ON ONE HELIOSTAT

Figure 13.

are needed to properly locate each facet in space.

Heliostat parameters are furnished by the group 5 data in Figure 14. Heliostat identifying numbers, the number of heliostats to be treated, the prealignment strategy, and the emergency parameters are all input here. If a new heliostat distribution is to be input, its x, y, z coordinates are read here along with heliostat design parameters. These variables are shown in Figures 15-16.

The time-data input for group 6 are shown in Figure 17. Here the calculation times and prealignment time are specified.

Group 7 of the input gives the atmospheric data. The variables in Figure 18 specify the model atmosphere to be used when solar insolation is to be calculated. The pressure and temperature variables also have a slight effect on the solar refraction.

The appendix describes general program characteristics, limitations, running time, hardware and software requirements. An early version of the users manual is also available for greater detail (Ref. 1). Let us assume you are now convinced that HELIOS is easy to use. Is it reasonable to use? What real tests of the code are available for checking code accuracy?

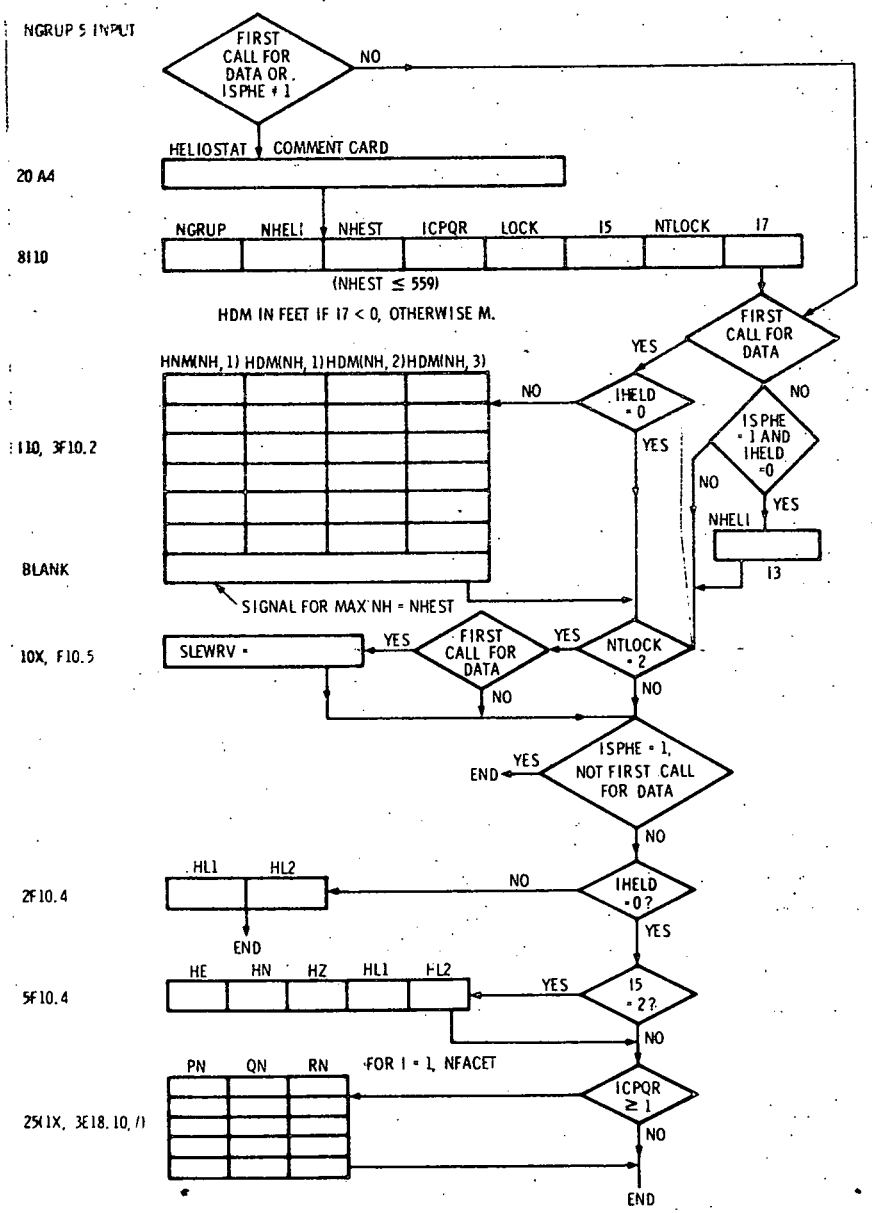

Figure 14. Group 5 input flow chart.

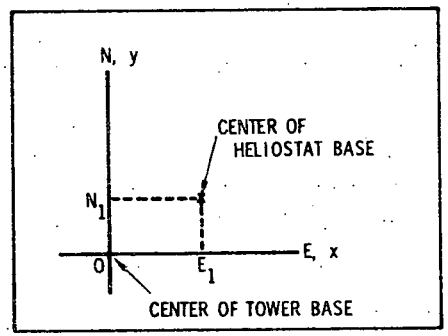

HELIOSTAT DEPLOYMENT IN TOWER COORDINATE SYSTEM

Figure 15. Heliostat deployment in Tower Coordinate System. x = HDM(NH,1), y = HDM(NH,2), z = HDM(NH,3).

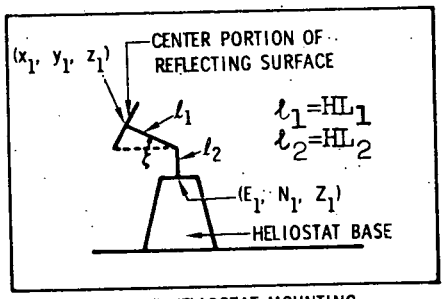

SAMPLE HELIOSTAT MOUNTING

Figure 16. Sample heliostat mounting.

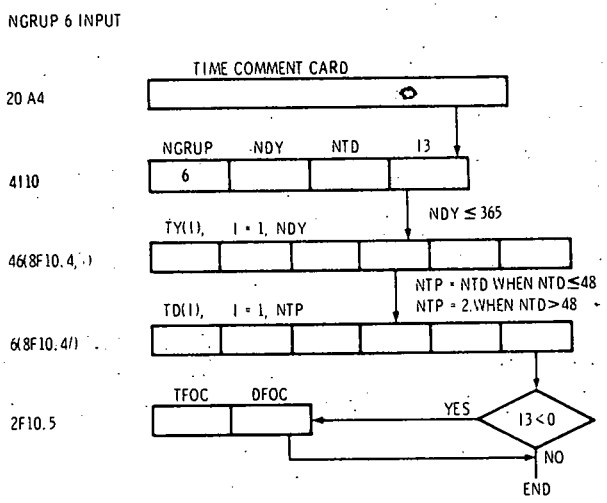

Figure 17. Group 6 input flow chart.

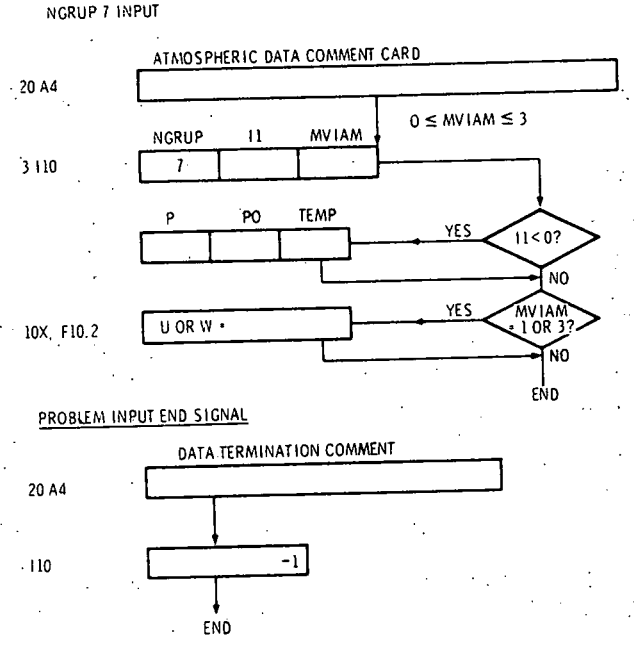

Figure 18. Group 7 input flow chart and end signal.

HELIOS CHECKS

Figure 19 summarizes the checks of HELIOS to date. Several verifications of the shape of the intensity pattern for a single mirror were made by Larryl Matthews. Shapes were checked near the saggital and tangential focal planes. Shape checks were also made for a few facets on a single heliostat in scale model experiments (Ref. 3). The shape of the energy flux pattern for a field of heliostats was verified by John Holmes.

CHECK POINTS FOR HELIOS

1. Scale model experiments for one heliostat by E. A. Igel, G. F. Bott, R. L. Hughes, April 1977.
2. MIRVAL computer code comparisons by J. D. Hankins ~ January 1977.
3. Comparisons with shape of hole in iron plate by John Holmes ~ May 1977.
4. Shape comparisons with image formed by 80" focal length spherical mirror by Larryl Matthews ~ April 1976.
5. Comparisons with Martin-Marietta data for one facet by W. Hart and C.N. Vittitoe ~ April 1977.

Future:

1. Comparison with measurements at Georgia Institute of Technology by B. G. Levi.
2. Comparison with measurements at the Solar Thermal Test Facility with concurrent measurement of incident sunshape.

Figure 19. Check points for HELIOS.

Magnitude and shape comparisons for the energy flux from one heliostat were reported by Joe Hankins to be consistent with his MIRVAL code. Magnitude and shape comparisons have also been made with experimental data collected by Martin Marietta for one facet. These data are given in Figures 20-21. Uncertainty in the sunshape and in the time of data collection suggest the agreement can be improved with more complete information. The sunshape used in the calculation is given in Figure 4. A larger error cone should improve the consistency shown here.

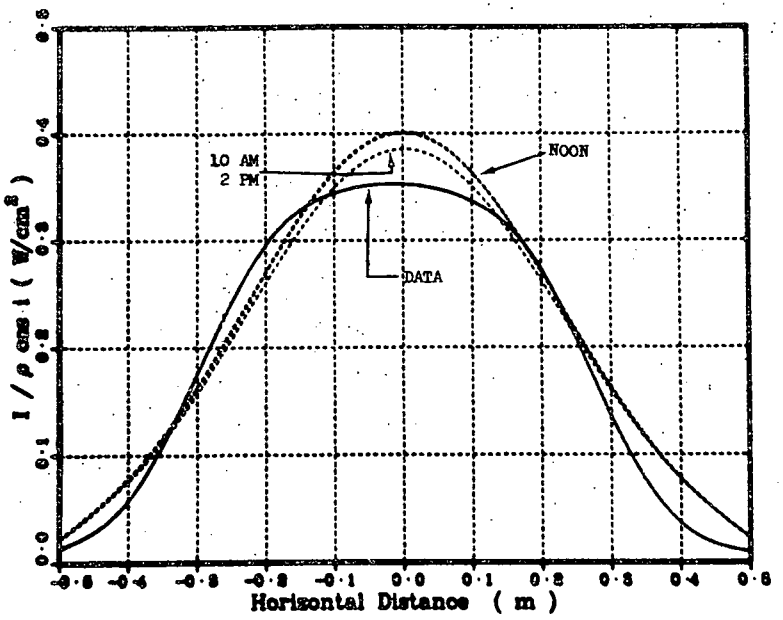

Target is 56.4 m along a line 34° to the east of south of the facet. Insolation is normalized to 0.08 W/cm². Latitude is 39.8° N as for Denver, Colorado. Target and facet heights are identical. The distance is horizontal distance across the target center. The planar target faces the facet.

Figure 20. Energy flux comparison with Martin Marietta data collected on November 23, 1976.

THE SHADOWING AND BLOCKING

One of the HELIOS options which is sometimes useful is the computer drawn plots indicating the extent of shadowing and blocking. The shadowing is illustrated by projecting the corners of each heliostat onto a plane through the tower base, orthogonal to the sun's central ray. An example was given in Figure 3. The blocking is given in Figure 22 as the projection of the corners of each heliostat onto a unit sphere with its origin at the center of the target aperture. The bar graphs at the bottom-left indicate the effective facet area (m^2) before and after shadowing and blocking. Other bar graphs give the power intercepted by the heliostats and the power incident upon the target aperture (in units of 10^5 W).

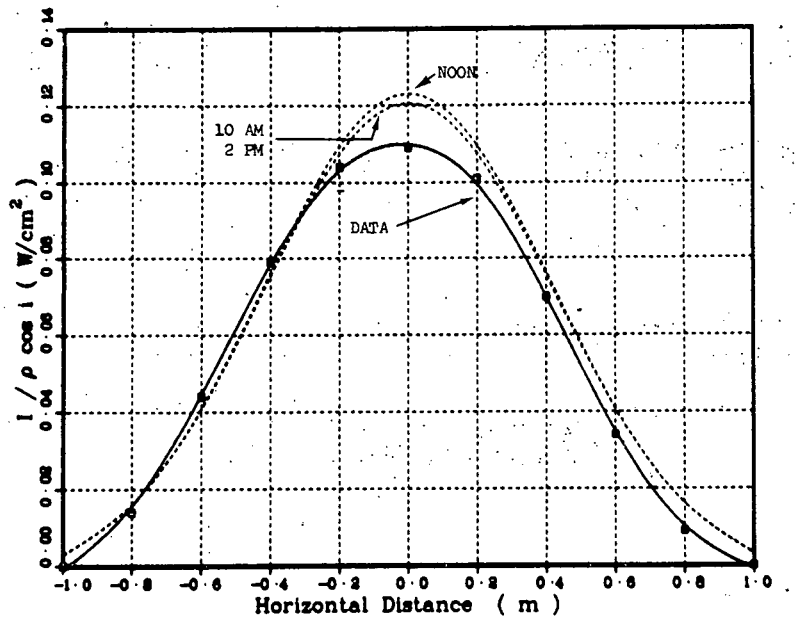

Target is 106.68 m along a line 34° to the east of south of the facet. Insolation is normalized to 0.08 W/cm^2. Latitude is 39.8° N as for Denver, Colorado. Target and facet heights are identical. The distance is horizontal distance across the target center. The planar target faces the facet.

Figure 21. Energy flux comparison with Martin Marietta data collected on September 28, 1976.

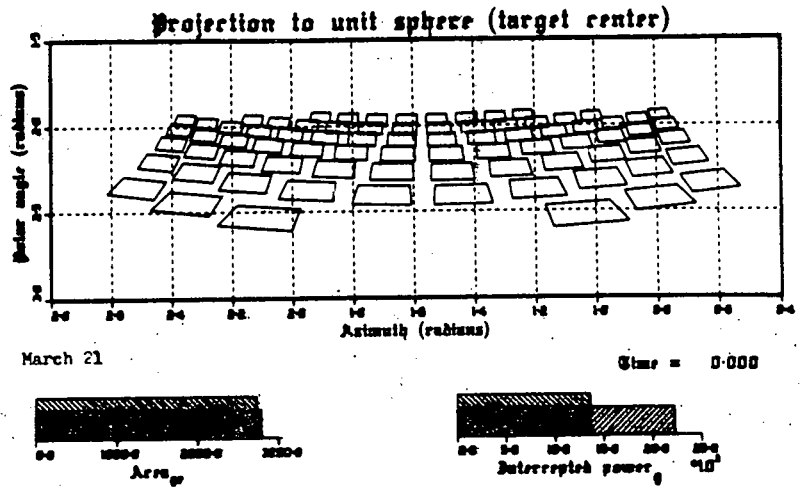

Figure 22. Blocking diagram.

ACKNOWLEDGEMENT

HELIOS has benefited from interactions with many individuals. Much of its flexibility resulted from discussions with J. T. Holmes, D. J. Kuehl, and L. K. Matthews of Sandia Laboratories. Extension to new heliostat deployments resulted from contact with B. G. Levi of Georgia Tech and with W. Hart and J. Williamson of Martin-Marietta. C. S. Hoyle of SLL furnished the subroutine giving the facet-shape that results from stress analysis. P. Van Delinder and W. C. Burd at SLA provided guidance through the early plotting pitfalls. Further benefits are expected from interactions at this workshop.

APPENDIX 1. HELIOS CODE SUMMARY

HELIOS purpose: The code was developed to evaluate proposed designs for central receiver solar energy collector systems, to perform safety calculations on the threat to personnel and to the facility itself, to determine how various input parameters alter the power collected, and to evaluate possible design trade-offs.

HELIOS structure: The code is designed with numerous subroutines for treating individual effects. This structure facilitates additions that have been necessary as special requirements appeared or as improvements became necessary. The additions also resulted in non-optimum code design which will likely remain for some time as effort remains concentrated upon additional options.

Mathematical method: The method for evaluating flux density is basically the cone-optics approach. Reflector surfaces are divided into small segments that are treated as infinitesimal mirrors that reflect a solar image onto the target surface.

HELIOS input: Input variables include atmospheric variables; sunshape parameters; coordinates for heliostat bases relative to the tower; heliostat design parameters, reflector shape information; data describing the uncertainty resulting from surface errors, suntracking errors, non-spectral reflection, and wind loading; focusing and alignment strategy; aim point coordinates; receiver design; calculation time; parameters indicating effects to be included; and the chosen output options.

HELIOS output: Three output options are available. The first gives the flux density (W/cm^2) produced by all the heliostats at the grid of target points. The power intercepted by the mirrors and that incident upon the target are given. The facet area reduced by the angle of incidence effect and the area further reduced by shadowing and blocking effects are given. These data are given for each designated calculation time.

The second output option yields the above output variables for each heliostat in addition to the total. The loss factor caused by light propagation between facet and receiver is also given for each heliostat.

The third output option is still more complex. It is especially useful for detailed examination of results for checking prior to a large computer run. It includes facet and heliostat alignment information, sun orientation, target point alignment information, and detailed shadowing and blocking information including lists of the blocked (shadowed) and blocking (shadowing) heliostats.

All the output options include (1) a table describing the built-in model of atmospheric mass as a function of apparent elevation angle of the sun, (2) a table describing the built-in model of atmospheric refraction as a function of solar elevation angle, (3) brief descriptions of the input data groups, (4) tabular distributions of the sunshape, the error cone, and the effective sunshape, (5) tower coordinates of each target point and the components of the unit vector normal to the target surface at each point in the grid, and (6) a listing of the main problem parameters. As a special output option, the three components of the energy flux density are available at each target point in the grid.

Present HELIOS limitations:

$1 \leq$ number of heliostats ≤ 559
$1 \leq$ number of facets/heliostat ≤ 25
$1 \leq$ number of target points ≤ 121

RELATED CODES:

BLOSH - movie generation for shadowing and blocking CDC-7600 15 s/frame for plot tape generation for moderate shadowing and blocking. About 50 s/frame for 222 heliostats in zones A-B of the Solar Thermal Test Facility for 4-5 PM on December 21.

CDC-6600 7 s/frame for post processing to obtain tape for microfiche generation of the DX4460 microfilm system.

PLO - plotting program for flux density distribution, shadowing and blocking diagrams, sunshape distribution, etc.

Running time: The required running time is highly dependent upon input options. It is dominated by the flux density calculation except at very late or early times when shadowing and blocking may be extensive. On CDC-7600 with perfect-focus option, the flux density calculation requires ~ 14.4 ms per facet for 121 target points. Zones A-B and A-C-D-E (222 heliostats) of the Solar Thermal Test Facility require 11 to 18 s for shadowing and blocking calculations as those effects reduce the effective mirror area by factors 0.99 to 0.81. Typical CDC 7600 run time for

222 heliostats with 25 facets/heliostat and 121 target points is 120 s including generation of the plot tape. These times should be multiplied by $\leq n^2$ if the facets are divided into a n x n mesh for more precise integration.

Computer hardware requirements: HELIOS is operational on the Sandia Laboratories CDC 6600 computer operating under Scope 3.3. The code requires 142,000 octal storage which may be reduced to 77,000 octal locations after the few seconds required for effective sunshape calculation. HELIOS is also operational on the Sandia Laboratories CDC 7600 under Scope 2.1.

Some auxiliary equipment are necessary. Printer - required; microfiche output - useful; punch - necessary for some options; auxiliary storage - necessary for recall of data temporarily on magnetic tape (disk).

Computer software requirements: The coding language is FORTRAN extended - version 4. Required subroutines from the Sandia Laboratories library that are not distributed by the computer manufacturer are:

FOURT - fast Fourier Transform

MINA - find minimum of a function

QNC7 - integration routine with checking routines ERRCHK, ONECHK, ERRPRT, ERXSET, and ERRGET.

SAXB - solve system of real linear algebraic equations with checking routines RFBS, RULD, and ERSTGT.

These routines are included on HELIOS program tapes. The routines are mentioned in the following reference.

R. E. Jones and C. B. Bailey, Brief Instructions for Using MATHLIB (Version 6.0), Sandia Laboratories Report SAND-75-0545, February 1976.

For CDC 6600 use, one other supplementary routine is available. The REDUCE subroutine allows reduction of the core storage by deletion of blank common that is no longer needed. REDUCE is written in COMPASS assembly language.

HELIOS status: The code is operational on CDC 6600 and CDC 7600 computers. Its evolution is still in progress.

Developer/Sponsor:

C. N. Vittitoe
F. Biggs
R. E. Lighthill
Theoretical Division 5231
Sandia Laboratories
Alb., New Mexico 87115

Central Receiver
Systems Branch
Div. of Solar Energy
Energy Research and Dev.
Administration
Washington, D.C. 20545

Documentation: C. N. Vittitoe, F. Biggs, and R. E. Lighthill, HELIOS: A Computer Program for Modeling the Solar Thermal Test Facility, A Users Guide, Sandia

Laboratories Report SAND-76-0346, March 1977, Second edition June 1977.

F. Biggs and C. N. Vittitoe, A Computational Model for Solar Concentrators, Sandia Laboratories Report SAND-76-0347, to be published.

Availability: HELIOS is available from the developers after the potential user obtains approval by the sponsor.

Date: HELIOS became operational in April 1976. The present version of the code was formed in August 1977.

REFERENCES

1. C. N. Vittitoe, F. Biggs, R. E. Lighthill, SAND-76-0346, HELIOS: A Computer Program for Modeling the Solar Thermal Test Facility. A Users Guide, June 1967.

2. F. Biggs and C. N. Vittitoe, SAND-76-0347, A Computational Model for Solar Concentrators, to be published.

3. E. A. Igel, G. F. Bott, R. L. Hughes, Sandia Laboratories Internal Memorandum, April 1977.

COMPUTER PROGRAM CONCEN FOR CALCULATION OF IRRADIATION OF SOLAR POWER CENTRAL RECEIVER

R. H. McFee

McDonnell Douglas Astronautics Company
Huntington Beach, CA 92647

ABSTRACT

Program CONCEN has been developed for the purpose of computing the flux density distribution, total incident and received instantaneous power, diurnal incident and received energy, and related quantities for a solar thermal power system consisting of an array of heliostat-supported mirrors and a central receiver, under a variety of conditions of insolation, mirror surface characteristics, and receiver geometry. Computation is accomplished by subdividing each mirror into 121 elements and summing element solar disk images at the receiver surface. Shading and blocking effects are treated by testing each element and setting its contribution to zero if shaded or blocked. Mirror surface effects are included by computing the slope variation of the element due to effects such as waviness, spherical curvature, deformation, and canting for focusing purposes. Any segment of the heliostat array can be selected, from a single heliostat to the entire array. Systematic or Monte Carlo random processing can be used as required. Output data include power contribution by heliostat array region, total power and energy figures, flux density table, and a flux density contour diagram.

INTRODUCTION

Program CONCEN was originally developed for the purpose of studying the effect of mirror surface irregularities on the performance of central-receiver solar power systems (Ref. 1). As the program developed, it has become more widely employed in the analysis of collector system performance (Ref. 2). At the present time, its purpose is to provide computation of flux density distribution on receiver surfaces, total incident power at the receiver location, total received power in the receiver aperture, fraction of power lost by shading and blocking, total diurnal energy incident and received, and several related quantities. The collector system includes a field of heliostats in an arbitrary array, any of four types of receiver configuration, and any arbitrarily-defined mirror surface shape. The program has been used as a tool in parametric studies, including error analyses, relative performance of different mirror geometries, safety considerations, and mirror focusing effectiveness.

ANALYTICAL APPROACH

The principal feature of the CONCEN program is the synthesis of the image from a heliostat mirror by the superposition and integration of circular sun images from elements of the mirror. Each mirror element behaves optically as a pinhole camera, forming a circular image that can be described in terms of the solar disk angular diameter and the slant range (see Fig. 1). The locations of the element images are referred to the plane normal to the line connecting the center of the heliostat mirror with the center reference point on the receiver (called the reflection-normal plane [RNP]), located at the receiver reference point. A grid of points on the receiver surface, at which flux density distribution is to be calculated, is then projected parallel to the reflected beam onto the RNP, where relations between grid points and image location and image flux density can be determined. The position of the element image on the RNP is related to the element location on the mirror and the orientation of the element normal with respect to the reference line. This orientation is influenced by mirror deviations caused by waviness, curvature, canting for focus, and structural deformations.

The loss of power due to shading and blocking of one mirror by adjacent mirrors is simply calculated by determining whether the element center lies within a shaded or blocked region of the mirror. If so, the element's contribution is assumed to be zero.

For heliostat arrays arranged in rectangular configurations, it is convenient to divide the array into cells in 11 rows and 11 columns. As the size of the array changes, the number of heliostats in each cell changes accordingly. Computation then is conducted with the cell arrangement. For some arrays it is desirable to trim out some of the cells.

With the large number of heliostats in the array, it becomes impractical to compute image positions for every element of every heliostat. Therefore, two approaches are employed to approximate the array performance. In one, the center heliostat is assumed to represent the performance of all heliostats in the cell. Every element on the heliostat is computed. The flux contributions are then multiplied by the number of heliostats in the cell. All cells which have not been trimmed are calculated to give the total array performance. In the other approach a Monte Carlo random sampling is used to approximate the whole array behavior. Individual elements are selected randomly from any heliostat in the array. By continuing to sample elements until the maximum flux density converges sufficiently, or until a maximum number of samples has been completed, the entire array performance is approximated. The latter approach has proven to be the more useful for analysis of full arrays of heliostats. For individual heliostat mirror performance, the systematic approach, where every element of the mirror is included, is more appropriate.

Solar position is determined by approximate ephemeris relations, given date, hour, and local latitude data. Insolation is computed by interpolation in an appropriate insolation versus sun elevation curve.

Tracking error is simulated by applying randomly a normal distribution of angular error to the orientation of each element, which is more convenient than requiring that all elements of a given mirror have the same tracking error.

Diurnal energy quantities are approximated by summing the power figures at equal time intervals from noon to sunset, then multiplying by two, times the time interval in hours, to give energy in watt hours. Annual energy figures may be determined by plotting the diurnal energy figures against date and integrating under the curve for a year.

In order to facilitate relative evaluation of collector performance, a contour diagram is prepared from the table of flux density distribution grid values by interpolation between adjacent rows and columns. The diagram is normalized at the peak flux density point for convenience. It appears in the printout along with

the tabular data.

ANALYSIS

Solar Position

The sun's angular position at any time is computed from the approximate ephemeris relations.

$$\alpha = \tan^{-1}\left[\frac{\sin h}{\cos h \sin L - \tan \delta \sin L}\right] \quad (1)$$

$$\epsilon = \sin^{-1}(\cos \delta \cos h \cos L + \sin \delta \sin L) \quad (2)$$

where:

α = solar azimuth angle

ϵ = solar elevation angle

h = hour angle = 15(12-H) deg

H = number of hours after midnight, solar time

δ = declination angle

$= \sin^{-1}(\sin 23° \sin(\frac{360D}{365.25}))$ deg.

D = number of days after vernal equinox

L = local latitude, deg.

For the purposes of this analysis, the fine corrections to describe the solar ephemeris precisely are not necessary, since the image positions are calculated relative to the nominal tracking line for each heliostat, and slight solar position errors would have a negligible effects.

Mirror-Receiver Geometry

The heliostats are assumed to be laid out in known locations on a horizontal plane. The geometry of the relations between a mirror on an az-el mount, incoming and outgoing beams, and the receiver is shown in Fig. 2. Ground coordinates are defined as x_o, y_o, z_o, with x_o directed south, y_o east, and z_o vertically upward. Mirror coordinates (az-el), x_m, y_m, z_m, are defined with x_m horizontal, y_m directed upward, and z_m parallel to the mirror normal. Coordinates associated with the incident rays, x_s, y_s, z_s, are taken to be x_s horizontal, y_s directed upward, z_s directed toward the sun. The reflected beam coordinates x_r, y_r, z_r, are defined with x_r horizontal, y_r directed upward, and z_r along the reflected beam toward the receiver.

The relations between ground coordinates and incident, reflected, and mirror coordinates are given in terms of their direction coefficients by:

$$\begin{Bmatrix} x_s \\ y_s \\ z_s \end{Bmatrix} = \begin{bmatrix} -\sin\alpha & \cos\alpha & 0 \\ -\cos\alpha \sin\epsilon & -\sin\alpha \sin\epsilon & \cos\epsilon \\ \cos\alpha \cos\epsilon & \sin\alpha \cos\epsilon & \sin\epsilon \end{bmatrix} \begin{Bmatrix} x_o \\ y_o \\ z_o \end{Bmatrix}, \quad (3)$$

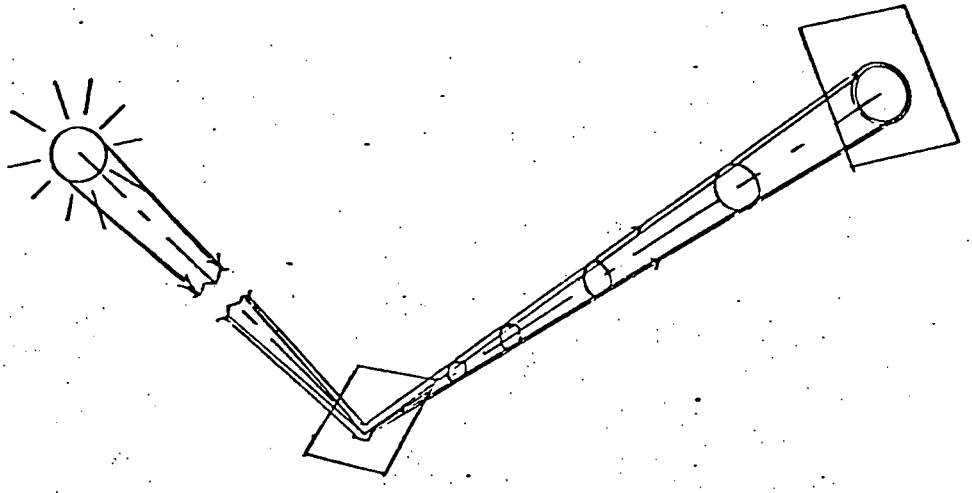

Figure 1. ELEMENT IMAGE FORMATION

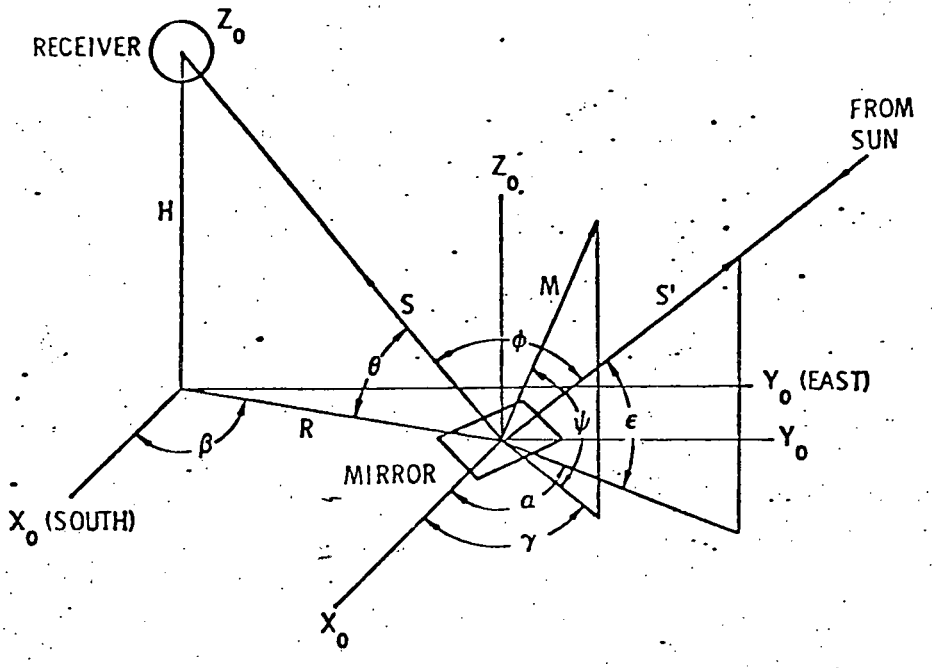

Figure 2. MIRROR-RECEIVER GEOMETRY

$$\begin{Bmatrix} x_r \\ y_r \\ z_r \end{Bmatrix} = \begin{bmatrix} \sin\beta & -\cos\beta & 0 \\ \cos\beta\sin\theta & \sin\beta\sin\theta & \cos\theta \\ -\cos\beta\cos\theta & -\sin\beta\cos\theta & \sin\theta \end{bmatrix} \begin{Bmatrix} x_o \\ y_o \\ z_o \end{Bmatrix}, \quad (4)$$

$$\begin{Bmatrix} x_m \\ y_m \\ z_m \end{Bmatrix} = \begin{bmatrix} -\sin\gamma & \cos\gamma & 0 \\ -\cos\gamma\sin\psi & -\sin\gamma\sin\psi & \cos\psi \\ \cos\gamma\cos\psi & \sin\gamma\cos\psi & \sin\psi \end{bmatrix} \begin{Bmatrix} x_o \\ y_o \\ z_o \end{Bmatrix}, \quad (5)$$

where:

β = mirror location angle from receiver base,
θ = receiver elevation angle from mirror,
γ = azimuth angle of mirror normal,
ψ = elevation of angle of mirror normal.

From the reflection law

$$M = \frac{S + S'}{2\cos(\phi/2)}, \quad (6)$$

where:

ϕ = angle between incident and reflected beams
$= \cos^{-1}(S \cdot S')$
$= \cos^{-1}(\sin\varepsilon\sin\theta - \cos\varepsilon\cos\theta\cos(\alpha-\beta))$ (7)
M = unit vector normal to the mirror surface
S = unit vector toward the receiver
S' = unit vector toward the sun

From Equations (3), (4), (5)

$$S' = \cos\alpha\cos\varepsilon\hat{i}_o + \sin\alpha\cos\varepsilon\hat{j}_o + \sin\varepsilon\hat{k}_o \quad (8)$$

$$S = -\cos\beta\cos\theta\hat{i}_o - \sin\beta\cos\theta\hat{j}_o + \sin\theta\hat{k}_o \quad (9)$$

$$M = \cos\gamma\cos\psi\hat{i}_o + \sin\gamma\cos\psi\hat{j}_o + \sin\psi\hat{k}_o \quad (10)$$

where $\hat{i}_o$, $\hat{j}_o$, $\hat{k}_o$ are unit vectors along the x_o, y_o, z_o axes.

With Equation (6)

$$M = \frac{1}{2\cos(\phi/2)}\left((\cos\alpha\cos\varepsilon - \cos\beta\cos\theta)\hat{i}_o + (\sin\alpha\cos\varepsilon - \sin\beta\cos\theta)\hat{j}_o + (\sin\varepsilon + \sin\theta)\hat{k}_o\right)$$

Equating direction cosines and solving for γ and ψ,

$$\gamma = \tan^{-1}\left[\frac{\cos\varepsilon\sin\alpha - \cos\theta\sin\beta}{\cos\varepsilon\cos\alpha - \cos\theta\cos\beta}\right] \quad (11)$$

$$\psi = \sin^{-1}\left[\frac{\sin\varepsilon + \sin\theta}{2\cos(\phi/2)}\right] \quad (12)$$

Image Position on Reflection-Normal Plane

The location of the center of the disk image from a mirror element on the RNP is given by:

$$x_n = x_r + S_r(\delta_{mx} + \delta_{trx})$$
$$y_n = y_r + S_r(\delta_{my} + \delta_{try}) \quad (13)$$

where:

S_r = slant range from mirror to receiver

x_n, y_n = coordinates of image center on RNP

x_r, y_r = RNP coordinates of mirror element center

δ_{mx}, δ_{my} = angular components of element slope deviation

$\delta_{trx}, \delta_{try}$ = angular components of tracking error

In terms of mirror coordinates, x_r, y_r can be determined by inverting Equation (5) and substituting in Equation (4).

$$x_r = \cos(\beta-\gamma)x_m - \sin\psi \sin(\beta-\gamma)y_m$$

$$y_r = \sin\theta \sin(\beta-\gamma)x_m + (\cos\theta \cos\psi - \sin\theta \sin\psi \cos(\beta-\gamma))y_m \quad (14)$$

The effect of the angular deviation of the element surface orientation may be derived from the reflection law (Equation 6). At any instant S′ is constant, and, for small changes in M,

$$dS = \sqrt{\delta_{mx}^2+\delta_{my}^2} = 2\,(S\cdot M)dM - 2(S\cdot dM)M \quad (15)$$

Since $M = k_m$, $dM = \delta_x \hat{i}_m + \delta_y \hat{j}_m$

where $\hat{i}_m$, $\hat{j}_m$, $\hat{k}_m$ are unit vectors along the x_m, y_m, z_m axes.

δ_x, δ_y = components of element angular deviation in mirror coordinates.

By referring all quantities to RNP coordinates, the slope deviation components can be determined as

$$\delta_{mx} = 2\delta_x(\cos\theta \cos\psi - \sin\theta \sin\psi \cos(\beta-\gamma)) - 2\delta_y \sin\theta \sin(\beta-\psi) \quad (16)$$

$$\delta_{my} = 2\delta_x \sin\psi \sin(\beta-\gamma) - 2\delta_y \cos(\beta-\theta)$$

Then Equation (13) becomes:

$$x_n = -\cos(\beta-\gamma)x_m - \sin\psi \sin(\beta-\gamma)y_m + S_r(2\delta_x(\cos\theta \cos\psi - \sin\theta \sin\psi \cos(\beta-\gamma)) - 2\delta_y \sin\theta \sin(\beta-\gamma) + \delta_{trx})$$

$$y_n = \sin\theta \sin(\beta-\gamma)x_m + (\cos\theta \cos\psi - \sin\theta \sin\psi \cos(\beta-\gamma))y_m + S_r(2\delta_x \sin\psi \sin(\beta-\gamma) - 2\delta_y\cos(\beta-\gamma) + \delta_{try}) \quad (17)$$

The element angular deviation components, δ_x, δ_y, are made up of several subcomponents due to as many different causes. Thus

$$\delta_x = \delta_{wx} + \delta_{cx} + \delta_{sx} + \delta_{slewx} + \delta_{Tx} + \delta_{Gx} + \delta_{Bx}$$

$$\delta_y = \delta_{xy} + \delta_{cy} + \delta_{sy} + \delta_{slewy} + \delta_{Ty} + \delta_{Gy} + \delta_{By} \quad (18)$$

where:

δ_{wx}, δ_{wy} = waviness components
δ_{cx}, δ_{cy} = spherical curvature components
δ_{sx}, δ_{sy} = focus canting components
$\delta_{slewx}, \delta_{slewy}$ = heliostat slewing components
δ_{Tx}, δ_{Ty} = temperature deformation components
δ_{Gx}, δ_{Gy} = gravity deformation components
δ_{Bx}, δ_{By} = wind load deformation components

Shading and Blocking

With the close proximity between neighboring mirrors in an efficient array under some solar position and mirror locations, loss of effective mirror area occurs by shading of one mirror by others and by blocking the reflected rays from one mirror by others. Since, in a large array, the orientation of one mirror is almost identical to that of its nearest neighbors, the shadows and blockage projections are the same size and orientation as the mirror itself, when viewed on the mirror plane. The positions of the projections vary with the mirror, receiver, and sun locations. It is necessary to consider the possible shading or blocking by each of the nearest neighboring mirrors. This is done by determining which, if any, mirror elements fall within the shadow or blockage from any neighbors. Those elements that are shaded or blocked then are assumed to contribute zero flux to the receiver. The geometry of the shading and blocking situation is shown in Fig. 3.

By expressing mirror coordinates in terms of incident coordinates, for shading, and RNP coordinates, for blocking, the shadow and blockage center positions on the mirror surface may be determined. The shadow positions, x_{ms}, y_{ms}, z_{ms}, are given by:

$$\begin{Bmatrix} x_{ms} \\ y_{ms} \end{Bmatrix} = \begin{bmatrix} \cos(\alpha-\gamma), & -\sin\varepsilon \sin(\alpha-\gamma), & \cos\varepsilon \sin(\alpha-\gamma) \\ \sin\psi \sin(\alpha-\gamma), & \sin\varepsilon \sin\psi\cos(\alpha-\gamma) + \cos\varepsilon \cos\psi, & \\ -\cos\varepsilon \sin\psi \cos(\alpha-\theta) + \sin\varepsilon \cos\psi & & \end{bmatrix} \cdot \begin{Bmatrix} -\sin\alpha x_{ho} + \cos\alpha y_{ho} \\ \sin\theta(\cos\beta x_{ho} + \sin\beta y_{ho}) \\ -\cos\theta(\cos\beta x_{ho} + \sin\beta y_{ho}) \\ -\frac{\cos\psi}{\cos(\phi/2)} (\cos\gamma x_{ho} + \sin\gamma y_{ho}) \end{Bmatrix} \quad (19)$$

and the blockage center positions, x_{mb}, y_{mb}, by

$$\begin{Bmatrix} x_{mb} \\ y_{mb} \end{Bmatrix} = \begin{bmatrix} -\cos(\beta-\gamma), & \sin\theta \sin(\beta-\gamma), & -\cos\theta \sin(\beta-\gamma) \\ -\sin\psi \sin(\beta-\gamma), & -\sin\theta \sin\psi \cos(\beta-\gamma) & \\ +\cos\theta \cos\psi, & \cos\theta \sin\psi \cos(\beta-\gamma) + \sin\theta \cos & \end{bmatrix}$$

$$\cdot\left\{\begin{array}{l}\sin\beta x_{ho} - \cos\beta y_{ho} \\ \sin\theta(\cos\beta x_{ho} + \sin\beta y_{ho}) \\ -\cos\theta(\cos\beta x_{ho} + \sin\beta y_{ho}) - \dfrac{\cos\psi}{\cos(\phi/2)} \\ \cdot(\cos\gamma x_{ho} + \sin\gamma y_{ho})\end{array}\right\} \quad (20)$$

Mirror Focusing

For some types of receiver where it is desirable to concentrate the reflected flux to pass through a small aperture, it is advantageous to shape the mirror surface to provide some focusing action. It is apparent that, even with ideal focusing, the smallest image that can be produced from a single mirror is a disk of diameter equal to the angular diameter of the sun (9.3 mr) times the slant range from mirror to receiver. Ideal focusing can be obtained by shaping the mirror to conform to a section of a paraboloid whose axis is along the line from the receiver to the sun. As the sun changes location, the paraboloid changes accordingly, as does the section representing the mirror surface.

To determine the slope departure components relative to the average mirror normal, it is only necessary to set the image position components on the RNP equal to zero and solve for the deviation angles as functions of the mirror coordinates. This is done with Equation (17), setting the tracking error to zero. The slope deviation components, δ_{sx},δ_{sy}, required for focus are then

$$\begin{aligned}\delta_{sx} = \frac{1}{2S_r\cos(\phi/2)}\,(&-\cos(\beta-\gamma)(\cos(\beta-\gamma)x_m \\ &- \sin\psi\,\sin(\beta-\gamma)y_m) - \sin\theta\,\sin(\beta-\gamma) \\ &(\sin\theta\,\sin(\beta-\gamma)x_m + (\cos\theta\,\cos\psi - \sin\theta\,\sin\psi \\ &\cos(\beta-\gamma))y_m\end{aligned} \quad (21)$$

$$\begin{aligned}\delta_{sy} = \frac{1}{2S_r\cos(\phi/2)}\,(&-\sin\psi\,\sin(\beta-\gamma)(\cos(\beta-\gamma)x_m \\ &- \sin\psi\,\sin(\beta-\gamma)y_m - (\cos\theta\,\cos\psi \\ &- \sin\theta\,\sin\psi\,\cos(\beta-\gamma))(\sin\theta\,\sin(\beta-\gamma)x_m \\ &+ (\cos\theta\,\cos\psi - \sin\theta\,\sin\psi\,\cos(\beta-\gamma))y_m\end{aligned}$$

Image Irradiance

The total flux in the image from each element is equal to the product of the direct insolation at the mirror, $\dot{q}$, the element area, A_e, the cosine of the incident angle, $\cos(\phi/2)$, the mirror reflectance, ρ, and the transmission of the atmospheric path between mirror and receiver, T_a.

$$\Phi_e = \dot{q}A_e\cos(\phi/2)\rho T_a \quad (22)$$

The flux density in the element image on the RNP, as a function of the distance from the image center, r, is

$$E_e = \frac{\Phi_e}{\pi r_s^2} F_{ld}(r) \quad (23)$$

where r_s = radius of solar image.
$= 4.65 \times 10^{-3} S_r$

The solar limb darkening factor, F_{ld}, is given by the empirical relation (Ref. 3)

$$F_{ld}(r) = \begin{cases} 1.23(0.44 + 0.56\sqrt{1 - \frac{r^2}{r_s^2}} & (r \leq r_s) \\ 0 & (r > r_s) \end{cases} \quad (24)$$

The image irradiance on the receiver surface, E_{rece}, is then

$$E_{rece} = E_e \cos \omega_{rec} \quad (25)$$

where ω_{rec} = angle of incidence on receiver surface.

The flux density at a particular point on the receiver surface is determined by locating the point's projection along the reflected ray to the RNP. The projection is then referred in position to the location of the image center on the RNP, and E_e is determined from Equation (23). The projection geometry depends on the receiver configuration. An external cylinder receiver geometry is shown in Fig. 4. Projection coordinates are obtained by rotating the receiver surface coordinates into the RNP coordinates.

To obtain the total received power onto a receiver, the fraction of each element image which falls within the projected boundaries of the receiver is calculated and summed. The geometry of the situation is shown in Fig. 5 for an external cylinder receiver and a rectangular aperture cavity receiver. The projection of the cylinder is independent of azimuth angle, and may be approximated by a rectangle of equivalent area. The projection of the cavity aperture is a parallelogram whose shape is related to azimuth, elevations, and cavity tilt angles. By determining the intersections of the circular image with the receiver projection sides by means of simultaneous equation solution, the fraction, F_i, of the image inside the receiver boundaries can be calculated. The total received power in the receiver aperture is then given by:

$$\Phi = \sum_{jk} F_{ijk} \Phi_{ejk} \quad (26)$$

COMPUTER PROGRAM

The approach used in Program CONCEN for the computation of power and energy quantities may be followed by reference to the flow chart shown in Fig's 6 thru 9.

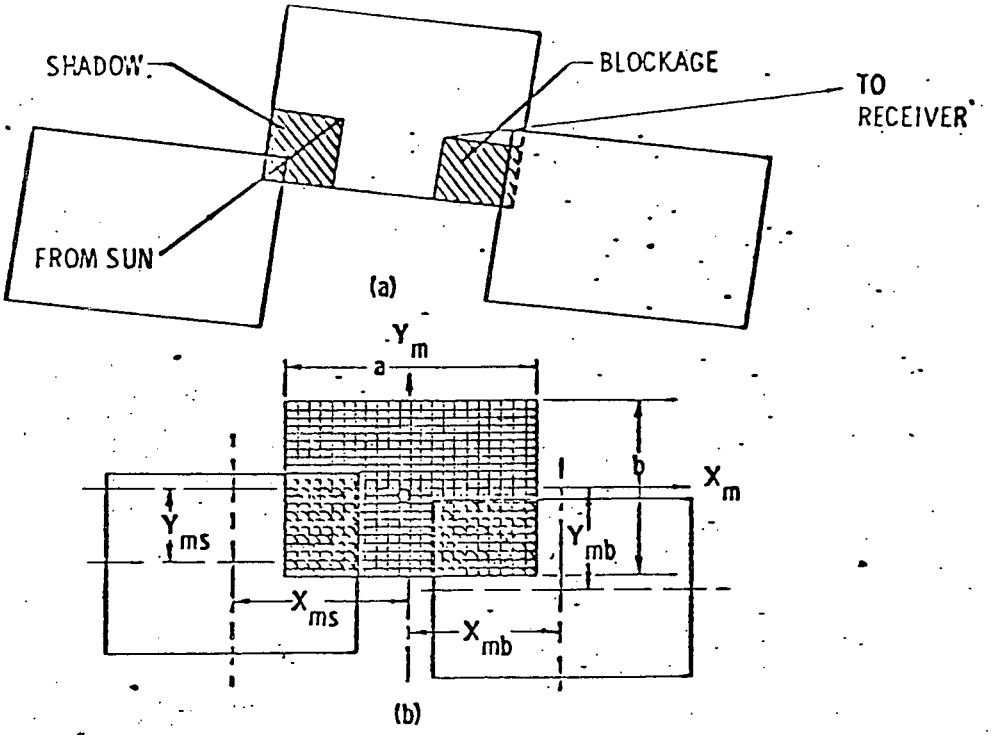

Figure 3. SHADING AND BLOCKING GEOMETRY

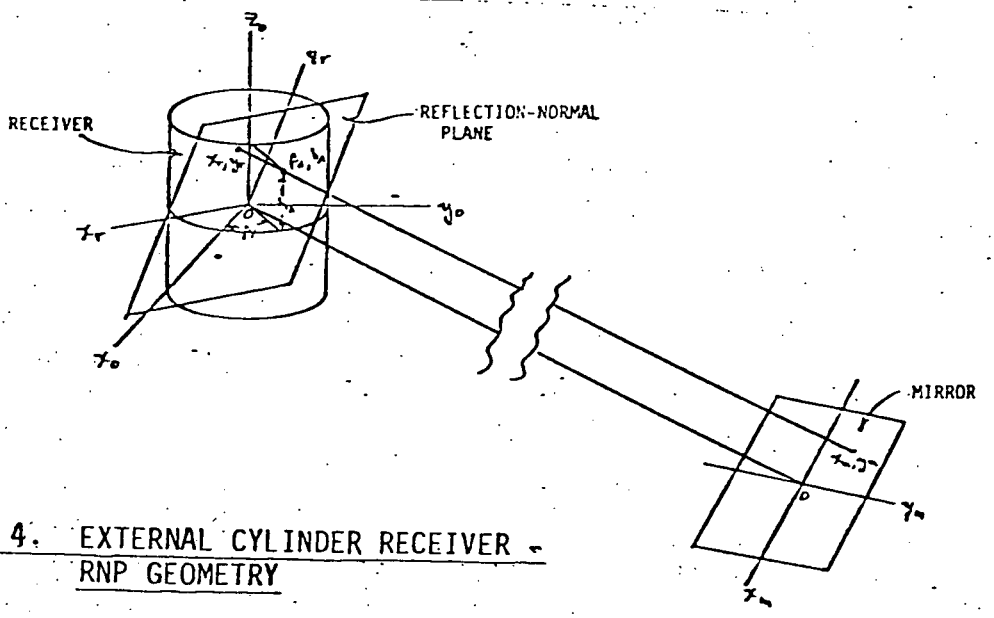

Figure 4. EXTERNAL CYLINDER RECEIVER - RNP GEOMETRY

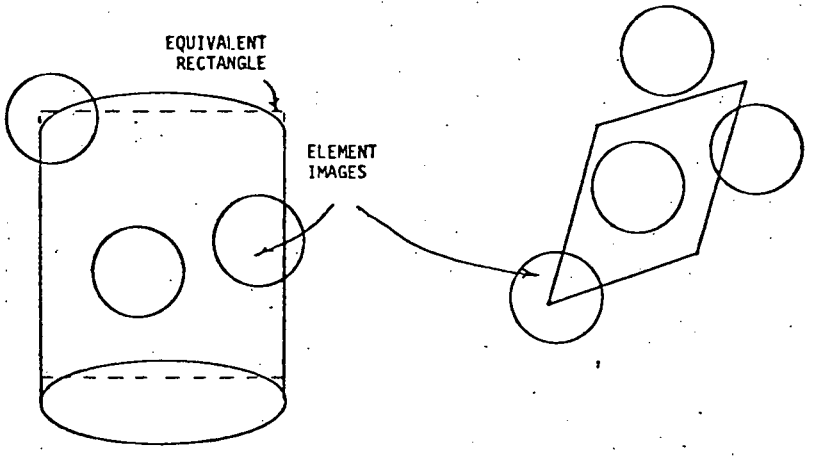

Figure 5. POWER INCLUSION GEOMETRY

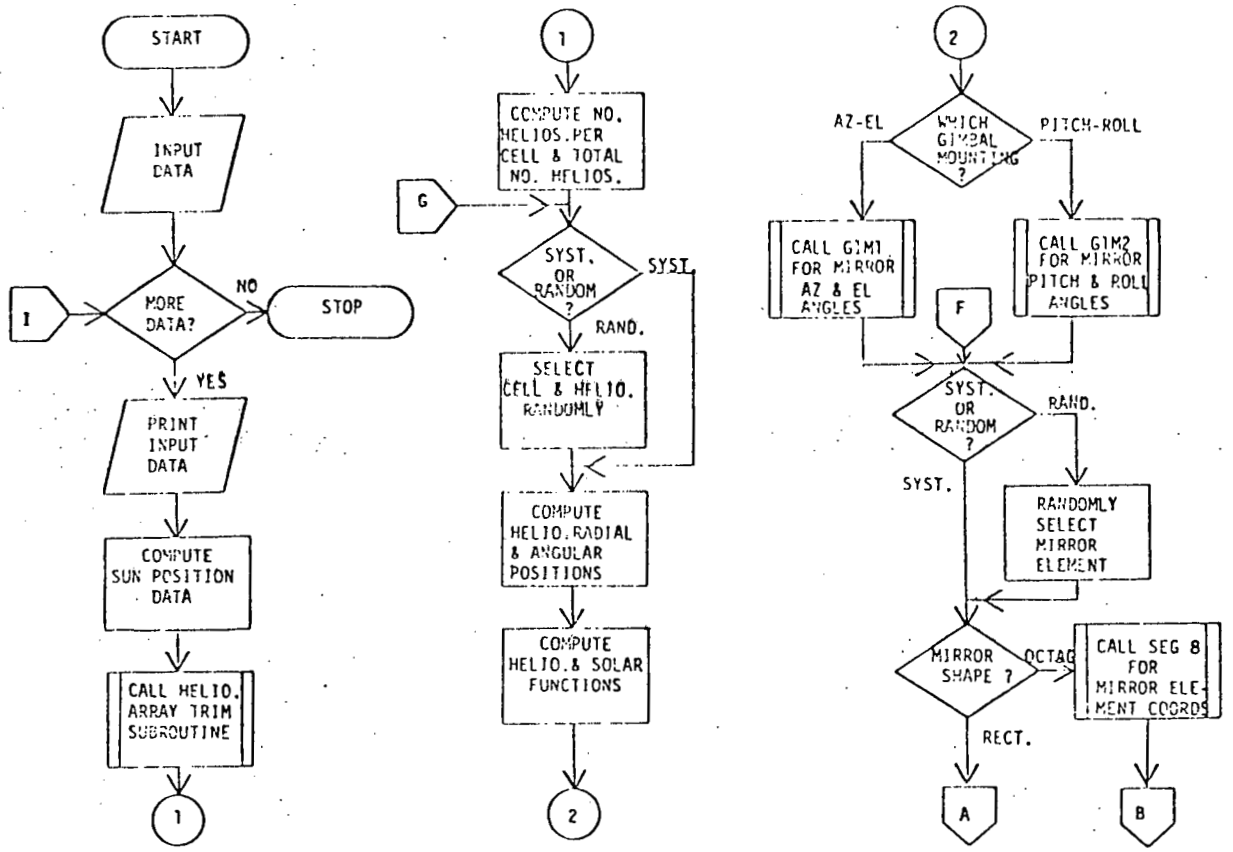

Figure 6. PROGRAM CONCEN FLOW CHART - 1

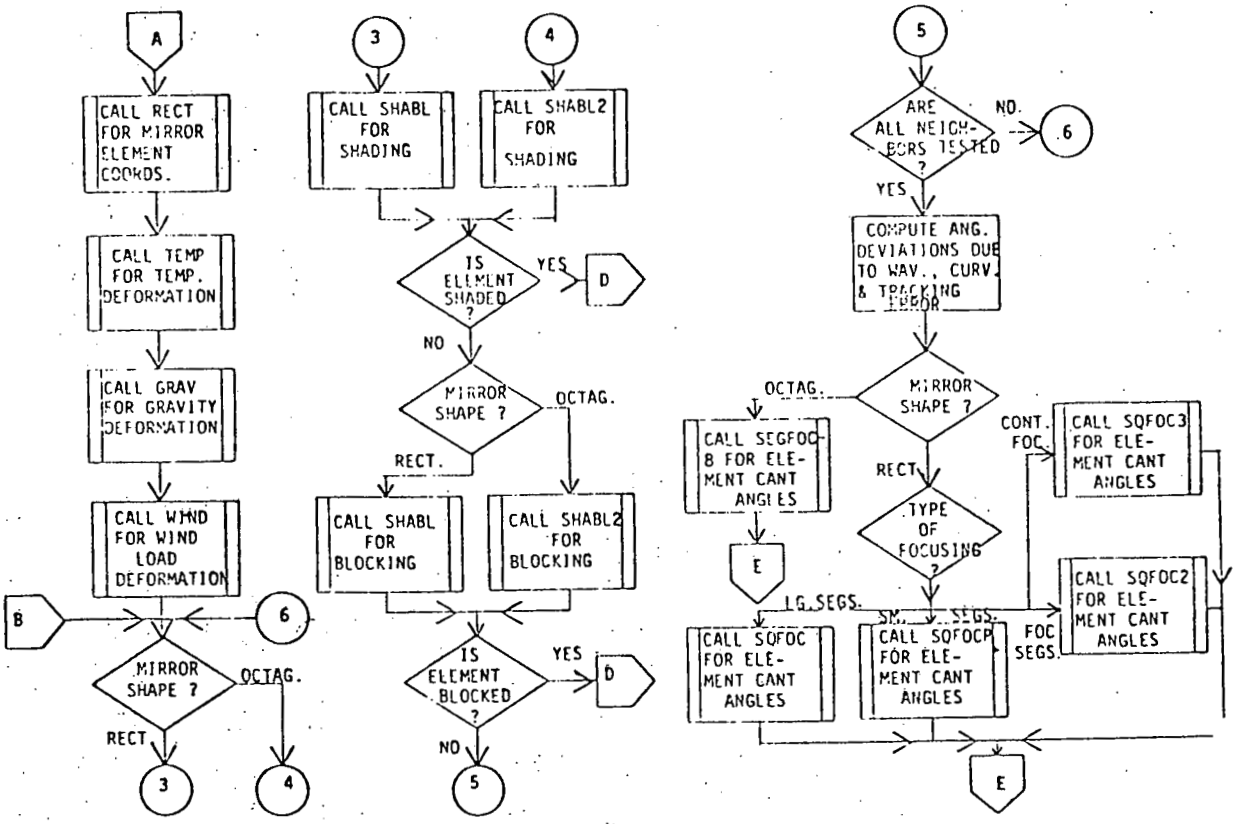

Figure 7. PROGRAM CONCEN FLOW CHART - 2

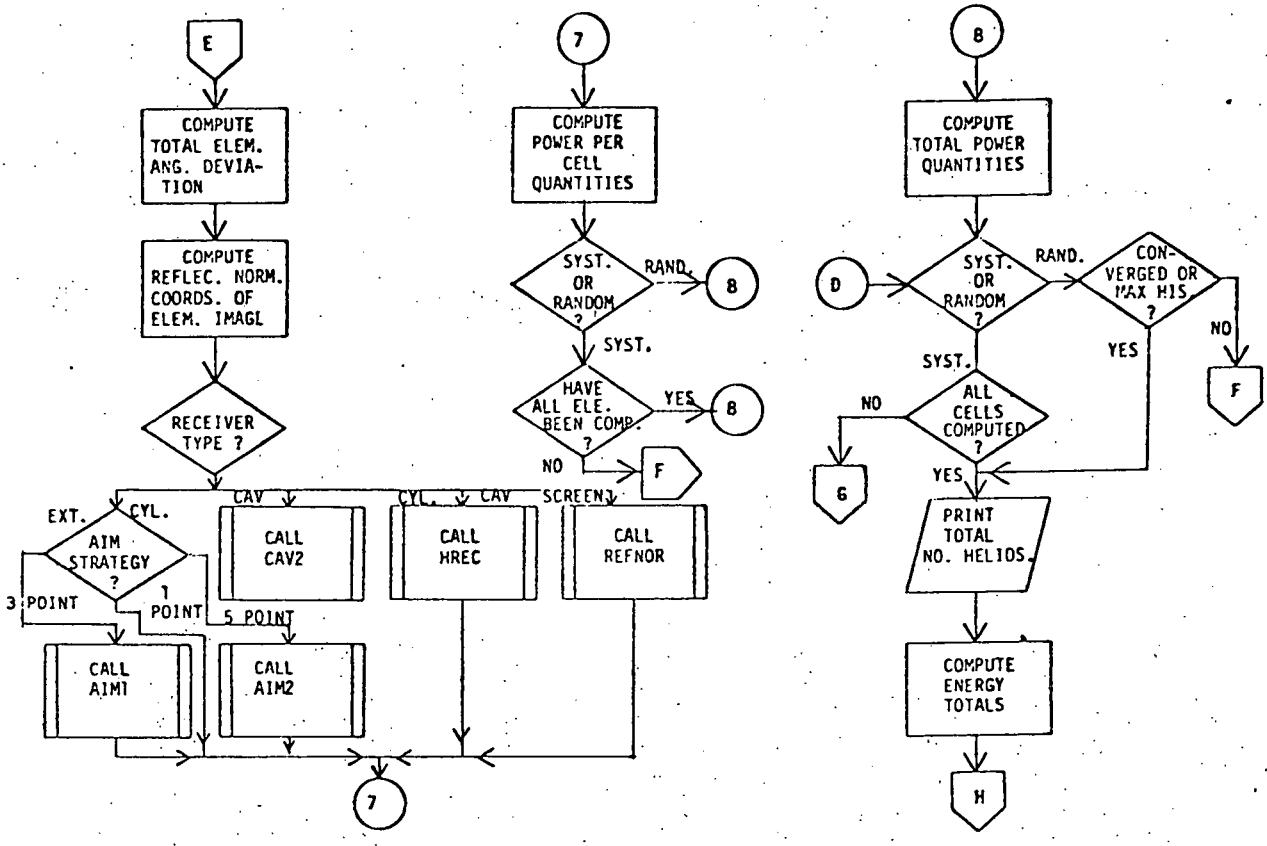

Figure 8. PROGRAM CONCEN FLOW CHART - 3

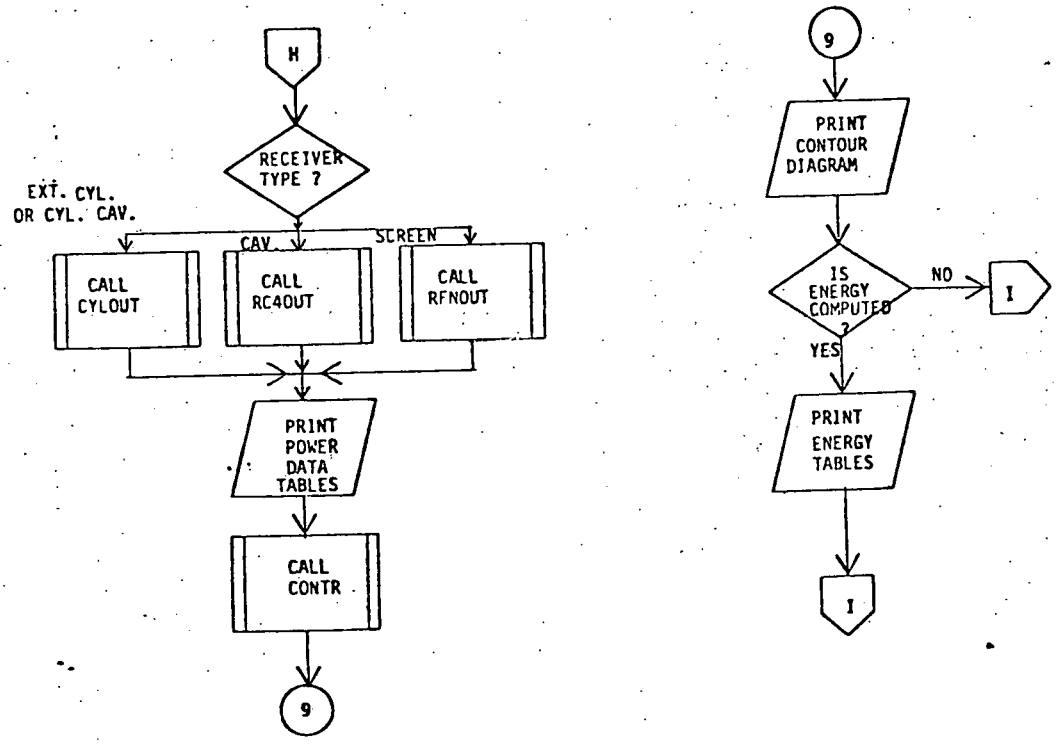

Figure 9. PROGRAM CONCEN FLOW CHART - 4

Subroutines are used for the following computations:

1. Trim unused cells from heliostat array
2. Gimbal angles
3. Shadow and blockage center positions
4. Mirror element coordinates
5. Temperature, gravity, and wind load deformation
6. Shading and blocking logic
7. Cant angles for segment focusing
8. Receiver surface flux density distribution
9. Cylindrical receiver aim strategy
10. Print output tables and other data
11. Print contour diagram

Multiple subroutines are provided where alternate functions are required. Two gimbal arrangements, two mirror configurations, four receiver designs, and four focusing approaches are included in the present program.

Both systematic and random Monte Carlo processing methods are available. Where the heliostat array is subdivided into 121 cells, the computation is looped 121 times for the systematic approach. For each cell the center mirror elements are processed by loops within the cell loops. For random processing, the elements are looped once, while the randomly-selected element, heliostat, and cell numbers are looped until the desired convergency is obtained, or until a pre-determined maximum number of histories (typically 5000-10,000) has been completed. Where a single heliostat is examined, systematic processing of all elements on the mirror is used.

Diurnal and annual energy figures are computed by summing power figures at intervals during the day, for diurnal energy, and integrating under the curve of diurnal energy versus date, for annual energy.

The output of the computation may be varied to suit the requirements, with appropriate switches to turn off flux density computation, data heading, etc. Typically, a run to determine total received power and flux density distribution on a receiver surface will consist of the following items in the printout.

1. Input data dump
2. Input data listing
3. 11 x 11 array listing fractions of power lost by shading and blocking and incident angle cosine for each cell
4. Total incident power and total power received by receiver
5. 11 x 11 array listing average power redirected and average power received by receiver per heliostat for each cell
6. 21 x 21 array listing flux density values at 441 point grid on receiver surface

7. Contour point diagram, derived from flux density table, giving contours in tenths of peak flux density.
8. Number of histories, and relative error, if random processing is used.

An example of a contour diagram of the flux density distribution on a screen from a single rectangular heliostat is shown in Fig. 10. The expected parallelogram shape is demonstrated, with the rounded corners due to the sun's disk shape.

PROGRAM EXTENSION

With the flexibility of the basic CONCEN program, it is possible to extend computation to several other receiver configurations, heliostat arrays, and gimbal mounts. An alternate gimbal mount arrangement, called pitch-roll, is already in the program, as is a cylindrical cavity receiver. Several heliostat arrays have been accommodated by minor changes in the program. A variety of special receiver configuration subroutines have been developed, including a generalized flat-walled cavity, cruciform, star-shape, and spherical receivers.

Using the elemental image numerical integration technique, a versatile and flexible analytical tool has been developed which can be applied to a great variety of solar power system design problems.

REFERENCES:

1. R. H. McFee, "Power Collection Reduction by Mirror Surface Non-Flatness and Tracking Error for a Central Receiver Solar Power System," Applied Optics, 14, 1493 (1975).
2. R. H. McFee, "Optical Systems for Large Scale Solar Power Plants," Proc. Electro-Optics/International Laser 1975 Conference, 1976.
3. J. C. Brandt and P. W. Hodge, "Solar System Astrophysics," McGraw-Hill, 1964, p. 58.

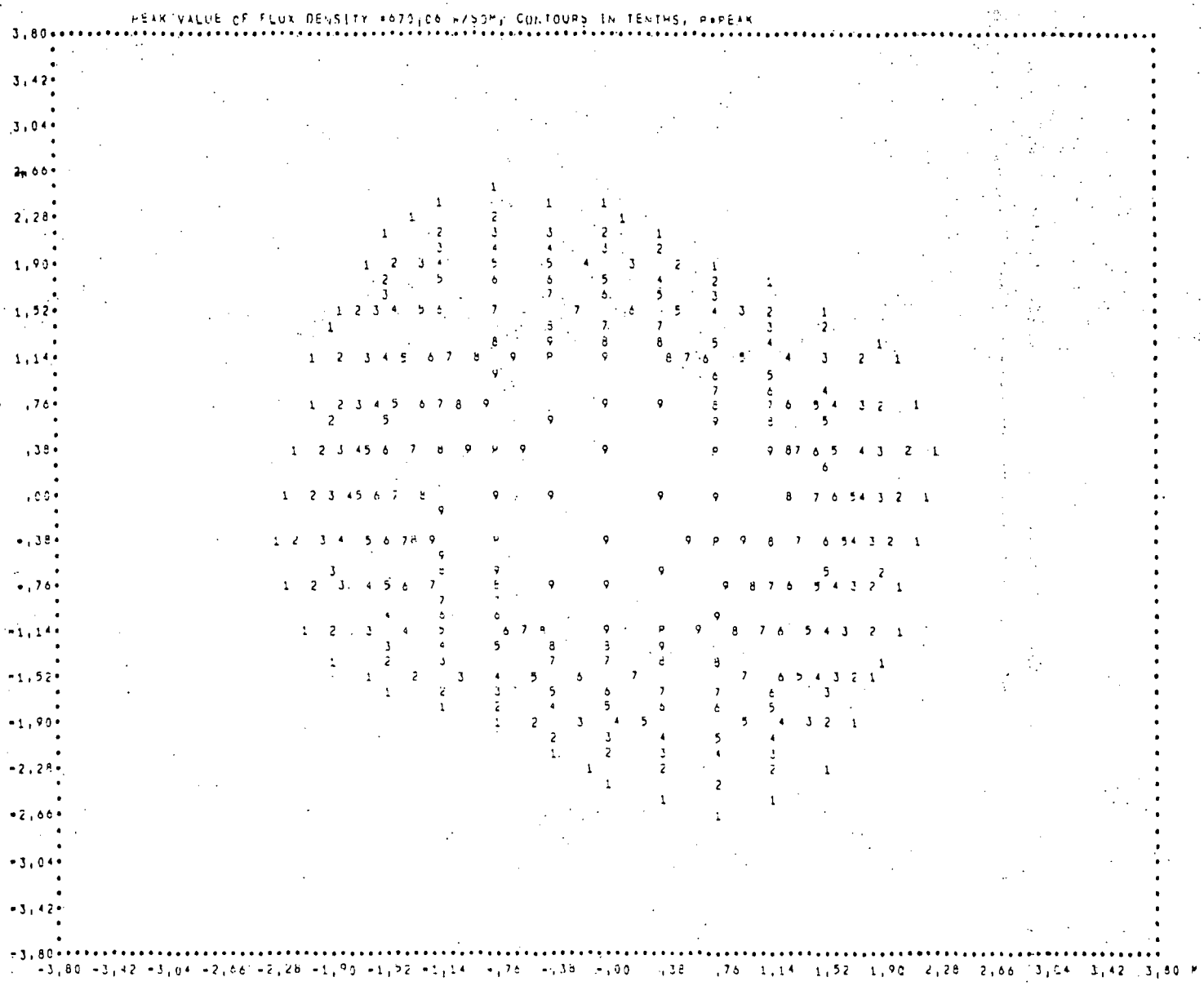

Figure 10. FLUX DENSITY CONTOUR DIAGRAM ON SCREEN FROM SINGLE HELIOSTAT

HASCM - A PROGRAM FOR CALCULATING THE PERFORMANCE OF A HELIOSTAT FIELD

Mark Rubeck
Solar Energy Systems Analyst
Boeing Engineering & Construction
Seattle, Washington

ABSTRACT

The Heliostat Array Simulation Computer Model (HASCM) was developed by Boeing to aid in the design and evaluation of the heliostat field in solar thermal electric power generating facility. The program accepts as input the dimensions and performance characteristics of the heliostats and the receiver. It takes into account the relative geometries of the various elements, as well as the efficiencies of the system components, to arrive at the heliostat field performance for a given design point time and location. The program uses a finite element method to compute field performance. It averages the performance of several reflected rays to arrive at an efficiency for a portion of the reflector. It then averages the portion efficiencies to compute the performance of a given heliostat.

This paper will present a list of the input options and variables available to the user. It will then describe the model itself, including the assumptions and algorithms which are utilized in computing field performance. Information will also be provided relating to the operation of the program. The capabilities of the model will be explained in more detail by presenting typical output and examining the role of this data in the determination of optimum heliostat design and overall field configuration.

INTRODUCTION

The Heliostat Array Simulation Computer Model was originally written in 1974 to support studies Boeing was conducting for the Electric Power Research Institute. It was rewritten in 1976 to conduct analyses of the collector subsystem as part of the Energy Research & Development Administration $10MW_e$ Pilot

Plant preliminary design effort.

A sketch of the heliostat designed by Boeing is shown in Figure 1. The key feature of this heliostat is its metallized plastic membrane reflector, stretched across a circular ring, housed in a protective enclosure of transparent plastic. The necessity of analyzing the performance of such a heliostat had a major influence on the methodology of this computer model.

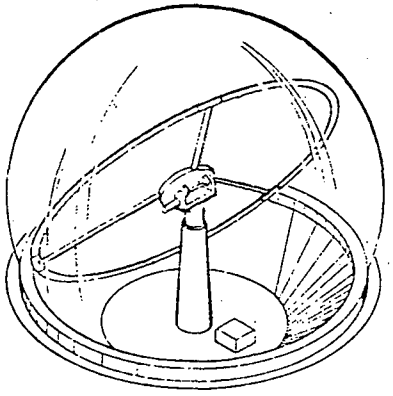

Figure 1: Boeing Heliostat Design

INPUT OPTIONS AND VARIABLES

The inputs to HASCM can be grouped into five major categories. There are those which refer to the heliostats, the receiver, the heliostat field layout, the design point (or point of evaluation), and the grid definition variables.

Several options are available in describing the heliostats. The mirrors can be square or round, and of any size. They can be flat, gravity focused, or mechanically focused. Gravity focusing affects membrane reflectors whose gravity caused deflection, and therefore focal length, varies as a function of the reflector elevation angle. Mechanically focused reflectors are of two types. Fixed focused reflectors keep their focal length constant, while "smart" focused reflectors vary their focal length throughout the day so as to minimize off-axis aberration, and therefore minimize overflow losses at the receiver.

The aiming error of the heliostat is assumed to be normally distributed in both the elevation and azimuth axes. So the only inputs needed are the standard deviation of the distribution in each axis. The surface irregularity of the mirror is also assumed to be normally distributed, and its standard deviation is an input.

The reflectivity of the mirror is another variable. The model considers reflectivity as a function of the incidence angle of the incoming light with the mirror surface. Material properties of the reflector cause its reflectivity to vary with this incidence angle.

The point to which the heliostat is to direct the reflected light, its aim point, is also an input to the model.

The program has the capability to analyze heliostat fields of enclosed, or domed, heliostats. In this case, the size of the dome and the transmissivity of the dome material are inputs. As with reflectivity, transmissivity is considered as a function of incidence angle with the incoming and reflected direct insolation. The effect of incidence angle is more pronounced in this case, than with reflectivity, as normal and highly obtuse transmissivity differ substantially.

In order to examine the performance of the heliostat field when used in conjunction with various receiver designs, the model provides several receiver geometries to choose from. A cylindrical surface receiver, annular aperture cavity receiver, rectangular aperture cavity receiver, and circular aperture cavity receiver are all modelled. The inputs relating to these four receivers are as follows: cylinder - altitude, radius, absorptivity versus incidence angle; annular aperture-aperture radius, height, slope; rectangular aperture - aperture height and width; circular aperture - aperture radius. The azimuth and elevation angles of the rectangular and circular aperture are also variable. The aperture can face any direction and be tilted at any angle from vertical to downward facing.

The field is assumed to be square with the receiver tower at its center. The heliostats are arranged in a North-South, East-West rectangular grid pattern. The field is described by its width, the receiver height, and the center-to-center spacing of the heliostats in the North-South and East-West directions.

The design point, or point at which the field performance is to be evaluated, consists of three variables: the site latitude, the solar declination angle (which corresponds to the date), and the time.

The final category of inputs are the grid definition variables. Since the program analyzes large numbers of elements by examining the performance of a few, it is necessary to specify exactly how many will be considered. The heliostat field is analyzed by dividing it into sections, the number of which is a variable. In addition, each section can have a different mirror size, heliostat spacing, and mirror aim point. The reflectors are also modelled as a grid of elements, again a variable. Finally, the cone of reflected light from each mirror element is examined by looking at a square grid of rays within this cone.

THE MODEL

The Heliostat Array Simulation Computer Model is broken into several subroutines, each performing a part of the total heliostat field analysis. A top level flow chart of the program is presented in Figure 2. A brief description of each of these subroutines follows.

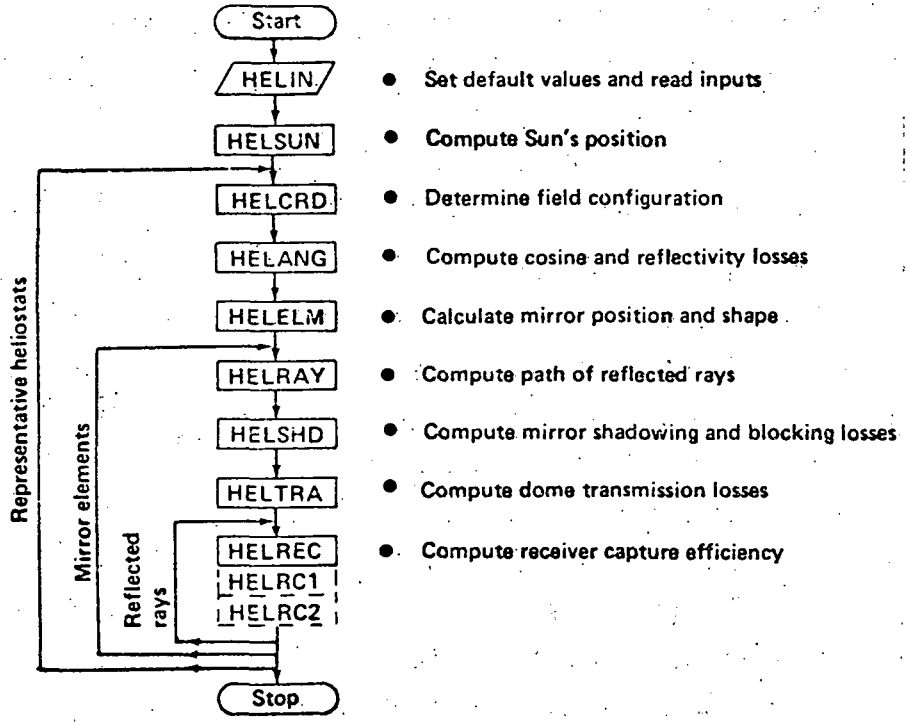

Figure 2: HASCM Subroutines

HELIN reads and writes the values of the input variables. It first sets the default values of these variables. It then makes any necessary changes to the default conditions as indicated in the input deck. The resultant list of inputs is then printed out.

HELSUN calculates the coordinates of the sun relative to the heliostat field. The latitude, date, and time at the power plant are used to determine the elevation angle of the sun above the horizon and the azimuth angle of the sun from South. These values provide the information necessary to compute the coordinates of the sun in a 3-dimensional coordinate system centered at the heliostat field. This system regards South as positive x, West as positive y, and up as positive z.

HELCRD determines the configuration of the heliostat field. First, the field is analytically divided into a square grid. The input values for field width and number of grid sections are used to compute the location, in the heliostat field coordinate system, of the central or representative heliostat in each field section. The performance calculated for this heliostat will be used to typify the performance of every heliostat in that field section. Values of heliostat center-to-center spacing in the North-South and East-West directions allow the program to compute the total heliostat area and number of heliostats in each field section. These values, combined with the performance

of the representative heliostats, will be used to derive the performance of every field section.

HELANG calculates mirror cosine and reflectivity losses. The coordinates of the representative heliostat center, the center of the solar disk, and the aim point are combined to yield the unit normal vector to the mirror center. This allows computation of the incidence angle of the incoming specular insolation with the mirror surface. The cosine of this angle is the fraction of the mirror area which is perpendicular to the insolation. The incidence angle is used to find the mirror reflectivity in a table look-up procedure.

HELELM calculates mirror position and shape. The previously computed mirror unit normal yields values for mirror azimuth and elevation angles. The radius of curvature of the mirror is computed as a function of its focusing strategy: flat, gravity focused, or mechanically focused. The mirror is analytically partitioned into a square grid and the unit normal to each of these mirror elements is computed. A random number generator is coupled with a normal distribution function to give values for mirror surface smoothness and aiming error in both azimuth and elevation. These are used to modify the values for mirror element unit normals. An aiming error is assigned to each element on the mirror to represent the fact that every mirror in the field section has a different aiming error.

HELRAY takes the mirror element unit normals and the sun's position to arrive at the reflected ray from each element. It also calls the remaining subroutines, which calculate shadowing, blocking, transmission, and overflow losses for each mirror element. It averages these element efficiencies over the entire mirror and combines this with reflectivity and cosine losses to compute representative mirror efficiency.

HELSHD calculates mirror efficiency with regards to shadowing and blocking by surrounding mirrors. It considers the eight mirrors which surround a representative heliostat. The incoming and reflected ray from every mirror element is tested to see if it is shadowed or blocked, i.e., if it intersects a surrounding mirror.

HELTRA is called only if the heliostats being evaluated have protective dome enclosures. It calculates energy lost due to light passage through the dome of the representative heliostat or through the dome of a surrounding heliostat. It tests not only for intersection of incoming and reflected light with a dome;

but computes the angle of incidence of the intersection, and accesses a table look-up function to arrive at transmissivity as a function of incidence angle. This subroutine will handle light rays which pass through more than one dome.

HELREC calculates the fraction of reflected energy captured by a cylindrical surface receiver. Until now the program has assumed the sun to be a point source of light. In order to accurately model the reflected image, accounting for the width of the sun, the insolation reflected from a mirror element is treated as a cone of light. A grid is overlaid on the circular cross section of the cone to determine the reflected rays to be examined. Each ray is tested for intersection with the receiver. The incidence angle of the intersection is calculated and table look-up gives absorptivity for a given incidence angle. The efficiency of the rays reflected from an element are averaged to give an element's receiver capture efficiency.

If the receiver being considered is a cavity receiver with a planar aperture (square or circular) then HELRC1 rather than HELREC, will calculate the fraction of reflected energy captured by the receiver. It is similar to HELREC but doesn't require absorptivity versus incidence angle considerations. HELRC2 is called when the power plant has a cavity receiver with an annular aperture.

OPERATORS INFORMATION

The Heliostat Array Simulation Computer Model is coded in standard IBM FORTRAN IV language using EBCDIC card format, compatible with IBM 360/370 computer systems. The program consists of about 1200 cards (including comments) and is totally self-contained in batch execution, with two exceptions. A random number generator function and its initialization subroutine are both part of the system software. A user would have to change these instructions to access his own system software. Otherwise, the program uses only standard FORTRAN instructions, and conversion to other computer systems would not be difficult.

Central Processing Unit run time for FORTRAN compilation is five seconds and for LINKEDIT is one second. Execution time is input dependent, relating mainly to the number of field sections, mirror elements, and reflected rays used in each case. A typical case takes about seven CPU seconds and requires five pages of output.

PROGRAM OUTPUT

The output from each case begins with a listing of the inputs and their definitions. This is followed by the elevation and azimuth angles of the sun for the latitude, day, and time specified in the inputs. The remainder of the output is a table of performance for the representative heliostats. It includes mirror radius (or half side length for square mirrors), spacing, aim point (height on z axis), representative heliostat coordinates, mirror azimuth angle, mirror elevation angle, and heliostat efficiency for each field section. It also prints the number of heliostats and total reflector area in each section. Figures 3 and 4 are the first two pages of a typical output. These outputs are for a single set of inputs. Several input cases can be contained in the input deck and the program will run each case separately and print the outputs for each.

APPLICATIONS

HASCM is used in conducting parametric studies to aid in the determination of preferred heliostat design. Heliostat dimensions and characteristics, such as mirror size, aiming error, and focusing strategy can be studied by inputting different values for them into HASCM. Combining the results with cost data will allow selection of a cost-optimum design.

As an example, refer to Figure 5. The first graph shows that as reflector diameter increases, the number of heliostats needed to meet the thermal requirement of the receiver decreases. This is because each heliostat is delivering more energy to the receiver. But if these larger heliostats suffer greater overflow losses, the total required reflector area will be greater. So going to bigger heliostats reduces per unit costs, such as control electronics, but increases per area costs, such as mirrors. A cost study, shown in the second graph, takes into account the relative weight of these costs. When the performance and cost data are combined, the third graph results. From this, a cost-optimum design point can be selected.

Another application of HASCM is the determination of heliostat field configuration. In this case, the output from HASCM serves as input to the Field Layout Optimization Program (FLOP). As seen in Figure 6, HASCM computes heliostat efficiencies, number of heliostats, and effective heliostat area (total reflector area times efficiency) for each field section. FLOP takes this data, along with the specular insolation and the receiver thermal requirement to determine

```
FOCUS  =    0                  = 0 PLASTIC MEMBRANE, GRAVITY FOCUSSED
                               = 1 MECHANICALLY FOCUSSED
                               = 2 FLAT

MIRROR =    0                  = 0 CIRCULAR
                               = 1 SQUARE

RCVR   =    0                  = 0 CYLINDRICAL SURFACE RECEIVER
                               = 1 ANNULAR APERTURE RECEIVER
                               = 2 RECTANGULAR APERTURE RECEIVER
                               = 3 CIRCULAR APERTURE RECEIVER

DELTA  =     0.0     DEGREES   DECLINATION
L      =    34.90    DEGREES   NORTH LATITUDE
H      =     0.0     DEGREES   HOURS AFTER NOON TIMES FIFTEEN
W      =   800.00    METERS    FIELD WIDTH
N      =     8.                NUMBER OF FIELD SECTION ROWS
NE     =     5.                NUMBER OF MIRROR ELEMENT ROWS
ASIGAZ =     0.00200 RADIANS   STANDARD DEVIATION OF AIMING ERROR IN THE AZIMUTH
ASIGEL =     0.00200 RADIANS   STANDARD DEVIATION OF AIMING ERROR IN THE ELEVATION
SSIGT  =     0.0     RADIANS   STANDARD DEVIATION OF MIRROR SURFACE ERROR
NR     =     3.                NUMBER OF SOLAR WIDTH CIRCLE ROWS
HT     =    80.00    METERS    HEIGHT OF RECEIVER CENTER
R      =     3.50    METERS    RECEIVER RADIUS
ALT    =    12.50    METERS    RECEIVER HEIGHT
RATIO  =     0.920             RATIO OF MIRROR RADIUS TO DOME RADIUS (RATIO = 0. MEANS NO DOMES)

INANG  =  0.0    10.000  20.000  30.000  40.000  50.000  60.000  70.000  80.000  90.000   INCIDENCE ANGLE
REF    =  0.886  0.908   0.919   0.930   0.932   0.935   0.935   0.935   0.935   0.935    MIRROR REFLECTIVITY
TRANS  =  0.874  0.871   0.869   0.864   0.854   0.831   0.803   0.700   0.506   0.0      DOME TRANSMISSIVITY
ABZ    =  1.000  1.000   1.000   1.000   1.000   1.000   1.000   0.770   0.530   0.300    RECEIVER ABSORPTIVITY

* * * * * * * * * * * * * * * * * * * * * * * * * * * * * * * * * * * * * * * * * * * *

I                          FIELD SECTION ROW
J                          FIELD SECTION COLUMN
S                  METERS  MIRROR RADIUS
DNS                METERS  CENTER-TO-CENTER NORTH-SOUTH HELIOSTAT SPACING
DEW                METERS  CENTER-TO-CENTER EAST-WEST HELIOSTAT SPACING
AP                 METERS  HEIGHT OF AIM POINT
XM                 METERS  REPRESENTATIVE HELIOSTAT X-COORDINATE (WHERE WEST IS POSITIVE)
YM                 METERS  REPRESENTATIVE HELIOSTAT Y-COORDINATE (WHERE SOUTH IS POSITIVE)
AMSEC              SQ METERS TOTAL MIRROR AREA
NUM                        NUMBER OF HELIOSTATS
PHI                DEGREES MIRROR AZIMUTH ANGLE
PSI                DEGREES MIRROR ELEVATION ANGLE
MEFF                       HELIOSTAT EFFICIENCY

* * * * * * * * * * * * * * * * * * * * * * * * * * * * * * * * * * * * * * * * * * * *

ALPHA  =    55.10    DEGREES   SOLAR ELEVATION ANGLE
Z      =     0.0     DEGREES   SOLAR AZIMUTH ANGLE
```

Figure 3: Sample Output

I	J	[illegible]	DNS	DEW	AP	XM	YM	AMSEC	NUM	PHI	PSI	MEFF
1	1	3.93	15.00	10.00	80.57	-350.00	350.00	3234.77	66.67	100.27	53.88	0.34
1	2	3.93	15.00	10.00	80.66	-250.00	350.00	3234.77	66.67	111.81	58.25	0.26
1	3	3.93	15.00	10.00	80.74	-150.00	350.00	3234.77	66.67	130.42	63.51	0.26
1	4	3.93	15.00	10.00	80.80	-50.00	350.00	3234.77	66.67	160.73	67.93	0.28
1	5	3.93	15.00	10.00	80.80	50.00	350.00	3234.77	66.67	-160.73	67.93	0.28
1	6	3.93	15.00	10.00	80.74	150.00	350.00	3234.77	66.67	-130.42	63.51	0.26
1	7	3.93	15.00	10.00	80.66	250.00	350.00	3234.77	66.67	-111.81	58.25	0.25
1	8	3.93	15.00	10.00	80.57	350.00	350.00	3234.77	66.67	-100.27	53.88	0.33
2	1	3.93	15.00	10.00	80.66	-350.00	250.00	3234.77	66.67	90.01	51.18	0.38
2	2	3.93	15.00	10.00	80.80	-250.00	250.00	3234.77	66.67	99.76	55.83	0.36
2	3	3.93	15.00	10.00	80.97	-150.00	250.00	3234.77	66.67	117.32	62.51	0.34
2	4	3.93	15.00	10.00	81.11	-50.00	250.00	3234.77	66.67	152.88	69.65	0.38
2	5	3.93	15.00	10.00	81.11	50.00	250.00	3234.77	66.67	-152.88	69.65	0.38
2	6	3.93	15.00	10.00	80.97	150.00	250.00	3234.77	66.67	-117.32	62.51	0.34
2	7	3.93	15.00	10.00	80.80	250.00	250.00	3234.77	66.67	-99.76	55.83	0.38
2	8	3.93	15.00	10.00	80.66	350.00	250.00	3234.77	66.67	-90.01	51.18	0.38
3	1	3.93	15.00	10.00	80.74	-350.00	150.00	3234.77	66.67	78.34	47.89	0.29
3	2	3.93	15.00	10.00	80.97	-250.00	150.00	3234.77	66.67	84.85	52.27	0.37
3	3	3.93	15.00	10.00	81.34	-150.00	150.00	3234.77	66.67	97.90	60.03	0.44
3	4	3.93	15.00	10.00	81.81	-50.00	150.00	3234.77	66.67	134.52	72.50	0.45
3	5	3.93	15.00	10.00	81.81	50.00	150.00	3234.77	66.67	-134.52	72.50	0.45
3	6	3.93	15.00	10.00	81.34	150.00	150.00	3234.77	66.67	-97.90	60.03	0.42
3	7	3.93	15.00	10.00	80.97	250.00	150.00	3234.77	66.67	-84.85	52.27	0.37
3	8	3.93	15.00	10.00	80.74	350.00	150.00	3234.77	66.67	-78.34	47.89	0.29
4	1	3.93	15.00	10.00	80.80	-350.00	50.00	3234.77	66.67	65.84	44.24	0.18
4	2	3.93	15.00	10.00	81.11	-250.00	50.00	3234.77	66.67	67.73	47.58	0.25
4	3	3.93	15.00	10.00	81.81	-150.00	50.00	3234.77	66.67	71.28	54.55	0.41
4	4	3.93	15.00	10.00	84.17	-50.00	50.00	3234.77	66.67	77.39	73.04	0.55

Figure 4: Sample Output

the optimized field layout.

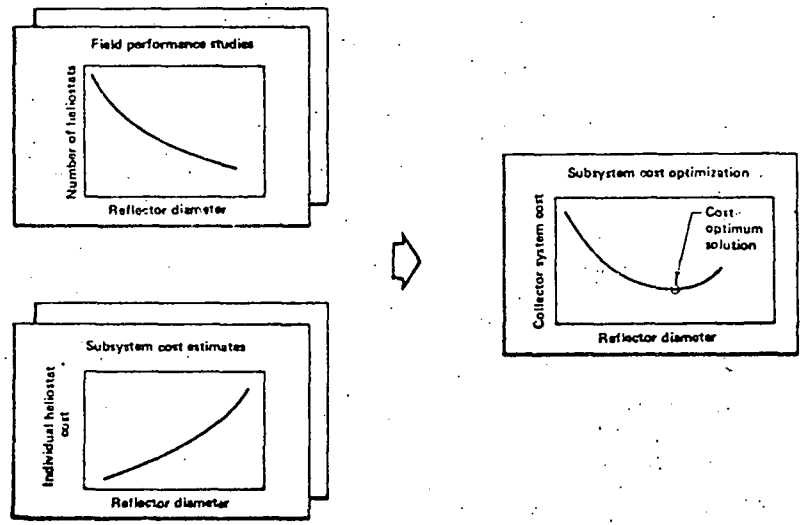

Figure 5: Parametric Studies

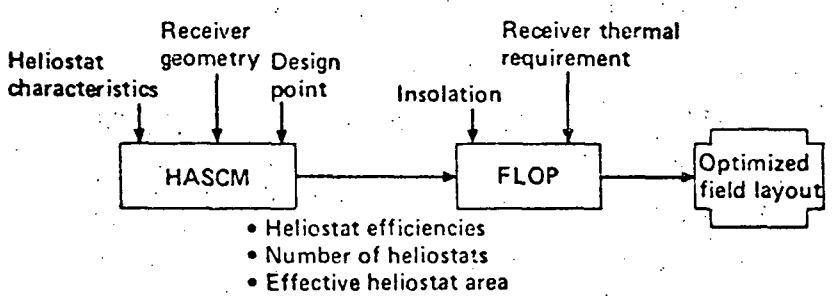

Figure 6: Field Design

The field design process begins by running HASCM several times, each time with different values for the North-South and East-West heliostat center-to-center spacing parameters. Smaller spacings will increase shadowing and blocking, while larger spacings will increase the field size and the distance from outer heliostats to the receiver (causing larger image sizes and more overflow losses). As a result of these runs, performance data for every section of the field for several spacing configurations will be available. FLOP will then determine which sections and which of the candidate spacings in each yield the field that delivers the specified receiver thermal requirement with the fewest number of heliostats. Modifying FLOP by providing cost calculating algorithms to minimize field cost will allow optimum field configuration by utilizing not only non-uniform spacing, but non-uniform heliostat size or focusing strategy.

An optimized field is pictured in Figure 7. (The receiver being considered is the cylindrical surface receiver. It has additional circumferential flux limitations which require some modification of the FLOP results). Note how FLOP determined the field perimeter as well as the spacing in each section. Just as one would expect, in order to minimize blocking, optimum North-South spacing increases as heliostats

get further from the tower in the North or South. The same is basically true for the East-West spacings. The clear area around the tower is accounted for outside the Field Layout Optimization Program.

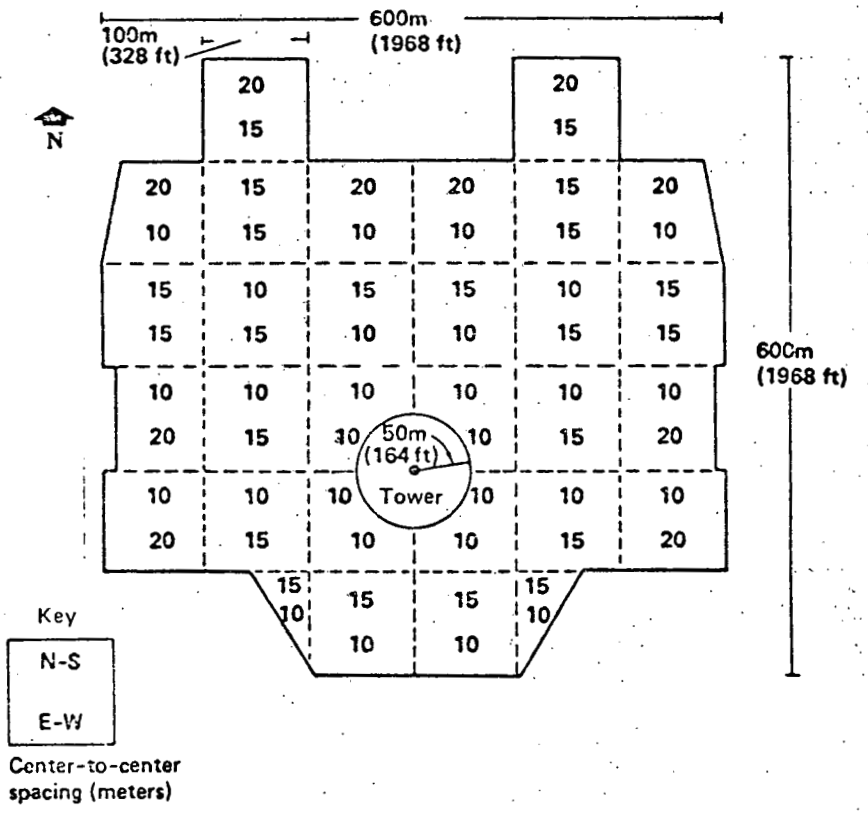

Figure 7: Optimized Field Layout

Once the field is totally described, as in Figure 7, a detailed determination of its performance can be computed by rerunning HASCM for this field configuration. The performance of the field at off-design points, i.e., other dates, and times, can be calculated. Finally, a detailed breakdown of the heliostat field efficiency into the various loss categories can be computed, as in Figure 8.

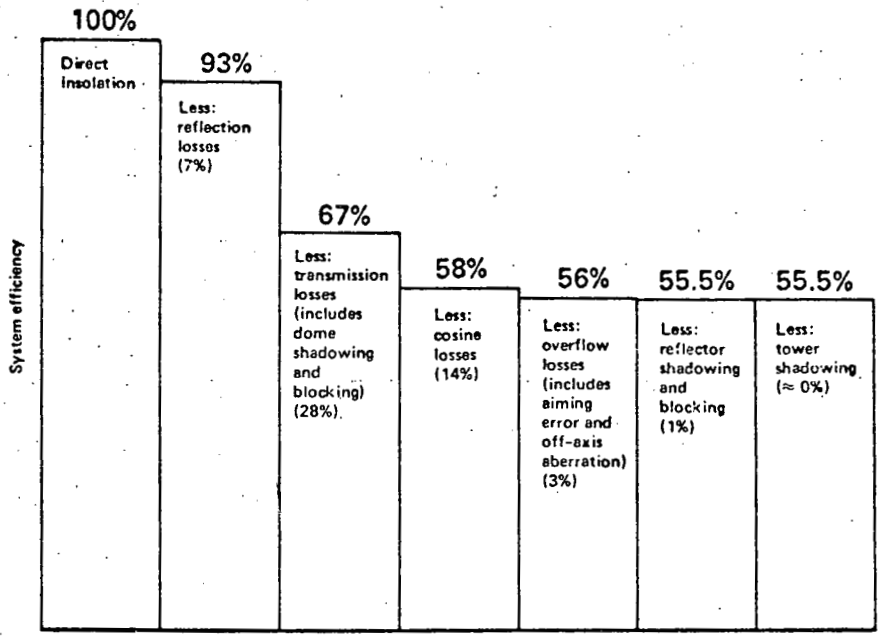

Figure 8: Heliostat Field Efficiencies

THIS PAGE

WAS INTENTIONALLY

LEFT BLANK

MONTE CARLO RAY TRACE SIMULATION FOR SOLAR CENTRAL RECEIVER SYSTEMS

G. A. Smith
Honeywell, Inc.
Energy Resources Center
2600 Ridgway Parkway
Minneapolis, Minnesota 55413

ABSTRACT

A Monte Carlo ray trace technique for the optical simulation of a solar central receiver system using a field of heliostats is presented. The ray trace technique has been used in analyzing heliostat and heliostat field trade-off issues and can provide flux maps for receiver design evaluation. The general technique has been applied to a variety of designs. This paper describes a specific design and the computer code used to calculate desired performance parameters. Sample results are shown.

INTRODUCTION

A solar central receiver system consists of a field of individually sun-tracking mirror units (heliostats) redirecting sunlight to a central station (receiver) where energy is absorbed by a working fluid for later conversion to electricity. Quite a variety of design options exist for both the heliostats and the receiver. The general Monte Carlo ray trace approach has been applied to several heliostat and heliostat field configurations and various receiver geometries, including both exposed tube receivers and cavities. (1, 2, 4).

The use of Monte Carlo ray trace methods was first applied by Honeywell over five years ago for the simulation of parabolic trough solar collectors (3). The extension of this work to paraboloid of revolution solar collectors and solar central receiver concepts developed gradually as Honeywell's involvement in solar energy systems widened. For the simulation of solar central receiver systems, the Monte Carlo ray trace software at first modeled a quite simple design involving single facet heliostats, a rectilinear field packing geometry and common geometric shapes for exposed tube receivers. As the design of a specific central receiver system evolved, the software was modified to accurately model the details of a more sophisticated system. In fact, the final computer code used in the analysis of a 10 MWe pilot plant (4) is necessarily quite design specific. It is a feature of the Monte Carlo ray trace technique that a great deal of design detail can be handled in the simulation.

The central receiver system, the computer code and simulation results described in this paper will show the level of detail which can be modeled using the Monte Carlo ray trace technique. It is beyond the scope of this paper to present the vector derivations used in the ray trace code, however, interested readers will find complete documentation on the methodology in Reference 4. This documentation also contains complete subroutine descriptions, a computer listing and other information pertinent to potential users.

CONCEPT DESCRIPTION

An artist's drawing of the 10 MWe solar pilot plant, designed by the team of Honeywell, Black & Veatch and Babcock & Wilcox, is shown in Figure 1. The design consists of the heliostat, receiver, storage and electric power generation subsystems. The storage and electric power generation subsystems are located in a clear area of the heliostat field surrounding the base of the tower. The tower is located one-half of the field outer radius south of the field center. Heliostats surround the tower and redirect incoming solar radiation to the receiver at the top of the tower. The optical performance of the concept can be simulated by modeling the heliostat and receiver subsystems.

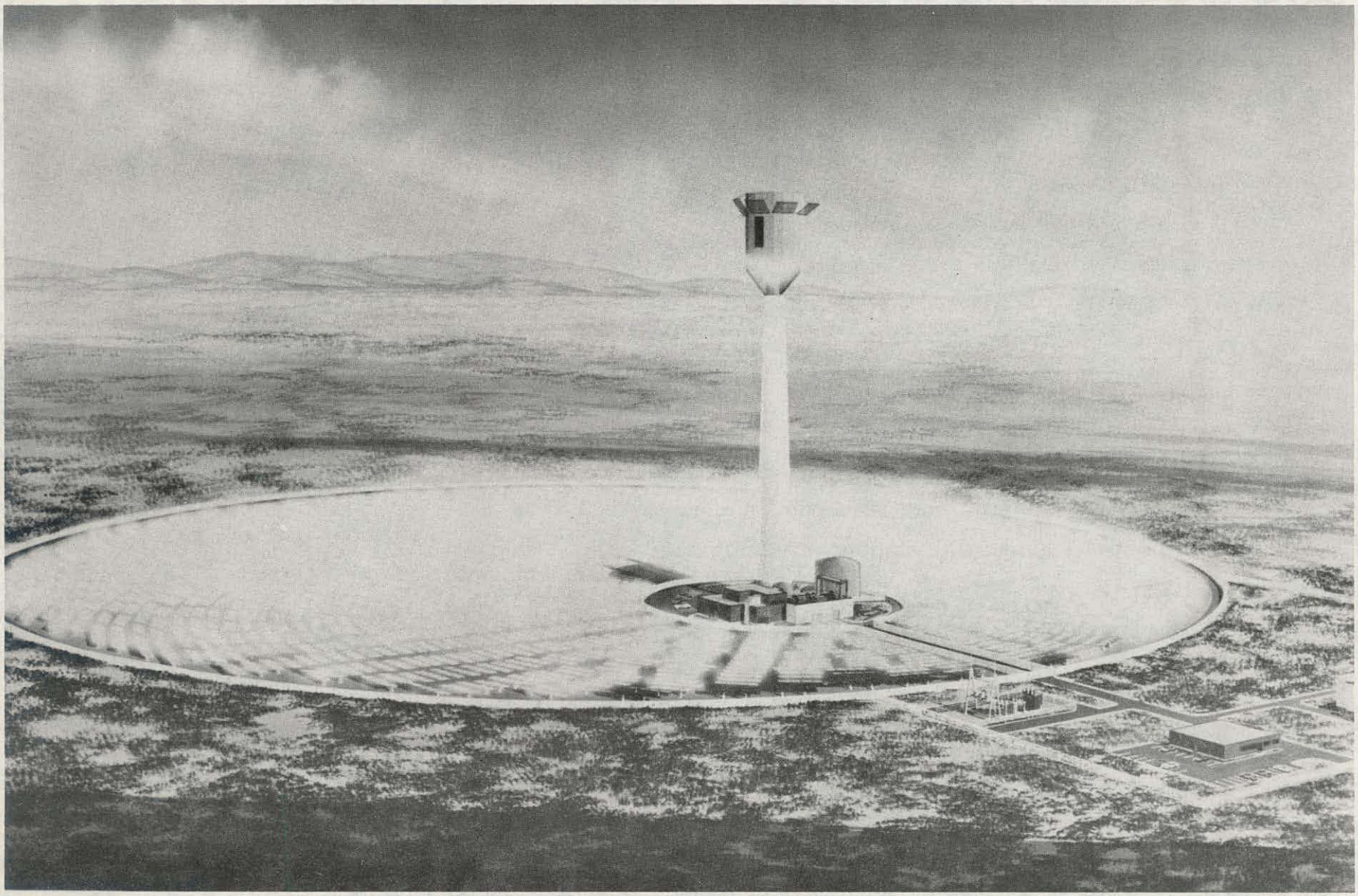

Figure 1. Artist's Drawing of the 10 MWe Solar Pilot Plant Designed by the Team of Honeywell, Black & Veatch, and Babcock & Wilcox

Each heliostat in the heliostat field has four mirror modules mounted on a single frame. The heliostat is shown in Figure 2. Each heliostat will be aligned so that each mirror module is aiming to a preselected point on the receiver aperture. This is done by toeing-in the outer mirrors slightly more than the inner mirrors. This alignment will be done for every heliostat in the field.

The heliostats track the motion of the sun to keep the reflected image on the receiver. Tracking is accomplished by rotation of the heliostat frame around the outer axis and the mirror facets about the inner axis. This movement is accomplished by motors operating two ball screw linear actuators for the outer axis and a motor acting on crank arms on each mirror connected to the motor through tie rods. Heliostats are non-uniformly spaced in the field with a resulting average ground cover (mirror area/field area) of 0.29.

The receiver is shown in Figure 3. It is located atop the concrete tower and is supported by three corbels. The tower top, the corbels and the receiver lower structure form the boundaries of the cavity aperture. Within the cylindrical cavity, the steam generator unit is mounted. Areas around the cavity aperture are covered with heat shields to protect the concrete and metal surfaces from spilled radiation.

ELEMENTS MODELED

The Monte Carlo ray trace simulation code models each element of the optical system including solar limb darkening, finite quality optics, a variable field geometry, tower and receiver shading, the details of the heliostat structure, the receiver supports and structure, and a heliostat aim strategy. Each element will be discussed and the assumptions used in each element will be described.

- Solar limb darkening involves the process of accounting for the finite size of the sun and the degradation in solar intensity as a function of angular distance from the sun's center. The limb darkened solar intensity profile used in the simulation code is shown in Figure 4. When used with the Monte Carlo technique, the intensity profile creates a weighted draw of rays over

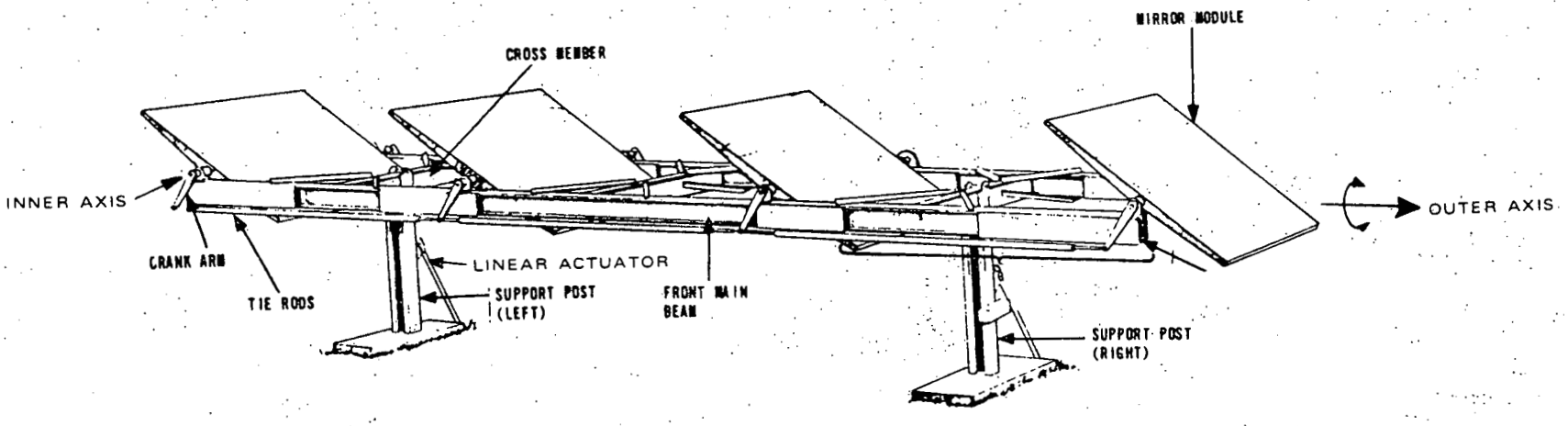

Figure 2. Pilot Plant Heliostat Design

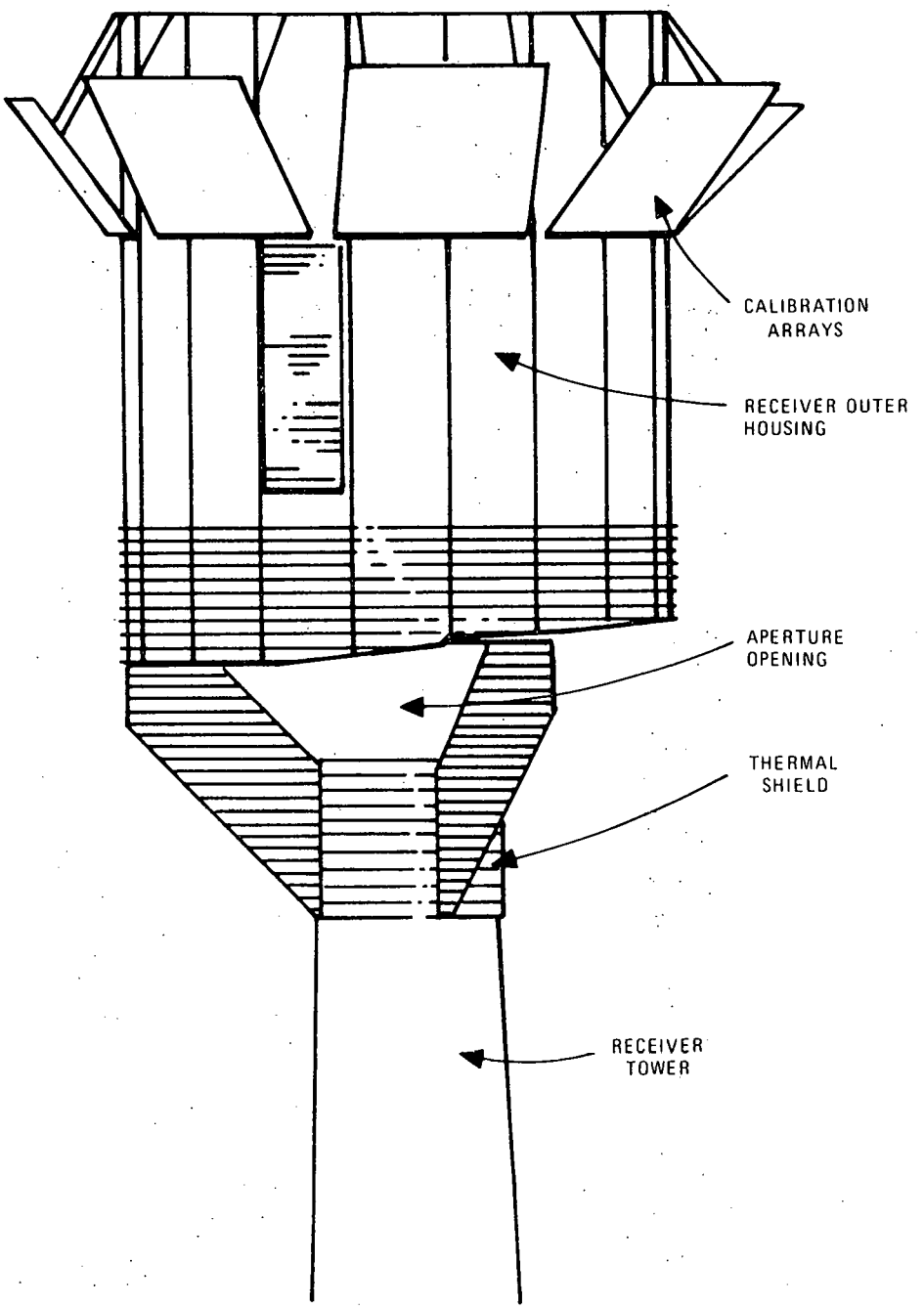

Figure 3. Pilot Plant Receiver Design

the sun radius. The weighted draw must be accomplished such that a sufficient number of randomly selected rays will statistically represent the sun's intensity pattern at the earth's surface.

The assumed intensity distribution shown in Figure 4 is based on measured data available 5 years ago and the effect of circumsolar radiation is ignored in this curve. An option to model the sun with limb darkening and circumsolar radiation does exist in the code, however, we have primarily used the limb darkened sun only. Errors in the redirected flux profile will be present to the extent that this data is in error.

- Finite quality optics are introduced into the model to account for uncertainties in tracking accuracy and mirror quality. There are four uncertain optical parameters that are assumed to be known only statistically. The first two parameters are uncertainties in the angular position of the two tracking drives. The second two parameters are the angular uncertainties in the mirror surface normal at any point on the mirror surface. We assume that each of these four parameters is statistically independent of each other or any other design parameter. For example, a given error in the mirror normal is equally likely anywhere on the mirror surface. The mirror is not known as a continuous surface with smooth waves or ripples but rather as a probability distribution of mirror normals perturbed from the mathematically correct shape by an assumed probability distribution. For each of the tracking drives, the distribution is assumed to be a normal distribution of angular error. For the mirror surface normal, the angular error from the ideal normal is also assumed to be a normal distribution and this error is assumed to be equally likely in any rotational direction. No dependence of these errors on wind, mirror attitude or position on the mirror is now included in the analysis.

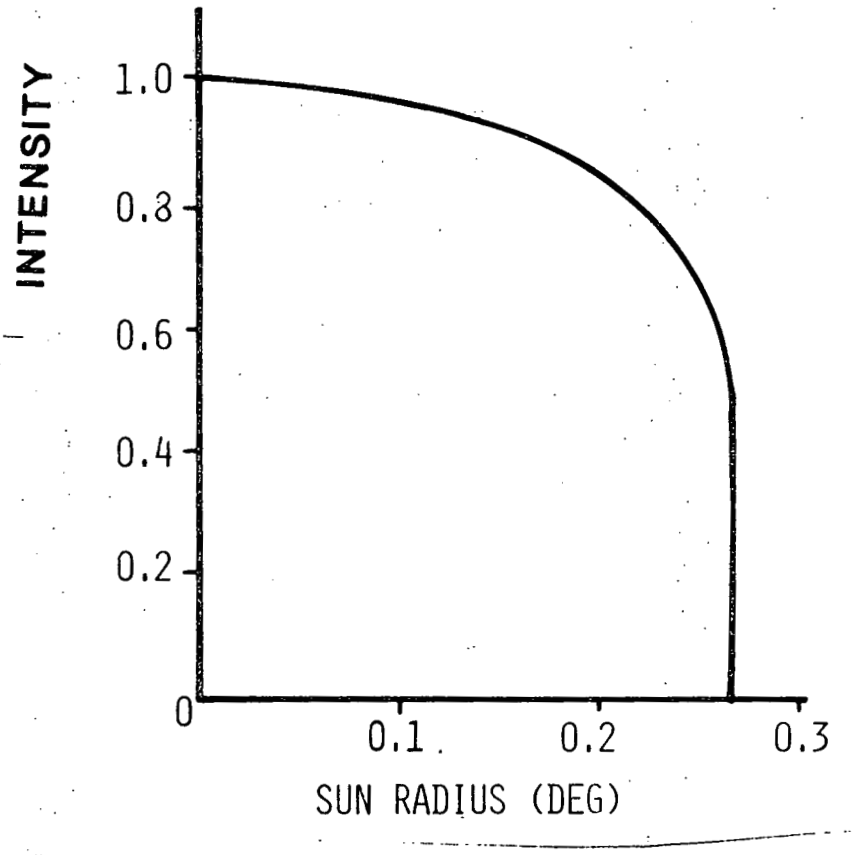

Figure 4. Solar Limb Darkening

- Variable field geometries available in this code are accomplished by changing the radial spacing between heliostats. Both uniform and non-uniform field packing may be used. The mirror module-to-mirror module spacing may also be varied but the code, as exists, is limited to four mirror modules per heliostat. Limits on the variability of the layout are largely dictated by the particular heliostat geometry as shown in Figure 2. If the specific frame structure shown were eliminated, the code can be applied to any number of mirror modules. This modification is relatively simple.

- Shadows cast by the tower and receiver are calculated assuming a point sun. To keep the shadow test simple the aperture is also assumed to block incoming solar radiation.

- The details of the hleiostat frame structure are modeled by evaluating ray interactions with the I-beam frame. Both outer I-beams, as well as three cross support I-beams are accounted for such that shading and blocking interference caused by the heliostat support structure is calculated.

- Receiver supports and surrounding structures are modeled as shown in Figure 3 such that the remaining aperture opening consists of a portion of a cone. This portion of a cone is complex in that the slant width of the aperture varies around the azimuth. Each support is modeled as a flat plane tangent to the aperture at the support center.

- Heliostat aim strategy is required to cause each heliostat to redirect energy at the nearest aperture opening. Thus, the aim strategy must guide the heliostat to miss the support structure. Unknowns in receiver position relative to the heliostat, as may be caused by wind, are ignored.

In addition to the above elements, the program now assumes that mirror reflectance and atmospheric attenuation effects can be accounted for by a simple

loss fraction of the incoming direct normal intensity. Thus, the wavelength dependence of these factors is ignored. Other versions of the Monte Carlo software have included the wavelength dependence of reflectance (2).

METHODOLOGY

Using the above models of the system elements, the method used to solve for the system performance is a Monte Carlo technique. Any Monte Carlo computation that yields quantitative results may be considered as estimating the value of a multiple integral. The simplest Monte Carlo approach is to observe random numbers, selected in such a way that they directly simulate the physical random processes of the problem at hand, and to deduce the required solution from the behavior of these numbers. As an example, the program can solve for the power entering the cavity aperture. Using the Monte Carlo technique, it is known that the ratio of the power into the cavity to the total power on the heliostat field is equal to the convergent ratio of randomly drawn rays which enter the cavity divided by the total number of rays drawn uniformly over the heliostat field. Appropriate scaling of each ray value for reflectance and absorptance losses, tracking and reflective surface errors, etc., is included in the Monte Carlo simulation.

The simulation is accomplished by randomly selecting a number of sun rays to describe the sun's intensity pattern, allowing the rays to impinge upon an imaginary plane covering the heliostat field and tracing the rays to determine whether they strike the ground, a mirror surface, the receiver, etc. The rays drawn must represent the sun's power at the time simulated so each ray is given a relative weighted value as a function of the time and the number of rays drawn. If annual energy is being calculated then each ray carries the appropriate amount of energy.

The general program flow to follow the physics of each interaction of individual rays through the optics train is shown in Figure 5. All executive-level tests are shown in the flow chart, from the mirror hit test to the receiver hit test. At each check point along the ray path the value of the ray is appropriately

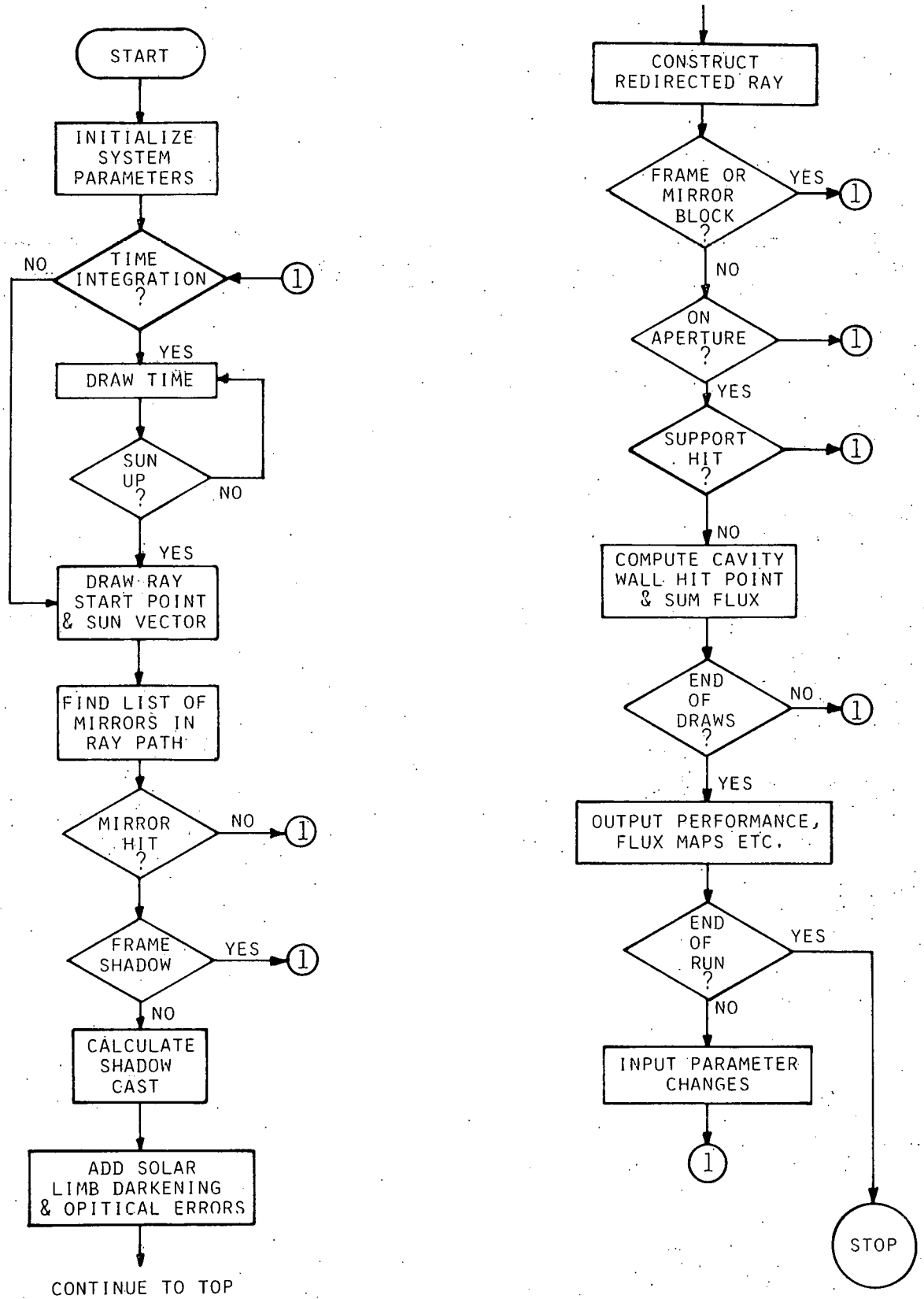

Figure 5. Simulation Program Flow Chart

scaled and the final destination of each ray traced is kept track of in the program accounting.

INPUT/OUTPUT

Simulations are initiated by card input using the FORTRAN NAMELIST feature. All variables in the NAMELIST table are defaulted to a specific central receiver baseline model. Only those portions of the model which change from the baseline need be input by card. The input parameters which may be varied are shown below;

- Time Point or Time Integration Option
- Field Specifications
  - outer field radius
  - inner field radius
  - ground cover (uniform or nonuniform)
- Heliostat Specifications
  - facet dimensions
  - frame dimensions
  - tracking error statistics
  - optical error statistics
  - focusing strategy
  - toe-in strategy
- Receiver Specifications
  - tower height
  - tower location
  - support size
  - support location
  - aperture size and shape
  - aim height
  - cavity dimensions
- Plant Latitude
- Initial Random Seed and Number of Draws

Outputs of the ray trace code include both non-dimensional and dimensional parameters. Non-dimensional ratios are formed by any desired ratio of ray counts by final ray destination. For example, the ratio of rays which hit supports to the rays which were redirected from the field is convenient in analyzing the effect of various aim strategies. The possible ray destinations which are kept track of are;

Rays drawn before sunrise
Rays drawn when the sun was too low on horizon

Rays which were in the tower shadow
Rays drawn that hit the open field
Rays which frame shadowed on adjacent heliostat
Rays which frame shadowed on same heliostat
Rays which frame blocked on same heliostat
Rays which mirror blocked on same heliostat
Rays which frame blocked on adjacent heliostat
Rays which mirror blocked on adjacent heliostat
Rays which missed low of the aperture
Rays which missed high of the aperture
Rays which missed wide
Rays which hit supports
Rays which whistled-through the aperture
Rays which hit walls of the cavity
Rays which hit roof of the cavity

The ray counts, modified by weighting each rays value, are turned into dimensional performance parameters. Available as outputs are the following:

- Power or Energy Value Calculated are:
  - Total available
  - Total on mirrors
  - Total lost in tower shadow
  - Total lost in mirror shadows
  - Total leaving mirrors
  - Total lost to blockage
  - Total on cavity supports
  - Total which whistled-through
  - Total which missed aperture
- Calculated Maps Include:
  - Flux on cavity walls
  - Flux on cavity ceiling
  - Redirected flux from field cells
  - Shadow losses in field cells
  - Blockage losses in field cells
  - Aperture misses from field cells
  - Whistles-through from field cells
  - Support hits from field cells

In addition, the distribution of redirected energy over the year is output for annual energy runs.

RESULTS

As an example of the use of the simulation code output, Figure 6 shows the 10 MW_e pilot plant power stair step

for design time plant performance. The design time for the pilot plant was specified as Winter Solstice at 2 p.m. The output of the ray trace code provides the power values from the top of the stair-step (total power available = 60.70 MW_t) to the cavity input power (40.85 MW_t). Power losses due to cosine effect, shading, blocking and aperture effects are all computed within the ray trace code. The code can provide this performance break-down for any time point or for any time integration interval desired. A separate computer program, which accounts for reradiation conduction and convection losses is used to convert direct solar power into the cavity to the absorbed power. The absorbed power is converted to net electric power using turbine heat balance data.

To establish cavity performance, the program which calculates absorbed thermal power needs more information than simply the cavity input power. The distribution of this input power on the cavity walls is required. The ray trace procedure can provide this type of data. For the pilot plant design, a map of the distribution of power on the cavity walls is shown in Figure 7 for the equinox day at solar noon. Flux isopleths are shown over the cavity interior. The flux shown is an incident, or direct, solar flux striking the cavity walls. The view of the flux map has opened the cavity cylinder to look at a planar surface.

The flux map shows two relatively high flux spots on the south wall. South is defined as 180 degrees and north is zero or 360 degrees in the figure. The hot spots occur on the south wall because a majority of the heliostats are in the north field. These heliostats aim at the north aperture opening and the energy strikes the opposite or south wall. At the bottom of the south wall we see that the flux isopleths run off the cavity. The slight loss of flux is approximately one percent of the redirected power. This loss could be avoided if the receiver had been designed with a larger upper aperture tilt angle. The baseline aperture tilt was selected to optimize the net annual energy and some loss through the aperture is acceptable. The pilot plant preliminary design receiver upper aperture tilt is shown in the flux map figure by the dashed line representing the cavity interior boundary.

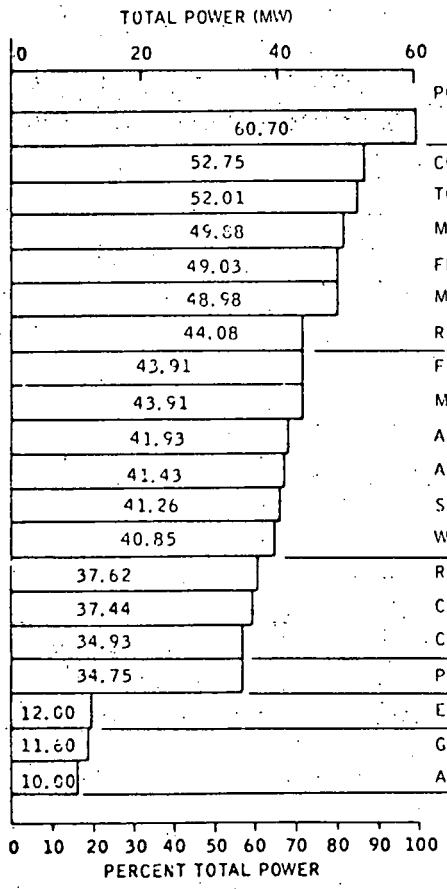

POWER LOSS	% LOSS OF AVAILABLE POWER	AVAILABLE POWER SOLAR INPUT (DNI X MIRROR AREA)	% TOTAL AVAILABLE POWER 100
COSINE	13.1		
TOWER SHADOW	1.4		
MIRROR SHADOW	4.1		
FRAME SHADOW	1.7		
MIRROR FACET EDGE	0.1		
REFLECTANCE	10.0	REDIRECTED	72.6
FRAME BLOCK	0.4		
MIRROR BLOCK	0.0		
ATMOSPHERIC ATTENUATION	4.5		
APERTURE MISSES	1.2		
SUPPORT STRUCTURE HITS	0.4		
WHISTLE THROUGHS	1.0	CAVITY INPUT	67.3
RERADIATION	7.9		
CONDUCTION	0.5		
CONVECTION	6.7	ABSORBED	57.6
PIPING	0.5	TURBINE INPUT	57.3
ELECTRIC CONVERSION	65.5	GROSS ELECT. OUTPUT	19.8
GENERATOR	3.3		
AUXILIARY	13.8	NET ELECT. OUTPUT	16.5

Figure 6. Pilot Plant Design Point Performance

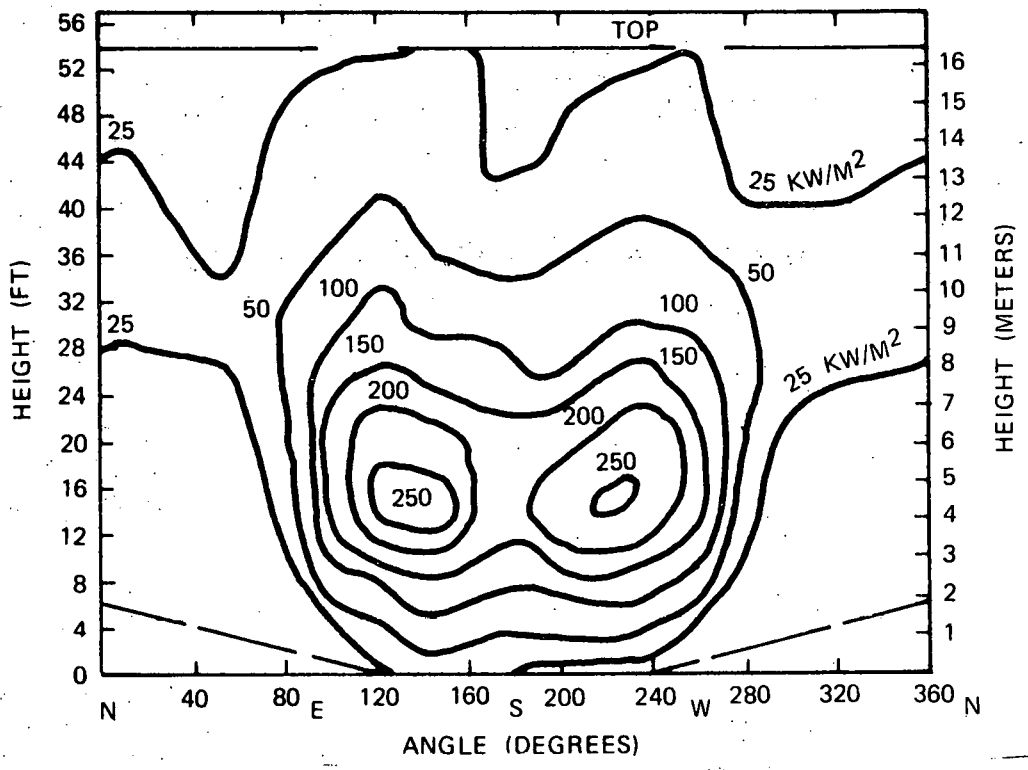

Figure 7. Cavity Wall Flux Map for Equinox Noon

It is important to point out that the high flux regions are located at the bottom half of the cavity wall where the boiler surface is present. The boiler surfaces can accept a local flux peak of 400 kW/m^2, while the superheater surfaces should not exceed 150 kW/m^2 absorbed flux. The differences in allowable peaks is primarily due to the poorer heat transfer in the superheater tubes. Poor heat transfer can cause overtemperature and stress problems. In the upper, or superheater regions, a slightly more uniform circumferential flux distribution is shown, with the flux peak near 100 kW/m^2.

CONCLUSIONS

This paper has shown how Monte Carlo ray trace simulation techniques can effectively be used for the analysis of the optical performance of a specific detailed solar central receiver design. It has also been pointed out that the same basic Monte Carlo ray trace technique has been applied to a wide variety of design alternatives. The technique has been shown to be an extremely powerful tool for predicting the optical performance of simple to sophisticated solar central receiver systems.

ACKNOWLEDGEMENT

The authors' work with the Monte Carlo ray trace simulation code was primarily performed under ERDA contract E(04-3)-1109 for the preliminary design of a 10 MW_e solar central receiver pilot plant.

Special thanks must go to Mr. J.M. Hammer of Honeywell for his instructive assistance in the continuous process of modifying and improving the simulation code. Mr. B. Buchholz, Mr. D. Turck and Ms. E. Williams of Honeywell were all extremely helpful in the development of the code version presented here and their efforts are appreciated.

REFERENCES

1. Dynamic Conversion of Solar Generated Heat to Electricity, Final Report on Contract NAS3-18014,

Honeywell and Black & Veatch. Report No. NASA CR-134724.

2. "A Monte Carlo Simulation of the Central Receiver Concept for the Dynamic Conversion of Solar Generated Heat to Electricity", E. Fourakis and J.M. Hammer, Paper presented at 1974 ISES Conference.

3. University of Minnesota/Honeywell Research Applied to Solar Thermal Power Systems, Progress Reports Nos. 1 and 2, NSF/RANN/SE/GI-34871/PR/73/1, 2.

4. Solar Pilot Plant, Phase I, Preliminary Design Report, Honeywell, Final Report on ERDA Contract No. E(04-3)-1109. See Volume II, books 1 and 2.

DESCRIPTION OF MIRVAL

Dr. Joe D. Hankins
Member of Technical Staff
Sandia Laboratories
Livermore, California

MIRVAL (MIRror eVALuation) is a Monte Carle ray trace program which is designed to assess the overall optical performance of arbitrary deployments of heliostats used in the central receiver or power tower concept. Briefly, the geometry of the heliostat field, the tower, and the receiver along with miscellaneous physical data such as mirror reflectivity, insolation, etc., are input and thermal power into the receiver and the thermal power density on the plane of the receiver opening are output. By properly choosing control parameter values, anyone of three versions of four different heliostats and any of three receivers can be selected for a run.

Prior to the beginning of the Monte Carlo trials, an impact region for randomly selected rays is determined as follows: First, a sphere is constructed about the center of each heliostat which is just large enough to contain the heliostat in any possible orientation. Then a rectangular box is constructed which is large enough to contain the spheres. Any light ray which strikes a heliostat must strike an illuminated face of the box first. A condensed description of a Monte Carlo trial will now be given to communicate a feel for the way the program works.

A time is selected at random from a predetermined interval according to a uniform distribution. To obtain the performance at a fixed time, the beginning and ending points of the time integration interval are made equal. The sun position is then determined from the selected time and latitude of the site.

Next, a sun ray is selected by choosing a point uniformly from the parallel projection of the illuminated faces of the box onto a plane perpendicular to the direction of the center of the sun. The direction of the ray is determined by selecting a point uniformly from the apparent sun disk. If N rays are to be traced, that is, if N Monte Carlo trials are to be made, then the ray carries AI/N units of power where A is the projected area and I is the insolation (power per unit of area normal to the direction of the sun).

The validity of the Monte Carlo process is most easily seen for a fixed-time run. Then the position of the sun is constant and thus the amount of solar power falling on the box is the same for each Monte Carlo run. In this case one counts the number of rays that strike the box, N, and also counts the number of rays, N_R, which enter the receiver. It is intuitively obvious that the ratio N_R/N approaches the probability, p, that a ray which strikes the box will enter the receiver, as N increases. The quantity of power incident in the receiver is then p times the amount of power, AI, incident on the box. Thus (N_R/N) (AI) provides a good estimate of the power provided N is large enough. It is also clear that in this (fixed time) case the set of Monte Carlo experiments forms a Bernoulli sequence and thus confidence levels are easily found [1]. The confidence level for a given number of trials is essentially independent of the number of loss processes and/or integrations that the ray is subject to on its journey to the aperture. This accounts for the popularity of Monte Carlo methods whenever the corresponding numerical integration method would lead to a large number of iterated integrations.

If the ray hits the tower before it would have hit the box, a tally corresponding to this event is augmented by one and the next ray is selected. Otherwise, the ray is traced from the point of entering the box to the point of exit. Prior to the beginning of the trials, the box is partitioned into an appropriate set of rectangular cells and an array is created that contains the mirror numbers of those mirrors whose centers lie approximately within a heliostat radius of any point in the cell. Thus, the cells through which the ray has passed are quickly computed and a list of possible mirror targets is provided. Partitioning the box in this manner is extremely useful since it reduces the number of candidate mirrors for impact; irregular deployments of mirrors are handled without approximation as readily as regular ones and the machine time for analysis is independent of the number of heliostats deployed.

From amongst the mirrors which are candidates for impact, an efficient method is used to obtain the first (if any) of the mirrors hit. If none is hit, then a "hits the ground" tally is augmented and a new ray is selected. If one is hit, then it is first determined whether the impact actually lies between two mirror facets. If so, the "hits the ground" tally is augmented and a new ray is selected. Otherwise, one next determines whether the ray is absorbed during reflection. If it is, then an appropriate tally is made and a new ray is selected. Otherwise, the next


step is to determine the direction of the normal to the surface of the facet at the point of impact. To find the normal, the following information is needed:

1. The intended surface figure. In MIRVAL, the facet surfaces are either spherical or parabolic with arbitrarily assignable focal length including infinity for flat facets and negative values for mirrors which have been distorted.
2. The calibration time of the particular mirror impacted. Calibration time refers to the time of year and day when a mirror is adjusted to give the desired pattern on the interior of the receiver.
3. The aiming strategy. An aiming strategy is defined by specifying a point, relative to the receiver, to which a ray from the center of the sun shall be reflected if it impacts in the center of the center facet of the given heliostat. This point is the aimpoint and may be different for different heliostats.
4. The relative orientation of mirror facets. The orientation of the central facet of a heliostat is determined by the aimpoint. The relative orientation of the remaining facets can be prespecified in several different ways. The relative orientation need not be the same for different heliostats.
5. The magnitude of aiming point errors. MIRVAL permits uncertainty in achieving a given aiming point strategy. In MIRVAL, the azimuth and elevation angles of the central normal are normally distributed random variables whose means are equal to the intended values determined by the aiming point strategy and whose standard deviations are input parameters.
6. The magnitude of slope errors. In addition to the perturbation of the normal due to previously defined aiming point errors the normal to the surface at the impact point is given an additional (independent) error (the slope error) to account for imperfections in achieving the desired smooth figure.

With this information, the surface normal and the reflected ray are determined. The reflected ray is again traced through the box to the point of exit and a list of mirrors whose backs may be hit is obtained. These are culled and then checked for impact. If an impact occurs, an appropriate tally is made and a new trial starts. Otherwise, the ray is traced to the receiver. If it misses the receiver a new trial is started; otherwise, the position of impact within or on the receiver is computed and a power flux density map is built up.

The sun position in MIRVAL is determined by assuming

that one year is exactly 365 days and the earth's orbit is a circle. The insolation at the plant site is an input in the fixed-time case. For time integration runs, the insolation I at time t is given in

$$I(t) = K \rho \frac{M(t)}{M_o}$$

where M (t) is the atmospheric mass traversed by a light ray at time t, M_o is the atmospheric mass that would be traversed by a vertical ray, and K and ρ are empirical constants (See [2]).

The output obtained from time points runs include the following:

Total power into the receiver.

Power flux density map on (or in the interior of) the receiver.

Diagram showing light rays impacts on the plane in the receiver opening.

Views of the mirror field as seen from the receiver and as seen from the sun.

Performance of mirror field averaged over the zones of a predetermined partition, including:

- Fraction of mirror area shadowed by tower, by other mirrors, and by tower or other mirrors.
- Fraction of the reflected power that is blocked by mirrors.
- Spillage - fraction of the power that clears the mirrors but which fails to hit the desired part of the receiver.
- Power efficiency - power to the desired part of the
- receiver divided by the sum of the area of the mirrors.
- Field efficiency - cosine of incidence angle times spillage.

The output is appropriately modified for a time integration run.

The code is organized into portions which deal with field geometry, mirror geometry, mirror surface figure, aiming point strategy, and insolation. These portions are modularized so that changes in one of them produce very few if any changes in the others.

MIRVAL is written in CDC Fortran Extended and is operational on a CDC 6600. A CDC extended core is used for storage of large arrays and a local graphics package is utilized. These two features would no doubt require modification if MIRVAL were to be used at other installations. Run times for accurate mirror by mirror performance and 100+ entry flux maps require from one to three hours. For total power into the receiver or for the performance on one mirror, fair accuracy is achieved with runs of about 10 minutes. These running times are to be expected with a Monte Carlo program in which the objectives are detailed and accura e simulation and simplicity of programming changes to modules.

Thus, MIRVAL provides a flexible tool for evaluating proposed designs. It may not be the best tool for synthesizing a design in which many computer runs are required and in which some of the features modeled in MIRVAL may be irrelevant.

REFERENCES

(1) Feller, W., An Introduction to Probability Theory and Its Applications, Volume 1, 2nd Edition, 1962, p. 176.

(2) Garnier, B. J. and Ohmura, A., Evaluation of Surface Variations in Solar Radiation Income, Solar Energy 13, 22, 1970.

THIS PAGE

WAS INTENTIONALLY

LEFT BLANK

COLLECTOR FIELD OPTIMIZATION AND LAYOUT

F. W. Lipps
Solar Energy Laboratory
University of Houston
Houston, Texas 77004

ABSTRACT

A preliminary study via the LOSS program suggests that radial stagger neighborhoods are desirable for an optimized collector field. This conclusion is supported by the more comprehensive RCELL optimization program, and the subsequent layout processor which generates a complete set of heliostat coordinates.

The RCELL program generates optimized heliostat spacing coordinates for the representative heliostats of a uniform cell structure in the collector field for the power tower system. RCELL inputs a trial set of spacing coordinates and outputs an improved set of estimates based on a sample of variations. A convergent optimization is obtained by iterating the solution with successively smaller variations and by adjusting the input figure of merit to equal the output figure of merit. This program contains an adequate cost model, and an adequate optical model for the net annual receiver power, so that a meaningful figure of merit can be computed. It also outputs a brief performance summary.

1.0 INTRODUCTION

In this talk we are concerned with the optical behavior of the collector field and its interaction with the receiver. We have a computer model of this behavior and will consider methods which lead to an economically

optimized design of the collector field. We will consider:

1. The nature of the desired optimization and the resulting figure of merit.
2. The economic model for the commercial system.
3. The design requirements.
4. The basic variables of the collector field geometry and various practical subsets.
5. The mathematical formulation of the optimization and its computerized solution.
6. The optimized collector field geometry.

The collector field contains a large number of heliostats whose location with respect to the receiver and with respect to each other creates an intricate design problem. Heliostat location is measured with respect to the base of the tower. An optimized set of heliostat coordinates provides an optimized collector field for the present purposes.

The tower-top receiver is designed to absorb solar energy and to deliver this energy to an electric utility for electric power production. The best economic measure of performance for this composite system is a suitably adjusted busbar cost estimate for the output electric power. However, we feel that an effort to optimize the collector field geometry via busbar cost would make the collector field design too difficult, and much too dependent on the design of the thermal storage system, the turbo-generator system and the capacity displacement credits. It seems desirable to consider the tower-top receiver as a source of thermal energy which can be "sold" to the utility system and therefore the cost of thermal energy at the base of the tower can be used as a suitable figure of merit for the optimization of the collector field.

Specifically, we assume a figure of merit equal to system cost divided by net annual thermal energy delivered at the base of the tower. The use of annual thermal energy implies that thermal energy is always useful to the utility. This assumption would be invalid for a seasonal application such as irrigation pumping. It is not uniformly valid for utilities; however, it should be valid in an energy hungry community, if the power plant is assumed to incorporate three to six hours of thermal storage. In the future, we may consider ways of biasing the energy towards desirable times, but for the present we accept the verdict of the system performance analysis. By cost, we mean cost traceable to the system prior to delivery of the energy at the base of the tower. Of this cost,

the heliostat field is predominant, and hence is a worthly object for optimization.

At this point we must mention the source of energy, i.e., the insolation, and the loss model for our system. The system collects direct beam solar insolation at a site which will experience local weather conditions. However, we are not concerned with the specific details of the insolation record, but instead, we are concerned with predictable average insolation behavior which will determine the outcome of investment decisions. Consequently, it is reasonable to use our analytic insolation model with a percent of possible insolation factor. The following list of energy loss mechanisms is proposed:

1. Percent of possible insolation due to local weather conditions.
2. Heliostat related factors: reflectivity, dust, guidance errors and malfunction.
3. Shading and blocking losses due to neighboring heliostats.
4. Start up and shut down losses due to wasted insolation and heat.
5. Atmospheric transmission losses between heliostat and receiver.
6. Receiver related factors: interception, absorptivity, emissivity, convection and conduction.
7. Parasitic energy requirements for heliostat guidance and coolant pumping.

The central receiver system concept is an optical concept and as such it can be optimized over many design variables which are not included in the collector field layout. The heliostats are optimized for mass production cost savings and performance under reasonable loads. This is basically a mechanical problem and the resulting heliostat design is an input to the collector field problem. Usually heliostat size is fixed. The tower design is also basically a mechanical problem; however, in this case we specify tower height to satisfy the name plate power requirements for the utility power plant. Consequently, the tower height becomes a by-product of the collector field optimization.

The receiver design also affects the optical performance of the system. However, for our purposes, it is assumed given. Receiver size was optimized at an earlier stage when various receiver geometries were being considered. The receiver size is adequate to handle the required power and its configuration is appropriate for the anticipated variation in flux distribution with time. The resulting interception must be acceptable and can be optimized by varying the

aiming strategy, which is independent of the collector field layout. See Table 1.

Table 1. Interception Performance Averages for MDAC External Cylindrical Receivers

System	Aiming Strategy	Interception	Flux Spillage
Commercial	3 Point	95.8%	4.2%
	Hi-Lo	97.0%	3.0%
Pilot	Hi-Lo	98.0%	2.0%

The receiver design is complicated by many considerations. For the present, we assume either a cylindrical external receiver or a flat external receiver. The two most serious design requirements (in addition to interception) are the peak flux density limit and the average flux density requirement. Any heat transfer device has a flux density limit, beyond which some form of damage or malfunction will occur.

The cylindrical receiver contains 24 panels each having an input and an output manifold with sensors and controls. Flow control must be positive, and for two phase flow, a limited range of flow control is possible. Consequently we must maintain a minimum panel power at all times during useful operations. Furthermore, the manifolds will fail to distribute flow satisfactorily to each of the tubes in a given panel, if the flux gradient across the panel is excessive. Hence, we also have a maximum flux gradient limit. Similar considerations apply to any receiver.

The design procedure is as follows:

1. Set scale of system by specifying the total thermal power at equinox noon.
2. Scale receiver dimensions to satisfy flux density limit assuming that adjustments will be made in the aiming strategy.
3. Optimize the collective field.
4. Adjust the aiming strategy to reduce the bright spots on the receiver.
5. Adjust the trim of the field to satisfy panel power minimum if necessary. At 35° latitude, the southern field tends to be weak, and becomes weaker as latitude increases. A slight departure from optimization may be required here, although the use of preheat panels in the southern quadrant of the receiver removes most of the problem.
6. Scale tower height and collector field to achieve exactly the desired system power level.
7. Generate final heliostat coordinates. We must give a complete list of coordinates for roughly 20,000 heliostats allowing for free turning of

the heliostats, roads, tower exclusion, and heliostate access ways. Each heliostat must have a suitable designation for the surveyors, and the subsequent control connections.

At this point we usually assume that the heliostats are identical and that the centers of the heliostats are co-planar so that the collector field is flat, although it may have a slope. Allowance for contours in the collector field is a step beyond the current state of the art. The intersections of the tower center line with the plane of the heliostats determines a natural origin for the coordinates of the heliostats in the collector field. The complete list of heliostat coordinates can be visualized as a set with the following additional structure. Let H be a heliostat in the set of heliostats S, so that the list of heliostat coordinates, $\hat{L}$, can be expressed as

$$\hat{L} = \{(x_H,y_H)|H \in S\},$$

where (x_H,y_H) gives the coordinates of heliostat H. Now let H be identified by a pair of integers (i,j) such that

$$H \leftrightarrow (i_H,j_H),$$

i.e., H is one to one correspondence with (i_H,j_H). Consequently the list of coordinates can be written as

$$\hat{L} = \{[x(i,j),y(i,j)]|(i,j) \in S\}$$

and the mapping from S to the collector field is given by the functions x(i,j) and y(i,j) which are determined by the optimization procedure. If the coordinates are expressed in units of heliostat width, we can visualize the coordinate mapping as an actual layout process in which the heliostats are moved from a storage area where they are kept in a state of rectangular closest packing, so that their coordinates are (i_H,j_H) in heliostat units. Currently we expect that i will be a circle label and j will be an azimuth label.

Historically, we have approached the collector field design by assuming the simplest possible layout and gradually adding variables, but never allowing a chaotic solution to occur. In general the optimization is non-unique and leads to chaotic solutions similar to dislocations in a crystal. This type of result is to be expected from a straight forward rigorous minimization of the figure of merit. For example, if L is an arbitrary set of heliostat coordinates and F is the figure of merit, then the optimization implies that,

$$\hat{F} = \underset{\{L\}}{\text{MIN}}\ F(L) = F(\hat{L}),$$

where $\hat{L}$ is the optimized coordinate set. The function F(L) is difficult to construct, for several reasons.

1. There are many independent variables.

2. The insolation average must be performed numerically.
3. The instantaneous reflected power from each heliostat is a function of the heliostat coordinates, which has at least eight analytic branches. (We expect non-analytic behavior from every shading and blocking event. Normally eight neighbors can contribute events, hence eight branches.)

However, F(L), can be defined as follows. Let

$$F(L) = C(L)/E(L)$$

where C(L) is the dollar cost of the system and E(L) is the net annual thermal power delivered at the base of the tower. C(L) is determined by the economic model. E(L) is determined by the optical model of the system. We can write

$$E(L) = a\, E_o(L) - b,$$

and then

$$E_o(L) = \sum_{H \epsilon S} \eta_H g_H(L) A_H,$$

where

- A_H is the reflective area of a heliostat,
- $g_H(L)$ is the annual total thermal energy reflected by heliostat H in a field specified by L,
- η_H is the receiver interception factor for heliostat H, which is assumed to be time independent for purposes of simplicity, and
- $E_o(L)$ is the annual thermal power incident on the receiver.

The coefficients a and b contain all other losses, so that E(L) becomes the net thermal energy delivered at the base of the tower.

Currently, our computer facility is able to generate quantities such as $E_o(L)$ for a collector field, only if the summation is limited to several hundred terms. Consequently we are forced to a system of representative heliostats, which is called the "cell-wise approximation for large collector fields". The expression for $E_o(L)$ is replaced by

$$E_o(L) = \sum_c n_c \eta_c g_c(D_c) A_H,$$

where n_c is the number of heliostats in a cell c. Consequently,

$$\eta_c g_c(D_c) = \eta_H g_H(L),$$

where H is the representative heliostat for cell c. The variables D_c are the displacements of the appropriate neighbors with respect to the representative heliostat. Hence D_c is a function of L, but not vice-versa in general.

The cell-wise optimization procedure presented in Reference 1 proceeds along lines suggested by the expression for $E_o(L)$. Unfortunately, it leads to a solution for the displacements and not the coordinates themselves. Fortunately, the results for the displacements vary smoothly from cell to cell. The use of

representatives implies that each heliostat in a cell has a similar neighborhood. This assumption greatly reduces the number of independent displacements. In practice we solve for two components, a radial-x component and an azimuthal-y component, as shown in Figure 1. The results show that y is nearly constant throughout the collector field, and that x is nearly independent of azimuth with respect to the tower. Furthermore, x can be represented as a quadratic function of the tower elevation angle. Figure 1 defines cornfield and staggered neighborhoods.

2.0 THE LOSS PROGRAM FOR A PRELIMINARY OPTIMIZATION

The LOSS program shows the amount of ground space required by a heliostat at each of the representative locations in the collector field. This program calculates the MWH/m^2 of lost energy due to a single neighbor as a function of displacement from the representative heliostat. The LOSS program provides a good sun sample for the whole year and utilizes a very efficient version of the shading and blocking processor which neglects overlapping events. Overlapping events are rare under optimized conditions. The LOSS prints provide a good starting point for further collector field optimization

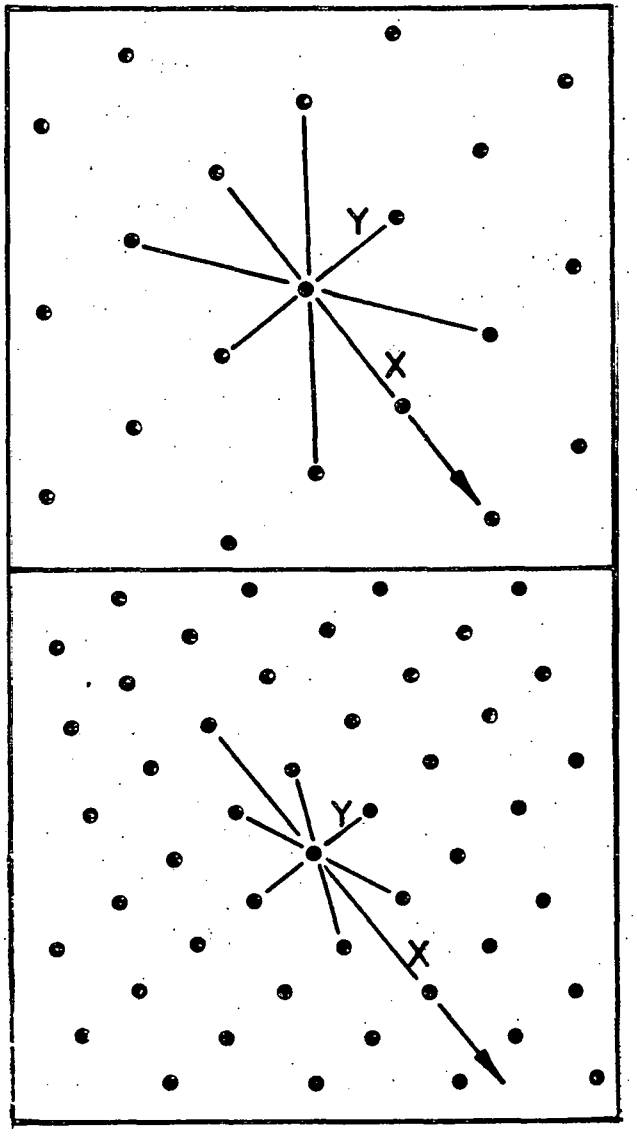

Figure 1 Upper figure shows a Radial Cornfield neighborhood; Lower figure shows a Radial Stagger neighborhood.

25479

HELIOSTAT LOSS FOOTPRINTS
ANNUAL SHADING AND BLOCKING LOSS

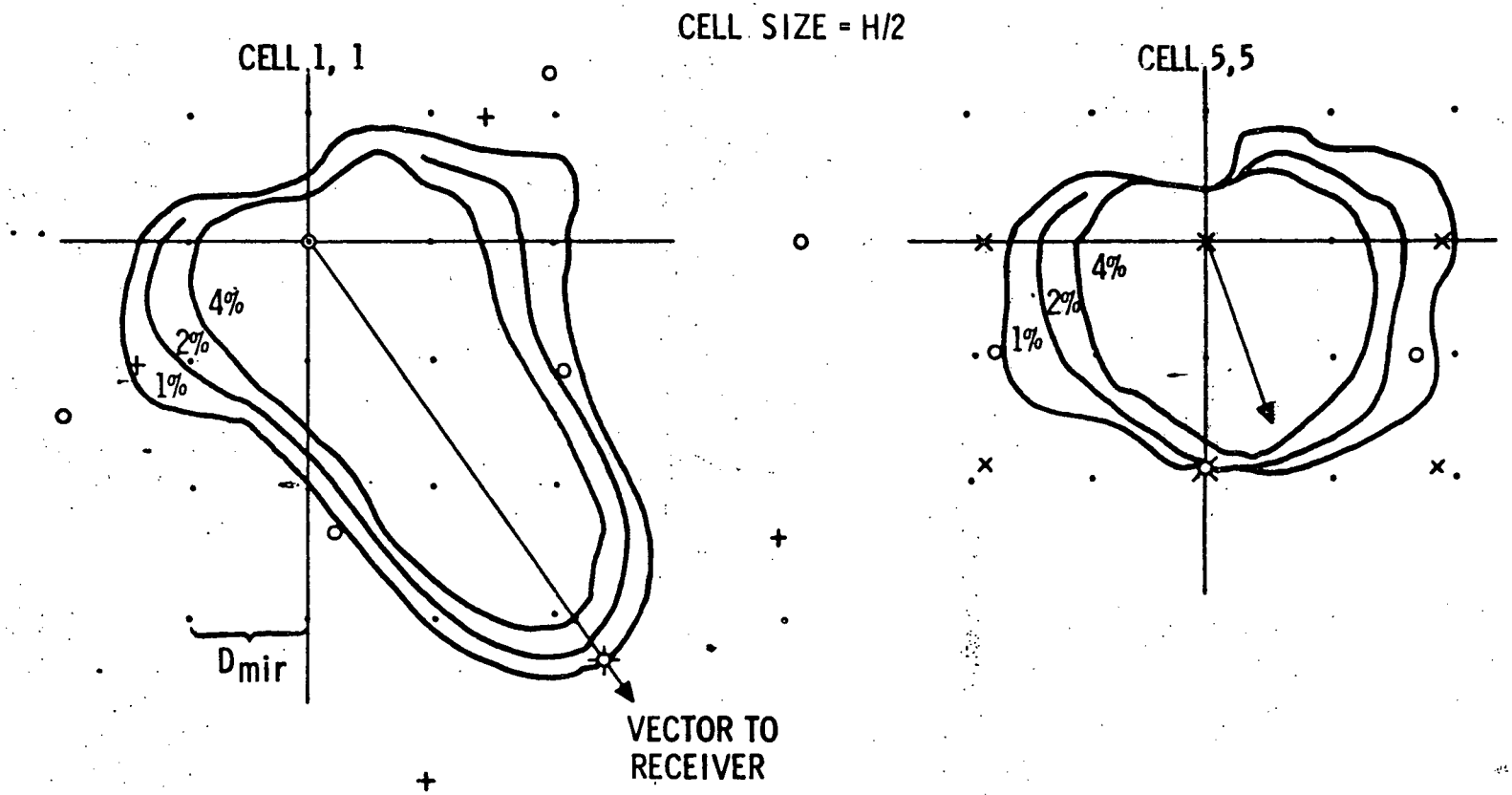

LOCATION OF NEIGHBORS
- o RADIAL STAGGER
- × RADIAL ORTHOGONAL

LOCATION OF NEIGHBORS
- o N - S STAGGER
- × NORTH-SOUTH EAST-WEST

Figure 2 Heliostat Loss Footprints

studies. See Figure 2. This is a small stand alone program which can provide various comparison and/or sensitivity studies.

The LOSS program provided the following table, which shows the percentage of advantage (i.e., higher ground coverage) for the radial stagger arrangement as compared to the next best alternative. Negatives indicate that a better alternative occurs. The radial cornfield is never best although it beats radial stagger in 3 out of 121 cells. The 24 negative entries represent 14 cells in which N-S cornfields are best and 10 cells in which N-S staggers are best. The occurrence of large negatives in the southern field suggests that it might need special treatment, but this is not confirmed by the pilot plant study which assumed radial stagger throughout. The complications and unaccounted losses associated with chaotic cell boundaries and varying cell configurations were avoided by using the radial stagger array throughout our final commercial and pilot plant studies.

Table 2. Percent of Advantage for Radial Stagger
(Note that J = 1 to 6 is the West Half Field)

	J = 1	2	3	4	5	6
I = 1	6.7	2.9	-3.0	-5.1	13.3	0.0
2	6.5	12.2	1.2	2.9	13.5	0.0
3	5.0	-0.6	-5.3	1.3	16.2	0.0
4	-1.0	-6.8	-7.1	3.5	8.8	0.0
5	5.9	1.0	-1.1	2.8	2.0	10.0
6	6.8	4.3	-5.5	-7.2	-10.8	5.2
7	11.6	12.2	7.6	6.5	-4.3	0.0
8	12.8	3.8	3.0	-11.8	5.1	Tower
9	-6.6	-1.5	-6.5	-12.8	4.8	0.0
10	5.8	-18.6	-11.1	-14.3	-.006	0.0
11	11.0	-4.9	-10.5	-11.1	7.7	0.0

3.0 TYPICAL RESULTS FROM RCELL

3.1 Purpose

The RCELL program generates optimized heliostat spacing coordinates for the representative heliostats of a uniform cell structure in the collector field. RCELL inputs a trial set of spacing coordinates and outputs an improved set of estimates based on a sample of

variations and by adjusting the input figure of merit to equal the output figure of merit. This program contains an adequate cost model and an adequate optical model for the net annual receiver power so that a meaningful figure of merit can be computed. It also outputs a brief performance summary.

3.2 Main Features

The RCELL program integrates the reflected power from a set of representative heliostats over a useful day which starts and stops at a specified elevation angle. The time between sun samples is varied to emphasize the more complex behavior at low sun angles. We typically use 19 samples/day and 7 days from solstice to solstice. Consequently, we assume a symmetric year and an east-west symmetric collector field.

The neighborhood of the representative heliostat can be selected from the four options:

Radial Stagger, N/S Stagger,
Radial Cornfield, and N/S Cornfield.

However, at present we are committed to the radial stagger option, as this option has been found to give best performance in a majority of the cells.

Each neighborhood is parameterized by an x and a y spacing coordinate. Both coordinates are given four variations independently. In the radial stagger case

x is the radial coordinate and
y is the azimuthal coordinate.

This set of 16 variations provides a basis for estimating all of the partial derivatives which are required by the optimization theory, provided that the solution occurs within the range of the variations. Consequently we expect to apply our iterative approach to the final solution by progressively decreasing the size of the variations.

After estimating a set of optimum coordinates the data base is interpolated to provide estimates for the performance of the optimized system. At this point it is also possible to determine the optimum trim (i.e., the set of excluded cells which are too remote for effectiveness). And finally, we output a performance summary which includes a new figure of merit.

3.3 Executive Requirements

The executive program contains permanent assignments

for the following files:

PFILE	for the print file,
XYPLOT	for coordinate print file,
SAMPLE	storage for expensive data,
DATA	for coefficients of (x,y) data from PLOTϕ or alternatively the (x,y) data itself.

It also requires active assignments for

AA1	containing the source programs, and
PANEL	for interception data.

The SAMPLE data can be reused in an optional mode which allows modifications of various inputs such as the figure of merit or even the interception data, without repeating the most CPU costly run. See Figure 3.

The (x,y) data files are small data files of 66 lines which can be accessed and edited to remove bad cells and to merge data from several runs.

The XYPLOT output file is designed for PLOTϕ which prints, plots and performs a variety of linear fits on the (x,y) data. In the future PLOTϕ can be expanded to drive a CALCOMPER.

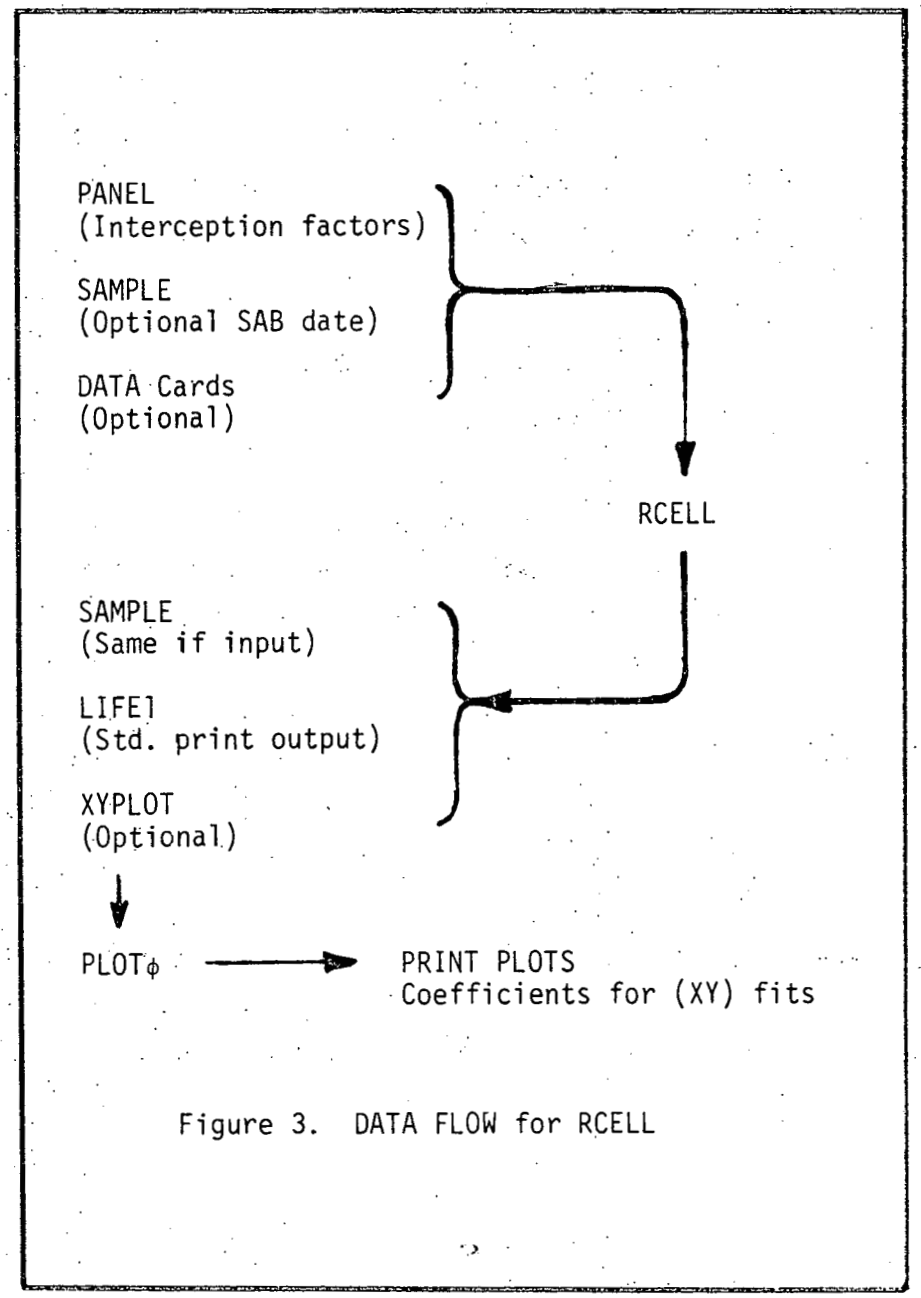

Figure 3. DATA FLOW for RCELL

3.4 Inputs to RCELL

The following list is self-explanatory and is complete except for an alternate source of input for selected variables via the DATA cards after the @XQT card in the executive program.

INPUT DATA

JDVEQ = 2442859	JULIAN DAY OF VERNAL EQUINOX
ALPHAL = .004660	SOLAR LIMB ANGLE IN RADIANS
XLAT = 35.	LATITUDE OF SITE IN DEGREES
ESUND = 15.0	ELEVATION OF SUN AT STARTUP
NGON = 4	NUMBER OF SIDES FOR HELIOSTAT
NTOW = 2	CELLS FROM CENTER TO TOWER
IMAX = 19	SAMPLE HOURS = 3,7,11,...
JMAX = 7	SAMPLE DAYS
NREAD = 66	LINES IN (x,y) DATA FILE ACELL
JTAPE = 1	1 TO WRITE BCELL; 0 NOT
LTAPE = 1	1 TO WRITE SAMPLE; -1 TO READ; 0 NOT
KTAPE = 1	1 TO READ PANEL; 0 NOT
KPANL = 1	FIRST PANEL FOR FINT
NCEL = 1	CELLS ACROSS COLLECTOR FIELD
NGEO = 4	CELLS IN DISPLACEMENT ARRAY
NDIV = 10	DIVISIONS for INTERPOLATOR
ICNTR = 1	0 FOR NO DAILY PRINT; 1 FOR 3 DAYS; 2 FOR EVERY DAY
IAXIS = 1	INDEX OF MOUNTING SYSTEM
ISUN = 1	0 FOR UNIFORM WTS; 1 FOR SINE WTS
HT = 259.	HEIGHT OF TOWER IN METERS
DA = HT/1.41421	SPACING BETWEEN CELL CENTERS
DMIR = 6.502	WIDTH OF HELIOSTAT IN METERS
HGLASS = 37.932463	AREA OF GLASS/HELIOS.
DGEO = 1./10.	CELL SPACING FOR LOSE PRINTS
CMW = 1.44	CM OF ATMOSPHERIC WATER VAPOR
REARTH = 6370.	RADIUS OF EARTH IN KILOMETERS
HATMOS = 8.430	HEIGHT OF ATMOSPHERE IN KILOMETERS
RH = REARTH/HAIMOS	CONTAINS CONSTANTS FOR COST MODEL (100 MWE)
CFIXD = 7.260E6	FIXED COST IN DOLLARS
CTOWR = 8.5E6*((HT-22.)/308.)**2 + 1.86E6*HI/315	TOWER COST
C1 = 66.	HELIO. COST IN $/M2 -- 1ST OPTION
C2 = 83.	HELIO. COST IN $/M2 -- 2ND OPTION
C3 = 100.	HELIO. COST IN $/M2 -- 3RD OPTION
FM1 = 45.6	FIGURE OF MERIT IN $/MWH FOR C1
FM2 = 53.4	FIGURE OF MERIT IN $/MWH FOR C2
FM3 = 61.2	FIGURE OF MERIT IN $/MWH FOR C3
CL = 1.08	COST OF LAND IN $/M2
CW = 3.30	COST OF WIRING IN $/M
NF = 25	HELIOS./FIELD CONTROLLER
BOILER = 1.525	CONV&RAD. LOSSES IN MW/BOILER PANEL

HEATER = .762	CONV&RAD. LOSSES IN MW/PRE-HEAT PANEL
HYEARS = 3315.	HOURS/YEAR FOR SUN ABOVE 15 DEG.
PREPAN = 3	HALF OF PRE-HEAT PANELS
ABSOR = .95	ABSORPTIVITY
REFLT = .91*1.0	REFLECTIVITY AND DUST

3.5 Summary of Outputs from RCELL

LISTING FOR EXECUTIVE PROGRAM
LISTING FOR RCELL INPUTS
INTERCEPTION FACTORS FROM RECEIVER PROGRAM
SLANT DISTANCE FROM HELIOSTAT TO RECEIVER
SAMPLE OF SUN POSITIONS FOR GIVEN LATITUDE
LOSS PARAMETER SUMMARY
LOSSES/YR IN MWH/M2 VERSUS DISPLACEMENT FOR CELL (I,J)
  OPTION FOR NEIGHBORHOOD
  INPUT (x,y) IN HELIOSTAT WIDTH
  OUTPUT (x,y) IN HELIOSTAT WIDTH
  OPTIMUM VARIATION (x,y) (dimensionless mutliplier)
  DAILY KWH/M2 AND ANNUAL MWH/M2 FOR ZERO S & B
  LOSS FRACTION (4 x 4) (λ_c in Optimization Notes)
  TOTAL ENERGY (4 x 4) (E in Optimizaton Notes)
  LAGRANGIAN ENERGY (3 x 3) (E+f∂_fE in Optim. Notes)
  GRADIENT ENERGY (3 x 3) (∂_fE in Optimization Notes)
  TRANSVERSE ENERGY (3 x 3) (∂_fE in Optimization Notes)
OPTIMUM LOCATOR PLOT
  ZEROS FOR ∂_tE = 0
  STARS FOR E_L = E
OPTIMIZED FIELD SUMMARY
  TRIM CONTROL MATRIX
  NUMBER OF HELIOSTATS/CELL
  TOTAL NUMBER OF HELIOSTATS
  TOTAL AREA OF GLASS
  MAXIMUM NUMBER OF HELIOSTATS/CELL
  RCELL FACTOR
  AREA OF HELIOSTAT
  AREA OF SEGMENTS
LAGRANGIAN PARAMETERS FOR OPTIMIZATION
TOTAL ENERGY IN MWH/M2 FOR OPTIMUM SPACINGS
EQUINOON POWER IN KW/M2 FOR OPTIMUM SPACINGS
ACCURACY OF SOLUTION FOR OPTIMUM SPACINGS
FRACTION OF ENERGY LOST FOR OPTIMUM SPACINGS
PARTIAL OF ENERGY BY DENSITY FOR OPTIMUM SPACINGS
TRIM RATIO FOR OPTIMUM SPACINGS
FRACTION OF GROUND COVERED (f) FOR OPTIMUM SPACINGS
ORTHOGONAL COORDINATE (t) FOR OPTIMUM,SPACINGS
FIRST SPACING COORDINATE (x) FOR OPTIMUM SPACINGS
SECOND SPACING COORDINATE (y) FOR OPTIMUM SPACINGS

PERFORMANCE SUMMARY AND COST BREAKDOWN
  EQUINOX POWER

ANNUAL POWER
FIXED COSTS
TOWER COSTS
LAND COSTS
WIRING COSTS
HELIOSTAT COSTS (3 options)
TOTAL COSTS (3 options)
FIGURE OF MERIT (3 options)

3.6 Summary of Theory for RCELL

See Reference 1 for a complete discussion of the optimization theory. The figure of merit is given by

$$F = C_S/E_T,$$

where E_T is the total thermal energy output per year and C_S is the relevant total system cost in dollars. The economic model gives

$$C_S = C_o + C_H(A_T + C_+A_L)$$

$$C_+ = \alpha\sum_c \phi_c + \beta\sum_c \phi_c f_c^{\frac{1}{2}}$$

$$\alpha = C_L/C_H = .0164$$

$$\beta = C_W B/C_H = .0145,$$

where C_o is the fixed cost, C_H is the cost of heliostats/m^2, C_L is the cost of land/m^2, and C_W is the cost of wire/m. A_L is the area of land/cell, ϕ_c is the fraction of cell included in the field, and f_c is the ground coverage in the included part of the cell.

A_T is the total area of glass in the collector field, and is given by

$$A_T = \sum_c A_c = \sum_c \phi_c f_c A_L,$$

where $\sum_c$ represents a sum over cells in the collector field. The total thermal energy is given by

$$E_T = \sum_c E_c \eta_c = S_o(\sum_c \lambda_c \eta_c A_c),$$

where η_c is the interception fraction which is input from the PANEL file, S_o is annual total direct beam insolation as discussed in appendix B, and λ_c is a dimensionless efficiency for cell c. λ_c depends on shading and blocking events which can occur throughout the year.

At this point we parametrize the collector field neighborhood at cell c. Let (x_c,y_c) represent the radial and azimuthal spacing coordinates in units of heliostat width. We have

$$f_c = a_c/x_c y_c$$

and it is useful to define a shape parameter

$$t_c = \tfrac{1}{2}(x_c^2 - y_c^2),$$

so that

$$\lambda_c(x_c,y_c) = \lambda_c(f_c,t_c).$$

The functions (f_c,t_c) form a system of orthogonal hyperbola as shown in Figure 4.

According to Reference 1, at the optimum point (x_c^*,y_c^*), we have

$$\tilde{\mu} = \mu_c(x_c^*,y_c^*),$$

and

$$0 = \partial_t\lambda_c(x_c^*,y_c^*),$$

where

$$\tilde{\mu} = C_H/(FS_o)$$

and

$$\mu_c(x_c,y_c) = (\lambda_c + f_c\partial_f\lambda_c)\eta_c.$$

4.0 TYPICAL RESULTS FROM RCELL

Table 2 shows a typical performance summary from RCELL. The more interesting (x,y) outputs are print plotted by PLOTϕ. Some early results are shown in Figures 5 and 6. Remember that RCELL may be iterated for three reasons:

1. to converge the input figure of merit to the output figure of merit;
2. to reduce the step size in the sample of variations in order to better approximate ∂_f and ∂_t; and
3. to converge the output power on the design day

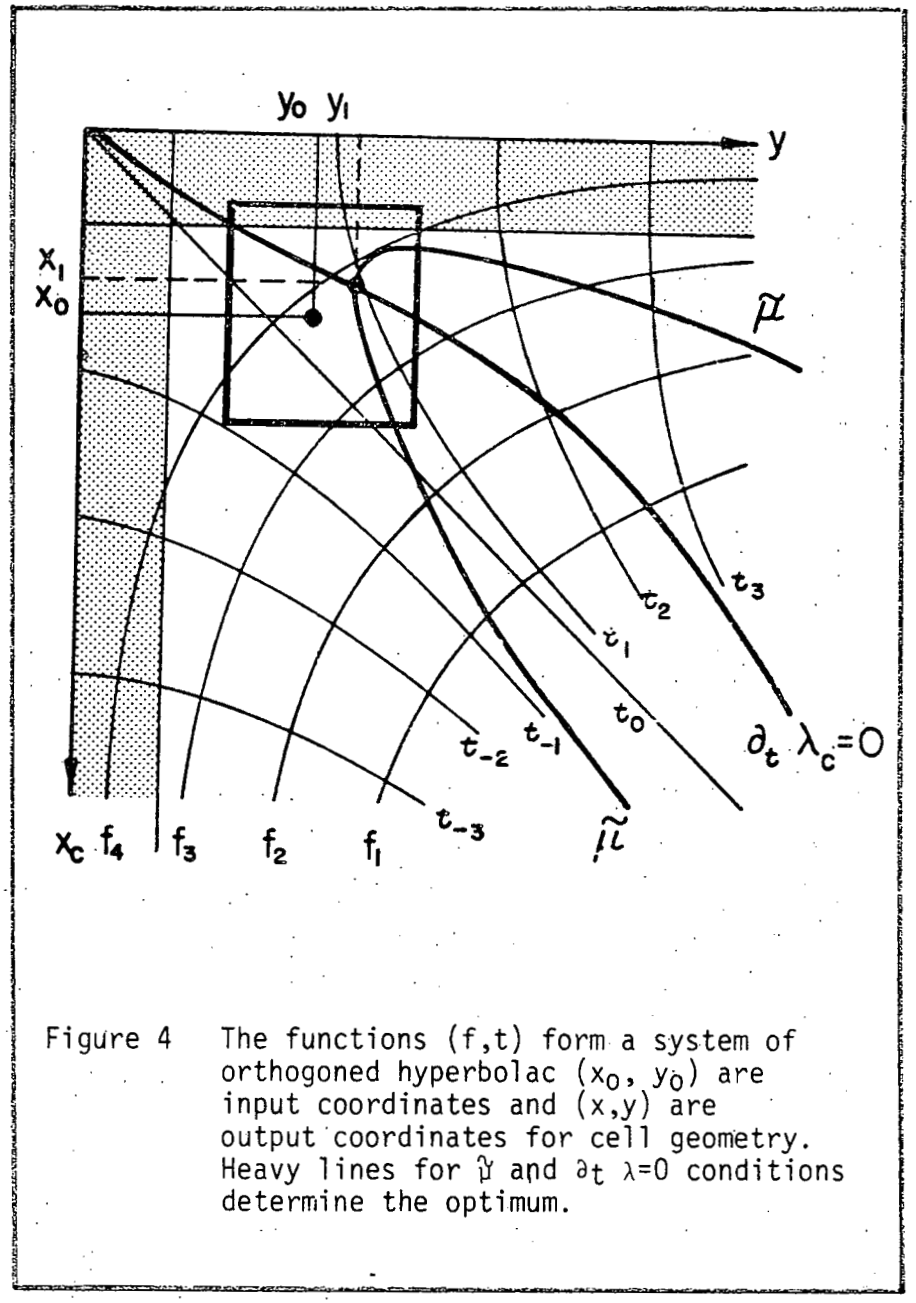

Figure 4 The functions (f,t) form a system of orthogoned hyperbolac (x_o, y_o) are input coordinates and (x,y) are output coordinates for cell geometry. Heavy lines for $\tilde{\mu}$ and $\partial_t\ \lambda=0$ conditions determine the optimum.

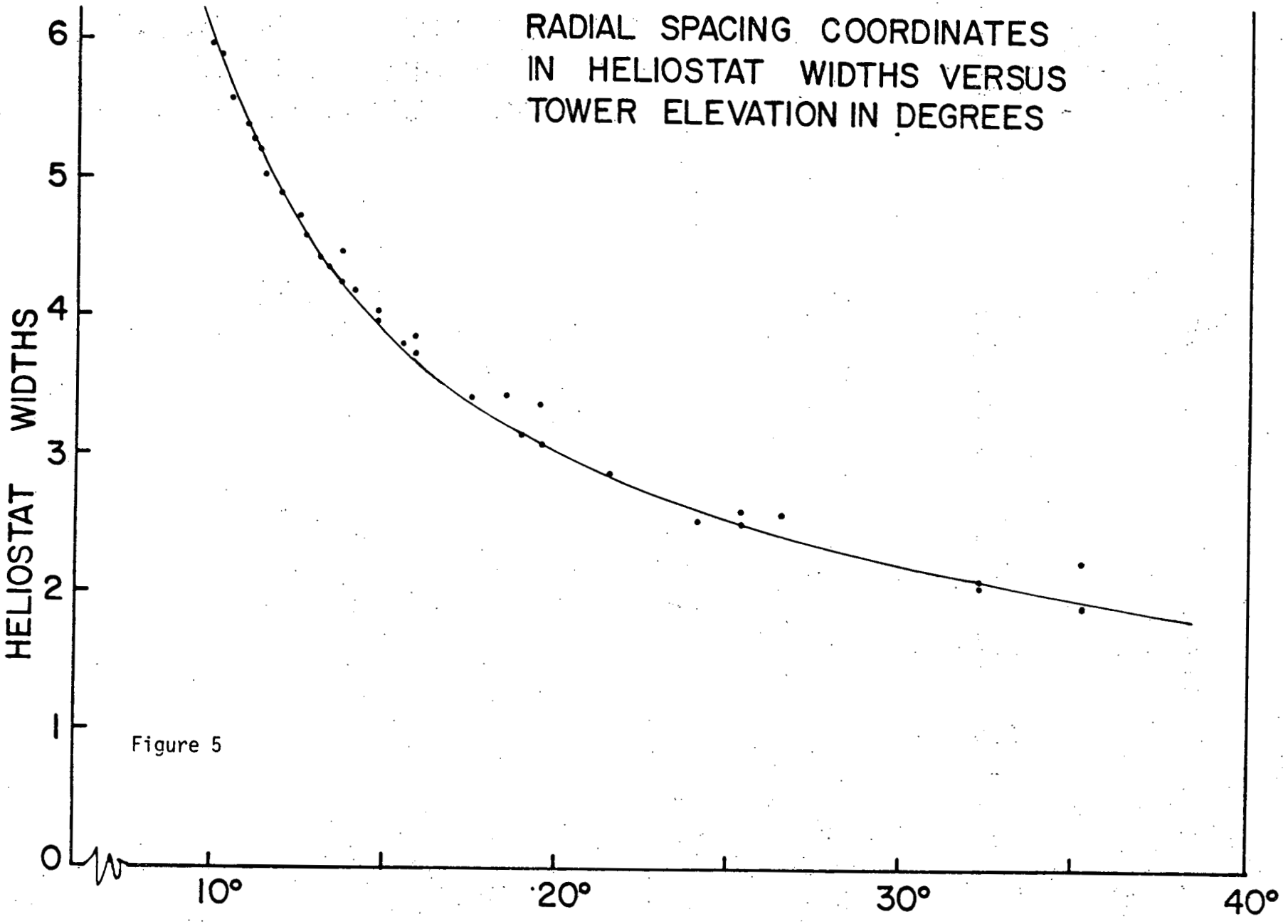
RADIAL SPACING COORDINATES
IN HELIOSTAT WIDTHS VERSUS
TOWER ELEVATION IN DEGREES
HELIOSTAT WIDTHS
0
1
2
3
4
5
6
10°
20°
30°
40°

Figure 5

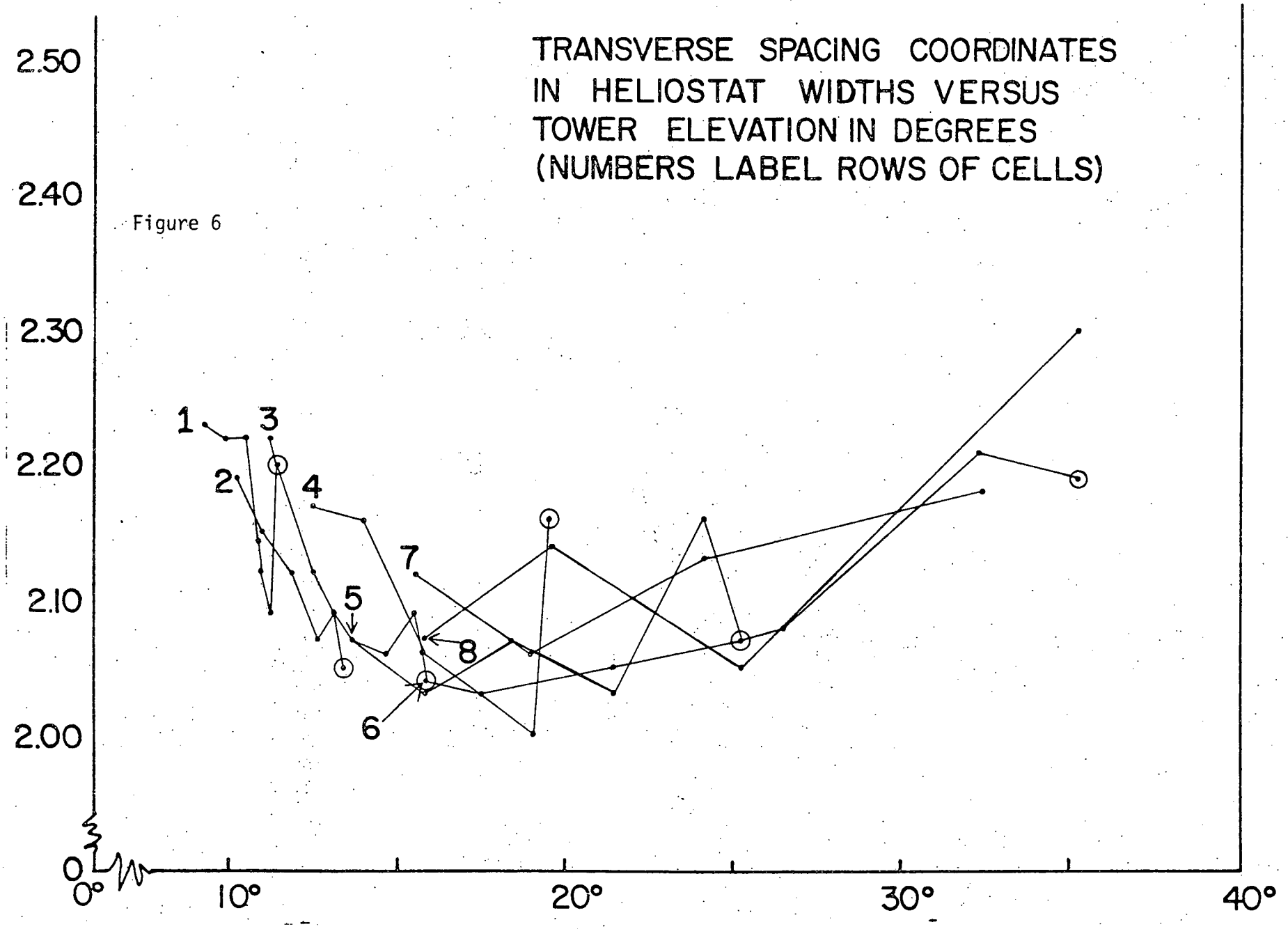
TRANSVERSE SPACING COORDINATES
IN HELIOSTAT WIDTHS VERSUS
TOWER ELEVATION IN DEGREES
(NUMBERS LABEL ROWS OF CELLS)
2.50
2.40
2.30
2.20
2.10
2.00
0
0°
10°
20°
30°
40°
1
2
3
4
5
6
7
8

Figure 6

to the design requirement. (This is achieved by adjusting the tower height and computing new PANEL files.)

Only the step size adjustment can affect the scatter in the (x,y) plots as shown in Figures 5 and 6. Experience shows that some points will converge as the step size is decreased but most will not. This is due to accidental shading and blocking behavior in certain cells which cannot be completely averaged out. However, caution is needed in these interpretations because the sun sample may not be good enough in some cases.

We conclude that the expressions

$$x = A/\theta + B + C\theta,$$

and

$$y = D,$$

where

$$\theta = \tan^{-1}(H_T/(x^2 + y^2)^{\frac{1}{2}})$$

represents the collector field geometry for field layout, in terms of the constants A, B, C, and D.

5.0 THE LAYOUT PROGRAMS

5.1 Introduction to the LAYOUT Programs

The RCELL program determines the collector field geometry at selected representative points in the collector field without regard for the interaction between neighboring cells which occurs when an actual layout is attempted. If each cell were filled with a uniform field having the (x,y) spacing parameters output by RCELL the mismatch at cell boundaries would be very costly in terms of deleted heliostats. The boundary problem will still occur if an attempt is made to blend the cells instead of filling them with uniform arrays. But fortunately, the results from RCELL indicate that circular fields are very near optimal, so that only zonal boundary problems occur. Figure 7 shows the structure of the LAYOUT programs.

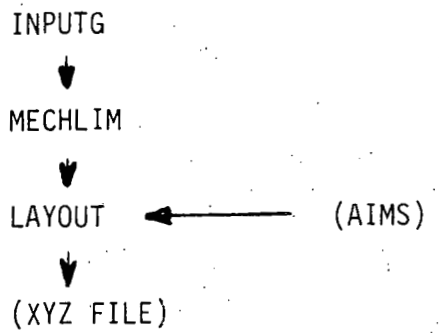

Figure 7. Structure of LAYOUT Programs

5.2 The COMMECH Subroutine

The results of the RCELL optimization program suggests that the field of heliostats for the commercial system consists of concentric circles of heliostats with the tower at the center. The subroutine COMMECH is designed to utilize the information provided by RCELL to produce the commercial system's set of heliostat coordinates. In addition, a minimum spacing, or mechanical limit, is imposed such that no two heliostats are allowed to be closer than the measure specified.

COMMECH is called by INPUTG, the initializing and calling program, and determines the radii and azimuths of the circular field. A starting radius is the largest of all circles to be generated. A maximum azimuthal spacing is chosen for the first circle. A radial spacing function, produced by RCELL, generates the next two circles, each having the same angular spacing between their heliostats. This process is repeated until the azimuthal spacing along the arc reaches a specified minimum. At this point, the number of heliostats on the next circle is reduced by some integer ratio (for example, 7/6 or 4/3). This is turn gives the maximum azimuthal spacing along the arc for the first circle in the new zone as well as the new angular separation which remains constant until the next zone is encountered.

A zone contains a group of successive circles having the same number of heliostats per unit azimuthal angle. Zone boundaries occur when two neighboring circles have different azimuthal spacings. For counting purposes, the vectored variable ISLIP is assigned the value one for the first circle in each zone and is zero for all other circles. The circle preceding this first circle usually has deleted heliostats due to excessive blocking so that the number of heliostats on it is the same. However, deletes are reckoned within another subroutine which calculates actual coordinates based on the occurrence of unity in the ISLIP vector.

Each zone is required to have an odd number of circles to expedite the layout of a symmetric field. The exception is the last zone which terminates at an exclusion radius. No heliostats are permitted within the exclusion radius. Should the last circle in a zone give that zone an even number of circles, that circle becomes the first circle of the next zone to meet the above requirement.

In addition to the starting radius, which defines the outermost circle, a trim vector RSECT is obtained from

RCELL. RSECT contains the angle at which each circle of heliostats terminates. This angle is measured from due South. For instance, if RSECT is 45° for a certain circle, it terminates Southeast of the tower, and Southwest of the tower due to the symmetry of the field. This effect is expected for the Northern latitudes where an optimum field has more heliostats North of the tower. RSECT can be input as data or can take a functional form such that the trim angle is a function of radius. RSECT is never zero for a circle, because there is a road south of the tower which is currently 66 feet wide. If the input function or data gives zero, a default value of the RSECT is calculated based on the input width of the South road.

Throughout the calculation of radii and azimuths for the field, mechanical limits must be satisfied. The minimum spacing between heliostats on the same circle as determined from RCELL is well above the limit. Likewise heliostats located on a radial line from the tower are spaced well above the mechanical limit since they are separated by another circle of heliostats according to the radial stagger procedure. The intermediate circle contains heliostats that are located neither radially nor tangentially from a given representative. They are located on a diagonal or spiral that runs through the field and constitutes the only important consideration for mechanical limits. The distance to a diagonal neighboring heliostat is calculated at each circle as the radii are being constructed. If the distance is shorter than the limit, the radius of the inner circle is reduced until the mechanical limit is satisfied. Then the calculation is repeated for the circle of reduced radius, until all diagonal radii are properly separated. This includes the more complicated computation involving those circles near a zone boundary which may have changed azimuths in the vicinity of a deleted heliostat. See Figure 8.

The field is currently divided into eight 45° sectors. Based upon this circle-sector cell model, the following outputs are produced in addition to those mentioned above: The ground area per cell and the number of heliostats per cell are displayed as well as the fraction of ground covered by heliostats in each cell. Fractional (I,J) values are also output for correlating the location of the circle-sector cells with the (I,J) cells from the RCELL program.

COMMECH generates the radius of each circle, the azimuth, the RSECT and ISECT vectors and NROW, which is the number of circles. COMMECH outputs to a subroutine

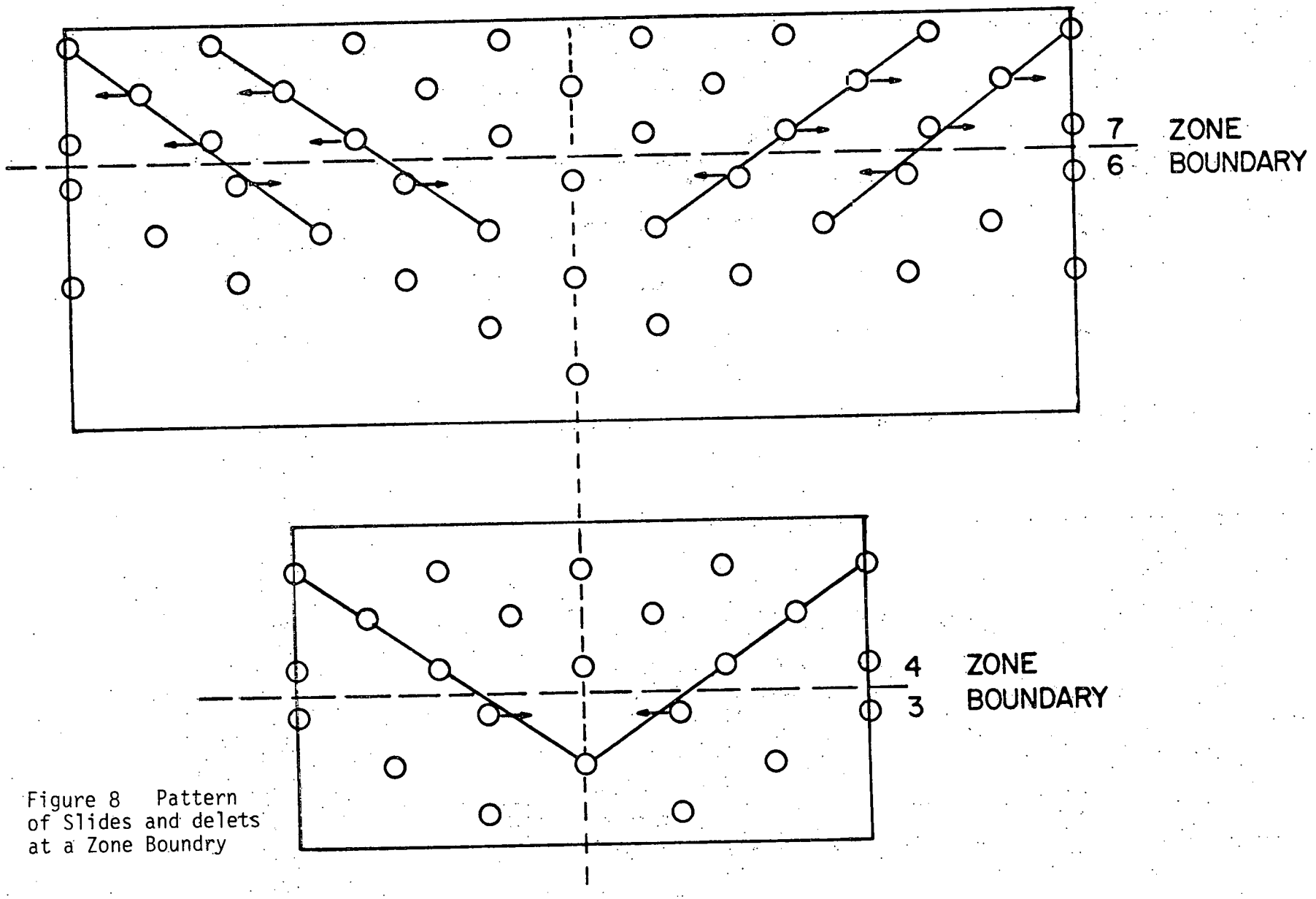

Figure 8 Pattern of Slides and delets at a Zone Boundry

called COMMLAYOUT.

5.3 The COMMLAYOUT Subroutine

The actual (x,y) coordiantes for the commerical field are generated by the subroutine COMMLAYOUT. The subroutine is called by COMMECH which supplies the information needed to produce coordinates. If aiming points for the heliostats are supplied in terms of (I,J) or circle-sector cell locations, each heliostat can also have a specific aiming point assigned to it in terms of a positive or negative vertical displacement on the receiver.

The main portion of COMMLAYOUT consists of a loop which runs from one to NROW, the number of circles in the field. At each circle the proper internal subroutine is called according to the position of the zone boundaries as determined by ISLIP. Once a specific set of azimuthal slides and deleted heliostats has been determined for the chosen zone ratios, i.e., 7/6 or 4/3, specific internal subroutines can be constructed and called when appropriate.

The internal subroutines are simple in principle since all the heliostats are constrained to a certain radius. This leaves only the azimuth to be determined in light of heliostat deletes, slides and the trim angles contained in RSECT. The first and last circles in a zone are begun a full azimuthal spacing off of due North and continue clockwise until the trim angle is encountered. Between the first and last circles of a zone, the starting point alternates between a half and full azimuthal spacing off of due North. This results in the radial stagger layout. Heliostat locations due North of the tower are not included because a North road is assumed.

An aiming point is assigned to a heliostat based on input data for (I,J) or circle-sector cells. After the (x,y) location has been calculated, the heliostat is determined to lie within a certain cell which is associated with an aiming point. The aiming points alternate in sign along a circle incorporating the two point high-low aiming strategy.

The coordinates and aiming points are dumped to a tape and/or print file one circle at a time. For the symmetric Western half of the field, which is not output, one need only replace the positive y coordinates by their negatives.

APPENDIX A. REMARKS CONCERNING THE SEL/UH COMPUTER PROGRAM REFERENCE MANUAL AND CODE CENTER

Having just given out copies of the Reference Manual, let me hasten to add that all suggestions in regard to the code center and the Reference Manual are welcome. The manual will serve to identify programs. It will provide a current list of references, and it can serve as a log for ingoing and outgoing programs at the code center. I have made an effort to organize the various approaches to the simulation problem. There is also a list of components which are required by the central receiver system model. Obviously, this list needs enlarging.

APPENDIX B. ANNUAL INSOLATION VERSUS LATITUDE AND STARTUP ANGLE

At the end of the manual there are three extra tables which can be considered as dessert after a salad of programs. The tables give annual sunlight hours, annual direct beam energy at normal incidence and annual direct beam energy at horizonal incidence versus latitude and startup angle. Each entry represents an integral over the year for a given latitude and startup angle. Startup angle delimits the daily time integrals to that portion of the day for which the solar elevation angle exceeds the startup angle. Diurnal and annual motion are uniform but solar obliquity, declination and mean longitude follow the Nautical Ephemeris Handbook formulas. Compensation for varying solar distance is included but the year is symmetrized about the solstices which misrepresents solar distance to some extent. These tables represent a guassian quadrature based on 35 points/day and 37 days/year. The integrated sunlight hours would be exact, except for effects due to the equation of time which render the north and south latitudes slightly asymmetric. The direct beam insolation at normal incidence is based on Allen's clear air model which is somewhat optimistic. We have assumed sea level and 1.44 cm of water.

It is interesting to consider the startup losses at 35° of latitude, assuming a 15° startup angle. The tables show

- 22.0% losses for the sunlight hours,
- 13.3% losses for the direct beam at normal incidence, and
- 3.7% losses for the direct beam at horizontal incidence.

The central receiver system makes reasonably efficient

use of the direct beam at normal incidence so that the 13.3% figure becomes a rough estimate of startup losses. Notice that this is the largest single loss in the system, except for the sunlight which hits on the ground.

The question of land use can be considered as follows. A typical central receiver system may deliver a total thermal power $P_t = 1.534 \times 10^6$ MWH/YR at the base of the tower. This system requires $.869 \times 10^6$ m^2 of glass at a ground coverage of .261, so that the total land used is given by

$$A_L = .869 \times 10^6/.261 = 3.33 \times 10^6 \ m^2 .$$

Consequently, the energy density of useful thermal power per square meter of land is given by

$$P_T/A_L = 1.534 \times 10^6/3.33 \times 10^6$$
$$= .461 \ MWH/m^2YR,$$

which compares to 2.014 MWH/m^2YR for the annual direct beam at horizontal incidence, 35° latitude and 15° of startup. The efficiency of land use becomes

$$\eta_L = .461/2.014 = 22.9\%.$$

For a comparison we can formulate the efficiency of glass use as follows. From the tables, we see that

$F_N = 3.214$ MWH/m^2YR at normal incidence,

and

$F_H = 2.014$ MWH/m^2YR at horizonal incidence

assuming 35° latitude and 15° of startup angle. The efficiency of glass use becomes

$$\eta_G = (P_t/A_T)/F_N$$
$$= 1.765/3.214 = 54.9\%$$

Clearly, $F_H/F_N = .627$, and

$$\eta_L = (F_H/F_G)\ f_G\eta_G$$
$$= 1.596 \times .261\eta_G = .417\eta_G$$
$$= 22.9\% .$$

We feel that this is an adequately good use of land, and compares favorably to photosynthesis.

REFERENCES

(1) Lipps, F.W., and L.L. Vant-Hull, A Cellwise Method for the Optimization of Large Central Receiver Systems, accepted by SOLAR ENERGY.

CONCLUDING DISCUSSION

INTRODUCTION

The two-day workshop concluded with a general discussion Thursday afternoon, August 11. The discussion covered a number of issues summarized in the following pages. Major points of discussion were:

1. The desirability of additional workshops sharing information on Central Receiver Systems.

2. The establishment of a bibliography of materials related to Central Receiver Optics: e.g. ERDA reports, publications by those working in the field, and relatively inaccessible information from abroad, such as Russian papers.

3. Standardization of terms in a glossary.

4. Standardization of terminology in the treatment of radiometric quantities.

5. Preparation of a standard set of initial inputs to enable valid comparisons of different models, such as programs similar to MIRVAL.

6. The need to correlate simulations with well instrumented and well defined experiments.

7. The need to estimate the accuracy of a result, for example, by keeping track of the number of cones contributing to a particular answer.

8. Availability of codes and the extent to which data are of a proprietary nature.

9. Maintenance of codes for retrieval in a nationwide system with the capability of allowing the programmer to update data [Code Center].

10. Provisions for including information about sucessful transfers of a code from one computer to another in the central data bank [Code Center].

11. Code Exchange. "Standard" Fortran.

12. A common Insolation Model.

13. The publication of an aperiodic newsletter to involved and interested personnel and firms.

14. Problems in studying stochastic data in the analysis of flux distributions; problems in determining the effects of systematic or stochastic process on flux distributions and on overall system performance.

1. The desirability of additional workshops sharing information on Central Receiver Systems.

2. The establishment of a bibliography of materials related to Central Receiver optics: e.g. ERDA reports, publications by those working in the field, and relatively inaccessible information from abroad, such as Russian papers.

3. Standardization of terms in a glossary.

5. Preparation of a standard set of initial inputs to enable valid comparisons of different models, as formulated in programs such as MIRVAL.

Roy Lee, Sandia Laboratories: I would like to thank all the speakers and participants. I feel it has been very useful and very helpful to listen to all the different talks on codes and techniques. I think it has been a very useful workshop, and I'd like to see others organized in the future. In the last two days, people have talked to me about possible things that we might want to discuss. For example, Professor Riaz had mentioned a possible set of standard inputs for code verification among the different codes.

Prof. M. Riaz, Electrical Engineering Department, University of Minnesota: Well, I've a list of four items that I thought might be of some interest. First, everybody who attends here might provide Lorin Vant-Hull with a complete listing of references that can be added so that we have a library. Probably most of the people working in the field are here and yet are not always aware of what everybody else is doing. The list should include available literature, not internal memos; certainly ERDA reports and literature you have discovered from abroad that others may not know of, Russian or French papers, for example.

Riaz: That's one set of comments. The other, which I have mentioned, in part, was some sort of a suggestive glossary or nomenclature of terms so that there might be some sort of standardization; so we agree, for example, whether zero degrees is north or south and whether an angle gives altitude with respect to the vertical or the horizontal; I can never be quite sure.

Riaz: Then it appeared to me that we've seen a number of approaches and very similar answers in many cases. At least for my own edification as an outsider, I would like to see a comparison eventually being performed. That's perhaps the idea of MIRVAL. I'd like to suggest that the comparison can be done by hypothesizing a case where we all agree on an arbitrary set

of inputs simplified at the outset and see what the outputs are. Let me just take, for example, Albuquerque. We know the size of the mirrors, and we know where they are, and we've decided on a tower and a particular receiver. With a certain set of assumptions, no guidance, no tracking error to start with, let's compare some of these outputs that you'll have available, using the same insolation models so that one can see the features in terms of length of time taken. That's something that would be very useful for an outsider like myself, and, I would assume, for ERDA, as well.

4. Standardization of terminology in the treatment of of radiometric quantities.

R. H. McFee, McDonnell Douglas: I am sure we would be very happy to participate in running a problem which has been submitted to various organizations. Another area, too, I think that really needs to be cleaned up is the proper terminology in what we call radiometric quantities. As an example, when you are talking about watts per square meter on the surface, you may talk about flux density. You talk about power received; you talk about flux. This has been used very carelessly. I don't think it's nitpicking; I think it is a basic thing that should be considered seriously to effect proper communications. Use the proper terms when we are discussing various quantities we wish to inter-compare.

6. The need to correlate simulations with well instrumented and well defined experiments.

Participant: Along that line of the sample problem, it would be nice if the sample problem could be selected as one where measurements were either on the way or planned because we get various ranges of results. The experiment might play a role in deciding which model is best, rather than trying to argue it out in pure modeling.

C. L. Laurence, Aerospace Corp.: Yes, I really feel the ultimate determination should be whether or not it agrees with what we would consider to be the best

6. The need to correlate simulations with well instrumented and well defined experiments.

available experimentation.

McFee: Well, what if it's not a clear-cut experiment. This is not an easy thing to come by because you may find it is very difficult to really know the parameters under which the experiment is conducted.

Lee: That's what we do at the test site.

Participant: It took them a long time to correlate the results of the Odellio test.

George G. Schrenk, Department of Mechanical Engineering, University of Pennsylvania: But it is certainly better to work against the experiment as a check, even though you would rather argue against one another for models.

Lee: That's why I suggested the test at Albuquerque as a reference.

Charles N. Vittitoe, Sandia Laboratories, Albuquerque: [Measurement is] one place where we learned from Odellio. For our tests there, we had built specific pieces of measuring equipment that we had gone to great pains to make as accurate as we possibly could for measuring full field intensities. So at Albuquerque, (the SMW STTF) we will have the capability to give you a wide selection of data of what's going on. We have, for instance, equipment to measure aerosols in the air, if you want to include that.

We have a circumsolar telescope there. We can get the data at the same time. We'll have a measuring system which will be available in the same November or December time frame, as will the field heliostats, which could be used to measure an actual full field. And, of course, we have the conventional equipment such as pyreheliometers, Eppleys, as well as a Kendall

7. The need to estimate the accuracy of a result, for example, by keeping track of the number of cones contributing to a particular answer.

(which is a much more accurate instrument). And a wide range of instrumentation certainly will be available in a November or December time frame. I think we could give you good information and probably more than you could use.

Lee: I think confirmation of experimental data is probably the best test. On the other hand, some times it might be kind of a complex type of thing to set up to go in terms of insolation, etc.

Vittitoe: Seems there's a need for several types of tests, too, because there are several parts to all the codes--maybe a one facet test, a one heliostat test, and a one field test.

Schrenk: I concur with that; I think therein lies the test of the basic models. It is best not to compound too many things together at the start. Deal with a single heliostat or a single concentrator. Deal with something that you can well define. Then worry about building up the field complexities, the shading and blocking, and all the other things you are going to fold into the systems model.

McFee: This will be set up in stages.

Schrenk: Yes, Set up in stages and concentrate first with the basic problems.

Lee: And then, maybe the final stages--

Participant: The final stages will be with the total system that you will simulate as far as the thermal system.

Schrenk: One specific comment continuing along this line but toward specifics on the codes, those codes that use cone concepts. We've seen a lot of approxi-

2. The establishment of a bibliography of materials related to Central Receiver optics: e.g. ERDA reports, publications by those working in the field,

mations of curved surfaces, planer surfaces, and so forth, by single cones. I'd like to urge a word of caution in this respect. If your image size is large compared to the facets you're approximating by a single cone . . . . that's a necessary condition for your approximation to hold; it's not a sufficient condition. And the reason I say it's not sufficient is the fact that you've got to be near the zone of focus. If you get away from that, you're going to get approximation errors, and you're going to approximate, for example, a smooth surface by planes and, depending on how you subdivide it, you get quite different results and scatter as you get away from the focal zone. So a suggestion I'd like to make as a handle for accuracy, a back of the envelope approach, is keep track of the number of cones contributing to a particular answer.

McFee: Oh, yes, I agree with that.

Schrenk: So that if you've got ten cones as a back of the envelope approximation to a particular answer, well, if you add one more, that's ten percent. A very simple approximation. On the other hand, if you have two cones, beware. That gives you a judge as an approximation and it would be useful, I think, to know some of these numbers. Perhaps, some people are already bringing them out, but I think it's useful as a general rule to deal with this type of number as a feel for approximate accuracy.

Lee: You certainly want to look at the sensitivity [to consider] how good the approximation is.

Lee: Here's another area. Phillip Torvinen, not here now, mentions [setting] up a bibliography, as Professor Riaz also mentioned. I wonder where we should have that set up. Where is the central place that we can put [it]? Houston will have the code

and relatively inaccessible information from abroad, such as Russian papers.

13. The publication of an aperiodic newsletter to involved and interested personnel and firms.

11. Code Exchange. "Standard" Fortran.

8. Availability of codes and the extent to which data are of a proprietary nature.

center. I was wondering whether the documentation should also be a part of the center.

Vant-Hull: Perhaps. I am sure we would be willing to do that.

Schrenk: In that respect, a newsletter or periodic publication that would carry this type of information could be very useful.

Lee: Perhaps it would be a good idea [not to publish] unless information had been obtained and [first] circulated around.

Vant-Hull: Something like an aperiodic update to the reference volume on our existing codes which Fred Lipps [Solar Energy Laboratory, University of Houston] distributed earlier.

Schrenk: And along with that, it could carry listings of different programs, whether they would be in a code center or not. Also, a synopsis of different people working in different areas would be useful. What codes are around? [Are they] in your library or not? What are the different codes around? And who has them? What's the purpose of each code?

Lee: Another area that quite a lot of people are asking about is the code exchange, of course, and there are lots of problems in relation to code exchange. One of the primary problems is the proprietary type problem. I was wondering, just as a matter of curiosity, [if] that wasn't quite decided on by each individual contractor or company. How many of those codes are actually proprietary and how many are actually going to be released to the public?

McFee: Our code [McDonnell Douglas] at the present time is . . . considered to be basically proprietary.

However, I think there's a good chance that the management will make a decision to make it available on some sort of basis. I can't say myself at the present time.

Lee: I assume the Houston code will be released to the public.

Vant-Hull: You bought it. [laughter] Or paid for it, anyway.

Lee: How about the Honeywell code?

Gary Smith, Honeywell, Inc.: We delivered that to ERDA.

Lee: So that will be public domain. How about Boeing?

Mark Rubeck, Boeing Engineering & Construction: Boeing's code is also ERDA property now. That's the simulation code. The optimization program is proprietary.

Lee: The optimization is proprietary. Let's see, what else?

Fred Lipps, Solar Energy Laboratory, University of Houston: The two Sandia codes. I take it they're both non-proprietary.

Lee: Yes, they are in the public domain--when they are ready for release. When it is internal, we don't want to release it. But when it's ready for release, it will be released.

Frank Biggs, Sandia Laboratories, Albuquerque: HELIOS has already been transferred to several external agencies. We will continue to do that with

9. Maintenance of codes for retrieval in a nationwide system with the capability of allowing the programmer to update data [Code Center].

ERDA approval even while it's evolving. Georgia Tech has it [and] several other places.

Lee: I think that as long as it is not related to contract applications we need ERDA's approval on a case by case basis for distribution of MIRVAL or HELIOS.

Lipps: With regard to the code center, it may be that it doesn't have to be localized. For instance, it doesn't matter to me whether a user obtains MIRVAL from me or from Livermore. If I put it in here (our user's document) with an explanation of what it is, I can say right there where to get it. We don't have to have it just so someone else can get it.

Lee: You'd think that one performs a service distributing it. We certainly appreciate that.

Lipps: Well, we don't have to be the middle man, do we?

Lee: I don't know.

Vant-Hull: We can distribute it if you like. We probably can't read the code at the moment. So, it might be the people would rather get a copy from the author rather than from someone who is simply maintaining a copy of the code.

Lipps: That's exactly right. If all of you are CDC people, then why bring it over here and try to service you from our Honeywell computer?

Lee: In that sense, then, the code center will be just an information documentation depository.

Lipps: Sure, all I have to know is the name of the code, where it is, and what documents are on it.

Vant-Hull: I think in the long run that we would be interested in having the codes and translate them onto our computer and perhaps do some interchanges, but that's a long term effort--on the level we are working now.

Schrenk: Go a step further than that. I think the really key role is information exchange, and the code is secondary. --That is as far as the actual punched cards can make out from your local machine. What I'd like to suggest is that those who want to make the codes available or plan to make them available consider maintaining those codes on nation-wide services. For example, those with CDC codes consider maintaining them on CDC Cybernet, which means that you no longer have to transport them from computer to computer and deal with compatibilities. You have the creator, who can maintain that code on a big machine, one similar to what he's developed it on, and anybody that wants to us it contacts CDC, pays for the time, and goes and uses it.

Lee: Well, you know, not everybody's on Cybernet.

Schrenk: It's available in practically every big city in the country. You can call your local CDC office and walk over to the terminal, drop your cards in and use it. That deals with the compatibility problem.

Lee: I agree, but most of the time you'd like to run it in your own computer, and using the commercial CDC is an expensive operation.

Schrenk: Shall I simply say the problems of realistically transferring many thousand card programs across computers become very difficult; even the same manufacturer's computers have many machine-dependent special features. When you cut across machines from

CDC to IBM, good luck. You've a major rewrite on your hands. And then you have to question the validation against [the author's meaning], or have you made some changes that louse something up or change something. I'd like to really encourage the original creator of the code to maintain it on a nationwide service to make it available.

Lipps: Well, we can put such information in the manual. If it is on a Cybernet system, we can put it in as such. But mostly I think we're not dealing with conversational computers.

Schrenk: The Cybernet is not conversational and doesn't have to be. Cybernet is bulk Fortran and remote access. So I'm not talking APL. APL's another system, but Cybernet happens to be the nationwide CDC hookup with remote access so that you can maintain any program you want in the system.

Lee: Yes, that's one approach. But if you don't have a Cybernet hookup and you have to go to Cybernet, you might just as well go to the source rather than pay for time.

Schrenk: Well, but you don't. Cybernet has an operative program. You don't have to get the punch cards and fight the compatibility. There's a source deck called Cybernet Source and object decks there, or maybe just object decks alone, and you're essentially putting the input into the program. So it's like walking into Sandia, for example, for MIRVAL, and having the thing already operational. All you [must do] is create the inputs and drop it into the hopper, drop the proper cards in and use it.

10. Provisions for including information about sucessful transfers of a code from one computer to another in the central data bank [Code Center].

Participant: Along these lines, if someone does successfully transfer codes from one computer to another, that might be valuable information to put in the data bank.

8. Availability of codes and the extent to which data are of a proprietary nature.

Lee: That's a good suggestion. See how many codes had been implemented in combination.

Vant-Hull: I don't believe you finished your list of proprietary codes. For example, Black and Veatch?

Lee: Oh, yes. I assume it will be proprietary and will not be released to the public.

Edward J. McBride, Black & Veatch: Black and Veatch has never specifically considered the terms and condition on which we would release the codes, either for use as a sealed black box or as an open listing. If there are serious prospective users, I would suggest they call me at Black and Veatch. I will not be the person who will make that decision. I don't even know who will make it now, which is why I suggest you call me, and I will make sure that within a day or two I do have the name of the person at Black and Veatch who will be making the decisions under what situations our codes would be released. We're totally flexible at the moment. It would probably be the easiest code to transfer in the sense that a person can call Scientific Time-Sharing and get a user number and through internal software modifi--not modification--I just type the number into my machine, and you can dial your local number and you can use the code. I have to know your number, and I'll have to know your log, but I just have to know what number you want to load it onto, and I have to give you certain information. And then you can call up and use it. So all that's necessary is that we do it beforehand. There is no possibility of converting the code to any other system.

Lee: Let me ask a related question. Will you supply all the information to Houston's code center, [in] this form and give them a tape or whatever?

McBride: I can't speak for Black & Veatch management, but there are two chances of it happening--slim and none. [Laughter]

Vant-Hull: There's the intermediate level where you might maintain your proprietary rights to it. Give us documentation on it for users so that people can find out by looking at our library whether they want to go to your codes.

McBride: That involves one small problem, and it's just whether there are potential users. We have not spent our time and money developing the type of users' manual that someone not familiar with the code would need to use it. Now every code has little tricks. You remember not to put the heliostat locations at integer points, but you always add .001 meters. Little things you just remember. I mean occasionally things happen. Our users' manual for internal use enables me and the people that work with me and for me to use the codes. But if they have a little mistake, they can walk eight feet and say, "Hey--I forgot." Unless there are serious prospective users, I do not know whether we would spend our time and money developing that manual. Obviously, the one we have is near what you saw today.

Vant-Hull: Which is nearly enough for someone to decide whether he would like to use your code. And I'm suggesting, in that sense, that you have already put this into a publication manual.

McBride: I'm sure something of that nature can be arranged with no problem.

Lee: How about Aerospace?

Laurence: Anything that we have, with the permission of anything we might have gotten from somebody else,

would be available. Presently, we have a program that has been specialized for use in the pilot plant evaluations. So, primarily, it's got all the geometries. The basic theory and operation of the program is the theory shown by Ray McFee. That's the [issue of] basic equations and fundamental techniques, and so forth. It has been changed a lot, expanded a lot to fit all the various geometries and the various techniques that have been advanced for the pilot plant designs. But since it does contain Dr. McFee's techniques and equations, and so forth, we couldn't release it unless McDonnell Douglas said it was okay.

Vant-Hull: And then one might be better off getting it from them, where it would not be specialized.

Laurence: The two versions are different. We've gone our way, and he's gone his.

Lee: You know, in the future, if there are other projects that are related to the pilot plant and a prospective contractor wants to use that, I can tell you, it remands to the public to be certain he can use it. No other comment on this area of proprietary codes?

11. Code Exchange. "Standard" Fortran.

Yesterday afternoon, Lorin, Fred, Mike, and Steve Orbon and myself talked about code exchange. Our problem involves code exchange, especially between different computers. There are problems even between the same computers. The result of that conversation is that maybe there should be some kind of standard required of people who generate codes so that the "portability" problem would be easier.

Lee: You know there is such a thing as ANSI Standard Fortran, which essentially all computers can accept. Maybe, some people should try to use some kind of standard set of graphics, statistical packages etc.,

for ease of exchange.

McBride: Most of the codes that we're talking about here are not proprietary, with development via ERDA funding many of them. Isn't the problem not so much developing a set of standards, but implementing one? We've never developed a code that I know of at Black and Veatch under ERDA funding, so I'm just a little bit ignorant on this. But I personally worked at Boeing one summer, and I was writing some computer software in Fortran for the Air Force, and I had a rigid list of rules that I was required to comply with. Is it possible that the rules have just not been enforced, rather than needing rules?

Lee: There are no standard rules, for example at ERDA. I'm sure if you'd been in the Army, they might have better guidelines.

Laurence: I was wondering about the ANSI; is it standard FORTRAN? If you stick to those rules, do most computers compile it?

Lee: Well, with some minor modifications.

Laurence: Because I invoked an option on our CDC that tells me every statement I've got that's ANSI incompatible. And I got lots of comments. [laughter] Unfortunately . . . I'm not sure it's very flexible because I sure like those little extras--format statements and things like that.

Lee: I think this is a very difficult problem, and I just want to bring it up so anybody can say a few words about it. People are constantly trying to exchange codes, and there's always a problem.

Lee: Is there any other area people would like to discuss?

12. A common insolation Model.

Vant-Hull: I guess one more possibility is to say something about the insolation model that people use. It may be that it's impossible to convince everyone to use the same insolation model, but, surely, it should be possible to crank out the insolation model. . . in most cases, anyway. I don't know that there is a standard insolation model that we can agree on. If someone thinks there is, I would like to hear his suggestions. The model we use is a pure, clear air which has no allowance for clouds or turbidity. . . .

Riaz: I would say one kilowatt per meter squared at all times. [laughter]

Vant-Hull: Well, I think that's what ERDA has done, only they chose 950 watts/m^2 to confuse the issue. But for optimization that's unrealistic because you clearly don't get that when the sun is variable in the sky. What we do is also not completely realistic.

Lee: Isn't there a one year data tape from China Lake that we can use for direct insolation? Is one year enough? It's better than none.

Vant-Hull: But the Aerospace insolation tapes are made up by picking a year of horizontal data at Inyokern and trying to figure out how to get direct beam data from that. So I think that's probably even less good than the year's data that has been obtained recently at Barstow.

Lee: Well, I guess we don't really want to talk about realistic data.

Laurence: I disavow all knowledge of those Aerospace tapes.

Lipps: I object strongly to using real insolation data, as data for any one year is totally spurious.

Participant: I think the Inyokern tapes, for example, have very low insolation for winter. There are months there with essentially no direct beam sunlight, but there's your problem.

Lipps: The only thing that you can do which is better than idealized insolation, is [provide] well-founded correlations. For instance, if you know very well that at the site you have problems in the winter, you ought to put it in; but, if you don't really know what the correlations are, then you really ought to use an idealized insolation. Now, there are two ways to get that: you either get it out of the astronomical people who have good air measurements that are smooth to begin with, or you take . . . a lot of data and smooth it out statistically. The kind of data that we need now--direct beam--there isn't enough of. There surely isn't enough that's been looked over well enough that the "glitches" are all out of it.

Lipps: There's getting to be quite a bit of direct beam data accumulated. But putting that in a format where I think anyone would be happy with using it other than to crank through the performance of a typical year of a particular power plant, if that should be a requirement, would be a lot of work.

Lee: There are TDF 14 tapes with a horizontal sensor, and we use that with an accurate model to come up with at least a whole stream of direct insolation. That would mean everybody uses the same thing and that's impossible.

Participant: That requires you to run your simulation routine for every hour of every day of the year before you can use that.

Lee: That correlation is very cheap. There are cloud covers, etc., that can be involved in a standard

correlation. Any other comments?

McFee: I think you have a similar situation impressed on this circumsolar radiation as well as the atmospheric attenuation in the intermediate path between heliostat and receiver . . . not as significant as the insolation period. However, we do need to use them in any model of precision, and that needs to be standardized to some degree, perhaps.

Lee: Right.

Laurence: As I've heard various papers, I've heard people who are taking into account different effects. Some people neglect this; some people are taking this into account; some people get concerned about different things. Very few of us have gotten it all in there, and I'd like to encourage everybody to write up those specialized aspects. I don't know how we'll disseminate that kind of information, but it would be very useful material to other people. I'm talking about things like wind deflection effects and special studies. And I know a lot of people are going to be modelling the circumsolar effects. Again, that varies an awful lot, too, and I don't know how that's going to be done.

Arlon Hunt, Lawrence Berkeley Laboratory: Right, Berkeley is working very hard on that problem and will come up with some specific answers designed for applications such as ours.

Lee: LBL will come out with tapes, data tapes, that we can get or card decks that you can get and go off and use it as a standard.

Laurence: Yes, but I agree with Fred that with the computer programs we're going to need models.

Lipps: Well, anyhow, I'd started a checklist, and the circumsolar is an item that's not in there, and I can put it in. [laughter] And you're welcome to return as many ideas like that as possible. That's the reason we can update the things like this catalogue. Of course, it won't be any good unless we mail it out often enough . . . and I don't know about that.

13. The publication of an aperiodic newsletter to involved and interested personnel and firms.

Hunt: I think the first thing is to get people that look at our circumsolar date to make any comments they are willing to make. And I think we can attempt to update this once within a few months and get it out and then consider where we go from there.

Lee: Again, I think an idea of an aperiodic newsletter is the best thing. Anytime you feel you're comfortable, you send out some information. You send it to everybody.

Vant-Hull: For example, the bibliography that people send us--bibliographic lists--we can compile after a while, and [when] we seem to be not getting many anymore, either send it out or send a note that we have it available for anyone who asks for it.

Lee: I think that is a great thing for information exchange, and I think we should try to encourage everyone to try and do that. Concentrate information like the bibliography and other information like that [in] Houston, and Houston, in turn, can distribute it. Any other area?

14. Problems in studing stochastic data in the analysis of flux distributions; problems in determining the effects of systematic or stochastic processes on flux distributions and on overall system performance.

John D. Reichert, Electrical Engineering Department, Texas Tech University: I'm kind of curious what the state of the attitude is toward the kind of stochastic data that you have in the distribution inside a receiver where you're trying to interface with the guys who've got to pick up the light and absorb it and

and get it to the fluid, and they, for some reason or other, didn't care what the distribution is either on the outside or on the inside of the receiver.

Lee: You're talking about the Flux distribution?

Reichert: Yes. The guy after us [who] has to get it into his fluid. Some Sins in computing the optical distribution are forgiven by the thermal transfer. The fluid doesn't care about some of these things, but we have various deploys and presences of winds and this deploys them a little bit. And then there's a stochastic kind of error that has to do with the specs that we met when we put the mirrors up. So there's a kind of uncertainty involved when we predict a concentration distribution. I think that before we build the system, we would like to estimate what is the likelihood that the specific system that you build, trying to represent this idealized case, will actually give a distribution that looks like the one we expect. Now, the methods I think people are using are of two kinds: [1] Some people try to blame it on the sun and speak of an effective sun size. That's largely when the wind rattles the rig a little bit, so that it's just sweeping the sun back and forth a little bit in that particular element and you try to blame it on the sun . . . and it's kind of like the sun is bigger in the sky. And then you need some rule of thumb for how much bigger and what kind of wind or how much bigger and what kind of tolerance in the specs or how much bigger and what kind of work crew you've got to set them up. [2] The other kind of philosophy would be to assign some kind of a priori probability distribution function and then attempt to do an expected concentration and, maybe, a moment of that concentration. . . and [estimate] what kind of shape . . . the world [is] in in that situation.

Lee: I don't know; it depends. I think the heat transfer people would probably be happy to discuss a flux map--a single average map. I don't know anybody who has given that much thought to the probability of distribution.

Vant-Hull: Well, one can do some worst case things. For example, with the wind, rather than putting it in stochastically, you could say the wind is blowing from the north and every heliostat deflects . . . . What does that do to the location of the flux zone or the peakedness of the flux?. . .

Reichert: It's hard, Lorin, to know what worst case is. The wind blows and redistributes the flux in the peak, and the thermal guy says, "Great, that spreads the flux over a bigger transfer area.". . . It's a little hard to judge what worst limit is in these things; performance is so many codes downstream from the optical concentration code that you've got to talk to three guys later down to find if that change in the distribution hurt them.

Vant-Hull: But you can find out how big the change is.

Lee: Get an estimate. I don't know.

Reichert: I think there's a lot to be said if you can get some kind of correlation just for oversizing the sun a little bit . . . say, if the disc of the sun is bigger than it really is. That's simplest of all wrong methods, and I think that one has a lot to be said for it.

Lee: That's one way . . . one experiment we can do.

Reichert: Yes. I think we can use that method, and I think a number of people in the room have done so.

Lee: Well, if there's no other comment then, we'll close the meeting and everybody's free to organize his own discussion group and continue from there. And again, I thank everybody for participating. I'd also like to thank the Houston people for organizing this [workshop].

The transcription of the discussion has been edited to retain essential dialogue.

A complete record of the discussion is available on two cassette tapes at a cost of $8.00 for the set. Tapes may be ordered by writing to:

Coordinator, Solar Workshop
Solar Energy Laboratory 105 EOA
University of Houston
4800 Calhoun Road
Houston, Texas 77004

Responsibility for editing the discussion rests with the Coordinator of the Solar Workshop on Methods for Optical Analysis of Central Receiver Systems.

ERDA WORKSHOP ON METHODS FOR OPTICAL ANALYSIS OF CENTRAL RECEIVER SYSTEMS

ORGANIZED BY THE SOLAR ENERGY LABORATORY
UNIVERSITY OF HOUSTON
FOR SANDIA LABORATORIES--LIVERMORE

AUGUST 10,11 1977 [RECEPTION-AUGUST 9]

SCHEDULE — TUESDAY, AUGUST 9, 1977

5:00 P.M. 2ND FLOOR LOBBY CONTINUING EDUCATION CENTER	REGISTRATION [TELEPHONE: 749-3566]
5:00-8:00 P.M. DINING ROOM UNIVERSITY OF HOUSTON HOTEL	NO-HOST DINNER [DUTCH TREAT]
7:00 P.M. SCORPIUS ROOM--275 CONTINUING EDUCATION CENTER	MEETING ON WORKSHOP PROCEEDINGS: Persons delivering presentations will meet with the Coordinator to submit typed presentations for the Proceedings.
8:15 P.M. GEMINI ROOM--228 CONTINUING EDUCATION CENTER	COCKTAIL RECEPTION

THE UNIVERSITY OF HOUSTON HOTEL AND CONTINUING EDUCATION CENTER ARE ADJACENT FACILITIES ON THE UNIVERSITY OF HOUSTON CENTRAL CAMPUS. THERE IS FREE UNDERGROUND PARKING FOR HOTEL GUESTS.

ERDA WORKSHOP ON METHODS FOR OPTICAL ANALYSIS OF CENTRAL RECEIVER SYSTEMS

ORGANIZED BY THE SOLAR ENERGY LABORATORY
UNIVERSITY OF HOUSTON
FOR SANDIA LABORATORIES--LIVERMORE

AUGUST 10-11, 1977

SCHEDULE — WEDNESDAY, AUGUST 10, 1977

7:30 A.M. LEO ROOM--210D	CONTINENTAL BREAKFAST
8:00 A.M. SOLAR ROOM--180	CALL TO ORDER / INTRODUCTIONS Lorin L. Vant-Hull, University of Houston
	OPENING ADDRESSES Barry Munitz, Interim Chancellor Central Campus, University of Houston Roy Lee, Sandia: ERDA
	1ST SESSION--INDIVIDUAL HELIOSTAT OPTICS Roy Lee, Sandia Laboratories, Livermore (Chairman)
8:30 A.M. SOLAR ROOM--180	FUNDAMENTAL PHYSICS OF CONE OPTICS George Schrenk, University of Pennsylvania
9:30 A.M. SOLAR ROOM--180	IMAGE GENERATION Mike Walzel, University of Houston
10:00 A.M. SOLAR ROOM--180	Coffee Break
10:15 A.M. SOLAR ROOM--180	SHADING AND BLOCKING PROCESSOR AND RECEIVER MODEL Fred Lipps, University of Houston
10:45 A.M. SOLAR ROOM--180	ABERRATIONS, APERTURE EFFICIENCY, ETC., FOR THE 5MW TEST FACILITY HELIOSTAT Walter Hart, Martin-Marietta
11:45 A.M. AQUARIUS ROOM--210	LUNCHEON (RECONVENE AT 1:00 P.M. in SOLAR ROOM)

PRESENTATIONS AND DISCUSSIONS WILL BE RECORDED ON AUDIO CASSETTES. CASSETTES WILL BE AVAILABLE FOR PURCHASE. DETAILS WILL BE ANNOUNCED AT THE WORKSHOP.

ERDA WORKSHOP ON METHODS FOR OPTICAL ANALYSIS OF CENTRAL RECEIVER SYSTEMS

ORGANIZED BY THE SOLAR ENERGY LABORATORY
UNIVERSITY OF HOUSTON
FOR SANDIA LABORATORIES--LIVERMORE

AUGUST 10-11, 1977

SCHEDULE	WEDNESDAY, AUGUST 10, 1977

1:00 P.M. — 2ND SESSION--HELIOSTAT ARRAYS
SOLAR ROOM--180 — Roy Lee, Sandia Laboratories, Livermore (Chairman)

ANALYTIC CALCULATION OF CENTRAL RECEIVER FLUX
Mahmoud Riaz, University of Minnesota

2:00 P.M. — CENTRAL RECEIVER OPTICS
SOLAR ROOM--180 — Ed McBride, Black & Veatch Consulting Engineers

3:00 P.M. — Refreshments: Punch and Cookies
SOLAR ROOM--180

3:15 P.M. — CIRCUMSOLAR RADIATION DATA FOR CENTRAL RECEIVER SIMULATION
SOLAR ROOM--180 — Arlon Hunt, Donald Grether and Michael Wahlig
Lawrence Berkeley Laboratory, Berkeley, California

3:45 P.M. — STRATEGY OF OPTICAL CALCULATIONS FOR FIXED MIRRORS
SOLAR ROOM--180 — John D. Reichert, Texas Tech

4:15 P.M. — HELIOS: COMPUTER SIMULATION OF A FIELD OF HELIOSTATS
SOLAR ROOM--180 — Frank Biggs and Charles Vittitoe, Sandia Laboratories, Albuquerque

5:30 P.M. — CONCLUSION OF WEDNESDAY WORKSHOP

6:30 P.M. — LOAD BUSES TO SAN JACINTO INN FOR SEAFOOD DINNER
FRONT ENTRANCE
CONTINUING EDUCATION
CENTER & HOTEL

7:30 P.M. — DINNER AT THE SAN JACINTO INN (DUTCH TREAT)

ERDA WORKSHOP ON METHODS FOR OPTICAL ANALYSIS OF CENTRAL RECEIVER SYSTEMS

ORGANIZED BY THE SOLAR ENERGY LABORATORY
UNIVERSITY OF HOUSTON
FOR SANDIA LABORATORIES--LIVERMORE

AUGUST 10-11, 1977

SCHEDULE	THURSDAY, AUGUST 11, 1977
7:30 A.M. LEO ROOM--210D	CONTINENTAL BREAKFAST
8:00 A.M. SOLAR ROOM--180	CONTINUATION OF 2ND SESSION Lorin L. Vant-Hull, University of Houston [Chairman]
	CONCEN: A HELIOSTAT OR ARRAY RAY TRACE SIMULATION CODE Ray McFee, McDonnell Douglas Astronautics Co.
9:00 A.M. SOLAR ROOM--180	HELIOSTAT ARRAY SIMULATION Mark Rubeck, Boeing Engineering & Construction Co.
10:00 A.M. SOLAR ROOM--180	Coffee Break
10:15 A.M. SOLAR ROOM--180	MONTE CARLO RAY TRACE SIMULATION FOR A HELIOSTAT OR POWER TOWER FIELD Gary Smith, Honeywell
11:30 A.M.	Check-out, University Hotel
NOON AQUARIUS ROOM--210	LUNCHEON
1:00 P.M. SOLAR ROOM--180	RECONVENE

ERDA WORKSHOP ON METHODS FOR OPTICAL ANALYSIS OF CENTRAL RECEIVER SYSTEMS

ORGANIZED BY THE SOLAR ENERGY LABORATORY
UNIVERSITY OF HOUSTON
FOR SANDIA LABORATORIES--LIVERMORE

AUGUST 10-11, 1977

SCHEDULE — THURSDAY, AUGUST 11, 1977

1:00 P.M. SOLAR ROOM--180	3RD SESSION--OPTIMIZATION / DISCUSSION Lorin L. Vant-Hull, University of Houston [Chairman]
	MIRVEL: A MONTE CARLO RAY TRACE CODE FOR SOLAR TOWER OPTICS Joe Hankins, Sandia Laboratories, Livermore
2:00 P.M. SOLAR ROOM--180	COLLECTOR FIELD OPTIMIZATION AND LAYOUT Fred Lipps, University of Houston
2:45 P.M. SOLAR ROOM--180	GENERAL DISCUSSION Roy Lee, Sandia Laboratories, Livermore
	--Suggested Code Improvements --Authors' Desires --Users' Desires --Future Developments
3:15 P.M. SOLAR ROOM--180	Refreshments: Coke, 7UP
3:30 P.M. SOLAR ROOM--180	OPEN AND GROUP DISCUSSIONS (SELF-ORGANIZED) CODE INTERCHANGE
	Departure to airport; check flight departures. Intercontinental Airport is 25 miles from the University by freeway through central Houston:

Latest cab departure:	4:00	4:20	4:30	4:40	5:00	5:30	6:00	7:00
Flight departures: ↓	5:30	6:00	6:30	7:00	7:00	7:15	7:30	8:30

5:00 P.M. UNIVERSITY HOTEL	NO-HOST DINNER [DUTCH TREAT] (Room Reservations may be held over Thursday evening in the University Hotel)

THIS PAGE

WAS INTENTIONALLY

LEFT BLANK

ROSTER OF PARTICIPANTS
August 10-11, 1977

Babu Bapna
Westinghouse
P. O. Box 10864
Pittsburgh, Pennsylvania 15236
(412) 892 5600 x 6713

Andrew H. Bass, Jr.
University of Pennsylvania
Department of Mechanical Engineering
Philadelphia, Pennsylvania 19174
(215) 243 6496

Frank Biggs
Sandia Laboratories
P. O. Box 5800
Albuquerque, New Mexico 87115
(505) 264 7367

Floyd Blake
Martin Marietta
Denver, Colorado
(303) 979 7000

Terence B. Clark
Ford Aerospace & Communications Corp.
Aeronutronic Division
Ford Road
Newport Beach, California 92663
(712) 459 6227

K. J. Daniel
General Electric
Schenectady, New York
(518) 385 9451

S. Bear Davis
Sanders Associates
MER 12 1214
95 Canal Street
Nashua, New Hampshire
03060
(603) 885 3212

Theodore Dellin
Solar Technology Division 8131
Sandia Laboratories
Livermore, California 94550
(415) 422 2564

Joel DuBow
Electrical Engineering Department
Colorado State University
Fort Collins, Colorado 80523
(303) 491 8235

James C. Eastwood
Garrett AiResearch of Los Angeles
Building 36, Dept. 93-5
2525 West 190th Street
Torrance, California
(213) 323 9500

Nabil El Gabalawi
Jet Propulsion Laboratory
4800 Oak Grove Drive
Building 277, Room 204
Pasadena, California 91103
(213) 354 3160/5388

Peter B. Grytness
Mann-Russell Electronics
1401 Thorne Road
Tacoma, Washington 98421
(206) 383 1591

Joe D. Hankins
Sandia Laboratories
Livermore, California
(415) 422 2830

Walt Hart
Martin Marietta
Denver, Colorado
(303) 979 7000

Arlon Hunt
Building 50-205C
Lawrence Berkeley Laboratory
Berkeley, California 94720

Philip O. Jarvinen
Energy Systems Engineering
MIT-Lincoln Laboratory
Lexington, Massachusetts
(617) 862 5500 x 7591

Theo L. Johnson
Atomics International
8900 DeSoto Avenue
Canoga Park, California 91504

M. M. Katzer
General Electric
Schenectady, New York
(518) 385 7457

W. F. Knightly
General Electric
Building 23, Room 334
Schenectady, New York 12345
(518) 385 4988

C. L. Laurence
Aerospace Corp.
El Segundo, California
(213) 648 6150

E. Y. Lam
Bechtel Corp.
P. O. Box 3965
San Francisco, California 94119
(415) 768 6895

Pat Leary
Sandia Laboratories
Livermore, California
(415) 422 2830

Roy Y. Lee
Sandia Laboratories
Livermore, California 94550
(415) 422 2127

Frederick W. Lipps
University of Houston
Solar Energy Laboratory
Houston, Texas 77004
(713) 749 4861

S. D. Luedders
Stearns-Roger Engineering Co.
P. O. Box 5880
Denver, Colorado 80217
(303) 770 6400

K. L. Matthews
Sandia Laboratories
Division 5713
Albuquerque, New Mexico 87115
(505) 264 6061

Edward J. McBride
Black & Veatch
P. O. Box 8405
Kansas City, Missouri 64114
(913) 967 2162

R. H. McFee
McDonnell Douglas
Huntington Beach, California
(714) 896 2364

Stephen J. Orbon
Westinghouse Advanced Reactor Division
P. O. Box 158
Madison, Pennsylvania 15663
(412) 722 5681

Joseph Protole
MS 725-5
Honeywell, Inc.
Avionics Division
US Hwy 19
St. Petersburg, Florida 33733
531 4621

John D. Reichert
Texas Tech University
Electrical Engineering
Lubbock, Texas 79409
(806) 742 3441

D. L. Renschler
General Electric
Schenectady, New York
(518) 385 3302

M. Riaz
University of Minnesota
Electrical Engineering Department
Minneapolis, Minnesota
(612) 373 2472

Mark Rubeck
Boeing Engineering & Construction
Seattle, Washington
(206) 773 2441

George F. Russell
Mann-Russell Electronics
Tacoma, Washington 98421
(206) 383 1591

George G. Schrenk
University of Pennsylvania
Department of Mechanical Engineering
Philadelphia, Pennsylvania
(215) 243 5121

John B. Sinacori
Aeronautical Consultant
P. O. Box 37
Aromas, California 95004
(408) 724 1945

Gary Smith
Honeywell, Inc.
Minneapolis, Minnesota
(612) 378 4960

Larry Stoddard
Black & Veatch
P-5A1; Box 8405
Kansas City, Missouri
(913) 967 2377

Kathryn Szabat
Brookhaven National Laboratory
Accelerator Dept. Building 911
Upton, New York
(516) 345 4636

Kevin Thompson
Optical Sciences Center
University of Arizona
Tucson, Arizona 85711
(602) 884 3460

Lorin L. Vant-Hull
Solar Energy Laboratory
University of Houston
Houston, Texas 77004
(713) 749 4861

Charles N. Vittitoe
Sandia Laboratories
P. O. Box 5800
Albuquerque, New Mexico 87115
(505) 264 5275

Kenneth J. Waldron
University of Houston
Department of Mechanical Engineering
Houston, Texas 77004
(713) 749 4455

Michael D. Walzel
Solar Energy Laboratory
University of Houston
Houston, Texas 77004
(713) 749 4861

L. Wen
Jet Propulsion Laboratory
4800 Oak Grove Drive
Pasadena, California 91011
(213) 354 3578

Michael Wolf
Black & Veatch
P-5A1; Box 8405
Kansas City, Missouri 64114

James B. Woodard
Sandia Laboratories
Livermore, California 94550
(415) 422 2049

TAPED PROCEEDINGS

Cassette tape recordings are available of the complete proceedings of the ERDA Solar Workshop on Methods for Optical Analysis of Central Receiver Systems, Organized by the University of Houston Solar Energy Laboratory for Sandia Laboratories, Livermore, August 10-11, 1977. A complete set of fourteen 90-minute tapes may be purchased at a cost of $56.00. Tapes of individual papers may be purchased at a cost of $4.00 each.

Write:

Coordinator, Solar Workshop
Solar Energy Laboratory--105EOA
University of Houston
Houston, Texas 77004